Zia Kazemi

Droplet Impaction on Solid Surfaces Exposed to Impinging Jet Fires

Doktoravhandling
for graden doktor ingeniør

Trondheim, desember 2005

Norges teknisk-naturvitenskapelige universitet
Fakultet for ingeniørvitenskap og teknologi
Institutt for energi- og prosessteknikk

NTNU
Norges teknisk-naturvitenskapelige universitet

Doktoravhandling
for graden doktor ingeniør

Fakultet for ingeniørvitenskap og teknologi
Institutt for energi- og prosessteknikk

ISBN 82-471-8108-8 (trykt utg.)
ISBN 82-471-8106-1 (elektr utg.)
ISSN 1503-8181

Doktoravhandlinger ved NTNU, 2006:169

Trykt av Tapir Uttrykk

Droplet Impaction on Solid Surfaces Exposed to Impinging Jet Fires

A doctoral dissertation

by

Zia Kazemi

Submitted in partial fulfillment of
the requirements for the degree of

Doktor Ingeniør

Department of Energy and Process Engineering
Norwegian University of Science and Technology
N-7491 Trondheim, Norway

December 2005

Preface

The aim of the present work is to investigate the phenomenon of *hot spot* in steel components when exposed to large hydrocarbon fires. The event would take place by exploring its mechanism of occurrence and finding a method to prevent or mitigate it by means of water droplets. By hot spot, it means deep heat or localized high temperature pulses in solids, typically identified and recognized by red-hot or glowing points on a surface. This addresses particularly oil and gas installations offshore and onshore, chemical plants, etc.

The work is carried out experimentally both with laboratory and large scale equipments. The later which also comprises major part of the research was among others composed of unconfined jet fire. Under way one gained access to the CFD-code Kameleon FireEx which made it tempting and interesting to validate the experimental results contra calculations using the code. This extended the scope of the work in proportion to the original plan.

The experimental part of the study was performed in four phases. In the first stage a bench scale steel plate was studied, while in the second and third stage focus was made on a full scale quadratic steel channel and steel plates, respectively. Water droplets were not applied in event of the steel channel. The fire in case of bench scale experiments was introduced by a burner connected to a 17-kg propane bottle, while the fire source for field experiments was a 14 MW high momentum turbulent propane jet flame. In addition the jet flame itself was characterized in a comprehensive work, which originally was not part of the plan.

The CFD part of the study concerned modeling of the jet flame and full scale experiments with steel channel and steel plates.

Acknowledgment

I would like to express my sincere gratitude to my supervisor Professor Bjørn F. Magnussen for his continuous advise, inspiration, encouragement, and support through the process of my dissertation. I am greatly indebted to express my warm appreciation to my first supervisor Professor Odd Andreas Asbjørnsen whom unfortunately passed away early in the process of my work, and my present advisor Associate Professor Erling Østerbø whom together encouraged and supported me in getting started a Ph.D. program. I would like to thank Mr. Østerbø also for his continuous advise and interest for my work.

I highly appreciate my previous employer Stord Haugesund University College (SHUC) through whom I was a fellowship and they made the conditions favorable for my work. Thanks are due to Professor Torgrim Log at SHUC for assisting me in choosing the research area, a number of fruitful discussions, and reading and commenting the manuscript. I would like particularly to appreciate Mr. Gisle Kleppe for his valuable support for providing and helping me with the data logging program LabView and other software related issues, as well as discussions regarding instrumentation. Thanks are also extended to my fellow Ph.D. student Mr. Leiv Anfin Drange for working on a joint project including numerous discussions. The teamwork resulted in publishing an article which is discussed under "Characterization of Jet Flame" in Section 4.2.2. I am also grateful to Mr. Gerad Wanger and Mr. Arnstein Gjestland for a number of software supports concerning UNICS used in CFD part of the work.

I wish to express my truthful gratitude to the staffs at the safety course center ResQ AS for making the conditions favorable to carry out my full scale experiments.

ComputIT AS, the owner and developer of CFD-code Kameleon FireEx, is greatly acknowledged for a number of CFD discussions through the entire work.

The process of accomplishment of this thesis has gone through by getting impulses and inspirations from several text books on research methodology

[1, 2, 3, 4, 5, 6, 7, 8]. While the typesetting and documentation was prepared with LaTeX. Since this was the author's very first time to use LaTeX, it required some readings on related topics in various literature [9, 10, 11, 12, 13, 14, 15, 16, 17, 18, 19, 20]. For preparation of the bibliography, the program BibTexMng was used, and the results were implemented in LaTeX.

Summary

The thermal response of hot surfaces exposed to impinging jet fire and subsequent impacting water droplets is investigated. The research was done mainly experimentally by utilizing three different concepts. This included experiments on a laboratory scale steel plate and large outdoor fire tests with a quadratic steel channel and steel plates. Besides the horizontal jet flame itself was characterized in a comprehensive study. As a comparative study, the last three types of the experiment were additionally modeled by the CFD-code Kameleon FireEx for validation of results.

Benchmark steel plate: The purpose of the experiments done on bench scale steel plate (L $\times$ W $\times$ T : 300 $\times$ 200 $\times$ 8 mm) was mainly to map data on wetting temperature, water droplet size, droplet impingement angle, and droplet velocity prior to large scale jet fire tests. The droplet release angle normal to hot surface gives best cooling effect, when the surface is oriented in upright position. The partial wetting begins at about 165 °C. When the surface is positioned in horizontal plane, the droplet of about 5 mm in diameter wets the hot surface partially at around 240–250 °C within an impaction distance of 20 cm. At about 150 °C, the droplet is entirely attached to the surface with almost zero contact angle, and cools down the solid at a critical heat flux equivalent to 1750 kW/m^2. The cooling effectiveness is about 8 % with a Weber number of 68.

Jet fire test with steel channel: Although in the event of horizontal channel (L $\times$ W $\times$ T : 1000 $\times$ 200 $\times$ 8 mm) water droplets were not applied, however, the knowledge gained with jet fire tests gave valuable information about temperature progress in solids (steels and insulation) and their response to impinging jet fire during long duration experiments. The temperature of the insulated area of the channel keeps 200 °C below that of the exposed surface, as long as the insulation material remained intact. Upon long test fire durations, the insulation either burns or degrades despite protection in a metal encasing. This possibly reveals that the passive fire protection

does not necessary guaranty the solids subjected to fire would survive, when the exposure time is extended, although in this study the surface keeps its consistency.

Jet fire test with steel plates: Two types of plate (L × W × T : 300 × 300 × 10 mm) were employed, where one of them was insulated with 70 mm rockwool material on the rear side. Despite high elevated temperatures of the steel plates, one depressed the surface temperatures by water droplets from film boiling to nucleate boiling regime by a water mass flux of 4.4 kg/m^{2}s per plate, when spray nozzles were located outside the flame region. As the gas pressure was raised from 5 bar to 10 bar, the average critical heat flux for non-insulated and insulated plate increased by about 40 % to around 2100 kW/m^2 and 75 % to 2000 kW/m^2, respectively. While the average minimum heat flux increased approximately by 35 % to 410 kW/m^2 and 150 % to 380 kW/m^2, respectively. The radiation level on the surrounding area within a 3 m radial distance increases by a factor of 1.5–2 upon increase of gas pressure. However, it drops by 25 % when deluge is applied, due to cooling of the flame.

In case of spray nozzles located directly within the flame, the surface temperatures remained within nucleate boiling regime almost throughout the experiments. To ensure the temperatures are maintained at this regime, it requires a minimum mass flux of 1.1 kg/m^{2}s per plate. However, to keep the dry patches completely away, the flow rate needs to be fortified to about 2.6-2.7 kg/m^{2}s. The average droplet size (SMD) in the event of earlier is around 650 μm, while that of the later is about 450 μm.

Characterization of jet flame: The horizontal flame of concern was about 5.5 m long, in addition to a lift-off distance of 60 cm. The warmest region of the flame is about 70 % downstream the visible length of the flame, with an average temperature of about 1100 °C across the concerned cross section. The corresponding radiation at this section along the jet centerline is around 185 kW/m^2. While the radiation level at 1.5 m radial distance outside the flame is about 50 kW/m^2. The highest temperature of the flame across almost any cross section is somewhere between the flame core and the outer edge of the flame.

CFD verification: The CFD-code predicts well the exposed surface temperature of the steel channel, while that of the insulated area is predicted too high. The calculated surface temperature of the non-insulated steel plate is well comparable with that of the experiments, both before and after activation of deluge. But that of the insulated plate as well as the insulation

material is estimated too high. The code predicts almost the same flame length, but slightly shorter lift-off distance. Otherwise, the simulated flame is more influenced by buoyancy at the end part of the flame than the experiment flame does.

Contents

List of Figures

List of Tables

Nomenclature

A	interface area of a drop or bubble	[m^2]
A_{fu}	surface area of fuel	[m^2]
a	constant in soot model	[-]
a_o	constant in soot model	[-]
B	flame lift-off distance	[m]
b	constant in soot model	[-]
C	constant in heat transfer model for film boiling	[-]
C	stoichiometric molar concentration of fuel	[mol/mol]
C_p	specific heat capacity	[J/kgK]
C_{sf}	constant in heat transfer model for nucleate boiling	[-]
C_μ	constant in $k-\epsilon$ model	[-]
$C_{\epsilon 1}$	constant in ϵ equation	[-]
$C_{\epsilon 2}$	constant in ϵ equation	[-]
c_{fu}	fuel concentration	[kg/m^3]
c_j	molar concentration of species j	[mol/mol]
$\mathcal{D}$	mass diffusivity	[m^2/s]
D	cylinder or sphere diameter, orifice diameter	[m]
D_a	Damköhler number (θ/τ_c)	[-]
D_{aK}	Damköhler-Karlovitz number (τ/τ_c)	[-]
D_j	mass diffusion coefficient for species j	[-]
D_{jm}	multicomponent binary diffusion coefficient for species j	[-]
D_{max}	maximum diameter of fireball	[m]
D_p	pool diameter	[m]
d_{max}	maximum droplet diameter	[m]
d_p	soot particle diameter	[Å]
d_g	outside diameter of heat flux gage	[m]
E	radiative power	[kW/m^2]
F	body forces	[N]

F	radiation fraction	[-]
f	constant in soot model	[-]
f_c	mass concentration of carbon	[kg/kg]
f_i	acceleration in x_i-direction	[m/s^2]
G	water mass flux	[kg/m^{2}s]
g	constant in soot model	[-]
g	gravitational acceleration	[m/s^2]
g_o	constant in soot model	[-]
H_c	combustion heat of fuel	[kJ/kg]
H_v	vaporisation heat of fuel	[kJ/kg]
h	convection heat transfer coefficient	[W/m^{2}K]
h	static specific enthalpy	[J/kg=m^2/s^2]
h_L	latent heat of vaporization	[J/kg]
J_j	molar diffusion concentration of species j	[mol/mol]
k	turbulent kinetic energy	[J/kg=m^2/s^2]
k	thermal conductivity	[W/mK]
L	flame length, particle size	[m]
l	characteristic turbulent length scale, thickness	[m]
M_{fu}	total fuel mass	[kg]
M_w	molecular weight of fuel	[g/mol]
m	molar ratio of reactants to products	[mol/mol]
m_j	molecular weight of component j	[g/mol]
m_p	soot particle mass	[kg/part]
$\dot{m}$	mass flow rate	[kg/s]
$\dot{m}''$	mass burning rate	[kg/m^{2}s]
N	soot particle concentration	[kg/kg]
n	radical nuclei concentration	[parts/m^{3}s]
n	unit vector normal to drop surface	[-]
n_o	spontaneous formation rate of radical nuclei	[parts/m^{3}s]
P_k	production term in k equation	[W/kg=m^2/s^3]
p	static pressure	[N/m^2]
Q	combustion heat release	[MW]
q	dissipation in Cascade model	[W/kg=m^2/s^3]
q_T	total heat transfer	[kJ=kWs]
$\dot{q}''$	heat flux	[W/m^2]
R	curvature radius of leading edge of drop	[m]
R	distance from point source, radius of wetted area	[m]
R_{fu}	reaction rate of fuel	[mol/ls]
R_{pr}	reaction rate of product	[mol/ls]
R_k	reaction rate of species k	[kg$_k$/m^{3}s]
$R_{n,f}$	rate of formation radical nuclei	[parts/m^{3}s]

$R_{s,f}$	rate of soot particle formation	[kg/m^{3}s]
Re_K	turbulent Reynolds number ($=u'\lambda/\nu$)	[-]
$Re_{l'}$	characteristic turbulent Reynolds number ($=u'l'/\nu$)	[-]
Re_λ	Kolmogorov turbulent Reynolds number ($=u'\eta/\nu$)	[-]
r	oxidant-to-fuel weight ratio	[kg/kg]
r	radial coordinate in spherical coordinates	[m]
r	radial coordinate tangent to solid surface	[m]
S	surface emmisive power	[kW/m^2]
S_h	reaction energy at static enthalpy	[kg/ms^3]
s	curvilinear distance along flame axis	[m]
T	temperature	[K]
t	time	[s]
U	overall heat transfer coefficient	[W/m^{2}K]
u	fluid or jet velocity	[m/s]
u_i	velocity component in x_i-direction	[m/s]
u_j	velocity component in x_j-direction	[m/s]
u_k	velocity component in x_k-direction	[m/s]
u_L	laminar flame speed	[m/s]
u_r	velocity component in radial direction in spherical coordinates	[m/s]
u_θ	velocity component in tangential direction in spherical coordinates	[m/s]
u_ϕ	velocity component in axial direction in spherical coordinates	[m/s]
V	volume	[m^3]
v	Kolmogorov's micro velocity scale	[m/s]
v	wind velocity, droplet velocity	[m/s]
W	mass fraction of fuel in stoichiometric mixture	[kg/kg]
w	energy transfer in Cascade model	[W/kg=m^2/s^3]
x_a	vapor molar fraction in air	[mol/mol]
x_i	cartesian coordinate in i-direction	[m]
x_i	vapor molar fraction at droplet-surface interface	[mol/mol]
x_j	cartesian coordinate in j-direction	[m]
x_k	cartesian coordinate in k-direction	[m]
Y	mass fraction	[kg/kg]
y	axial coordinate normal to solid surface	[m]
z	non-dimensional radius (r/R)	[-]
z	vertical distance of drop hanging from a surface	[m]

Greek symbols

α	thermal diffusivity	[m^2/s]
β	shape factor or wetting parameter	[-]
ϵ	dissipation rate of turbulent kinetic energy	[W/kg=m^2/s^3]
ϵ	surface emissivity, sensor absorptance	[-]
θ	tangential coordinate in spherical coordinates	[m]
θ	turbulence time scale	[s]
θ_a	advancing liquid-solid contact angle	[degree]
γ	square root of thermal inertia ($\sqrt{c_p \rho k}$)	[W$s^{0.5}/m^2$K]
η	cooling effectiveness	[-]
δ	shape parameter	[-]
δ_{ij}	Kronecker-delta (=1 when $i = j$; =0 when $i \neq j$)	[-]
δ_L	laminar flame thickness	[m]
λ	viscosity coefficient	[kg/ms]
μ	dynamic molecular viscosity	[kg/ms]
μ_B	bulk viscosity	[kg/ms]
ν	kinematic molecular viscosity	[m^2/s]
ξ_{max}	maximum spread factor	[-]
ξ	mixture fraction	[-]
ϑ	drop-solid contact angle	[degree]
ρ	fluid density	[kg/m^3]
σ	Stefan-Boltzmann constant (5.67×10^{-8})	[W/m^2K^4]
σ	surface tension of drop	[N/m]
σ_k	Schmidt number for turbulence energy k	[-]
σ_ϵ	Schmidt number for dissipation ϵ	[-]
Φ	viscous dissipation function	[J/m^2kg]
ϕ	view factor	[-]
ϕ	axial coordinate in spherical coordinates	[m]
τ	atmospheric transmissivity	[-]
τ	Kolmogorov's micro time scale	[s]
τ_c	chemical time scale for flame	[s]
τ	viscous shear tensor	[N/m^2]
ω	characteristic strain rate	[1/s]

Superscripts

$\prime$	fluctuating value
$\prime$, $\prime\prime$	characteristics turbulent scale
$\prime\prime$	per unit area
$\prime\prime\prime$	volumetric quantity
$*$	fine structure in EDC, critical value
$-$	mean value
$\hat{}$	dispersed phase quantity

Subscripts

0	initial value
a	air, average
b	boiling
c	convection
d	diffuse emitter
e	excess, exit, effective, expanded value
F	flame, furnace
f	liquid phase
fg	liquid-vapor phase
fu	fuel
g	vapor phase
i	isotropic emitter
ox	oxidizer
pr	product
sat	saturation
s	surface
ss	steady state
t	turbulent, transient
w	water, surface
∞	ambient condition

Chapter 1

Introduction

This chapter describes the background, the objectives, and how the thesis is organized.

1.1 Background

During the last decades there have been numerous critical incidents, accidents and disasters worldwide involving leakage and uncontrolled combustion of liquefied petroleum gases (LPG). The events include storage, transportation both in pipes and by vehicles, and processing of LPG. Prevention of disasters is a major concern for the oil and gas industry. The hazardous situations occur on- and offshore. An uncontrolled gas leak can result in three major hazards: fire, explosion, and toxic release. A leak of LPG to the atmosphere will result in a mixture of combustible gas and air. In a region along the axis of the gas release, which is rich on combustible gas, and the surrounding air, there will be a zone where petroleum gas and oxygen is mixed, and the concentration is within the flammability limits. This is the region where combustion can occur. The concentration of the LPG will be governed by two factors. Due to the physical properties of the gases at normal temperatures (propane boils at -42.2 °C, butane boils at -0.6 °C), a gas leak is likely to produce a jet controlled mixing due to entrainment near the release, and an atmospheric mixing further away.

But once the fire accident is a fact the necessary measures should be taken immediately in order to limit the escalation of the fire and its hazardous consequences, and hopefully to bring the situation under control. In such cases it is essential to protect actively the exposed components (pipes, storage tanks, and any other units containing hydrocarbons), while at the same time the attempt shall be made to stop the fuel supply to the fire.

For the past two decades a number of mathematical models have been developed to predict the fluid flow characteristics in general (e.g Flow-3D, CFX-4, and CFD-ACE). To predict the behavior of combustion, fire, and explosion, more specific models have been developed such as Kameleon FireEx, COBRA, SOFIE, UMPFIRE, SMARTFIRE, JASMINE, PHAST, and FLACS (explosion). The models are verified by checking for consistency with experimental results. These and similar numerical codes have shown to be effective tools to predict the occurrence and dimension of an event, and its consequences on the surrounding area.

1.2 Objectives

The main scope of this PhD thesis is to study the mechanism of *hot spot* formation in metal objects when exposed to high momentum turbulent jet flames, and investigate how the water droplets affect or prevent the development of hot spots. Special attention shall be made to water droplets size, droplets velocity, water mass flux, and droplets impingement angle as essential parameters to increase the wetting impact.

When an uninsulated, hydrocarbon-bearing object on- or offshore, e.g. pipes, storage tanks, separators, etc., is exposed to large hydrocarbon fires, after a short time the material temperature will rise very rapidly to a high level and causing physical weakness of the material toward tearing point as the exposure time is prolonged. Material impairment combined with building up pressure of the fluid inside the system due to heating and eventually boiling and expansion, may at the end cause material rapture followed by catastrophic results. An effective method to avoid such incident is to cool down the exposed surfaces by water droplets in early phase of the fire, which in turn reduces the build-up pressure.

The train accident in 5^{th} April 2000, in Norway (Lillestrøm) is a good up-to-date example of using such method. An LPG freight train crashed with an ordinary freight train, which stood at standstill on the station. Two LPG tank carriages containing 92 tonnes LPG (mainly propane) smashed end-to-end, damaging manholes on both tanks. Liquid propane initiated to leak out and evaporated to gas, a highly flammable vapor which can ignite and flashing back near the leakage point. Shortly after fire broke out, possibly caused by sparking from the electrical installations or break systems. The flame covered the upper region of both tanks above the liquid level and began heating the liquid and the tanks. While the tanks still remained intact, quick handling by cooling down the exposed areas of both tanks prevented indeed

a possible disastrous BLEVE[1]-incident [21]. See Figure 1.1. There are a number of examples of LPG incidents worldwide, among others the disaster outside Mexico City in 1984, or very recent explosion at oil terminal complex, the Buncefield depot outside London 11^{th} December 2005, while this work is about to be brought to end. Fortunately the incident ended up without loose of life.

Figure 1.1: Cooling down of tanks after train accident in Lillestrøm [21]

To author's knowledge little research has been done on phenomenon of hot spot, while some research works have been carried out with hydrocarbon fires using water spray as a protection medium. This is discussed under Chapter 3 Review of Previous Work on Hot Spot.

[1]BLEVE (Boiling Liquid Expanding Vapor Explosion) is a fire as a result of sudden release of a fluid under pressure. The resulting flash on ground may cover an area hundreds of meters of diameter. The blast wave has tremendous force. The fire ball rises on a thermal column radiating heat, and falling droplets of cool gas cause fires and burns for hundreds of meters around the explosion area.

1.3 Outline of the Thesis

In addition to this introductory part, the basic theory related to this work is covered by Chapter 2. This includes synopsis of theories of turbulent combustion and transport phenomenon with water droplets as well as their governing equations.

Chapter 3 investigates the previous research done on or related to similar issues in this work, which includes mechanism of various hydrocarbon fires and employing liquid droplet in cooling down hot surfaces.

Description of experimental program and setup is given in Chapter 4. Each experimental apparatus is described in detail. This includes jet fire source, benchmark steel plate, large scale jet fire tests with steel channel and steel plates, equipment utilized in characterizing the jet flame, water spray system, and heat flux gage calibration oven.

The experimental results obtained for each setup are visualized and analyzed thoroughly in Chapter 5. A conclusion was then made for each group based on the analysis and interpretation accomplished. In Chapter 6 the experimental work was modeled using CFD-code Kameleon FireEx (hereafter called KFX), and the results attained were presented and discussed on similar manner. While in Chapter 7 the data achieved from the experiment and calculation are compared and discussed.

Ultimately, the essential parts of the work are summarized and a final conclusion is drawn in Chapter 8, before concluding the thesis by listing up recommendations for further work in Chapter 9.

Chapter 2

Basic Theory

2.1 Introduction

The focus in this chapter shall be on principle theories behind and related to the experimental work done in this thesis. In Section 2.2 the basic equations for diffusion turbulent combustion, heat transfer and contribution from soot shall be treated. More specific about equations governing the diffusion jet flames shall be covered in Section 3.1, while in Section 2.3 the droplets theory, its structure and mechanism shall be discussed.

2.2 Turbulent Combustion

Technically almost all types of flow are turbulent. It could be flow inside a tube or other arrangements, or flows around them. On the same manner most of the flames are turbulent, i.e. the turbulence in the flow controls the mixture and so saying the combustion. The physical processes in turbulent combustion can be expressed mathematically through equation of conservation of mass, energy and momentum (impulse, mass motion). This corresponds to the continuity equation, the first law of thermodynamics and the Newton's second law[1].

2.2.1 Basic Equations

For a single-phase flow the governing equations (continuity and momentum) are given as:

[1] $\mathbf{F} = \frac{d(m\mathbf{V})}{dt}$, where $\mathbf{V}$ is mass diffusion velocity.

$$\frac{\partial \rho}{\partial t} + \frac{\partial}{\partial x_j}(\rho u_j) = 0, \tag{2.1}$$

$$\frac{\partial}{\partial t}(\rho u_j) + \frac{\partial}{\partial x_j}(\rho u_i u_j) = -\frac{\partial p}{\partial x_i} + \frac{\partial \tau_{ij}}{\partial x_j} + \rho f_i. \tag{2.2}$$

The stress tensor for a Newtonian fluid is given by

$$\tau_{ij} = \mu \left(\frac{\partial u_i}{\partial x_j} + \frac{\partial u_j}{\partial x_i} \right) + \left(\mu_B - \frac{2}{3}\mu \right) \frac{\partial u_k}{\partial x_k} \delta_{ij}, \tag{2.3}$$

where μ is dynamic molecular viscosity and $\mu_B = \lambda + \frac{2}{3}\mu$ is bulk viscosity. With Stokes hypothesis one sets $\lambda = -\frac{2}{3}\mu$, or $\mu_B = 0$ [22, 23].

Often distant forces such as gravitation are ignored so that the last term in Equation (2.2) is dropped. In many numerical programming systems the continuity equation is replaced by an equation for pressure-correction, which is emerged by combining continuity and momentum equation [22, 24].

In a mixture of different species one must have an equation for concentration or mass fraction of species,

$$\frac{\partial}{\partial t}(\rho Y_k) + \frac{\partial}{\partial x_j}(\rho Y_k u_j) = \frac{\partial}{\partial x_j} \left(\rho \mathcal{D} \frac{\partial Y_k}{\partial x_j} \right) + R_k, \tag{2.4}$$

where $\mathcal{D}$ is diffusion coefficient and is set equal for all species [22, 25, 26].

If number of species in the mixture is N one then needs $N-1$ equations. The last mass fraction can be calculated from the relation $\sum_k Y_k = 1$.

The energy equation can be written in a number of ways and with many simplifications. Quite often, but not always, an equation for static enthalpy is most adequate:

$$\frac{\partial}{\partial t}(\rho h) + \frac{\partial}{\partial x_j}(\rho h u_j) = \frac{\partial}{\partial x_j} \left(\rho \alpha \frac{\partial h}{\partial x_j} \right) + S_k, \tag{2.5}$$

where $\alpha = \lambda / (\rho C_p)$ is thermal diffusivity. This form of equation with enthalpy gradient in diffusion term assumes that the gas is ideal or the pressure is constant so that $h = h(T)$. Fourier's law for thermal conductivity

has temperature gradient, not enthalpy gradient, so that one has to do some rearrangements. The content of the source term is dependent upon simplifying assumptions done. The temperature can be found from the function $h(T)$. Finally one needs an equation of state for the pressure; $p = p(\rho, T)$ or $\rho = \rho(p, T)$, and an expression for the reaction term R_k. In that case one may actually solve the equation sets for chemical reactions in single-phase flow.

2.2.2 The $k - \epsilon$ Model

Average turbulence energy is defined as the kinetic energy pr. unit mass of an average fluctuating fluid in motion ($\frac{1}{2}\overline{u_i' u_j'}$), and is denoted by k. While the dissipation rate of energy is defined as the average turbulence kinetic energy pr. unit time, and is denoted by ϵ.

A standard $k - \epsilon$ model for a flow with high Reynolds number is given as follows [22]:

Turbulent viscosity:

$$\mu_t = \rho \nu_t = C_\mu \rho \frac{k^2}{\epsilon}. \tag{2.6}$$

Reynolds stresses:

$$-\rho \overline{u_i' u_j'} = \mu_t \left(\frac{\partial \overline{u}_i}{\partial x_j} + \frac{\partial \overline{u}_j}{\partial x_i} \right) - \frac{2}{3} \rho k \delta_{ij}. \tag{2.7}$$

By solving the two Equations (2.6) and (2.7) one obtains

k-equation:

$$\frac{\partial}{\partial t}(\rho k) + \frac{\partial}{\partial x_j}(\rho k \overline{u}_j) = \frac{\partial}{\partial x_j} \left(\left(\mu + \frac{\mu_t}{\sigma_k} \right) \frac{\partial k}{\partial x_j} \right) + \rho P_k - \rho \epsilon, \tag{2.8}$$

ϵ-equation:

$$\frac{\partial}{\partial t}(\rho\epsilon) + \frac{\partial}{\partial x_j}(\rho\epsilon\overline{u}_j) = \frac{\partial}{\partial x_j}\left(\left(\mu + \frac{\mu_t}{\sigma_\epsilon}\right)\frac{\partial \epsilon}{\partial x_j}\right) + C_{\epsilon 1}\frac{\epsilon}{k}\rho P_k - C_{\epsilon 2}\frac{\epsilon}{k}\rho\epsilon, \quad (2.9)$$

where the first, second and third term on the right-hand side of the Equation (2.8) and (2.9) are diffusion, production, and dissipation term, respectively, and the production term is given as:

$$\rho P_k = \mu_t\left(\frac{\partial \overline{u}_i}{\partial x_j} + \frac{\partial \overline{u}_j}{\partial x_i}\right)\frac{\partial \overline{u}_i}{\partial x_j}. \quad (2.10)$$

The numerical values of the constants are [22, 27]:

$$\sigma_k = 1.0 \quad \sigma_\epsilon = 1.3 \quad C_{\epsilon 1} = 1.44 \quad C_{\epsilon 2} = 1.92 \quad C_\mu = 0.09. \quad (2.11)$$

The first $k-\epsilon$ model published was by Jones and Launder in 1972 [28], which also could be used for flows with low Reynolds number. The numerical values of constants are adjusted, and the most employed version was the model published by Launder and Spalding in 1974 [27]. The model is developed for incompressible flow, i.e. density is constant.

Note that the density here is kept constant. In event density changes, for example as a function of temperature, the Equation (2.7) takes the form:

$$-\rho\overline{u_i' u_j'} = \mu_t\left(\frac{\partial \overline{u}_i}{\partial x_j} + \frac{\partial \overline{u}_j}{\partial x_i}\right) - \frac{2}{3}\delta_{ij}\left(\rho k + \mu_t\frac{\partial \overline{u}_k}{\partial x_k}\right). \quad (2.12)$$

With another word the term $\partial\overline{u}_l/\partial x_l = 0$ when density is constant. Likewise this should be added to production term (Equation (2.10)) as well where Reynolds stresses are included, so that

$$\rho P_k = \mu_t\left(\frac{\partial \overline{u}_i}{\partial x_j} + \frac{\partial \overline{u}_j}{\partial x_i}\right)\frac{\partial \overline{u}_i}{\partial x_j} - \frac{2}{3}\left(\rho k + \mu_t\frac{\partial \overline{u}_k}{\partial x_k}\right)\frac{\partial \overline{u}_i}{\partial x_j}. \quad (2.13)$$

In the same manner counting for density variation in equations for k and ϵ it results in a correlation for pressure-strain-velocity, and the new form would be [25]

k-equation:

$$\frac{\partial}{\partial t}(\rho k) + \frac{\partial}{\partial x_j}(\rho k \overline{u}_j) = \frac{\partial}{\partial x_j}\left(\left(\mu + \frac{\mu_t}{\sigma_k}\right)\frac{\partial k}{\partial x_j}\right) - \rho\overline{u_i' u_j'}\frac{\partial \overline{u}_i}{\partial x_j} - \frac{\mu_t}{\rho^2}\frac{\partial \rho}{\partial x_i}\frac{\partial p}{\partial x_i} - \rho\epsilon, \tag{2.14}$$

ϵ-equation:

$$\frac{\partial}{\partial t}(\rho \epsilon) + \frac{\partial}{\partial x_j}(\rho \epsilon \overline{u}_j) = \frac{\partial}{\partial x_j}\left(\left(\mu + \frac{\mu_t}{\sigma_\epsilon}\right)\frac{\partial \epsilon}{\partial x_j}\right) - C_{\epsilon 1}\frac{\epsilon}{k}\left(\rho\overline{u_i' u_j'}\frac{\partial \overline{u}_i}{\partial x_j} - \frac{\mu_t}{\rho^2}\frac{\partial \rho}{\partial x_i}\frac{\partial p}{\partial x_i}\right) - C_{\epsilon 2}\frac{\epsilon}{k}\rho\epsilon, \tag{2.15}$$

where $\rho\overline{u_i' u_j'}$ in Equation (2.14) and (2.15) is given as defined by Equation (2.12).

2.2.3 Characterizing of Turbulent Flames

Chemical reactions and turbulent flows are extremely complicated phenomena. Some of the main points shall shall be briefly discussed here, and will bring to light some characteristic dimensions for combustion.

Turbulence Scales

For larger turbulence structures one has the velocity scale u', the length scale ℓ' and the time scale $\theta = \ell'/u'$. The resulting Reynolds number will be $Re_{\ell'} = u'\ell'/\nu$. Further the Taylor length scale λ gives the $Re_\lambda = u'\lambda/\nu \sim Re_{\ell'}^{1/2}$. In non-premixed flames θ is characteristic time for mixing of reactants, while in case of premixed flames it stands for inter mixture of heat (product) and the reactants.

For smaller turbulence structures the Kolmogorov microscale has defined velocity scale v, length scale η and time scale τ. By definition one may write $v = (\nu/\tau)^{1/2}$ and $\eta = (\nu\tau)^{1/2}$. These scales are characteristic for motions with large dissipation of turbulence energy, i.e. the viscous forces are large. The Reynolds number based on Kolmogorov's length scale will be $Re_K = u'\eta/\nu$.

The relation between large and small turbulence scales is: $\ell'/\eta \sim Re_\lambda^{3/2} \sim Re_{\ell'}^{3/4}$ (length scale), $\theta/\tau \sim Re_{\ell'}^{1/2}$ (time scale), and $Re_K \sim Re_\lambda^{1/2} \sim Re_{\ell'}^{1/4}$ [22].

Laminar Flame Dimensions

Characteristic dimensions for laminar *premixed flames* are flame velocity[2] u_L, flame thickness δ_L, and chemical time scale τ_c. As an example, one may imagine a flame front moving with a burning velocity u_L through a mixture of reactants. The time scale would then be the resident time in the flame zone, or the reaction time.

These dimensions are dependent upon reaction rate and diffusivity, and one may write $u_L \sim (\mathcal{D}/\tau_c)^{1/2}$ and $\delta_L \sim (\mathcal{D}\tau_c)^{1/2}$. The time scale τ_c can be defined from reaction rate of the fuel. One gets the relation $\tau_c \sim R_{fu}^{-1}$, and that will be dependent on type of species, concentration, and temperature.

In diffusion flames the velocity and thickness of the flame do not have any physical meaning, except the time scale. One may again define velocity scale u_L and length scale δ_L from τ_c as above.

In many occasions viscosity and diffusivity are approximately equal, or they vary nearly on the same way. This gives $u_L \sim (\nu/\tau_c)^{1/2}$ and $\delta_L \sim (\nu\tau_c)^{1/2}$. One may also include Schmidt number $Sc = \nu/\mathcal{D}$ as a parameter [22].

Dimensionless Groups

For turbulent flames the laminar scales are used as characteristic scales. This may be done based on the reaction rate and not from the geometry or the flow.

From Reynolds number above one has relation between length scales: η/δ_L, ℓ'/δ_L; relation between velocity scales: u'/u_L; and relation between time scales: $Da = \theta/\tau_c$ and $Da_K = \tau/\tau_c$. the last two expressions are called Damköhler number, the later is also called Karlovitz number K_a. For a rapid chemical reaction (small τ_c) the Damköhler number is large and vice-versa.

With some calculations one may determine the following relationships [22]:

$$\frac{u'}{u_L} \sim Re_{\ell'} \cdot \frac{\delta_L}{\ell'} \sim Re_{\ell'}^{-1/4} \cdot \frac{\delta_L}{\eta}, \tag{2.16}$$

$$Da_K = \frac{\tau}{\tau_c} \sim \left(\frac{\eta}{\delta_L}\right)^2 \sim Da \cdot Re_{\ell'}^{-1/2}, \tag{2.17}$$

[2]Flame velocity, which is also called burning velocity, normal combustion velocity, or laminar flame speed, is more precisely defined as the velocity at which unburned gases move through the combustion wave in the direction normal to the wave surface [29].

$$Da = \frac{\theta}{\tau_c} \sim \frac{\ell'}{\delta_L}\frac{u_L}{u'} \sim \left(\frac{\ell'}{\delta_L}\right)^2 Re_{\ell'}^{-1} \sim \left(\frac{\eta}{\delta_L}\right)^2 Re_{\ell'}^{1/2}, \tag{2.18}$$

$$\frac{\ell'}{\delta_L} \sim Re_{\ell'}^{3/4}\left(\frac{\eta}{\delta_L}\right). \tag{2.19}$$

One may further include the Froude number $Fr = \frac{U^2}{gL}$ (eventually Richardson number $Ri = -\frac{g}{\rho}\frac{d\rho}{dx_3}\left(\frac{du_1}{dx_3}\right)^{-2}$, where x_3 is directed upward toward the acceleration of gravity (g) which characterizes buoyancy forces. For large Froude number, i.e. $Fr > 100$, one may ignore the influence of buoyancy [22, 30].

Flame Types

One may unconditional consider that the flames with $\delta_L \ll \eta$ are quite different from flames with $\delta_L \gg \eta$ or $\delta_L \approx \ell'$.

A laminar flame front could be imagined as a thin flame with a flat reaction zone. With rapid reactions (little τ_c, δ_L, but large u_L) and weak turbulence (large θ, τ, ℓ', with little u') the reaction takes place in a layer as in laminar combustion. The turbulence will buckle the reaction zone such that the flame will become wrinkled.

With larger fluctuations the buckles will be transformed to small and large eddies, and the flame layer will be broken up. One may then experience the phenomena as many small flames, called flamelets. The reaction area (the flame) then becomes thicker.

With intensive turbulence (small θ, τ, ℓ', but large u') and slow reactions (large τ_c, little u_L) the reactions are scattered over a wider area. When the flame occupies the hole combustion zone, then one has a so called well stirred reactor.

As a matter of fact the reaction, particularly the heat generated, will influence the turbulence, and not only the other way round. Hot gases rise up and the buoyancy flow will lead to turbulence. On the other hand the growth in the heat may mitigate the turbulence. Furthermore, viscosity of the hot gases increases which also moderate the turbulence. The local Reynolds number in a flame is less than a similar flow without reaction, because the density drops and viscosity increases.

2.2.4 The Vortex Models

The concept concerns breaking up of eddies and subsequent molecular mixing. An eddy may simply be said containing chiefly one of the substances. When many such eddies with different substances are broken up, the molecules are mixed. The aim is to model the source term $\overline{R}_k$ in the balance equations.

In order to achieve proper combustion reaction, the reactants should be mixed molecularly and the hot combustion products should contribute to the reaction process by getting well mixed with the reactants. If the reactants are premixed, then the first condition is fulfilled.

By assuming infinitely fast chemistry, the reaction would be controlled by the mixing process or decomposing of the eddies.

Two models which utilize such eddy-break-up principle are briefly discussed below.

Eddy Breakup Model

This model was developed by Spalding [31] based on premixed and non-premixed combustion. But it is often grouped as under-premixed flames, for example by Bray [32] and Kuo [25].

For a simple reaction, *fuel* + *oxidant* → *product*, the mean reaction rate of the product formation is

$$\overline{R}_{pr} = -(1+r)\overline{R}_{fu} = C_{EBU}\frac{\epsilon}{k}\rho\sqrt{\overline{Y'^2_{fu}}}, \tag{2.20}$$

where r is oxidant-fuel weight ratio, C_{EBU} is a constant, and $\overline{Y'^2_{fu}}$ is mean fuel mass fraction.

In some literatures the above model has been modified and called *Modified Eddy Breakup Model*, which indeed uses the mean values in the Equation (2.20). These models principally correspond to Magnussen's model described below.

Eddy Dissipation Model

The first version of the model was presented by Magnussen and Hjertager [33]. The model uses the Spalding model as its background, but the main difference is that the Magnussen's model uses average massfraction, not the variance. The idea is that the reaction is limited and controlled by the species present with minimum amount. The model is developed and used for both premixed and non-premixed combustion. In literature the model is often referred to *Eddy Breakup Model*, as in the case for the Spalding's model.

The first version of the model defines the mean reaction rate of a fuel as

$$\overline{R}_{fu} = A \cdot \frac{\epsilon}{k} \rho \cdot min \left(\overline{Y}_{fu}, \frac{1}{r} \overline{Y}_{ox}, B \cdot \frac{1}{1+r} \overline{Y}_{pr} \right), \tag{2.21}$$

where min indicates the minimum value of the scale, while A and B are constants. The model is still used widely in a number av commercial CFD codes.

Eddy Dissipation Concept–Outline and Modeling Energy Transfer

One of the main concern of the Magnussen's EDC combustion model is about energy transfer from large to smaller scales eddies (cascade model). Combustion takes place where the mixture is molecular, mainly in eddies with fine structures where also the major part of dissipation of turbulence energy to heat occurs. The fine structures are not always evenly dispersed in time and room [22, 34].

An essential feature of the concept is that the molecular mixing between reactants, which is associated with the dissipation of turbulence, takes place in concentrated, isolated regions whose entire volume is only a small fraction of the total volume of the fluid [35].

The mechanical energy is transfered from the mean flow to large eddies, and then further to smaller and smaller eddies. The large eddies are tardy and contain major part of the kinetic energy. While, the smaller eddies swirl faster but contain less energy because they jointly have less mass. The smallest eddies have highest frequency and largest viscous stresses. Viscous friction transfers the mechanical energy to heat. The transportation (dissipation) occurs at all levels, but mostly in the smallest eddies. The spectrum of the large and small eddies are often called as an energy or *turbulence cascade*.

Figure 2.1 illustrates the model for transferring of mechanical energy from mean flow, through turbulence energy, to heat. w' is production of turbulence kinetic energy. The sum $q' + q'' + ... + q^*$ is dissipation rate of turbulence kinetic energy.

The first level in the structure is large eddies with high energy content. It is characterized with a turbulence velocity u', a length scale L', and a frequency or strain rate $\omega' = u'/L'$. This level represents the whole spectrum, because it contains the effect of smaller eddies. When computing mean turbulence equations, for example k and ϵ equations, one deals with the first level.

The next level represents part of the spectrum where characteristic frequency is $\omega'' = 2\omega'$, velocity u'', and length L''. Similarly it is assumed that

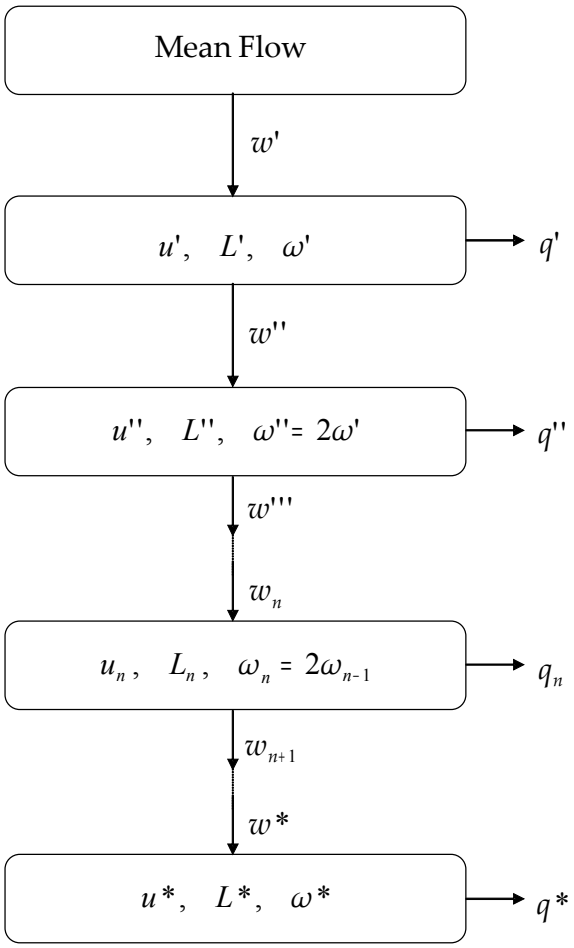

Figure 2.1: Turbulence Energy Cascade Model

this level too contains the effect of subsequent levels. On the same manner the n^{th} level is characterized by $\omega_n = 2\omega_{n-1}$, u_n, and L_n. On each level $\omega_n = u_n/L_n$. In the smallest eddies (fine structures) ω^*, u^*, and L^* are of the same order of magnitude as the Kolmogorov microscales (see Section 2.2.3).

Transferring from first to next level, w'', is equal to sum of all subsequent dissipations, so that the dissipation rate $\epsilon = q' + w''$.

Likewise, the transfer from first to second level must be a function of quantities linked to both levels. $\omega' = u'/L'$ is a typical characteristic strain rate (vorticity) for the first level, while u'' is a typical velocity scale for the second level. The friction work or dissipation at first level must be product of viscous stresses ($\nu\omega'$) and strain rate (ω') [22].

By definition the dissipation rate of turbulence energy for the first level

can then be expressed as

$$\epsilon' = \xi^2 \left(\underbrace{12\frac{u'}{L'} \cdot u''^2}_{i} + \underbrace{15\nu \left(\frac{u'}{L'}\right)^2}_{ii} \right), \tag{2.22}$$

where ξ is a constant, (i) represents the mechanical energy transfer to the next level, and (ii) represents the viscous dissipation into heat at the first level [36, 37].

And the turbulence energy balance for the second structure level is given by

$$\xi^2 \cdot 12\frac{u'}{L'} \cdot u''^2 = \xi^2 \left(12\frac{u''}{L''} \cdot u'''^2 + 15\nu \left(\frac{u''}{L''}\right)^2 \right). \tag{2.23}$$

This sequence of structure level can be continued down to a level where all the produced turbulence energy is dissipated into heat, i.e. fine structure characterized by ω^*, u^*, and L^*.

The turbulence energy transferred to fine structure level is

$$\omega^* = \xi^2 \cdot 6\frac{u^*}{L^*} \cdot u^{*2}, \tag{2.24}$$

and the dissipation given by

$$q^* = \xi^2 \cdot 15\nu \left(\frac{u^*}{L^*}\right)^2. \tag{2.25}$$

According to the model only a small portion of the dissipation of energy occurs in the highest level. The major part approximately 3/4 takes place at the fine structure level.

By introducing $\xi = 0.18$ one may arrive at following expressions for dissipation rate of kinetic energy [36]:

$$\epsilon = 0.2\frac{u'^3}{L'}, \tag{2.26}$$

$$\epsilon = 0.267\frac{u^{*3}}{L^*}, \tag{2.27}$$

and

$$\epsilon = 0.67\nu \left(\frac{u^*}{L^*}\right)^2. \tag{2.28}$$

Combining the two Equations (2.27) and (2.28) gives velocity and length scale for the fine structure

$$u^* = 1.74 \left(\epsilon\nu\right)^{\frac{1}{4}}, \tag{2.29}$$

and

$$L^* = 1.43 \left(\frac{\nu^3}{\epsilon}\right)^{\frac{1}{4}}. \tag{2.30}$$

The EDC model was developed for prediction of gaseous combustion reactions in turbulent flows. In the validation work done by Hjertager et al. [38] it is pointed out that the model was not able to predict the reaction-zone length, while a modified EDC model with a multiple time scale model gave reasonable results. None of the models were able to predict the effect of increasing Reynolds number.

Modeling Soot Formation in Turbulent Flames

It is well known that the major part of radiation is originated from soot in the flame, but soot shields too by intercepting radiation due to its high emissivity factor. Although a propane flame (studied in this work) does not contribute much to soot formation compared to other flame types, e.g. oil and solid based flames, it is anyhow subject to more formation of soot when the combustion occurs unconfined contra traditionally controlled combustion process, e.g. in a gas turbine. An issue which is of high concern for a combustion engineer.

Hereunder few expressions shall be sett up for calculating the rate of soot formation i turbulent flame based on the studies done by Magnussen [36, 39, 40].

The rate of formation of radical nuclei is determined by the equation:

$$R_{n,f} = n_o + (f - g)\, n - g_o n N, \tag{2.31}$$

where f, g, and g_o are constants, n is radical nuclei concentration, N is soot particle concentration, and n_o is spontaneous formation rate of radical nuclei given by:

$$n_o = 1.08 \cdot a_o \cdot f_c \cdot \overline{c}_{fu} \cdot exp\left(-\frac{E}{RT}\right), \tag{2.32}$$

where $\overline{c}_{fu}$ is the mean fuel concentration (kg/m^3) and f_c is the mass fraction of carbon in the fuel.

The rate of soot particle formation is as follows:

$$R_{s,f} = m_p \left(a - bN\right) n, \tag{2.33}$$

where m_p is the soot particle mass (kg/part), while a and b are constants.

The following numerical value are given to the constants: $(f - g) = 10^2$, $g_o = 10^{-15}$, $a = 10^5$, $b = 8 \cdot 10^{-14}$, and $E/R = 9 \cdot 10^4$. The soot density is taken as $\rho_s = 2$ g/cm^3.

The value of a_o is dependent on the soot particle diameter and is given by:

$$d_p^3 \cdot a_o = constant \tag{2.34}$$

with $d_p = 178.5$ Å[3] the value of $a_o = 12.5 \cdot 10^{36}$ parts/kgs.

[3] Å=Ångström=10^{-10} m

2.3 Transport Phenomenon with Water Droplets

A drop is defined as a mass of liquid in a liquid or gaseous medium, while a bubble is a mass of gas surrounded by liquid or gas. An example of the later is a soap bubble. Drops and bubbles may also appear more complex as pairs, or may be a drop or bubble entirely within another drop. Various drop and bubble structures are illustrated in Figure 2.2 [41].

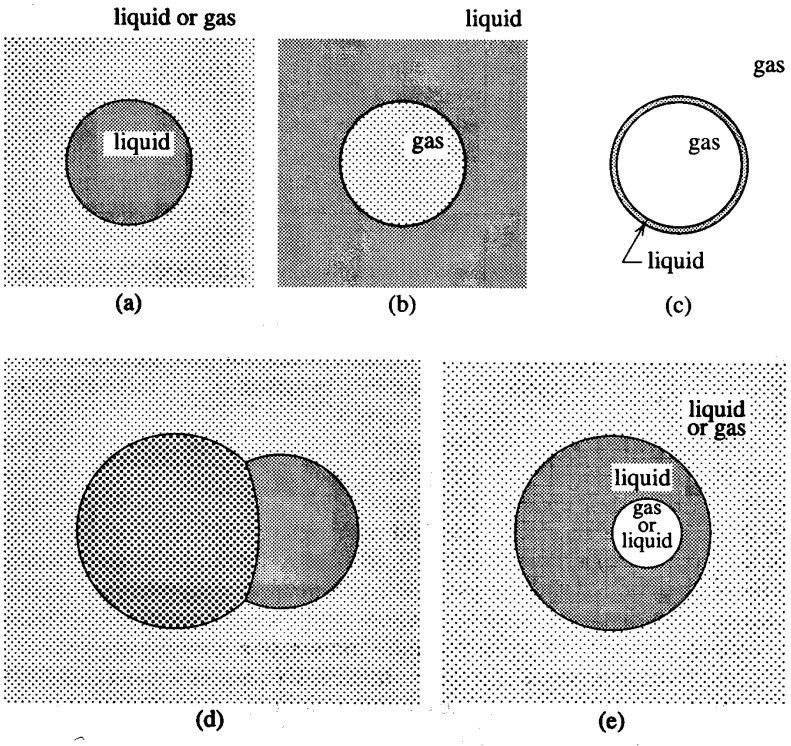

Figure 2.2: Different structures of drops and bubbles: (a) liquid drop, (b) gas bubble in liquid, (c) soap bubble, (d) compound drop with three interfaces, and (e) compound drop with two interfaces [41].

Analysis of drop and bubble mechanism in motion involves largely fluid mechanics which in turn is used for discussing heat and mass transfer. The transport processes are described by conservation equations (energy, mass, and momentum).

Energy conservation follows the first law of thermodynamics which leads to energy equation. While the rate of change of momentum in a given body of fluid is equal to the sum of all the forces on it. This is stated by Newton's second law and mathematically is expressed by Navier-Stokes momentum equation

$$\rho \frac{Du}{Dt} = -\nabla \rho + \mu \nabla^2 u + F, \tag{2.35}$$

where F is the sum of the body forces.

Mass conservation in a homogeneous fluid results in the continuity equation. In case more than one material is involved, one must also account for dissipation and convection. For a compressible fluid, the conservation equation is stated by

$$\frac{\partial \rho}{\partial t} + \nabla \cdot \rho u = 0. \tag{2.36}$$

For incompressible fluid, i.e. constant density, the first term is set to zero, and one obtains

$$\nabla \cdot u = 0. \tag{2.37}$$

2.3.1 Heat and Mass Transfer

Heat is transfered only when there is a temperature gradient. This is known as Fourier law, mathematically defined as

$$\dot{q} = -k \nabla T, \tag{2.38}$$

where $\dot{q}$ is the heat flux, k is the thermal conductivity, and T is the temperature distribution. Mass diffusion takes place due to a concentration gradient known as Fick's law, and is defined as

$$J_j = -D_j \nabla c_j, \qquad j = 1, 2, 3, ..., N, \tag{2.39}$$

were J_j is the molar diffusion flux vector, D_j is the mass diffusion coefficient, and c_j is the molar concentration of the j^{th} species in the mixture.

The Energy Equation

Rectangular Coordinates: Applying the Equation (2.38) combined with the first law of thermodynamics to a control volume, the energy equation may be stated as

$$\rho c_p \left(\frac{\partial T}{\partial t} + u \cdot \nabla T \right) = \nabla \cdot k \nabla T + \dot{q}''' + \mu \Phi, \tag{2.40}$$

where c_p is the specific heat, $\dot{q}'''$ is the volume heat flow rate, and Φ is the viscous dissipation function. For the most cases it is reasonable to assume that the density (ρ) and the thermal conductivity (k) are constant, and the viscous dissipation term (Φ) is negligible. And if heat is neither added nor removed from the system, then the Equation (2.40) will be simplified to

$$\frac{1}{\alpha}\left(\frac{\partial T}{\partial t} + u \cdot \nabla T\right) = \nabla^2 T, \tag{2.41}$$

where $\alpha = k/(\rho c_p)$ is the thermal diffusivity.

Spherical Coordinates: For most drops and bubbles a conventional spherical coordinate (r, θ, ϕ) is a natural system to apply. The energy Equation (2.41) written in this coordinate sysytem takes the form

$$\frac{1}{\alpha}\left(\frac{\partial T}{\partial t} + u_r\frac{\partial T}{\partial r} + \frac{u_\theta}{r}\frac{\partial T}{\partial \theta} + \frac{u_\phi}{r\sin\theta}\frac{\partial T}{\partial \phi}\right) = \frac{1}{r^2}\frac{\partial}{\partial r}\left(r^2\frac{\partial T}{\partial r}\right) + \frac{1}{r^2\sin\theta}\frac{\partial}{\partial \theta}\left(\sin\theta\frac{\partial T}{\partial \theta}\right) + \frac{1}{r^2\sin^2\theta}\frac{\partial^2 T}{\partial \phi^2}. \tag{2.42}$$

The Species Conservation Equation

Rectangular Coordinates: Applying the Fick's law to a multicomponent system with constant density (ρ) and mass diffusion coefficient (D_{jm}), the Equation (2.39) can be written as

$$\frac{1}{D_{jm}}\left(\frac{\partial c_j}{\partial t} + u \cdot \nabla c_j\right) = \nabla^2 c_j, \qquad j = 1, 2, 3, ..., (N-1). \tag{2.43}$$

The molar concentration for the species j is given by $c_j = \rho_j/m_j$, where m_j is the molecular weight of the component j.

Spherical Coordinates: Writing the Equation (2.43) in the spherical coordinates one obtains

$$\frac{\partial c_j}{\partial t} + u_r\frac{\partial c_j}{\partial r} + \frac{u_\theta}{r}\frac{\partial c_j}{\partial \theta} + \frac{u_\phi}{r\sin\theta}\frac{\partial c_j}{\partial \phi} = D_{jm}\left[\frac{1}{r^2}\frac{\partial}{\partial r}\left(r^2\frac{\partial c_j}{\partial r}\right) + \frac{1}{r^2\sin\theta}\frac{\partial}{\partial \theta}\left(\sin\theta\frac{\partial c_j}{\partial \theta}\right) + \frac{1}{r^2\sin^2\theta}\frac{\partial^2 c_j}{\partial \phi^2}\right], \quad j = 1, 2, 3, ..., (N-1). \tag{2.44}$$

Mean Transport Rates

The mean total heat flow rate across the interface area A of a drop or bubble is give by

$$\bar{\dot{q}} = -\frac{1}{A}\int_A k\nabla T \cdot n \cdot dA, \tag{2.45}$$

where n is unit vector normal to the surface [41]. The average heat flux is normally expressed in non-dimensional form called Nusselt number, and is given as

$$Nu = \frac{\bar{\dot{q}}L}{k\Delta T}, \tag{2.46}$$

where L corresponds to particle size and $\Delta T = (T_0 - T_\infty)$ is the temperature difference between the initial particle (or interface) and the ambient temperature.

In a similar manner, the mass transfer rate is expressed in a non-dimensional form stated by a Sherwood number as

$$Sh_j = \frac{\bar{J}_j L}{D_{jm}\Delta c_j} = -\frac{L}{D_{jm}A}\int_A D\nabla c_j \cdot n \cdot dA, \tag{2.47}$$

where $\bar{J}_j$ is the area-averaged molar flux and $\Delta c_j = (c_{j'0} - c_{j,\infty})$. $c_{j'0}$ is the molar concentration at interface and $c_{j,\infty}$ is the far-field concentration .

2.3.2 Shape and Size of Water Droplets

The shape and size of a fluid particle is vital for its motion and as well as the succeeding heat and mass transfer processes. For particle stability a balance between normal force, shear force, surface tension force, and gravity at its interface must be maintained. When the surface tension force is constant it acts to minimize the surface energy which then forces the particle to keep its spherical shape. With another word a particle will deform when it is exposed to non-uniform force due to motion, pressure, or temperature variations. The smaller particle tend to keep their spherical shapes due to their large surface to volume ratio.

Breaking up larger drops to a number of tiny drops would result in increased interfacial contact area with the surrounding medium, let say a solid surface. This situation provides the maximum amount of heat transfer rate. This may be demonstrated better visually as shown in Figure 2.3 in a two-dimensional form. On the left is shown two large drops resting on a surface,

while on the right side it is assumed that these are substituted with a number of smaller drops occupying the same total surface area. It is clearly obvious that the contact area has significantly increased. One drawback with very small drops, e.g. mist, with law evaporation temperature, such as water, impacting on hot surfaces is the high risk of early evaporation, if the purpose is to cool down the surface. This is further discussed in this section.

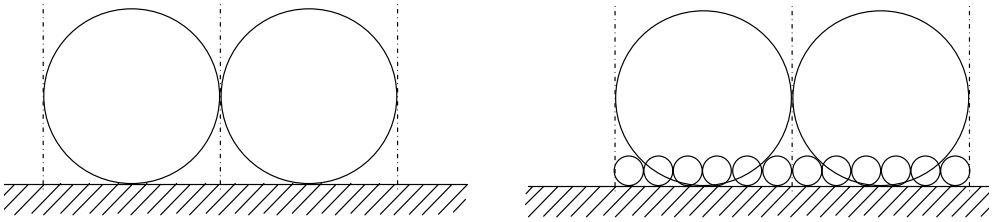

Figure 2.3: Comparison of contact area between large and small drops

An analytical example may more explicitly illustrate the above fact. Assuming a water droplet with 5 mm in diameter breaks up into 10 smaller drops of equal sizes. It is further assumed that the original and the smaller droplets all have nearly spherical form and the same ambient condition. The droplet contact area, A_d, may be found by the following expression

$$A_d = \frac{V}{d}, \tag{2.48}$$

where V is the droplet volume and d is the droplet diameter [42].

Using the above relationship gives a contact area for the first case $A_{d1} = 13\ mm^2$, while for the second case, i.e. ten smaller droplets, this quantity is equal to $A_{d2} = 28\ mm^2$. This means by breaking up a 5 mm droplet into ten smaller droplets the total contact area increases by a factor of 2.15. The factor increases, as the number of droplets increase.

Drops at Rest

When a static fluid particle, i.e. in mechanical equilibrium with the surrounding fluid, the governing equation between pressure balance and surface tension is

$$(\hat{p} - p) = \frac{2\sigma}{R}, \tag{2.49}$$

where $\hat{()}$ refers to dispersed phase quantities. For a non-spherical particle, the Equation (2.49) takes the form

$$(\hat{p} - p) = \sigma \left(\frac{1}{R_1} + \frac{1}{R_2} \right), \tag{2.50}$$

where R_1 and R_2 are the local radii of curvature.

The static particles may be either sitting on a surface or hanging from a surface. The equilibrium equation for such condition is derived to be

$$\Delta \rho g z = \sigma \left(\frac{2}{R_0} - \frac{1}{R_1} - \frac{1}{R_2} \right), \tag{2.51}$$

where z is the upward vertical distance from the nose of the particle on the axis of symmetry and R_0 is the curvature radius of the surface at the nose. The value of z for a sitting drop is negative, and the curvature radius (R_0) is maximum, corresponding to flattening of the drop. While, for the hanging drop the values are opposite and correspond to enlarged drop.

Drops in Motion

For stability of particles in motion, the normal and shear stress forces must be balanced at the interface separating the phases. If the surface viscosities are assumed to be zero, the normal interfacial stress condition for an incompressible Newtonian and spherical fluid in motion may be stated as [41]

$$\left(\hat{p} - 2\hat{\mu} \frac{\partial \hat{u}_r}{\partial r} \right) - \left(p - 2\mu \frac{\partial u_r}{\partial r} \right) = \frac{2\sigma}{R}, \tag{2.52}$$

and the shear stress condition is given by

$$\hat{\mu} \left[r \frac{\partial}{\partial r} \left(\frac{\hat{u}_\theta}{r} \right) + \frac{1}{r} \frac{\partial \hat{u}_r}{\partial \theta} \right] - \mu \left[r \frac{\partial}{\partial r} \left(\frac{u_\theta}{r} \right) + \frac{1}{r} \frac{\partial u_r}{\partial \theta} \right] = \frac{1}{R} \frac{d\sigma}{d\theta}, \tag{2.53}$$

where r is the radial and θ is the angular coordinate in a spherical coordinate system.

Drop Size Distribution

Fluid particles have a wide spectrum of sizes. The three different categories tabulated in Table 2.1 give an overview of drop size, their velocity in air, and the corresponding range of Reynolds number [41, 43].

Table 2.1: Drop Characteristics [41]

Category	Type	Size (μm)	Velocity in Air (m/s)	Reynolds Number
I	Mist	80-100	0.3-1	1-20
	Dizzle	200-500	1-3	20-100
	Raindrops	500-1000	3-20	100-10000
II	Clouds, fog, aerosol	1-100	0.0001-0.3	0.00001-1
III	Spray (cooling, sprinkles, etc.)	10-500	0.01-20	0.003-10000

The spray droplets in category III have also a velocity range of 0.0001-0.05 m/s in liquids such as water, with a Reynolds number in the range 0.001-3000. The extremely small drops can nucleate as a result of condensation downstream of the outlet in the expansion region of a supersonic nozzle. These drops may grow to significant sizes with further condensation.

In case of process bubbles, such as in cavitation, boiling, degassing, etc., the spectrum of size ranges between 1 μm to 1 mm. As an example, in boiling water, a nucleated bubble embryo size is about 5 μm. While in cavitation and fermentation the bubble size is about 10-100 μm.

Drop Interaction with Solid

When moving drops and bubbles interact with solid surfaces, their dynamic behavior as well as the associated heat and mass transfer near the surface boundaries will be greatly affected. The major effect of a solid wall on a fluid particle is to increase the drag force on it. There are also other effects such as drop deformation, and even breakup of the drop in the case of impact.

The motion of a drop near a wall is defined by its magnitude of velocity and orientation with regrad to the surface. The expressions for drag force for motion normal and parallel to the wall give the description of hydrodynamic resistance for spherical drops.

Dropwise Condensation: The dropwise condensation is a phenomenon that takes place when a drop is sitting on a solid surface. The mechanism of heat transfer is far more effective than filmwise condensation. Much research have

been done on this subject among others by Hampson et al. [44, 45, 46, 47, 48], who found that the dropwise condensation is favored over filmwise when the liquid poorly wets the surface. The wetting characteristics are determined by a drop-solid contact angle, ϑ, as shown in Figure 2.4 [41]. A liquid drop which gently wets a solid surface might have a contact angle $\vartheta = 0$, giving larger wetting surface area, such as motor oil on a metal surface, compared to drops with angle $\vartheta > 0$. The opposite and extreme situation might be a drop with no contact area, non-wetting, where the corresponding angle is $\vartheta = \pi$. In case of drops with very small contact angles, the process of dropwise condensation quickly turns over to filmwise condensation as the drops coalesce. To avoid this and to maintain dropwise condensation of for example steam, one may coat the surface with waxy matters which reduces the wettability condition, i.e. increasing the contact angles.

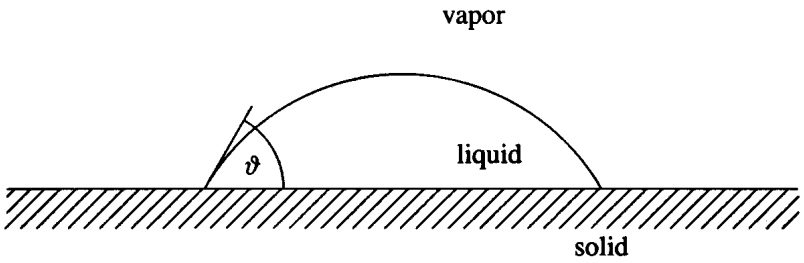

Figure 2.4: A sitting drop on a surface [41]

In literature one has landed two theories for mechanism of dropwise condensation on a surface. The first theory known as *nucleation theory* claims that the condensation occurs on a solid surface at nucleation site where the droplets start to grow, while the remainder of the surface stays dry [49, 50]. The second theory known as *film rapture theory*, which was firsts proposed by Jakob [51], postulates that vapor condenses on a dry area at the surface as a thin film until it reaches a critical thickness. At this phase the film breaks up into tiny droplets.

For condensation to remain locally within vapor (homogeneous nucleation), a nucleus of a critical radius has to be formed. Those with smaller radii would immediately evaporate, even in a slightly supersaturated environment. Although lower temperatures are favorable, the presence of liquid state is necessary for continued condensation. The state of condensation is increased as the temperature is lowered and/or a pitted surface is present. With the later the critical radius is physically achieved with even smaller number of molecules than in free space (heterogeneous nucleation) [41].

On a surface condensation starts with increasing drops with critical radii.

These drops coalesce and form larger drops, as shown in Figure 2.5 [48], which finally slide off by gravity. On a horizontal surface, external forces are needed to remove larger drops.

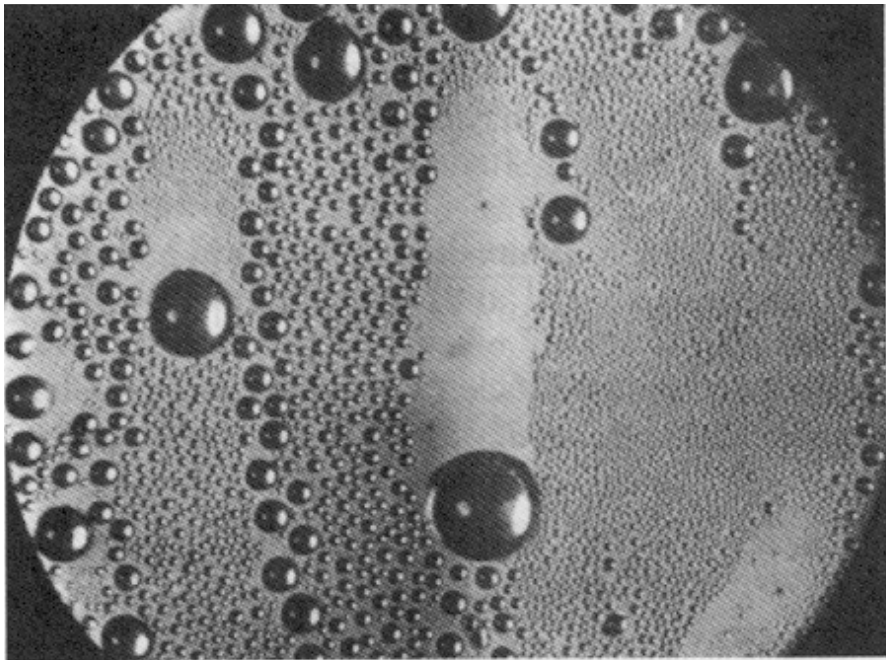

Figure 2.5: Dropwise condensation [48]

The most part of condensation heat transfer occurs at the edge of a drop. Tiny drops provides a very significant heat transfer area near the edges [52].

Pool Boiling: Boiling is a process of phase-change of a fluid from liquid to vapor near a solid surface, i.e. solid-liquid interface. When the phase-change occurs at liquid-vapor interface the process is referred to as evaporation. If pool boiling takes place in a stagnant liquid it is considered as natural convection boiling or some times referred to as saturated pool boiling, as illustrated in Figure 2.6. Boiling occurs when the surface temperature, T_w, exceeds the saturation temperature of the fluid, T_{sat}, at a given pressure. Whilst if boiling occurs in liquid in motion relative to the surface, it is defined as forced convection boiling [53].

Indeed when a drop contacts the surface, surface tension forces prevent the drop from entering the smaller cavities in which air or other gases are trapped. These cavities are known as *nucleation sites* and the bubbles that emerge from these cavities and detach from the surface are specified as *nucleated bubbles*. Typical boiler wall surface when first wetted, is experienced

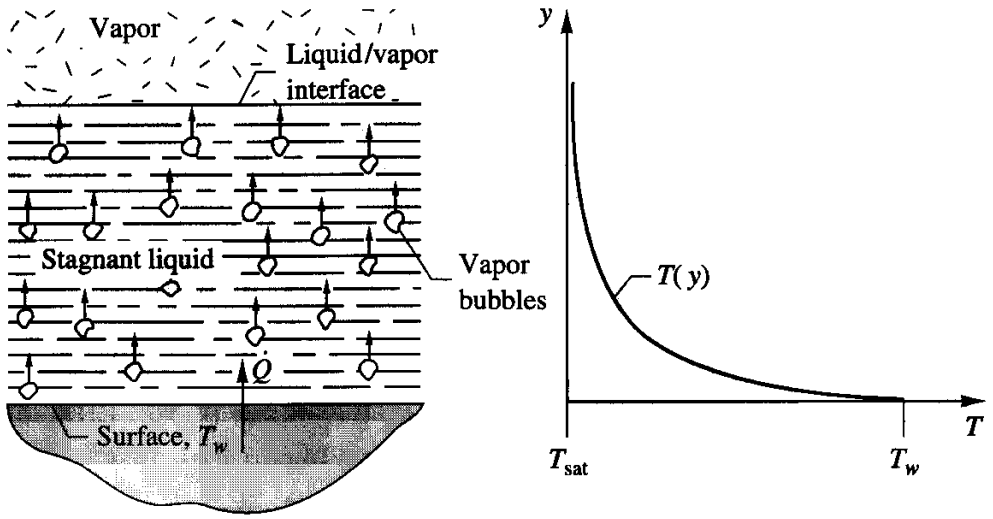

Figure 2.6: Pool boiling within a stagnant liquid [53]

to have nucleation site with radii in the range 2.5-7.5 μm [54].

Dropwise Evaporation: The evaporation of liquid sprays from solid surfaces with elevated temperature is an important issue in industrial application, in particular for cooling of hot surfaces. There are four physical phenomena associated with evaporation of droplets. The first one is referred to underheated evaporation, and the other three regimes are low, intermediate, and high superheats [41]. The amount of heat transfer varies to the degree of superheat similar to boiling curve in the superheated region. In literature the phenomena are also known as convection, nucleate boiling, transition boiling, and stable film boiling, respectively, as shown in boiling curve for water in Figure 2.7 [53]. In figure the heat flux is plotted as a function of the temperature difference between the surface and the the saturation temperature, called the *excess temperature*, ΔT_e.

Evaporation in the underheated zone is increased exponentially with the surface temperature up to the saturation temperature. Thereafter follows a large linear low-superheated evaporation followed by boiling characteristics curve. The state of underheated evaporation occurs only with drop temperature lower than the evaporation temperature at the ambient pressure. Evaporation takes place when the ambient vapor partial pressure is lower than the equilibrium pressure at liquid-vapor interface temperature. During the evaporation process the drop remains in touch with the surface, and the

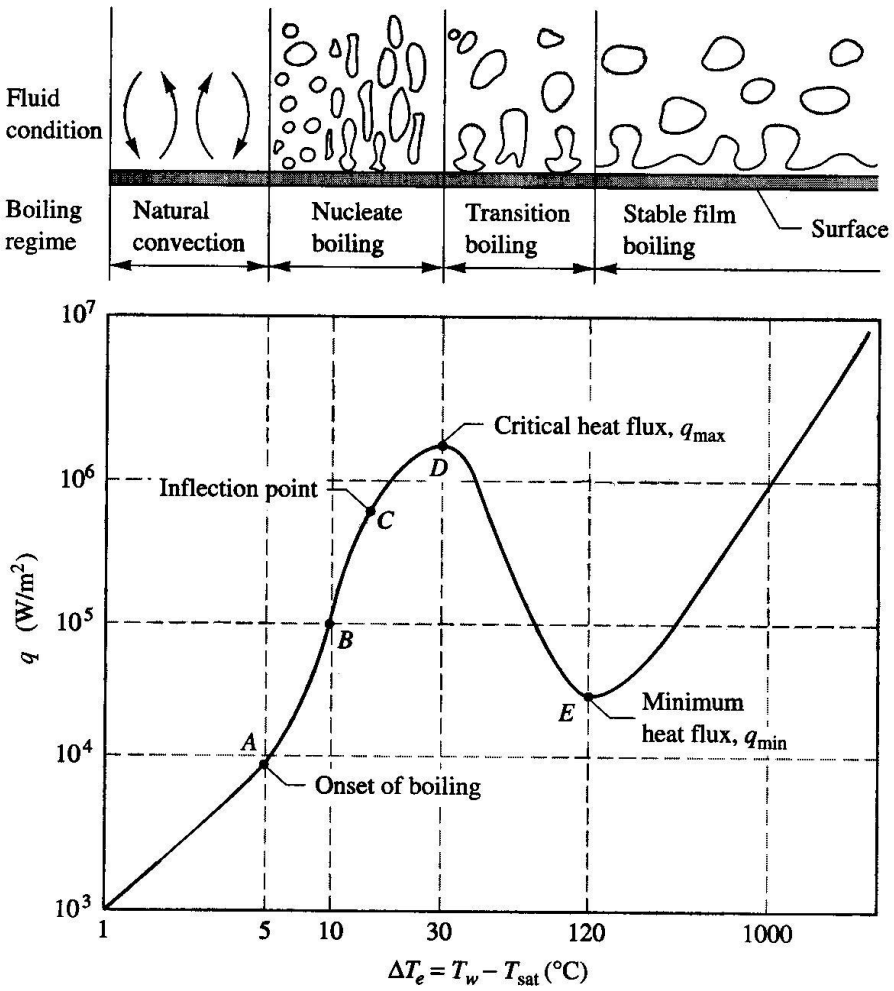

Figure 2.7: Boiling curve for water at atmospheric pressure [53]

nucleation starts at temperatures slightly lower than saturation temperature, i.e point A on the boiling curve.

In low-superheated evaporation the drop is still in contact with the solid, point A to B. Although with very thin drops, nucleation might be restrained. While in intermediate region, from point B to D, the nucleation takes place with enhanced heat transfer. With increasing solid temperature, the droplet tends to loose its contact with the surface and then heat transfer rate drops, point D to E. In the final region, i.e. high-superheat evaporation, the drop does not touch the solid (prevented by a vapor film), and heat transfer from the solid to the drop takes place through a vapor layer formed between them. This state is referred to *Leidenfrost* phenomenon, i.e. point E on the curve.

As it can be seen from the boiling curve the *natural convection boiling* exits if the excess temperature, ΔT_e, is less than 5 °C. The heat transfer may be determined using Newton's law of cooling as [53]

$$\dot{q}'' = h\left(T_w - T_{sat}\right) = h\Delta T_e, \tag{2.54}$$

where $\dot{q}''$ is the heat flux at surface during the boiling (W/m^2), h is the convection heat transfer coefficient (W/m^2K), and T_{sat} is the saturation temperature of the liquid (K).

Nucleate boiling initiates at approximately point A and occurs over the range $5\ ^\circ C \leq \Delta T_e < 30\ ^\circ C$, and the heat transfer correlation for this phase is given by

$$\dot{q}'' = \mu_f h_{fg} \sqrt{\frac{g\left(\rho_f - \rho_g\right)}{\sigma}} \left(\frac{C_{p,f}\Delta T_e}{C_{sf} h_{fg} \mathtt{Pr}_f^n}\right)^3, \tag{2.55}$$

where

μ_f = dynamic viscosity of saturated liquid (kg/ms)
h_{fg} = evaporation enthalpy (J/kg)
ρ_f = density of saturated liquid (kg/m^3)
ρ_g = density of saturated vapor (kg/m^3)
σ = surface tension at liquid-vapor interface (N/m)
$C_{p,f}$ = specific heat of saturated liquid (J/kgK)
C_{sf} = dimensionless constant
n = dimensionless constant
$\mathtt{Pr}_f$ = Prandtl number of saturated liquid ($\frac{\mu_f C_{p,f}}{k}$)
g = gravitational acceleration (9.81 m/s^2)
k = thermal conductivity of saturated liquid (W/mK)

Numerical values of experimental constants C_{sf} and n for water and variety of surfaces are provided in Table 2.2

Due to high heat transfer property of the point D on the curve, one may desire to operate near or at this point. The following relation may apply for the critical heat flux

Table 2.2: Values of C_{sf} and n for water with various surface combinations [53]

Surface Type	$\mathbf{C}_{sf}$	**n**
Brass	0.0060	1.0
Copper, polished	0.0130	1.0
Copper, lapped	0.0147	1.0
Copper, scored	0.0068	1.0
Nickel	0.0060	1.0
Platinum	0.0130	1.0
Stainless steel, chemically etched	0.0130	1.0
Stainless steel, ground and polished	0.0060	1.0
Stainless steel, mechanically polished	0.0130	1.0
Stainless steel, teflon pitted	0.0058	1.0

$$\dot{q}''_{max} = 0.149 \rho_g h_{fg} \left(\frac{g\sigma \left(\rho_f - \rho_g\right)}{\rho_g^2} \right)^{\frac{1}{4}}. \tag{2.56}$$

Transition boiling, sometimes called unstable film boiling, which is a rapid formation of vapor at the surface, occurs in the range $30\ ^\circ C \leq \Delta T_e < 120\ ^\circ C$. This region is trapped by the lower limit at critical point (D) and the upper limit at Leidenfrost point (E). The following correlation may be used to estimate the minimum heat flux at point E

$$\dot{q}''_{min} = 0.09 \rho_g h_{fg} \left(\frac{g\sigma \left(\rho_f - \rho_g\right)}{\left(\rho_f + \rho_g\right)^2} \right)^{\frac{1}{4}}. \tag{2.57}$$

Film boiling or a stable layer of vapor covering the surface exists if $\Delta T_e \geq 120\ ^\circ C$. At this stage the thermal radiation across the vapor layer will dominate the heat transfer from the surface as the temperature increases beyond point E, particularly when it exceeds about 330 °C. An expression may be used to estimate the convective heat transfer on cylinders and spheres is given by

$$\overline{\mathtt{Nu}}_D = \frac{\overline{h}_c D}{k_g} = C \left(\frac{g \left(\rho_f - \rho_g\right) h'_{fg} D^3}{\upsilon_g k_g \Delta T_e} \right)^{\frac{1}{4}}, \tag{2.58}$$

where

$\overline{\mathtt{Nu}}_D$ = average Nusselt number
$\overline{h}_c$ = average convection heat transfer coefficient (W/m^{2}K)
D = diameter of cylinder or sphere (m)
k_g = thermal conductivity of saturated vapor (W/mK)
ν_g = kinematic viscosity of saturated vapor (m^2/s)
C = constant (0.62 for horizontal cylinders & 0.67 for spheres)
$h_{fg}^{'}$ = modified enthalpy of vaporization ($h_{fg} + 0.8C_{p,g}\Delta T_e$) (J/kg)

The enthalpy $h_{fg}^{'}$ is the sensible heat required to maintain the temperature of the vapor layer above the saturation temperature.

To include the radiation contribution, the following correlation for combined convection and radiation heat transfer coefficient may be applied

$$\overline{h}^{\frac{4}{3}} = \overline{h}_c^{\frac{4}{3}} + \overline{h}_r \overline{h}^{\frac{1}{3}}, \tag{2.59}$$

where $\overline{h}$ is average combined heat transfer coefficient for convection and radiation (W/m^2 K) and $\overline{h}_r$ is average radiation heat transfer coefficient (W/m^2 K).

The radiation heat transfer coefficient, $\overline{h}_r$, is defined by the following expression [53]

$$\overline{h}_r = \frac{\epsilon\sigma\left(T_w^4 - T_{sat}^4\right)}{T_w - T_{sat}}, \tag{2.60}$$

where ϵ is the surface emissivity and σ is the Stefan-Boltzmann constant (5.67×10^{-8} W/m^{2}K^4).

Another approach for calculating the radiation heat transfer coefficient is given by the following correlation [54]

$$\overline{h}_r = 4\epsilon\sigma\left(\frac{T_w + T_{sat}}{2}\right)^3. \tag{2.61}$$

The photographs in Figure 2.8 show the different sequences in boiling regime for methanol, i.e. nucleate, transition, and film boiling, on a horizontal tube [53].

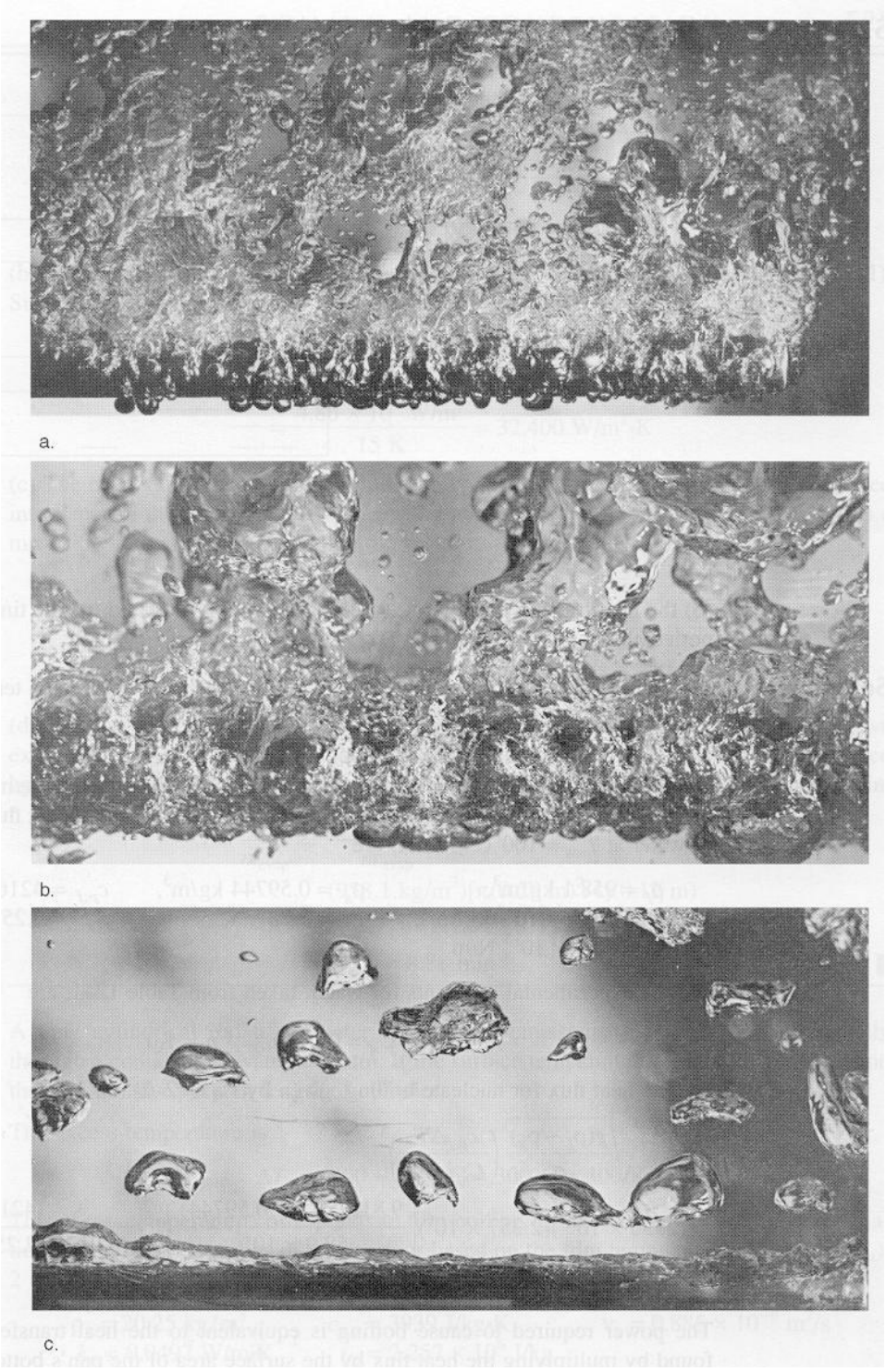

Figure 2.8: Boiling regimes for methanol on a horizontal tube: (a) nucleate boiling, (b) transition boiling and (c) film boiling [53]

Chapter 3

Review of Previous Work on Hot Spot

3.1 Jet Fires

Jet fire is a turbulent jet flame resulting from uncontrolled combustion of a fuel continuously released with some significant momentum. Practically it means combustion as a result of fuel leakage, e.g. fuel release from a pipeline failure/rapture, leakage along a flange, and etc. Jet fires can arise from release of gaseous, flashing liquid (two phase), and pure liquid inventories. The jet fires might also occur from an explosion or the burn back of a cloud fire[1]. Jet fires range from being barely visible, e.g. upstream part of high pressure natural gas flames, to highly unclear by dark soot, e.g. downstream section of heavier hydrocarbon jet flames such as propane.

Presence of source momentum in jet fires distinguishes them from the pool fires. Furthermore, jet fires have zero thermal inertia, and they reach full intensity almost instantaneously. On the other hand they can also be shut down very rapidly which is important in control and isolation strategies. In addition to initial release rate there are also other important parameters such as the change in release rate and the total duration time. Jet fires, like pool fires, might be influenced by an external factor such as wind which might affect the severity of fire [55].

Initial part of the jet flames is largely affected by source momentum, while further downstream the buoyancy forces due to hot flue gases and cross wind are the dominating factors. For gaseous fuels, some of the lowest momentum jet fires are the subsonic flares. The gas velocities in such flames are of the

[1]Cloud fire is a transient fire resulting from the ignition of a cloud of gas or vapor and not subject to significant flame acceleration due to effect of confinement or turbulence [55].

order of 50 m/s or less. Air entrainment in low velocity jet fires is not too efficient, they pose therefore with longer flame and are sooty, and as a result more radiant. The fuels with high molecular weight produces sooty flame too with high rate of radiation. Experiments with liquid propane at ambient temperature show that the release from a 10 mm nozzle diameter with a reservoir pressure of 20 bar and a flow rate of 2 kg/s produces a very sooty and highly radiant flame with an approximately length 15–20 m [55, 56].

Gas release with high pressure are normally choked. At some point beyond the release point the flow velocity is equal to that of local sound speed, i.e. sonic velocity, and there exits a number of expansion chocks structures downstream of the chock (this is further explained in next section). The jet flame starts further downstream with bluish color as a premixed flame and stabilizing the remaining turbulent diffusion flame. While the gas velocity at the chock region is of the magnitude of around 300 m/s, those further downstream are considerably lower. The source momentum dominates the buoyancy forces. In contrary to laminar jet flame (subsonic) the amount of air entrainment is quite higher. The resulting flame is a shorter, hotter and less sooty flame, i.e. less radiative (lower form factor and luminous). This is because combustion is more efficient. In some regions of the flame the major part of radiation may originate from carbon dioxide and water vapor molecular emissions rather than soot. An example to illustrate the dimension of such type of flame may be a release of natural gas at 200 bar from a hole with 10 mm diameter. The resulting discharge is about 3 kg/s giving a flame length 15–20 m.

In principle all types of fuel which are under certain pressure, i.e. fluid has some momentum upon release, are potential for jet fires. The most common types are:

- gas containing condensate (and water),
- some condensates,
- natural gas (C_1),
- associate gas ($C_1 - C_4$).

Indeed liquid jet fires might also arise from discharge of pressurized fluid such as crude oil, kerosene, diesel oil, lubricant, and etc. In such cases the liquid based diffusion flame is supported by the subsequent evaporating liquid.

Discharges above a certain flow rate for a given nozzle diameter may result in instability of the flame. Indeed there is a critical orifice below which a flame is only stable at very low or very high discharge pressures.

Jet flames are wind affected and their direction and path fluctuates as the air velocity changes.

3.1.1 Structure of Exit Turbulent Jet Flow

Consider a flow pattern of a jet issuing from a converging-diverging nozzle, known as *de Laval nozzle*. Assuming steady flow of a perfect gas with specified reservoir conditions and an exit gas pressure denoted by p_e.

Flow through the nozzle begins as soon as the exit pressure is reduced below the reservoir pressure p_0. If p_e is just slightly less than p_0 the flow is subsonic, and the pressure profile along the jet axis would be as curve a in Figure 3.1. As p_e reduces, the mass flow rate increases, and then the throat pressure decreases until it reaches a critical value (p^*) as shown by curve b. At this stage the p_e corresponds to sonic conditions at the throat with an isentropic flow. The flow is subsonic everywhere in the nozzle except at the throat, and the mass flow rate is maximum [57].

Assuming the exit pressure p_e is now reduced to a value corresponding to pressure curve g. The expansion is still isentropic and the flow is supersonic at the diverging portion of the nozzle. The pressure within the nozzle can not any further be reduced, but when the exit pressure is reduced to h the flow of the jet fluid issuing from the nozzle gets a complicated pattern. Thus, curves b and g represent two limits of exit pressure for isentropic flow. For exit pressures below b a shock wave forms within the diverging part of the nozzle, and changing the flow pattern from supersonic to subsonic flow. This is shown by curve d. At still lower exit pressure the flow adjusts itself through a series of shock waves with an average flow velocity of supersonic.

When the fluid leaves the nozzle at supersonic velocity and its pressure is exactly equals to the ambient (curve g), the nozzle is referred to *correctly expanded*. If the exit area is less than the correctly expanded nozzle, the flow is called *underexpanded* (curve f) and the jet fluid has a pressure greater than the surroundings. But, if the exit area is larger than the correctly expanded value, shock waves form within or just outside the nozzle and the flow type is called *overexpanded* as shown by curve h in Figure 3.1.

Because of entropy rise the overall flow is not isentropic, although the flow on either side of the shock may still be isentropic.

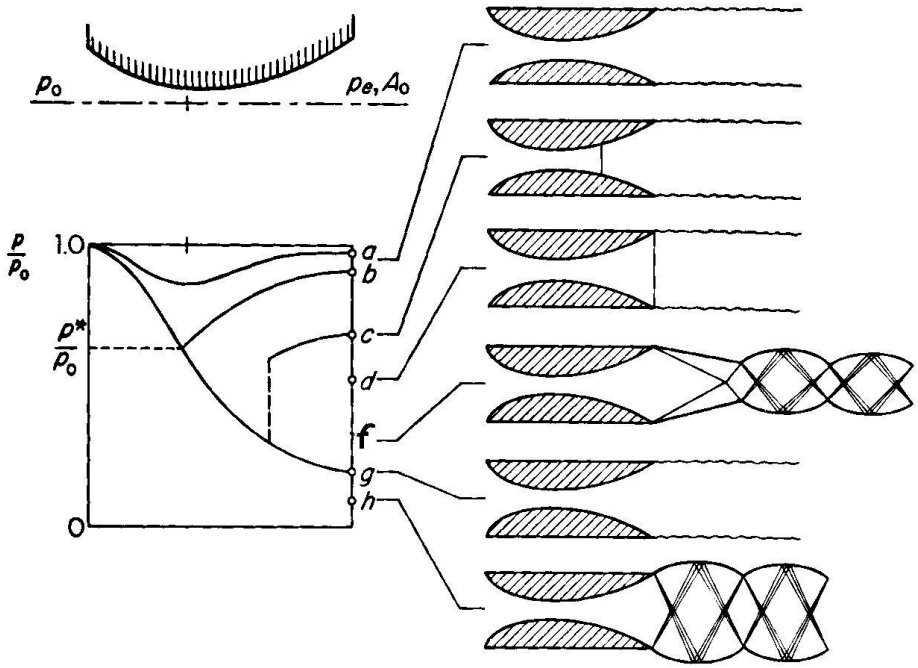

Figure 3.1: Pressure profile and exit jet configuration [57]

3.1.2 Jet Flame Shape

Vertical Flame Length

It is defined as the distance from the release point to the end of the flame. In case of wind or buoyancy forces the length may be the curvilinearly along the flame path, or it simply may be the straight distance line to the flame tip.

One of the simplest method for calculating the flame length in design of subsonic flare stacks is

$$L = 2.76Q^{0.452}, \tag{3.1}$$

where L is the flame length (m) and Q is the combustion heat released (MW). The correlation predicts reasonable for gaseous fuels and stack diameters in the range 500–800 mm [58].

An alternative correlation is given by Wertenbach [59]

$$L = 18.5\dot{m}^{0.41}, \tag{3.2}$$

where $\dot{m}$ is the fuel mass flow rate (kg/s).

The estimates of flame lengths for both sonic and subsonic gaseous flows through a hole diameter 102 mm reported by McMurray [60], show a subsonic vertical flame length about 30 % shorter than Equation (3.1) predicts. In the case of sonic flow it is estimated by

$$L = 1.422Q^{0.457}. \tag{3.3}$$

Suris et al. [61] developed an expression relating flame length to Froude number based on the jet flow condition just downstream of the nozzle using small scale vertical methane and propane flame as

$$L = AD\left(\frac{u^2}{gD}\right)^{0.2}, \tag{3.4}$$

where A is an empirical constant, D is the source hole diameter (m), u is the jet velocity downstream of the exit plane (m/s), and g is the acceleration of gravity (m/s^2).

The average value of the coefficient A according to various authors is given as follows

$$A = \begin{cases} 28 & \text{for methane flame,} \\ 40 & \text{for propane flame,} \\ 15 & \text{for hydrogen flame.} \end{cases}$$

Another correlation is derived by McCaffery [62] for vertical flame length based on subsonic and sonic release of natural gas for orifice diameter in the range 38–102 mm and a fire size up to 470 MW, and is given as

$$L = B + 200D_e, \tag{3.5}$$

where B is the flame lift-off distance (m) and D_e is the effective orifice diameter (m). In the case of subsonic flows the effective diameter is the actual hole size, while for sonic releases it is referred to the expanded jet diameter at atmospheric pressure.

An expression which concentrates on the turbulent mixing and buoyancy effects on the end part of the flame rather than conditions near the jet exit, estimates the length of small scale flames as given by

$$L = B + \frac{5.3D}{C_{fu}}\left[\frac{1}{m}\frac{T_F}{T_{fu}}\left(C_{fu} + (1 - C_{fu})\frac{M_a}{M_{fu}}\right)\right]^{\frac{1}{2}}, \tag{3.6}$$

where C_{fu} is the stoichiometric molar concentration of the fuel, T_F is the flame temperature (K), T_{fu} is the fuel vapor temperature at orifice exit (K),

m is the molar ratio of reactants to products, and $\frac{M_a}{M_{fu}}$ is the ratio of the molecular weight of the surrounding atmosphere to the jet fuel [63]. Using small orifice diameter of 3–7.6 mm, and wide variety of fuels the turbulent flame lengths may vary from 40 to 290 nozzle diameters with an error between 10 to 20 percent. It was further found that beyond a nozzle velocity sufficient to produce a fully turbulent flame, any further increase in the velocity had very little impact on the flame length.

A more precise correlation for predicting vertical flame length in still air is based on the Richardson ratio which determines the transition between the high and low jet momentum dominated regimes [64, 65]. This still air flame length, L_0, based om laboratory size flames is given by solving the equation

$$\left(\frac{2.85D_e}{L_0W}\right)^{\frac{2}{3}} = 0.2 + 0.024\left(\frac{g}{D_e^2u_e^2}\right)^{\frac{1}{3}} L_0, \tag{3.7}$$

where W is the mass fraction of fuel in stoichiometric mixture and u_e is the expanded jet velocity (m/s).

The flame length exposed to crosswind shortens significantly due to increased entrainment of the air, and the buoyancy effects are increasingly overshadowed.

The flame length found from Equation (3.1) or (3.2) can be used as the curvilinear length of the flame center line to predict the average axial velocity at any point in the flame as given by

$$u_a = 1.6\pi D_e u_j \left(\frac{1}{s} - \frac{1}{L}\right), \tag{3.8}$$

where u_a is the average axial gas velocity (m/s), u_0 is the initial jet velocity at ambient pressure (m/s), and s is the curvilinear distance along the flame axis (m) [55].

To correct for reduced length of the flame when subjected to crosswind one has introduced a factor [66], depending on the wind speed, to calculate the shortened flame length by

$$L = L_0\left(0.51e^{-0.4v} + 0.49\right), \tag{3.9}$$

where v is the wind velocity (m/s).

Flame Lift-Off

Flame lift-off is defined as the distance from the release point to the point at which a blue gaseous flame appears. Jet flames are usually lifted and the

flame base is not attached to nozzle tip. This is mainly due to the high velocity of effluent jet fuel, the strain rates, and the fuel rich zone near the release point.

Sønju and Hustad [67] having studied data for methane flames up to 1.6 MW and for subsonic propane flames up to 7.5 MW, and McCaffrey [68] using data from 7 MW methane flames for nozzle diameter of 30 mm, have come to the conclusion that the expression derived by Peters and Williams [69] predicted the lift-off distance, B (m), fairly well, and it is given by

$$B = 3.6 \cdot 10^{-3} u_e. \tag{3.10}$$

An alternative correlation which relates the data to vertical subsonic propane flow for orifice diameter of 10–80 mm is

$$B = 0.016 u D^{\frac{1}{2}}, \tag{3.11}$$

where u is the fluid source velocity (m/s) [70].

Another relationship which is based on sonic and subsonic flow for 20–470 MW methane flames states that

$$\frac{B}{u_e} = 2.5 - 5 \text{ ms}, \tag{3.12}$$

which indeed means the measurements expand on either side of Equation (3.10) [62].

After calculation of various lifted flames one has found that the flame lift-off position is the point at which the mean turbulent heat release rate exceeds a certain critical value. For natural gas flames this corresponds to 3 MW/m^3 while for propane flames is 10 MW/m^3 [71].

Non-Vertical Flame Length

There are very few models available for inclined releases. One correlation which concerns the natural gas flares [72] with flow ranges 3.5-25 kg/s at a release angle of 45° to the vertical, subject either to crosswind or downwind, predicts the trajectory flame length as

$$L = 1.555 Q^{0.467}, \tag{3.13}$$

where Q is the heat released based on the lower heat of the fuel combustion (MW).

Jet Fire Impingement and Heat Flux

As previously pointed out the major part of radiation from all luminous flames originates from the soot particles. This is typical for large scale fires, e.g. offshore. Whilst for smaller scale flames the radiation is dominated by hot gases, i.e. molecular emission from CO_2 and H_2O.

The factors with significant effect on the degree and type of radiation are the fuel type, the mass flow rate, and the jet discharge momentum which influences the subsequent air entrainment.

There have been carried out a numerous experimental studies on jet fire impingements and engulfments. The main conclusion of some of the results shall be highlighted here [55].

Studies done with intermediate scale for sonic and subsonic propane open jet flames show that the propane heat fluxes increase with increasing jet velocity to about 200 kW/m^2, where one estimates the convective component as the major contributor. While the trend for the methane flame was found to be about 150 kW/m^2.

The initial part of the flames is relatively cool and the greatest heat fluxes occur at impingement distances around 40 % downstream of the source.

Heat fluxes from sonic natural gas flames with mass flow rates up to 10 kg/s are between 50 to 300 kW/m^2. The areas of the maximum flux is very small and occur on a limited portion of the flame. The maximum average heat flux of the impinged area is approximately 200 kW/m^2. These flames are not optically thick, and higher radiation heat flux might be anticipated in much larger flames and in sonic flames of natural gas containing components with higher molecular weight.

In case of two-phase propane flames at low velocity with flow rates up to 20 kg/s the heat fluxes are in the range 50 to 250 kW/m^2, with the maximum average heat flux over the total flame impinged area about 150 kW/m^2.

The impingement characteristics are significantly influenced by the shape of exposed objects. The objects produce intense local turbulence, which generates fluctuating aerodynamic forces that may limit the continued existence of some fire protection materials.

3.1.3 Prediction of Heat Flux

Based on physical arguments and empirical correlations, semi-empirical methods are developed where most of them estimate flame shape and the magnitude of heat flux from jet fires to external objects [55]. In that occasion there are three types of model:

1. point source models, which assume that the source of the heat transfer radiation is a point,

2. multiple point source models, focusing on the effect of flame shape on the radiation heat flux by distributing radiating point sources along a modeled flame centerline trajectory, and

3. surface emitter models, which assume that the heat is emitted from the surface of a solid object as a tilted frustum of a cone or a cylinder.

Point Source Models

An approach which predicts the radiation from flares to far-field objects, usually more than two flame lengths away, whereas the exact flame shape hence the view factor is not a critical factor [58]. The radiation heat flux $\dot{q}''$ (kW/m^2) to an exposed object outside the flame is defined by

$$\dot{q}'' = \frac{\tau F Q}{4\pi R^2} \cos\alpha, \tag{3.14}$$

where τ is the atmospheric transmissivity, F is the fraction of the net combustion energy that leaves the flames as radiation, Q is the combustion heat released (kW), R is the distance (m) from the point source P to the exposed object T, and α is the angle between the normal to the receiving surface and the line connecting the point source to the object (PT), see Figure 3.2.

The point source is located at the middle of the flame trajectory given by the Equation (3.1). The magnitude of F factor is set to 0.2 for all natural gas flames and 0.3 for all other hydrocarbons [58].

Multiple Point Source Models

Some mathematical models such as WHAZAN by Technica assumes five point sources along the flame axis, each with a a radiation intensity $\frac{1}{5}th$ of the total radiative power. Then the received heat flux by the object is sum of the heat radiations predicted by Equation (3.14). The F factor is set to 0.2 regardless of fuel type.

Other models divide the flame into a number of radiation sources each with the same emissive radiative power E (kW/m^2) give as

$$E = \frac{FQ}{n}, \tag{3.15}$$

where F factor is for the whole flame and n is the number of point sources [60].

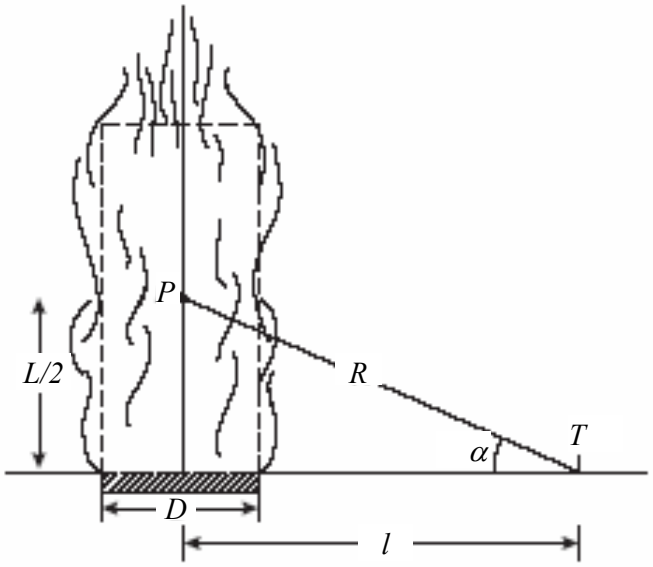

Figure 3.2: Estimation of radiant heat flux from point source P receiving at point T at a distance of l from a pool fire [73]

If the radiation source is an isotropic emitter, the heat flux from one point source $\dot{q}_i''$ (kW/m^2) to receiving object is defined by

$$\dot{q}_i'' = \frac{\tau E}{4\pi R^2} \cos\alpha. \tag{3.16}$$

The model assumes that the flame is transparent to radiation, so that the flux near the flame is likely overestimated.

If on the other hand the flame is a diffuse emitter, the heat flux from one point source $\dot{q}_d''$ (kW/m^2) to receiving object is given by

$$\dot{q}_d'' = \frac{\tau E}{\pi^2 R^2} \cos\alpha \cos\beta, \tag{3.17}$$

where β is the angle between the normal to the flame axis and the line connecting the point source to the receiving object.

Contrary to the previous case this model assumes that the flame is opaque to radiation, and as a result the flux near the flame tends to be underestimated.

By linking the two types of emitter, i.e. over- and underestimated flux, one may arrive at an expression representing a weighted average for each source given as

$$\dot{q}'' = A\dot{q}_i'' + (1 - A)\dot{q}_d'', \tag{3.18}$$

where A is a constant and its value is $0 \leqslant A \leqslant 1$.

Cook et al. [72, 74] has also used this mixed source model by setting $A = 0.5$ and dividing up the visible part of the jet flame symmetrically into a number of sources with the middle part of the flame as the maximum emissive power. Their radiation diffuse source model includes the term $4\pi r^2$ instead of $\pi^2 r^2$ in the denominator of Equation (3.17). Then they further defined the F factor based on the large scale vertical natural gas flames as given by

$$F = 0.321 - 0.418 \cdot 10^{-3} u, \tag{3.19}$$

where u is the jet exit velocity in m/s.

Surface Emitter Models

This model assumes that the flame is as a solid surface with a constant surface emissive power (SEP[2]) over the entire flame surface. SEP is calculated from the F factor and the total surface area. The model in spite of its lack of accuracy has a physical basis a little closer to reality than that of point source models [55]. The radiation flux, $\dot{q}''$ (kW/m^2), to an exposed object is then given by

$$\dot{q}'' = \tau \phi S, \tag{3.20}$$

where ϕ is the view factor and S is the average SEP (kW/m^2). The view factor ϕ which takes into account the geometrical relationship between the emitter and the receiver is defined as the fraction of the field of view from the receiving surface which is filled with flame. The view factor is equal to 1 if the entire field of view is filled with flame, otherwise it is less than 1. Its value may be determined using diagrams or tables.

The F factor for natural gas flames is given by

$$F = 0.21 e^{-0.00323 u_e} + 0.11, \tag{3.21}$$

where u_e is the expanded jet velocity at atmospheric pressure (m/s).

In order the above expression for F factor could be applied to other fuels as well, one has introduced correction factor by multiplying the right hand side of the Equation (3.21) by a function as given by [75]

$$f(M_w) = \begin{cases} 1 & M_w < 21, \\ \left(\frac{M_w}{21}\right)^{\frac{1}{2}} & 21 < M_w < 60, \\ 1.69 & M_w > 60, \end{cases} \tag{3.22}$$

[2]SEP is the rate of heat radiated outward per unit surface area of the flame.

where M_w is the molecular weight of the fuel (g/mol).

The SEP of the visible part of the flame can be estimated by the following statement [67]

$$S = \begin{cases} 5 + 3.9(L - B) & \text{for methane flame,} \\ 10 + 7.8(L - B) & \text{for propane flame,} \end{cases} \tag{3.23}$$

where L is the visible flame length (m) and B is the flame lift-off (m).

3.2 Brief Discussion of Other Hydrocarbon Fires

In this section three other types of accidental fires shall be shortly discussed. One is pool fires which break out as a result of a horizontal pool of a hydrocarbon. The other two types are identified as cloud fires and fireballs, known as transient fires, and they are as a result of flammable volume of leaked hydrocarbon either in gaseous form or two-phase mixture [55].

3.2.1 Pool Fires

A pool fire is defined as a turbulent diffusion fire above a horizontal pool of vaporising hydrocarbon fuel with zero or quite low initial momentum. Heat transfer back from the fire to the pool controls the evaporation rate and hence the fire size [55].

Stable liquids tend to burn uniformly. But it is possible to experience a running liquid fire as a result of continuing fuel leakage producing a flow of burning liquid over the surfaces below.

The mass burning rate, $\dot{m}''$ (kg/m^{2}s), for a pool fire composed of single component fuels which are liquids under ambient conditions, is predicted by

$$\dot{m}'' = \frac{0.001\Delta H_c}{\Delta H_v + C_p(T_b - T_o)}, \tag{3.24}$$

where ΔH_c & ΔH_v is the combustion and vaporisation heat of the fuel at its boiling point, respectively (kJ/kg), C_p is the specific heat capacity of the liquid fuel (kJ/kgK), and T_b & T_o is the boiling and initial temperature of the liquid, respectively (K) [76].

Another alternative to calculate the burning rate of the fuel may be found from

$$\dot{m}'' = \frac{\dot{Q}}{\Delta H_c A_{fu}}, \tag{3.25}$$

where $\dot{Q}$ is the total heat release rate (kW) and A_{fu} is the surface area of the fuel (m^2) [77].

However three regimes are distinguished. If the pool diameter is less than 0.03 m the flames are laminar, and the burning rate drops with increase in diameter. For diameter larger than 1 m the flames are considered as fully turbulent and mass burning rate becomes independent of diameter. While for diameters in the range between 0.03-1 m the transition behavior is observed [77].

The flame length may be predicted [78] by the correlation given as

$$\frac{L}{D_p} = 42 \left(\frac{\dot{m}''}{\rho_a \sqrt{g D_p}} \right)^{0.61}, \tag{3.26}$$

where ρ_a is the ambient air density (kg/m^3), g is the acceleration of gravity (m/s^2), and D_p is the pool diameter (m).

Another correlation based on small scale experiments predicts the flame height as follows [79]

$$\frac{L}{D_p} = 15.6 N^{\frac{1}{5}} - 1.02, \tag{3.27}$$

whereas the non-dimensional number N is derived from a modified Froude number [80] and is defined by

$$N = \left(\frac{C_{pa} T_a}{g \rho_a^2 \left(\frac{\Delta H_c}{r} \right)^3} \right) \frac{\dot{Q}^2}{D_p^5}, \tag{3.28}$$

where C_{pa} is the ambient heat capacity (kJ/kgK), T_a is the ambient temperature (K), and r is the stoichiometric mass ratio of air to fuel.

Since most of the terms in Equation (3.28) are known ($\Delta H_c / r \approx 3000$ kJ/kg), Equation (3.27) can then be simplified [77] and rewritten as

$$L = 0.23 \dot{Q}^{\frac{2}{5}} - 1.02 D_p. \tag{3.29}$$

To predict the amount of heat radiation emitted from a pool fire to the surrounding, one may make use of uniform SEP (kW/m^2) over the whole flame surface [55]. The following correlation using the data from gasoline, kerosene, and JP-5 may be applied [81]

$$S = 20 + 120 e^{-0.12 D_p}. \tag{3.30}$$

Based on experimental data from large-scale pool fire experiments, Shokri and Beyler [82] developed an empirical expression for incident heat-flux, $\dot{q}''$ (kW/m^2), from pool fires to vertical targets at ground level stated by

$$\dot{q}'' = 15.4 \left(\frac{l}{D_p} \right)^{-1.59}, \tag{3.31}$$

where l is the distance from center of the circular pool fire to the target. For non-circular pools the equivalent pool area may be approximated by an equivalent diameter as given by

$$D_p = \sqrt{\frac{4 A_{fu}}{\pi}}, \tag{3.32}$$

where A_{fu} corresponds to surface area (m^2) of the non-circular pool [73].

The above calculations assume that the flames are vertical and not influenced by wind.

3.2.2 Cloud Fires

As earlier indicated cloud fire is a transient fire resulting from the ignition of a cloud of gas or vapor and not subject to significant flame acceleration due to effect of confinement, obstruction, or turbulence.

The behavior of the released gas in the atmosphere concerning its formation and dispersion, unconfined and unobstructed, depends on if the gas is heavier or lighter than the air and on the initial momentum release.

The combustion characteristics of flammable vapor cloud depend on the fuel type, the release momentum, the density and temperature of the fuel-air mixture and the ambient conditions.

The flame sustainability and propagation speed is mainly dependent on the uniform local gas concentration and wind velocity. Regions with pockets of gas well isolated from the rest which result in non-connectivity of flammable gas may cause unsustained flame.

Based on large scale experiments [83, 84, 85] with LNG and liquefied propane spills on sea water a typical average flame speed for propane cloud relative to unburnt gas used to be 11–12 m/s at an ambient wind velocity of 7 m/s, while for methane it was in the range of 4.5–6 m/s.

The flame speed is linearly depended on wind velocity, and it is increased upon high momentum jet release and/or presence of obstacles as they both contribute to increasing rate of turbulence. The cloud flame speeds are slightly higher than the laminar flame speed.

The corresponding flame height for the above given flame speed is 9–12 m for propane and 7–15 m for methane. The thickness of the flame varied approximately inversely with the flame height.

Based on the surface emitter model the radiation heat flux from methane cloud fires measured in the experiments [85] showed values in range 140–225 kW/m^2 which is close to the values for LNG pool fires on water. For propane it was between 145–190 kW/m^2 which is quiet different from the values of propane pool fires.

3.2.3 Fireballs

A fireball is a rapid turbulent combustion of fuel as an expanding radiant ball of flame, or may be alternatively defined as a sudden ignition of concentrated flammable vapor either single fuel or diluted mixtures. Very often the fireballs

are associated with BLEVE (Boiling Liquid Expanding Vapor Explosion). BLEVE is defined as a fire as a result of sudden release of a fluid under pressure caused by catastrophic failure of the pressurized container [77].

There are a number of parameters which are decisive whether an ignition leads to a fireball or a cloud fire:

- *ignition time*: earlier ignition is more likely to lead to a fireball,
- *momentum release*: high momentum releases ignited quickly will result a fireball,
- *release direction*: vertically released fuels are more probable to produce fireball than horizontal releases due to buoyancy effects,
- *wind effect*: releases in still air are more subject to fireball since the wind tends to disperse the fuel-air mixture, and
- *ignition position*: ignition sources below the mixture give rise to a fireball than those situated on the side or top of the mixture since buoyancy contributes to fireball formation.

From the experiments with different fuel types based on the release range of 0.1–31 kg and backed by large fireball incidents involving fuel mass up to 200 tonnes, one has developed a correlation [86] to estimate the maximum diameter D_{max} (m) of fireball as given by

$$D_{max} = kM_{fu}^{0.33}, \tag{3.33}$$

where the constant $k = 6.2 - 6.3$ and M_{fu} is the total fuel mass (kg).

The fireball total duration time, i.e. the duration time of the visible flame, based on a number of large scale fire tests may be predicted by the statement given as

$$t = 1.089M_{fu}^{0.327}, \tag{3.34}$$

where t is the total combustion time (s).

When Equation (3.34) is applied to large releases it predicts to some extent higher duration time [86]. One good alternative to approximate the combustion duration time for large releases is given by the statement [87]

$$t = 0.41M_{fu}^{0.34}, \tag{3.35}$$

or using the expression [88]

$$t = 0.45M_{fu}^{0.33}. \tag{3.36}$$

The radiation heat from a fireball is maximum on the top areas of the flame, whilst it is lower on the lower portion because of the poor mixing and soot shielding [89]. Measurements done for butane fireballs indicate a radiation heat flux ranging 300–350 kW/m^2 and a spot up to 500 kW/m^2 from the highly emissive areas at the top.

The fraction of thermal radiation leaving the fireball, the F factor, is dependent on the release pressure [90], and is give by

$$F = 0.00325 P_{sv}^{0.32}, \tag{3.37}$$

where P_{sv} is the saturated vapor pressure before the release (Pa).

Because of the transient nature of fireballs, the effect on structures outside the flame is insignificant, while the radiation hazards to people is very serious.

3.3 Liquid Droplet Impaction on a Hot Surface

For the past three decades the fire hazards on installations offshore as well as onshore have received special attention in how to protect the surfaces exposed to fire by means of water spray. This has lead to a number of research works both of theoretical and practical character. The theoretical concern was made by CFD-studies, whiles the practical part was carried out by performing laboratory and large scales experiments.

In this section the efficacy of water droplets in cooling of hot surfaces, i.e. cooling effectiveness, will be reviewed. The focus among others shall be made on the droplet size, velocity, contact angel (advancing and receding), interface behavior during evaporation, and heat transfer.

3.3.1 Large Scale Studies

Two of the large scale studies done in this field funded by UK's Health and Safety Executive are carried out by Shell and British Gas which in brief shall be discussed [91, 92].

The scope and nature of both works are similar except type of the jet fuel used, whereas in the study done in 1997 the fuel utilized was liquid propane [91] while in 2000 it was butane [92]. In the later event the number of thermocouples attached to the target in the area subjected to hot spot were raised in order to increase the resolution and hence the surface temperature information.

Due to this fact, i.e. finer temperature resolution, and access to better illustrations the focus shall be made on the work performed in 2000, while now and then when necessary the results shall be compared. The objective of the later study using butane was to extend the understanding of jet fires. These types of fire were known to have somehow different features and may result in different findings [92].

Experimental set-up

The exposed object was an empty 13 tonne LPG storage tank with a dimension 2.17 m diameter $\times$ 7.5 m long equivalent to a total surface area of 61.3 m^2 (including spherically dished end cups). 85 thermocouples were attached to internal surface by capacitance discharge welder, with concentration on the area subject to hot spot. The vessel was also equipped with 24 water spray nozzles. The distribution and location of the thermocouples together with orientation of deluge nozzles are shown in Figure 3.3 [92]. The figure illustrates the surface of the tank as folded out in a two-dimensional

plane. The center line of the horizontal jet is approximately aligned with the thermocouple 27 so that the flame is targeting at this point.

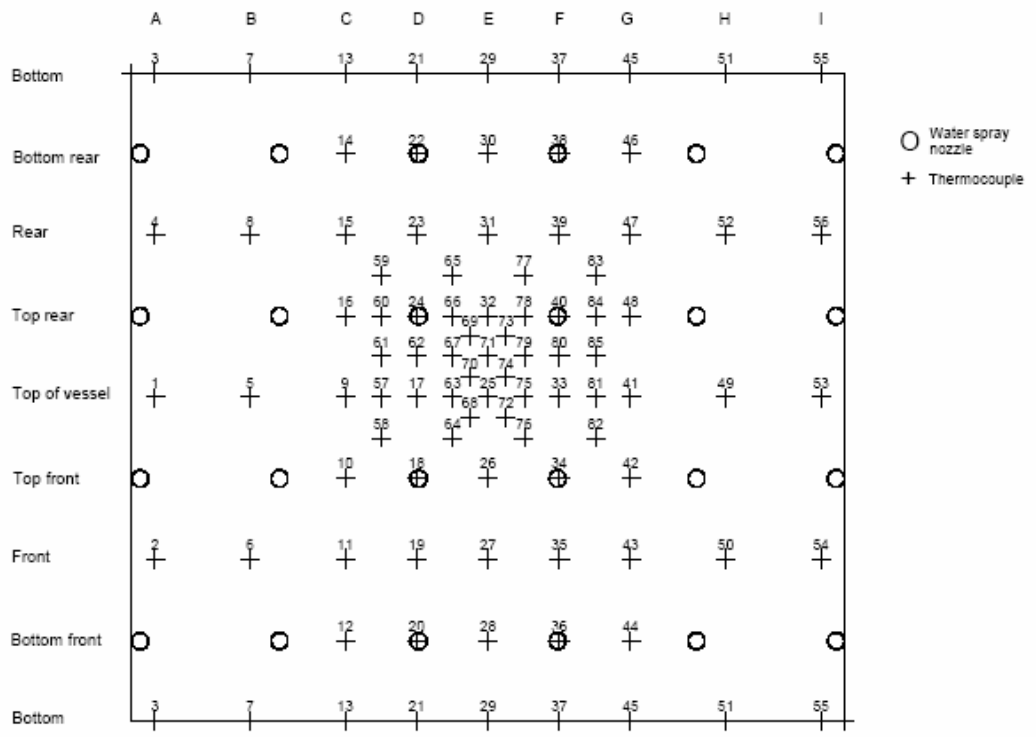

Figure 3.3: Location of thermocouples and deluge nozzles [92]

As it can be seen the area with more concentrated thermocouples, i.e. subject to hot spot, is located on the top of the vessel. One main reason that this area is more exposed to thermal stresses may be explained by the fact that the major part of the flame after impinging bends up due to buoyancy and reaching the top. The effect may be further elevated as the diameter of the flame is increased, i.e. larger orifice diameter at farther discharge distance.

The 24 water spray nozzles were distributed in six sectors each with sets of four around the vessel at an equal axial spacing. The nozzles were spraying on the tank with an application rate of 17.6 liters/m^{2}min which is about 73 % above the design value 10.2 liters/m^{2}min. Figure 3.4 shows the position of the deluge nozzles while a photograph in Figure 3.5 shows the deluge in operation [92].

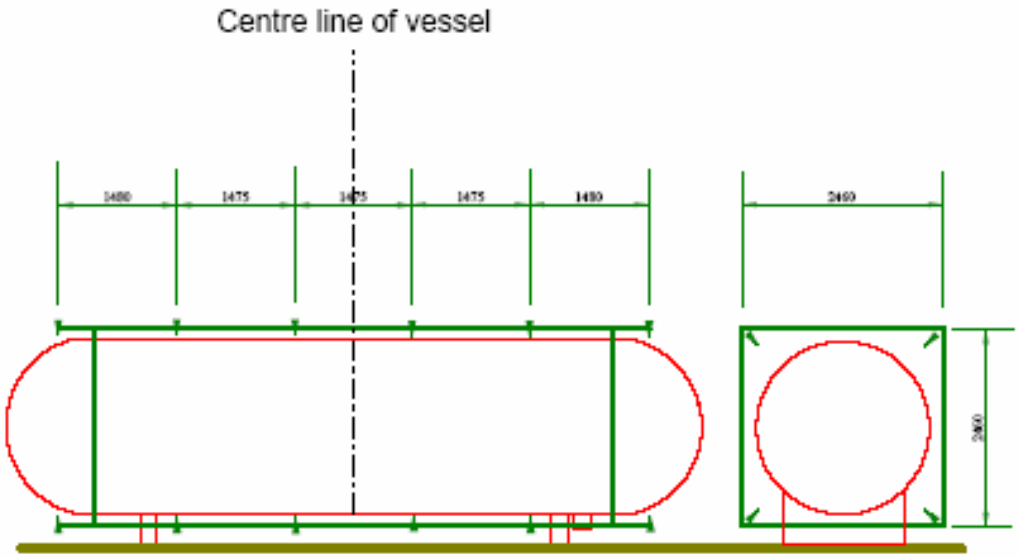

Figure 3.4: Position of water spray nozzles [92]

Figure 3.5: Water spray nozzles deluging the target [92]

The releases were through 12.5 and 25 mm sharp-edged orifice plates and a 50 mm full-bore with a liquid release rate of 1, 4, and 9 kg/s, respectively, and at three different discharge distances 1, 3, and 5 m. The tests were carried out with deluge on before the fire and with deluge delayed by 30 s. This resulted in conducting at least 18 sets of experiments. The discharge pressure and temperature for the tests roughly was 1.2 barg and 8 °C, respectively.

Figures 3.6 and 3.7 show photographs of two typical jet fire experiments without and with deluge, respectively. Both cases refer to release from a 25 mm nozzle at a 3 m stand-off distance.

Figure 3.6: Jet fire test without water spray [92]

Results and Discussion

The main concern of this study as well as the previous one with propane was, where possible, to keep the exposed surface temperature below 120 °C. This criterion was chosen because the earlier work has shown that this temperature is an indicative of having achieved critical conditions for failure of water film [93].

In presentation of the results temperatures below 0 °C indicate cold patches (liquid impingement causing patch of ice), between 0 and 120 °C refers to effective cooling, whiles above 120 °C corresponds to dry patches.

With deluge on from the start the surface temperature for all the cases except for a couple of largest releases was kept safely under 120 °C. Only the

Figure 3.7: Jet fire test with deluge [92]

aforementioned releases resulted in dry patches. The largest dry patch was observed in test with 50 mm orifice at 5 m distance. With another word, the deluge appeared to be more efficient for smaller releases at the closer distances.

While with deluge delayed by 30 s the dry patches formed rapidly and persist except for the smallest orifice, i.e. 12.5 mm. Again the largest dry patch was occurred with 50 mm nozzle at 5 m distance.

Observation of dry patches in both cases were also noted almost in similar manner in the testes with propane.

Figure 3.8 illustrates a typical temperature profile for one of the tests, in this case 50 mm nozzle at 1 m stand-off distance, 30 s delayed deluge. The abbreviation TK25 symbolizes thermocouple 25 and etc., also shown in figure is the line of 120 °C criterion.

At the thermocouple positions 63 and 64 the temperature never reached 120 °C before the initiation of the deluge 30 s after ignition. While the temperature at locations 66 and 69 exceeded the criterion point. But as soon as the water film was established at 50 s (location 66) and 90 s (location 69) the temperatures were depressed below 120 °C approximately 30 and 70 s, respectively, after activation of the deluge. As long as the water film was maintained the temperatures were kept below the criterion line and near the saturation point. At location 25 the temperature continued to rise but at a reduced rate with deluge on. Noting that all the thermocouples were located on the top and center area of the tank.

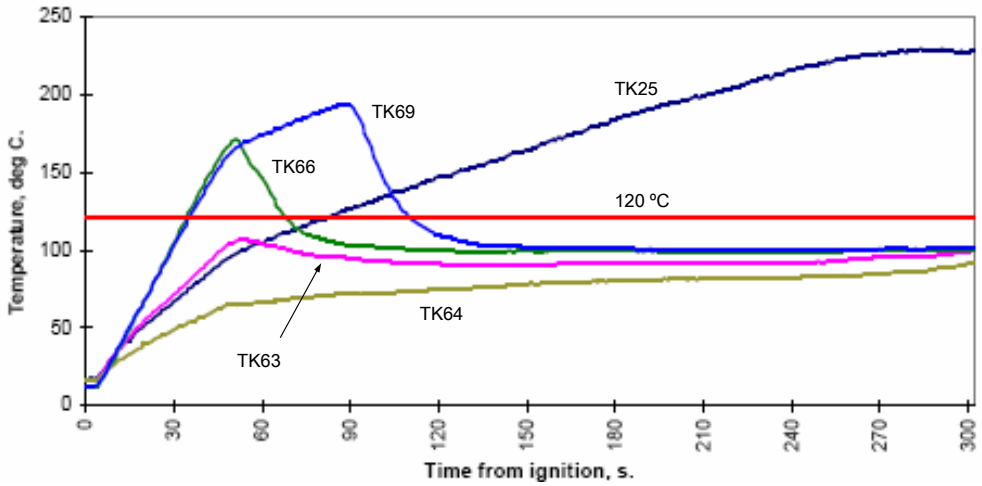

Figure 3.8: Wall temperature profile during the delayed deluge test with 50 mm bore & 1 m distance [92]

The dry patches are more obvious as shown in Figure 3.9 (before initiating the deluge) and Figure 3.10 (with deluge on) for a given specific time. The cold patches, i.e. icing on the wall at impinging point, are also shown.

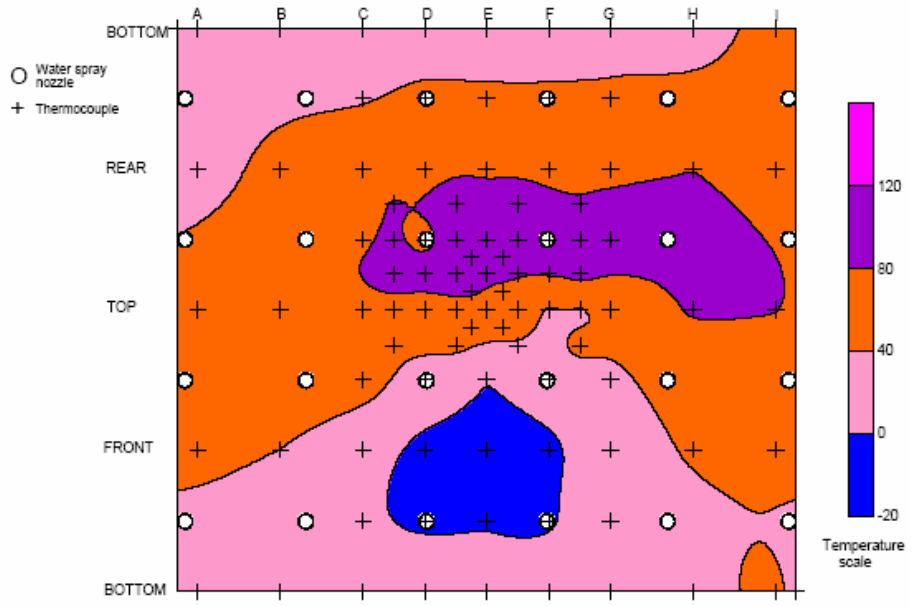

Figure 3.9: Wall temperature contours at 30 s, before deluge activated [92]

Employing water spray had two major impacts in protection of the object

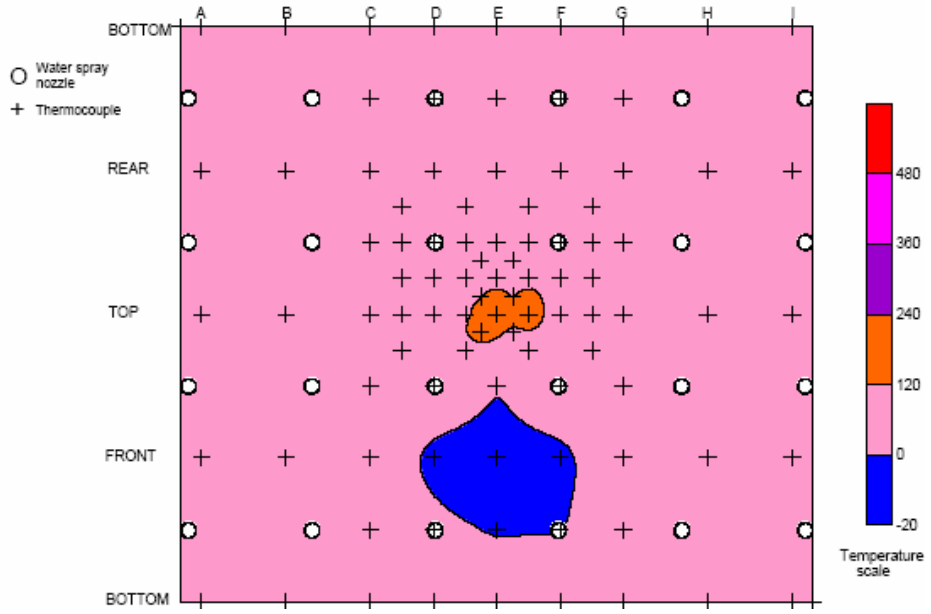

Figure 3.10: Wall temperature contours at 302 s, with deluge on [92]

exposed to fire. One is the direct cooling of the surface, the second effect is the amount of soot formation in the flame is reduced and causing lower luminosity hence reduction in radiation heat transfer. This results in a lower rate of temperature rise by a factor of between 2 and 5 [92] compared to undeluged case, which is pretty much similar to that found with propane, i.e. between 1.5 and 5.8 [91]. Rate of temperature growth is denoted by the unit °C/s.

In one test (25 mm hole, 3 m distance, delayed deluge) the duration time was prolonged in order to achieve equilibrium temperature. After 10 minutes the temperature at a small dry patch rose to 360 °C. The experiment was repeated, this time by blocking one of the spray nozzles in order to induce a larger dry spot. After about 20 minutes the equilibrium temperature reached to 580 °C. The steel wall will be severely weakened at this temperature but may not necessarily fail.

Conclusion

The results from both tests with propane and butane show that one cannot rely upon to maintain a water film over the entire tank although the water spray mass flux, i.e. 17.6 liters/m^{2}min, was over the design value.

The dry patches were smaller in case of the butane jet fires. In close releases with liquid impinging on the vessel it may cause local low temperature known as cold spots and icing.

3.3.2 Laboratory Scale Studies

To understand the dynamics of water droplets and to raise the cooling efficiency of water spray, a number of small scale studies have been performed and the phenomena such as evaporative cooling, droplet size, droplets velocity, and contact angle have been investigated.

Evaporative Cooling

As it was indicated in the previous section, the water film is not always easy to maintain despite of high mass flux of water. At high surface temperature the droplets jump over the surface and float over thin vapor layers [94]. As the surface temperature is lowered, wetting occurs. The transition between these two states is known as the Leidenfrost transition which describes the phenomenon of two-phase heat transfer [95]. Nucleation boiling occurs as the droplets wet the surface. At lower surface temperatures the bubble nucleation decreases and vaporization occurs at liquid-vapor interface. As the surface temperature is further dropped the rate of vaporization decreases and then the solid surface is covered with liquid.

Marzo [95] has studied dropwise cooling using two types of solid materials, one with high thermal conductivity (aluminum) and the other one with low thermal conductivity (Macor, an opaque glass like material), and heating the solid by two different methods, conduction and radiation. In order to eliminate the variation of the heat transfer characteristics of the droplet, deionized water was used and all mineral impurities and dissolved gases were removed. On a similar manner the solid chosen was with a uniform surface and it was rinsed with ethyl alcohol an deionized water prior to each experiment.

In case of the conduction the solid is heated from below the surface, while in the second case the heat input is provided by the radiant panels above the surface to simulate and create a fire-like environment.

To characterize the shape of the deposited droplets, one makes use of the shape factor, β, also known as the wetting parameter. It is defined as the ratio of the radius of the wetted region over the radius of the equivalent initial droplet volume as illustrated in Figure 3.11 [96]. The droplet size is varied between 10 to 50 μl (equivalent to a droplet diameter of 2.7 to 4.6 mm, respectively).

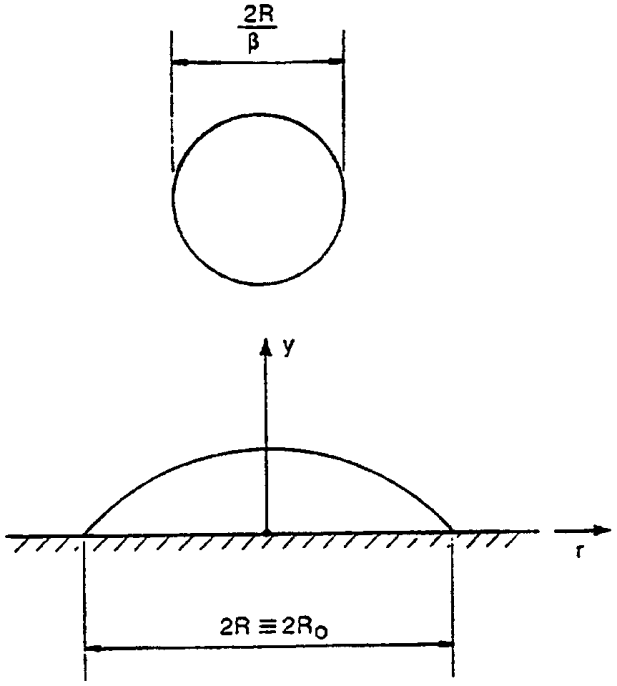

Figure 3.11: Parameter β and coordinate system (R =radius of wetted area; R_0 =initial radius of wetted area [96]

Conduction Heating: For gently or softly deposited water droplets[3] on aluminum the shape factor (β) ranges between 1.2 to 1.5 as the surface temperature is increased from 75 to 105 °C. Macor exhibits the same value of β, but for a temperature range of 90 to 180 °C. For sprayed water several studies have reported values up to 4.5 [97, 98]. Infrared equipment was used to capture the thermographic data providing one-dimensional transient temperature profile of the solid surrounding the droplet. Figure 3.12 demonstrates a such digital representation of a captured image, and Table 3.1 provides the total evaporation times as a function of droplet size and initial surface temperature [99].

The main conclusion is that as soon as the droplet is deposited, the liquid-vapor interface temperature drops considerably lower than the initial temperature of the solid surface. The nucleate boiling on aluminum starts at an initial solid surface temperature of about 103 °C, while in the case of Macor it is observed when the temperature approaches about 164 °C.

[3]It refers to release of droplets from a height up to 1.5 cm or 1.2-1.4 droplet diameters using a hypodermic needle device to dispense the water above the surface.

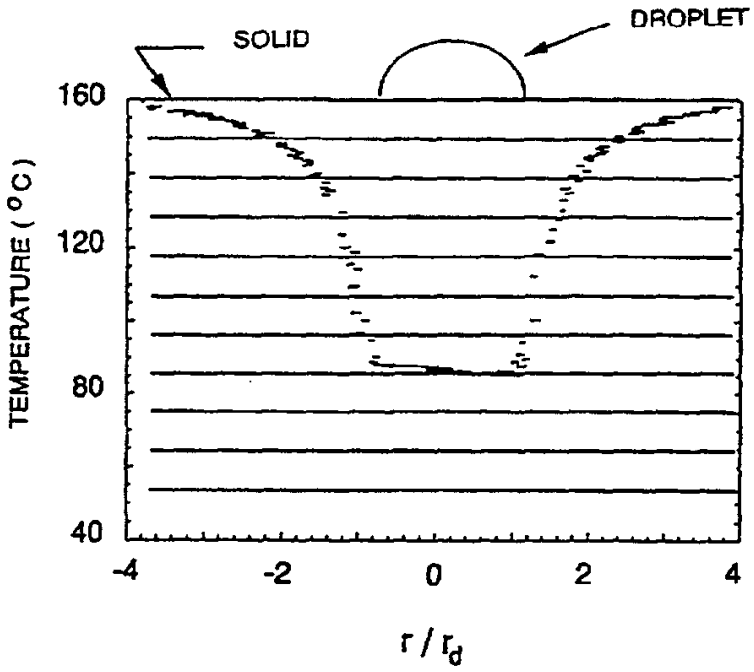

Figure 3.12: Thermographic image of a 50 μl droplet 40 s after deposition on Macor at 160 °C (r =radial surface coordinate; r_d =radius of wetted area [99])

Table 3.1: Evaporation time (s) for various droplet sizes [99]

Initial solid surface temperature (°C)	**Droplet size (µL)**		
	10	30	50
101	73	146	191
124	46	99	124
143	36	75	94
152	30	62	82
160	28	50	70

Radiation Heating: The direct radiant heat absorption at the liquid-vapor interface increase the interfacial temperature and decreases the surface tension. This leads to more initial spreading of the liquid droplets on the surface, which indicates that the liquid layer is thinner and the resistance due to the heat conduction through the liquid layer is reduced. Another effect of the reduced layer is that the contact angle at the droplet edge is less than in the

conduction case. The angle decreases as the droplet evaporates and reaching a limiting value between 7° and 10°, known as receding angle. At this stage the surface under the droplet shrinks and the liquid droplet continues to evaporate. When the initial value of the shape factor is increased the receding angle is reached sooner during the evaporation process.

Due to different mechanism of heat addition, i.e. from above the solid surface and in opposite direction to the conduction heating case, the lines of heat fluxes are diverging away from the droplet compaction point toward the cold depth of the material. While in the case of conduction the opposite is true, i.e. the lines of heat flux are converging from the hot depth of the solid toward the location of deposited droplet. As a result of this, the conduction contribution to the vaporization process from the solid through the liquid in the case of radiation heating is much lower. But this is compensated by higher rate of vaporization due to direct radiation heat input at the liquid-vapor interface. The overall vaporization time, anyhow, is similar for both mechanism of heating [95]. Investigation estimates that 20–30 % of the vaporization heat of water deposited on low-thermal conductivity material is due to direct incident radiation, and the remainder is from the conduction at the liquid-solid interface. The droplets heated by radiation spreads across the surface more than in the conduction case. This provides large surface area to absorb heat from above and a thinner liquid layer to transfer heat from below by conduction. [100].

Another observation using Macor indicates that the dissolved gases enhances the heat transfer from the solid surface by decreasing the incoming radiant input and causing a lower steady state temperature. It is further concluded that the major part of the cooling in the region of droplets occurs during the initial impingement of the water spray on the surface [101, 102].

Effect of Contact Angle: In order to understand and analyze the boiling phenomenon, interaction behavior of the droplet-solid, and spreading characteristics of the droplet better upon impact on a surface, one makes use of the parameter *contact angle* as illustrated in Figure 3.13 [103]. This was also discussed previously in Section 2.3.2. The angle is measured by obtaining images of the droplet using high speed video camera, and then analyzing it using data program such as AutoCAD.

In studying the dynamics of the impinging droplets, one distinguishes between dynamic advancing contact angle and dynamic receding contact angle, as shown in Figure 3.14. The advancing contact angle refers to the condition when the interface is advancing toward the vapor phase, while, the receding contact angle refers to the condition when the interface slides along the solid surface moving toward the liquid phase. They depend on the liquid, vapor,

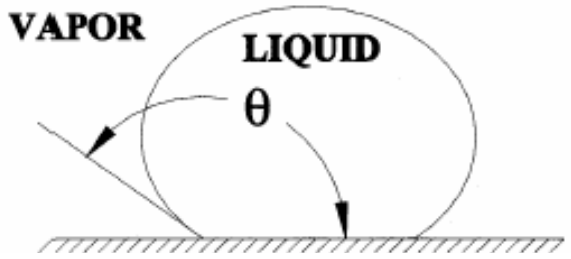

Figure 3.13: Droplet contact angle [103]

the material of the solid surface, the surface roughness, surface impurities either on on the liquid-vapor interface or the solid surface, and solid surface temperature [104].

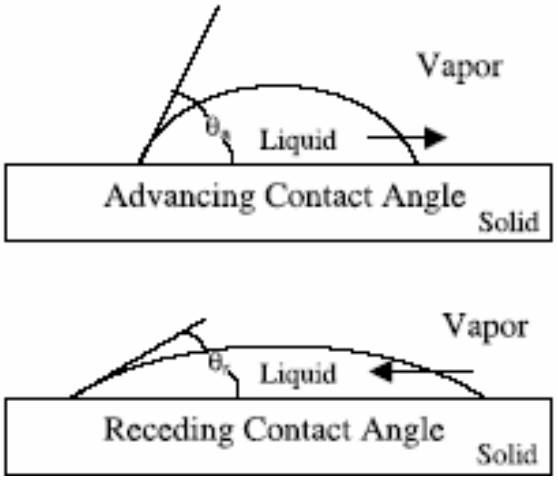

Figure 3.14: Advancing and receding contact angles [104]

For very smooth surfaces, the contact angle is seen to be higher. While for surfaces with higher roughness the contact angle is first decreased, and then increases with increasing roughness. The dynamic contact angle is higher than the dynamic receding contact angle for temperatures up to about 140 °C. For surface temperature 140-150 °C, the two angles remain at the same value for water impinging on a heated stainless steel or copper. This is the same temperature which leads the liquid into transition boiling [104]. At temperature of around 200 °C both angles increase, indicating the transition to the film boiling [103].

Varying the liquid-solid contact angle shows to have vital impact on the

evaporation of water droplets deposited on a solid surface. Liquid surface tension and solid-liquid contact angle are reduced by dissolving the surfactant sodium dodecyl sulfate in water. One investigation that illustrates this effect is done experimentally by adding the surfactant to water with two different concentrations, 100 ppm and 1000 ppm by weight. The initial droplet diameter was 2.05 mm (pure water), 2.02 mm (water with 100 ppm surfactant), and 2.07 mm (water with 1000 ppm surfactant). The droplets are released from a height of 50 mm onto a stainless steel surface with an impact velocity of 1 m/s. The solid surface temperature varied from 60 °C to 110 °C. The progress of the contact angle and the contact diameter is traced and measured using a video record of droplet evaporation.

The experiments carried out revealed that as the concentration of the surfactant increases, the contact angle of the droplet increases. This results in increasing initial droplet spreading on the surface and reduction in droplet thickness, and causing enhanced surface cooling. As a consequence the droplet evaporation rate increases. By decreasing the contact angle from 90° (pure water) to 20° (1000 ppm surfactant), the evaporation time reduces by approximately 50 %. This means while the cooling efficiency of the water is maximized, in practice it reduces considerably the amount of water required to distinguish fires, which in turn reduces the secondary damage due to excess water as well as reducing the risk of fire spreading due to over flooding [102, 105].

However, the contact angle cannot decrease under a minimum value, i.e. receding angle. As soon as this value is reached the contact angle remains constant, whilst the wetting area of the surface decreases.

Effect of Droplet Size and Velocity: Pasandideh et al. [106] have studied the impact of water droplets on hot stainless steel surface, using both experiments, analytical, and numerical model. Initial surface temperatures were varied between 50 to 120 °C (below boiling point), and impact velocity ranged from 0.5 to 4 m/s. They concluded that small, fast droplets cool more effectively than large, slow droplets. They conclude further, however, that impact velocity has only a very weak effect on surface temperature variation and heat flux. The main effect of increasing the impact velocity is, indeed, contribution to greater droplet spread, and consequently increases the wetted area across the surface which heat transfer takes place. Their analytical model predicts that for constant Reynolds number, Re[4], the cooling effectiveness increases with Weber number, We. But when $We \gg Re^{0.5}$, the cooling

[4]The mathematical expression for Re, We, and Pr is given in connection with Equation (3.48) on page 67.

effectiveness is independent of the droplet velocity or size and depends only on Pr.

Another study have measured the heat flux from a hot surface to droplets with uniform size and velocity in which $We = 100 - 200$ and $Re = 2000 - 3000$, and they found that the heat flux increased with impact velocity [107].

Schmidt and Boye [108] have experimentally examined the influence of the drop velocity and size on the heat transfer. They conclude that at constant heat fluxes and surface temperatures between 300 and 600 °C, the heat transfer coefficient increases significantly when the droplet velocity is raised. Contrary to this, the effect of the droplet size on the heat transfer coefficient is negligible for the tested droplets with diameter in the region 30 to 100 μm.

Another experimental investigation performed with droplet diameters ranged from 2.3 to 3.8 mm, water flux frequency of 2 to 15 droplets pr. second, and an impact velocity of 1.3 m/s, concludes that the higher heat fluxes are attainable with smaller droplets as these droplets would be more closely attached together than large droplets [109]. Heat fluxes as high as 3250 kW/m^2 were achieved with a coolant temperature of 24 °C. Preheating the droplets from 20 to 50 °C was found to decrease the heat flux by around 20 %.

Akhtar [110] have conducted experiments with droplet diameters between 80 and 140 μm and an average droplet velocity in the range 12.4 and 26.6 m/s with an impacting water mass flux of 0.32 to 0.84 kg/m^{2}s. The results reveal that the effect of raising the droplet velocity is not always to increase the heat flux. As a matter of fact above a certain velocity value further increase in velocity results the heat flux to decrease. The paper also concludes that in addition to dependency of droplet impaction behavior on Weber number and surface temperature, the ratio of surface contact time and heat-up time of impaction droplets might also affect the droplet behavior after impaction.

Theoretical Modeling: Upon a droplet impact on a solid surface the maximum temperature variation occurring in the solid underneath droplet, T_u, is the difference between the solid surface temperature prior to the droplet deposition and the liquid-solid interfacial temperature and can be obtained as

$$T_u = \frac{T_w \gamma_w + T_s \gamma_s}{\gamma_w + \gamma_s} \tag{3.38}$$

where T_w and T_s are the temperatures of water and solid surface, respectively, and γ is the square root of thermal inertia ($\sqrt{c_p \rho k}$). As it can be seen the temperature is strongly a function of thermal properties of the involved media, i.e. specific heat, density, and thermal conductivity [111, 112].

The above model predicts well for cases where the surface temperature does not undergo major changes during the droplet evaporation process which is most common for high thermal conductivity materials. The model is, however, unable to predict the thermal behavior of the low thermal conductivity solids which exhibit large temperature variations. In such case an approach to use the model may be possible by decoupling the liquid from the solid and imposing artificial boundary condition at the liquid-solid interface which assumes that the droplet would behave independently of the solid [113].

An analytical model to calculate the steady state surface temperature, T_{ss}, of radiantly heated Macor, cooled by water spray may be provided by [114]

$$T_{ss} = T_{s0} - \frac{h_L G}{U + \frac{k}{l}}, \tag{3.39}$$

where

$$\begin{aligned} T_{s0} &= \text{initial solid surface temperature} \\ h_L &= \text{water latent heat of vaporization} \\ G &= \text{water mass flux} \\ U &= \text{overall heat transfer coefficient} \\ k &= \text{thermal conductivity of Macor} \\ l &= \text{thickness of Macor} \end{aligned}$$

To predict the transient average temperature of the solid surface, T_{st}, the following form is suggested

$$T_{st} = (T_{s0} - T_{ss})\, e^{-at} + T_{ss}, \tag{3.40}$$

where a is a constant and t is the time [101, 114].

Based on experimental measurements one has developed a theoretical model to calculate the wetting parameter for surfaces with high thermal conductivity [96]. For the initial condition at deposition before the evaporation begins, i.e. at $t = 0$, the parameter β_0 is given by

$$\beta_0 = 0.009 T_{s0} + 0.6. \tag{3.41}$$

Values of the parameter for more general form, β, at any time during the evaporation process based on the instantaneous droplet volume may be

found using the formula for non-dimensional droplet thickness, $\frac{y}{R}$, given as

$$\frac{y}{R} = \left[\frac{\left(\frac{1}{\gamma}+\gamma\right)^2}{4} - \left(\frac{r}{R}\right)^2\right]^{\frac{1}{2}} - \left[\frac{\left(\frac{1}{\gamma}-\gamma\right)}{2}\right], \tag{3.42}$$

where y is the axial coordinate normal to solid surface originating at center of wetted area, R is the radius of wetted area, r is the radial coordinate tangent to solid surface originating at center of wetted area, and δ is the shape parameter given by

$$\delta = \left(\frac{4}{\beta^3} + \left(1+\frac{16}{\beta^6}\right)^{\frac{1}{2}}\right)^{\frac{1}{3}} + \left(\frac{4}{\beta^3} - \left(1+\frac{16}{\beta^6}\right)^{\frac{1}{2}}\right)^{\frac{1}{3}}. \tag{3.43}$$

At $t = 0$ the shape parameter is simplified to $\delta = \frac{y}{R}$.

By setting up the energy balance on the droplet, the corresponding instantaneous rate of evaporation may be written as

$$-\frac{dV}{dt} = \frac{1.248\pi R^2 h}{\rho_a c_{pa}} \left(\frac{\mathcal{D}}{\alpha_a}\right)^{\frac{2}{3}} \int_0^t \left(\frac{x_i - x_a}{1 - x_i}\right) z dz, \tag{3.44}$$

where

V = droplet volume
t = time
h = convective heat transfer coefficient
ρ_a = density of air
C_{pa} = specific heat of air
$\mathcal{D}$ = mass diffusivity
α_a = thermal diffusivity of air
x_i = vapor molar fraction at droplet-surface interface
x_a = vapor molar fraction in air
z = non-dimensional radius $(\frac{r}{R})$

Once the initial volume of the droplet is known, the Equation (3.44) may be used to determine the total evaporation time.

The local heat flux, q'', at liquid-vapor interface may be calculated by

$$\dot{q}'' = 0.624h \left(\frac{h_L}{c_{pa}}\right) \left(\frac{\mathcal{D}}{\alpha_a}\right)^{\frac{2}{3}} \left(\frac{x_i - x_a}{1 - x_i}\right). \tag{3.45}$$

Investigation shows that the central part of the droplet liquid-vapor interface does not contribute significantly to the evaporation process during the first 75 % of the evaporation time. While in the last 25 % of the process the heat flux is enhanced considerably contributed by the most part of the droplet surface due to the reduced thickness of the droplet. The results show that the heat flux is indeed highest at the droplet edge and almost three times the average heat flux at the beginning of the process [96].

The total heat transfer, q_T, from a hot surface to an impinging droplet during the time it spreads to its maximum wetting diameter can be calculated by

$$q_T = \dot{q}'' t A_{max}, \tag{3.46}$$

where A_{max} is the maximum wetted area ($\frac{\pi d_{max}^2}{4}$), d_{max} is maximum droplet diameter after spreading on the surface, and t is the required time for droplet to reach its maximum extent [106].

The cooling effectiveness, η, of how well an impinging droplet cools a surface is given by the dimensionless expression

$$\eta = \frac{2\xi_{max}^2}{Re^{0.5} Pr^{0.6}}, \tag{3.47}$$

where ξ_{max} is the maximum spread factor given by an analytical term as follows

$$\xi_{max} = \frac{d_{max}}{d_0} = \sqrt{\frac{We + 12}{3\left(1 - cos\theta_a\right) + 4\left(\frac{We}{Re^{0.5}}\right)}}, \tag{3.48}$$

where

$$
\begin{aligned}
Re &= \text{Reynolds number } (\frac{\rho v_0 d_0}{\mu}) \\
Pr &= \text{Prandtl number } (\frac{\mu C_p}{k}) \\
We &= \text{Weber number } (\frac{\rho v_0^2 d_0}{\sigma}) \\
\rho &= \text{density of droplet} \\
v_0 &= \text{droplet impact velocity} \\
d_0 &= \text{initial diameter of spherical droplet} \\
\mu &= \text{dynamic viscosity of droplet} \\
C_p &= \text{specific heat of droplet} \\
k &= \text{thermal conductivity of droplet} \\
\theta_a &= \text{advancing liquid-solid contact angle} \\
\sigma &= \text{liquid surface tension}
\end{aligned}
$$

At large droplet impact velocities, when $We \gg Re^{0.5}$ and $We \gg 12$, Equation (3.47) reduces to [106]

$$\eta = \frac{1}{2Pr^{0.6}}. \tag{3.49}$$

Chapter 4

Experimental Program

4.1 Introduction

The main equipment utilized includes a propane gas rig, a benchmark steel test plate, two full scale jet fire tests using a steel channel and steel plates as exposed objects, and equipment for characterizing the jet flame. Each one is described in detail in the following sections.

4.2 Test Facility

4.2.1 Propane Gas Rig

A rig consisting of a 14 m^3 propane tank, a pump and an evaporator to convert the propane from liquid to gas phase was used as a fire source. The size of the fire was about 14 MW, equivalent to an average burning rate 0.3 kg/s. The pressure drop for propane in gas phase across the nozzle was increased compared to the vapor pressure at ambient temperature. It was done by increasing the pressure by preheating prior to release of propane in liquid phase, before evaporating it into gas phase. This increased the turbulent energy of the jet compared to a release at ambient temperature. The pressure drop across the horizontally mounted nozzle was about 10.3 barg. Sonic propane gas releases were achieved at steady pressure and near steady flow. The heat supplied to the evaporator was provided by a hot water boiler, see Figure 4.1.

The gas was led through an 11.5 mm outlet nozzle located 1500 mm above ground level and expanded to ambient pressure through a series of shock waves. The physical dimension of the nozzle is shown in Figure 4.2. To ensure that the propane was in gas phase at release, a liquid switch was

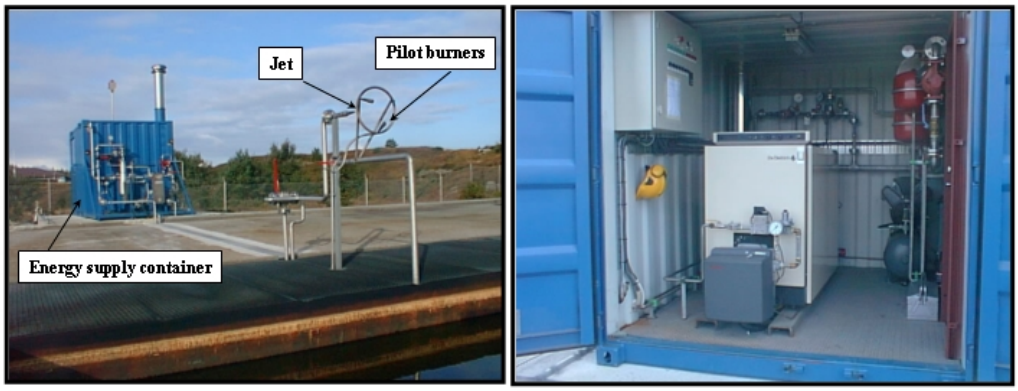

Figure 4.1: Nozzle and energy container externally (left) & internally (right)

installed between the evaporator and the nozzle, shutting down the supply of propane in case of liquid passing through the evaporator. To avoid blowout of the flame due to high velocity gradients of the gas jet, three pilot burners at low pressure were mounted around the release point as shown in Figure 4.1. In addition the system was equipped with a flare both for safety reason as well as pre-establishment of the jet flame.

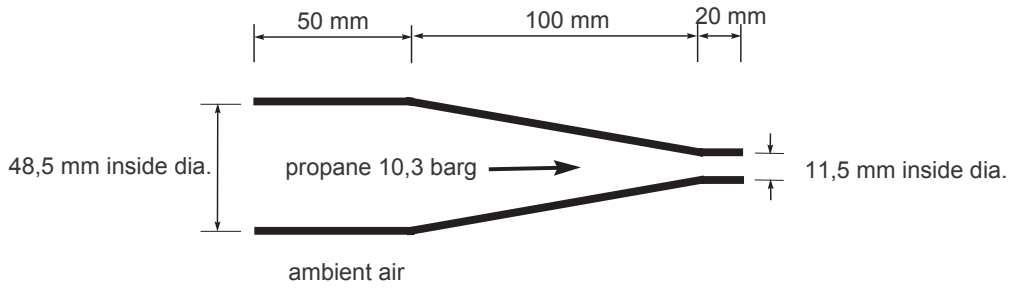

Figure 4.2: Outlet nozzle

4.2.2 Experimental Apparatus and Procedure

As indicated earlier the main object of this work was to investigate how to cope with hot spots on metal objects when exposed to high turbulent jet fires. The idea is to search for methods to depress the high temperature of the surface, e.g. 1000 °C, to under a safe level by applying water spray. Would it be at all possible to lower a highly elevated surface temperature to

a secure level below ($\ll$550 °C) and within reasonable time before it becomes critical? The present and the next chapter will attempt to give some answers.

As a fixed procedure the condition of the setup, i.e. equipment, instrumentation, etc., was always controlled before conducting the experiments. Likewise, the apparatus was always documented by photography before, during, and after the testes. In some cases additional visual documentation was made using DVD camera.

Benchmark Steel Plate

Prior to full scale experiments a series of benchmark experiments were conducted in laboratory in order to collect some preliminary information regarding wetting temperature, water droplet velocity, water mass flux, droplet size, and spraying (hitting) angle. The purpose was to be better equipped for the next phase when performing full scale tests, although the large scale fire would behave differently.

Experimental Apparatus: Two types of test were performed, applying water spray and single droplet impingement on hot surface. In case of test with water spray the source of heating was a propane flame initiating from a camping-like outlet nozzle connected via a hose to a 17-kg propane bottle with 8 bar overpressure at 20 °C ambient temperature. The approximately 180 mm long flame was located about 120 mm away from the surface. The flame had almost bluish color with a temperature about 1170 °C. Whilst in the single droplet test the steel surface was heated from below by conduction, simply using a 1500 W hot-plate with a diameter of 150 mm .

The exposed object was a rectangular stainless steel plate with a physical dimension L $\times$ W $\times$ T : 300 $\times$ 200 $\times$ 8 mm. To measure temperature of the surface two thermocouple wires were embedded within the plate. The location of the thermocouples were centered within the plate and 90 mm apart in horizontal direction and inserted 1 mm below the exposed surface. The thermocouple wires were of K-type, insulated with high temperature glass fiber, with junctions of 0.5 mm diameter. To assemble the thermocouples, two pairs of 7 mm deep holes were drilled into the plate on the back side. Each hole-pair were intended for one thermocouple wire where junction's bared-tip was fitted separately into a hole, attached to the bottom and fastened with a screw. This was to ensure that the two junctions had contact with each other via the steel plate and closed to the surface, i.e. 1 mm beneath the surface. The temperature readings were made by two digital portable units.

In case of test with the water spray, two different surface orientations were used. One with the surface tilted on a bench making 68° angle to

horizontal plane, and the case where the surface was mounted on horizontal plane facing upward. In both cases the flame centerline was normal to center of the surface. The idea of varying the surface orientation was to examine whether the cooling impact and eventually the wetting temperature could be different. A photograph of the setup is shown in Figure 4.3.

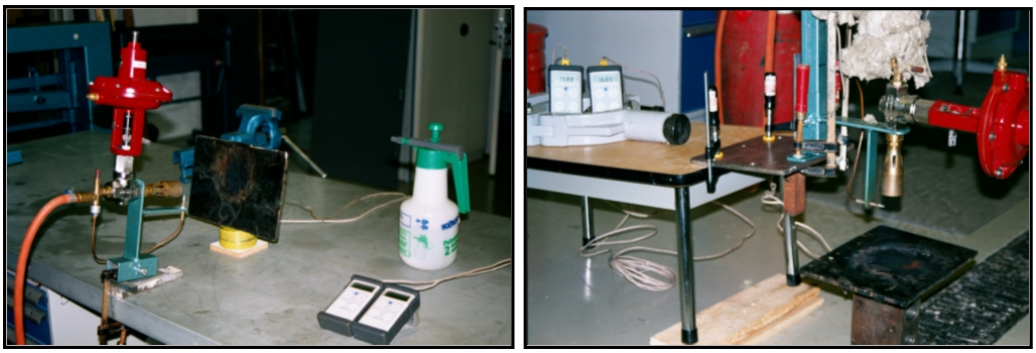

Figure 4.3: Bench scale steel plate in upright (left) and horizontal position right)

Water spray was applied manually using a simple hand-pump plant spray bottle, which could allow to vary the distance between the spray release point and the surface, the spraying angle, and water mass flux while performing the experiments. While single droplet was generated based on gravitation, simply using a can with a center hole on the bottom allowing exit of one drop at a time. This could generate about 1.5 drops per second based on 1/3 of the can was filled with liquid. The liquid temperature was about 9 °C. One could vary the drop size by modifying the hole diameter. Similarly the release-to-surface distance could be manually varied under the experiments, but not frequency of the droplet impact and the impaction angle which was only normal to the surface.

Experimental Procedure: In case of the surface in upright and horizontal position the established flame was targeted at the center of the surface and heated the steel plate to highest level possible, in this case about 520 °C at a distance of 120 mm. The heating was continued thereafter until the steady state was achieved before conducting the experiments. The steady state was attained when the two temperatures did not change for several minutes.

After achieving this state the water spray was impinged upon the hot surface. The flexibility of the hand-pump spray water was employed to vary the distance, impaction angle, and water mass flux to achieve optimal result, i.e. highest possible wetting temperature.

The distance was varied so that the spray area could cover the thermocouples region and as much the surrounding area as possible. By adjusting the distance one could also control the droplet size, i.e. the finer droplets are obtained when the distance is increased.

The angle of impact was varied from normal to about 45° to the surface in horizontal plane. While the mass flux was controlled when the droplet velocity was changed simply through varying the bottle pressure by the hand-pump.

With model based on conduction heating, the steel surface was placed on top of a 1500 W, 150 mm circular hot-plate and heated until the steady state was reached in a similar manner as in previous case. Maximum attainable temperature in this case was about 353 °C. Choosing this method of heating was mainly due to more practical procedure of rigging up the equipment.

After achieving the steady state surface temperature, the gravity-generated water droplet was gently impinged on the hot surface where the thermocouples were sitting. The distance as well as the droplet size was varied to find out the ideal combination to give highest possible wetting temperature.

Characterization of Jet Flame

The flame of concern in full scale fire studies, i.e. the high momentum turbulent propane jet flame, was characterized by conducting a number of outdoor experiments where temperature and heat flux were analyzed.

Experimental Apparatus: The measurement of temperature in the flame was quite comprehensive, while the heat flux measurement consisted of selected positions inside and outside the flame.

The temperature was recorded at 840 locations distributed over seven different cross sections in the flame. The cross sections normal to jet axis (or laying in yz-plane) were located at distances 2.5, 3.4, 3.7, 4.0, 4.3, 4.6, and 5.5 m from the outlet of the gas. Each cross section formed a grid of 120 measurement points, and their center points was situated on the jet axis, except the section far most downstream, i.e at 5.5 m, which was lifted up by 150 mm to compensate for buoyancy-end-lifted flame. The arrangement and an image of the setup is shown in the Figure 4.4.

The thermocouples used were of K-type, 5 m long, single-shield of 1.6 mm outside diameter with 0.23 mm conductors isolated by magnesium oxide. They were further connected by compensation cables to two laptop computers where the results were logged by an own-developed logging program based

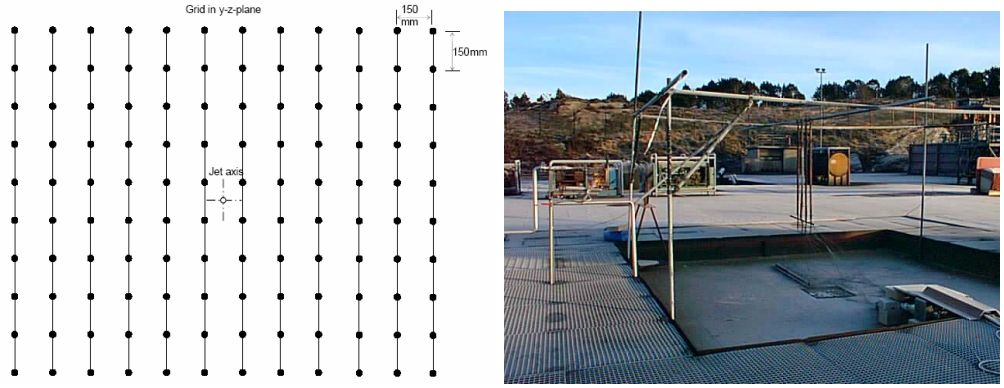

Figure 4.4: Setup for temperature measurement

on LabView[1].

Heat flux measurement was conducted at four locations inside the flame zone, along the jet axis (nearly on the flame centerline) at axial distances 2.0, 3.3, 4.6 and 5.9 m from the nozzle mouth, and two locations outside the flame in radial direction. The coordinate position of the later was x = 4.0 m & y = -1.5 m and x = 4.0 m & y = 3.0 m, where x lies on the jet axis and the nozzle coordinate is x=0.0 m, y=0.0 m, and z=1.5 m. Analysis was comprised of measuring radiation and total heat flux, i.e. convection and radiation. This implies that the flux meters were mounted in couples, and at each location radiation and total heat flux were measured. In addition a thermocouple of type K accompanied heat flux meters at each position. The flux meters were pointing horizontally, with their centerlines normal to the nozzle centerline. Sketches of the arrangement are shown in Figure 4.5 and 4.6.

All the flux meters were water cooled. In addition, the open casings (the view restrictor) around the black body portion of the radiometers located inside the combustion zone were purged by nitrogen gas in order to keep them clean from soot and other particles. The entire body of the flux meters, except the tip, and part of the connections, i.e. water hoses and transmission output signal cable were insulated and encased for further protection in a tube, 30 mm in diameter and 1000 m long. End part of the tube and the rest part of the connections were additionally insulated by 50 mm thick rockwool, 2000 m long. The flux meters were connected to the computer in similar manner and the results were stored. The setup is demonstrated by images shown in

[1]The program was developed by Mr. Gisle Kleppe at Engineering Department, Stord Haugesund University College.

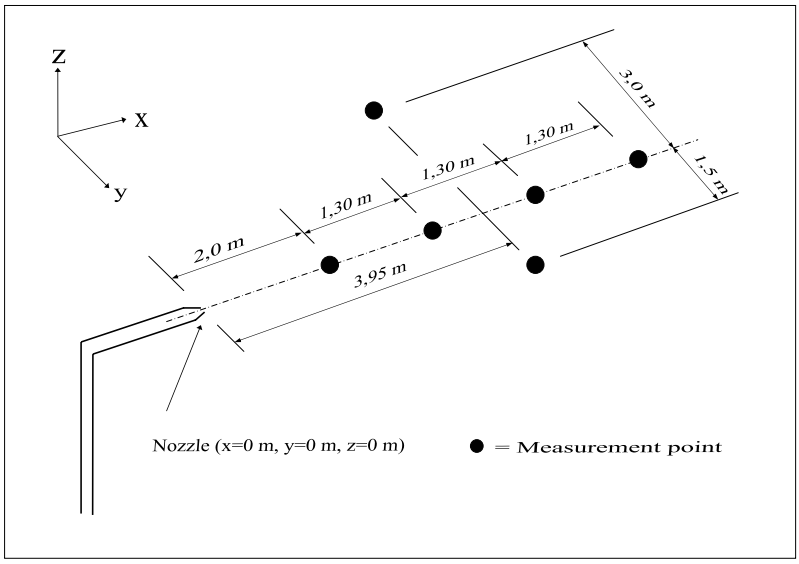

Figure 4.5: Measurement positions for heat flux sensors

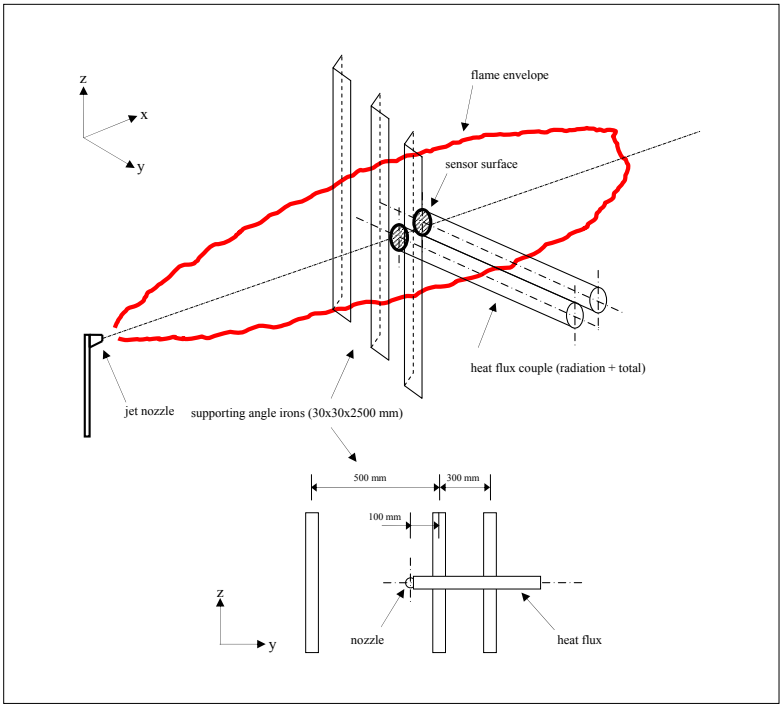

Figure 4.6: Detail setup for each pair of heat flux sensors

Figure 4.7. More description of the heat flux gages accompanied with several illustrations are given in Section 4.3 Instrumentation.

Figure 4.7: Heat flux setup prior to an experiment

More details are given in the article[2] "Characterization of a high momentum turbulent jet flame, a comparative study" in Appendix A.

Experimental Procedure: The temperature and heat flux measurement were conducted separately. This was primarily due to different setup, and secondarily the high sensitive flux meters could not physically withstand long duration of exposure in the flame compared to the thermocouples. The experiments were performed outdoors.

Due to a limited number of thermocouples (40 pcs.) which had to cover 120 measurement points at each cross section, it required three sets of experiments to be performed at each section. The arrangement based on 40 available thermocouples was mobile and could easily be moved across and along the jet axis as earlier shown by the image in Figure 4.4. Thus, a total number of 21 experiments were performed, in order to cover 840 measurement points. All the thermocouples were tested prior to the experiments to eliminate any possible malfunction. To optimize the experimental method, a number of experiments with different combinations were initially carried out which are not discussed here.

Prior to each experiment the ambient condition, i.e. wind speed, direction, and air temperature, were measured and any considerable change in wind direction and/or speed during the performance was noted. The

[2]The article is published in Volume 1 of the Conference Proceedings (pp. 683-689) of the 10^{th} International Fire Science & Engineering Conference Interflam 2004, Edinburgh, Scotland.

propane-fired boiler was then started to provide the evaporator with hot water for vaporizing the liquid propane. At the desired propane gas temperature, around 55 °C, the flame was initially stabilized at 10.5 psig pressure and a mass flow rate of 0.28 kg/s on the flare, before it was switched over to jet nozzle. Then, the data logging program was immediately started to store the results. Each test lasted for at least 60 seconds with 2 seconds interval data storage. The flow, pressure, and temperature were read at regular intervals on the corresponding display and recorded manually. The computer data logging was then temporary terminated, the jet flame was switched back to flare allowing to prepare for a new setup by simply relocating the temperature grid (composed of 40 thermocouples) into a new position, before reestablishment of the jet flame and new data logging. This procedure was repeated until all the 21 experiments were carried out.

In case of the heat flux measurement the cooling water and nitrogen purging system of the flux meters, except those located outside the flame zone, were activated before the jet flame was initiated. Figure 4.8 shows images taken from the experiments.

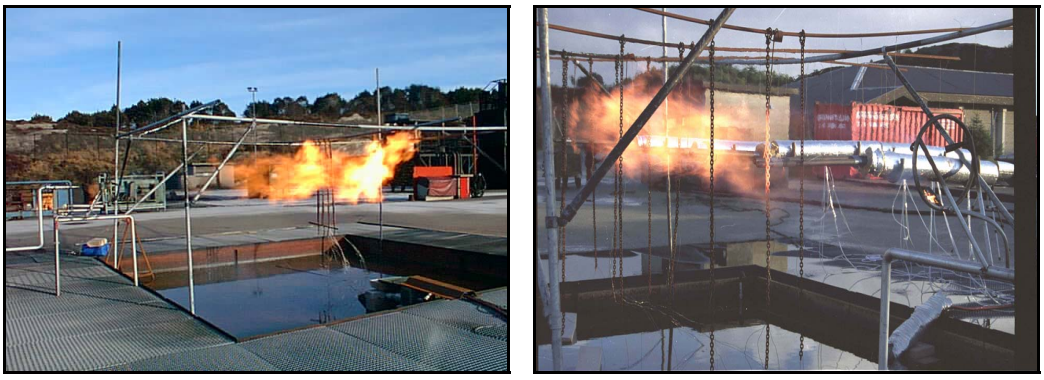

Figure 4.8: Jet flame test during temperature (left) and heat flux measurement (right)

Large Scale Jet Fire Test with Steel Channel

This setup was originally meant to be the main test object with full scale outdoor jet fire. Preliminary experiments planned with jet fire were performed, but no tests were conducted applying water spray. This was due to design complication of the test object, such as overall-size and weight, which made it unpractical for after-treatment, e.g. inspection, modification, and relocation. One decided then to terminate the further work at this stage and rather to

focus on a new concept solution as described later in Section "Large Scale Jet Fire Test with Steel Plates". However, the knowledge gained at this phase gave valuable pre-study information regarding temperature development and steels's and insulation's response to impinging fire during long duration experiments.

Experimental Apparatus: The chosen object was a quadratic steel channel with dimension L × W × T : $2000 \times 200 \times 8$ mm. The channel was prolonged by connecting to a 3 m long flexible pipe of 200 mm diameter at each end. The steel section (2000 mm) was divided in three parts. The middle part as the exposed section was 1000 mm long, while the other two parts each 500 mm long. The purpose was to make the setup practical for instrumentation and relocation. To access the internal area of the middle section for instrumentation, inspection, and modification an opening with cover was made on the rear side of the exposed area.

In order to make the study less complicated, only center area of one of the four surfaces of the middle section was exposed to fire. This was equivalent to 0.08 m^2 or 40 % of one surface area. The remainder part, i.e. the three other surfaces and the adjacent areas of the exposed surface, was insulated by encapsulating the middle section of the channel by a steel cage with 50 mm airspace filled with rockwool insulation material. See Figure 4.9. The elongated length of the channel at each side, i.e. steel and flexible pipe, was also insulated by 30 mm rockwool. The insulation material had a density equal to 105 kg/m^3, a thermal conductivity of 0.132 W/m K at 500 °C, and with a maximum application temperature 750 °C.

An induced air fan was connected to one end providing atmospheric air as cooling medium by pushing the air through the channel. The air fan with a delivery capacity of about 1100 m^3/h was equipped with pressure indicator and air flow meter, and could be regulated manually by an air damper. The purposes of using the air fan was meant to enable calculating the amount of heat transferred to the channel based on air temperatures at inlet and outlet of the channel and the air flow rate. Anyhow, the calculation was later dropped, since the focus was made on the steel plates as mentioned earlier. To create turbulence when air passing through the channel, two stationary blades were mounted, one at inlet and the other one at outlet as shown in Figure 4.10.

Ten thermocouples were mounted to take recod of temperature progress. Seven of them were embedded within the channel wall similarly as described in Section 4.2.2 Benchmark Steel Plate. Three of them were center aligned and located on the exposed area, while one was installed on the insulated part of the surface adjacent to the exposed area. The other three were mounted on

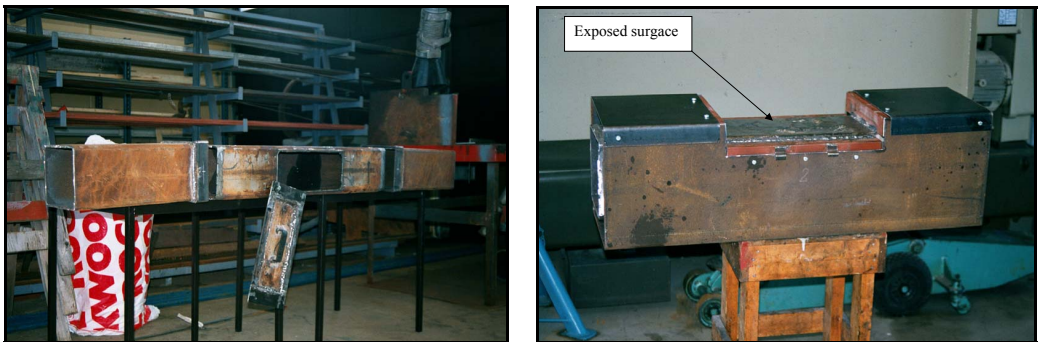

Figure 4.9: Early phase of construction (left) and exposed section (right)

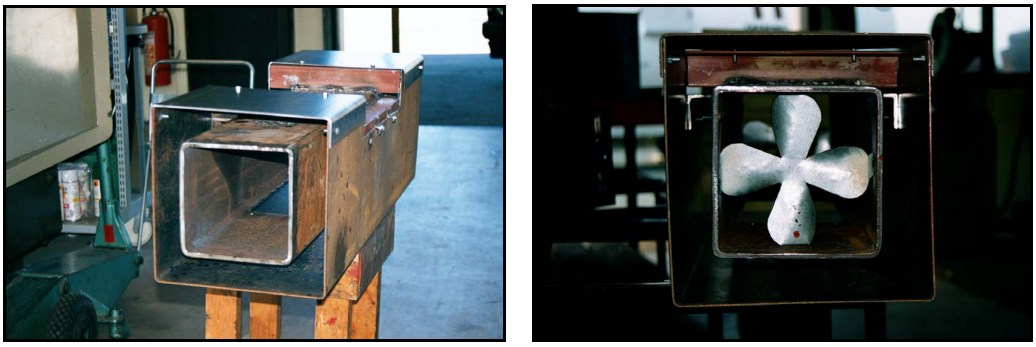

Figure 4.10: Encased channel and turbulence blades

the three insulated surfaces, one on each surface at the center point. In addition a thermocouple was fit into insulation material, on the exposed section. Temperature of the air flow at the channel inlet and outlet was measured, right before and after the blades, respectively. Also a thermocouple was installed right in front and closed to the exposed surface to measure the flame temperature at impinging point. The setup is illustrated in Figure 4.11. The thermocouples were connected to a data logging system via compensation cables and an analog-digital signal converter.

Experimental Procedure: The equipment was primary tested couple of times by exposing to diesel pool fire. The intention was to identify and eventually eliminate any possible fault and/or malfunction of any technical kind prior to jet fire tests. The object was located horizontally on two columns of concrete blocks about 1 m above ground level with exposed surface facing down. Right below the object a fuel tub 570 mm in diameter and 160 mm height was placed and filled with 13.1 kg gasoline. Two thermocouples were

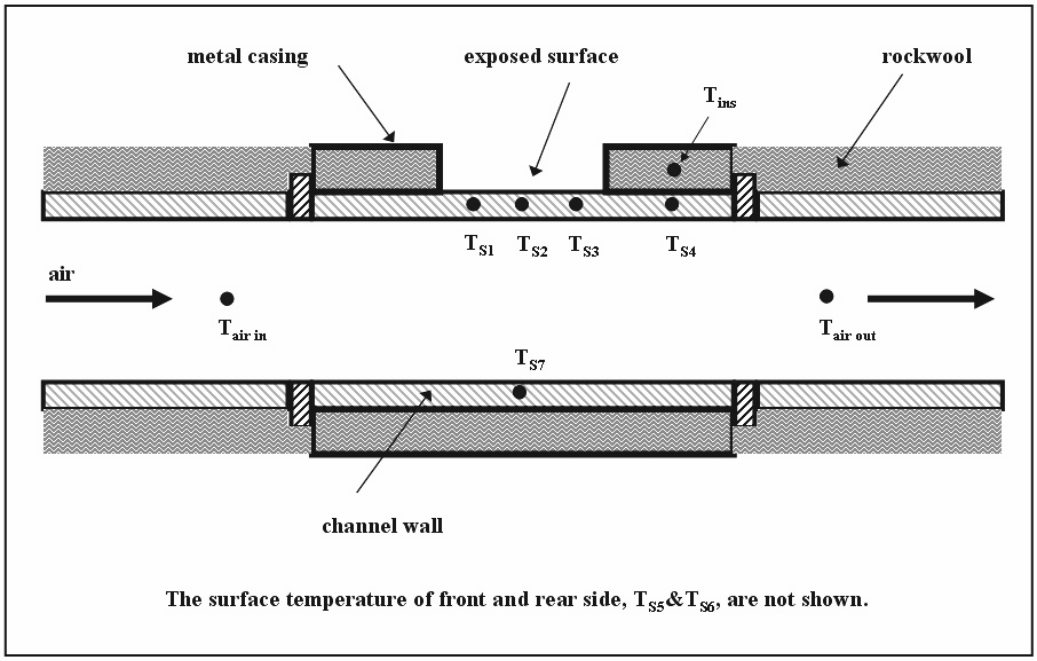

Figure 4.11: Cross-section of the steel channel setup with location of temperature measurement points

mounted above the fuel surface at heights 150 and 50 mm, respectively, to record the flame temperature. In one of the experiments the fuel tub was located on a scale to record the weight loss to calculate the mass burning rate. The air fan was then switched on and the computer data logging was started right before igniting the fuel. The experiment was continued until the whole fuel was burned up. The ambient condition temperature, wind velocity and direction were measured and noted down. An image of the test setup is shown in Figure 4.12.

In the event of major tests with jet fire the object was located on similar columns facing horizontally toward the jet nozzle with its center point on the same level as nozzle centerline, and with varying axial distance about 4000–5500 mm downstream the release point. These positions were chosen based on pre-simulations done with CFD-code KFX, which roughly represent the highest temperature zone. Right before the initiation of the jet fire the data logging system was started. Notification of ambient condition, gas property (temperature, pressure, flow rate) and establishing the jet flame followed the same procedure as described earlier. Photograph from one of the experiments is shown in Figure 4.13.

Figure 4.12: Pool fire setup with quadratic steel channel before and during a test

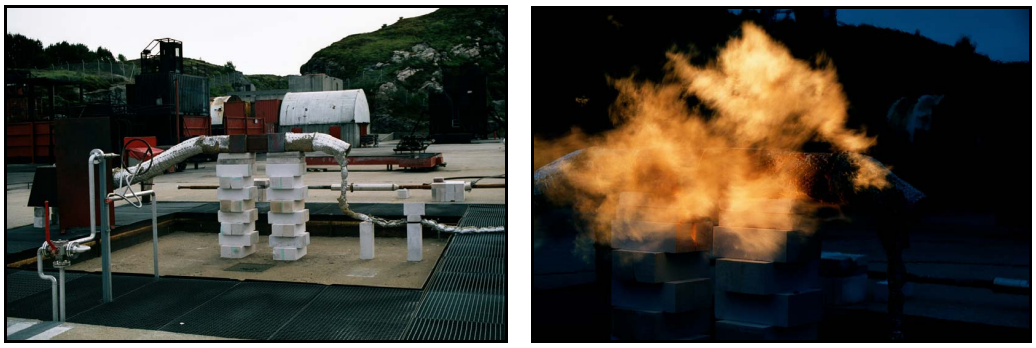

Figure 4.13: Jet fire test with quadratic steel channel before and during a test

Large Scale Jet Fire Test with Steel Plates

This setup constitutes the main experimental part of the work, where also water droplets are applied.

Experimental Apparatus: The test specimen is composed of two quadratic acid-proof stainless steel plates SS 316 with dimension L $\times$ W $\times$ T : 300 $\times$ 300 $\times$ 10 mm. To equip the plates with thermocouples, two 3 mm holes with 100 mm depth were drilled longitudinally into each plate through their edges. Thermocouples of 3 mm outside diameter were then fitted into the holes, so that their tips were situated about 3 mm beneath the surface and centered. See Figure 4.14

One of the plates was insulated on the rear side in order to study the impact of keeping the flame and water droplets away. The insulation consisted of a steel encasing of 70 mm depth welded on the rear side with its

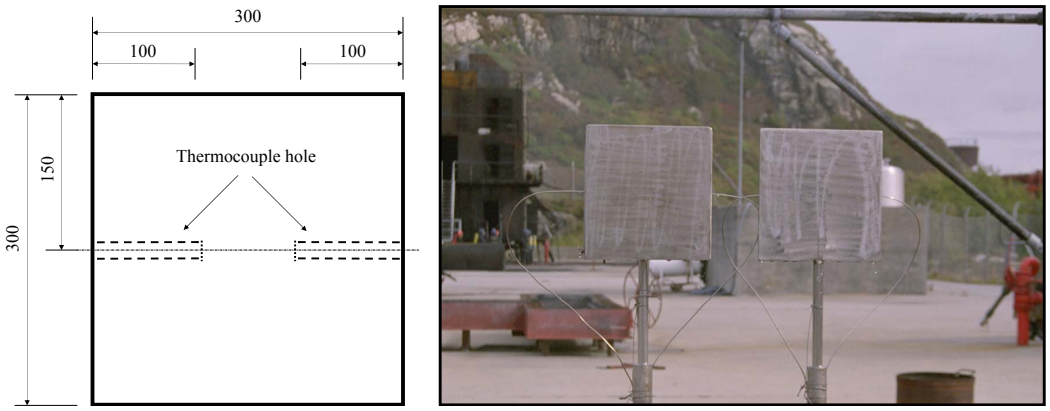

Figure 4.14: Setup of steel plates: thermocouple position (left) and mounted thermocouples (right)

topside inclined, to let the liquid droplets runs off. See the illustration shown in Figure 4.15. The encasing was additionally filled with rockwool insulation material. To trace the amount of heat transfered through the rockwool, one thermocouple was fit into middle point of the insulation.

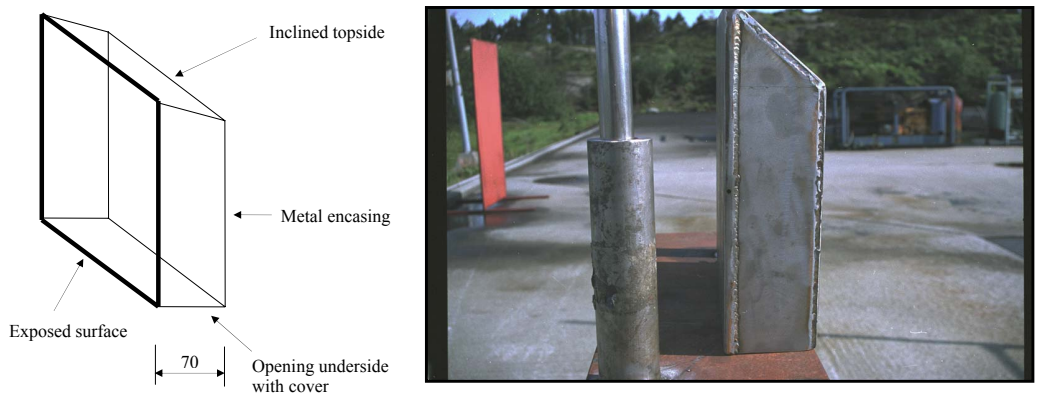

Figure 4.15: Insulated plate, hole for thermocouple is visible on plate edge

Both plates were firmly mounted on a robust metal tripod, 1270 mm height, to withstand the high momentum of turbulent jet flame. The plates facing the nozzle outlet had their center points on the same level as the jet nozzle centerline and about 4000 mm downstream the jet as shown in Figure 4.16. This position is roughly equivalent to 60 % downstream the visible flame length. In addition to mentioned above thermocouples, also two thermocouples were mounted few millimeters outside the exposed surfaces to keep record of the flame temperature at impacting points.

Figure 4.16: Exposed objects mounted on tripod

Experimental Procedure: Two types of experiments were performed. One with water spray nozzles located outside the flame, almost at the same axial distance as the jet. The other one, the spray nozzles were placed directly in the flame at two different axial distances. Each surface was impinged with water droplets through its own spray nozzle. Description of the spray system shall be reviewed in detail in Section 4.2.3.

Two different tests were carried out with spray nozzles outside the flame, where the gas pressure was varied. For this setup also three flux meters were used (both radiation and total flux), located outside the flame zone at radial distances 1500, 2000, and 3000 mm, respectively, from the jet centerline and at the same axial distance as the plates, i.e. 4000 mm. In each test the computer data logging was started prior to jet flame establishment. The

Figure 4.17: Setup with deluge outside flame, prior to (left) and during an experiment (right)

surfaces were exposed directly to fire without activating the water spray. This was continued until the steady state temperature of the surfaces was achieved and remained at least in several minutes, before applying spray water at constant mass flow rate. The cooling process continued until the surface temperature was brought down to the lowest level, i.e. evaporating temperature of water, and kept at steady state in several minutes before the experiments were terminated and data logging stopped. See the images shown in Figure 4.17 taken during one of the experiments.

The purpose of this type of test was to simulate an actual fire scenario which might occur, where the surface temperature might reach a critical level when activation of water spray is delayed, and if that so, would it be possible to bring down the surface temperature as quickly as possible.

In the second event where the spray nozzles were located directly in the flame, two different types of nozzles were used. One with 30° spray angle, circular cone spray, and one with 65° spray angle, square cone spray. The deluge nozzles were mounted on their own foundation at appropriate distances to cover the entire surface with liquid droplets even at the lower flow rate. As in previous case the data logging was started before gas release, but in contrary the deluge spray was activated with maximum mass flow rate at the start before the jet flame was initiated. The water flow rate was then gradually decreased after several minutes as long as the surface temperature was at steady state or did not increase significantly and was under control. This operation was continued until the flow rate reached its minimum value and apparently not covering the hole surface, consequently the temperature began to rise rapidly. At this stage the flow rate was increased back to the next lowest level, sufficient to suppress the temperature. The water flow rate continued to increase gradually with similar intervals as the first part of the experiment to its maximum value, before concluding the test and stopping the data logging. See the photography of the setup shown in Figure 4.18 during one of the experiments.

The intention of these tests was to keep the surface temperature on safe level and well below 550 °C at minimum required amount of mass flow rate during the entire test. With other word, this technique was an offensive method to prevent the high temperature of the surface, while at the same to investigate the opportunity to avoid formation of hot spot, or when it first arose attempting to cool down and eliminate it. This method had also advantages of ensuring water droplets reaching and covering completely the surfaces as well as to overcome the effect of crosswind comparing to the previous method.

Figure 4.18: Setup with deluge inside flame, prior to (left) and during an experiment (right)

4.2.3 Water Spray System

As mentioned previously, application of deluge in this work was only limited to jet fire experiments with stainless steel plates. The main supply water pipeline with an operating pressure of 10.5 barg could supply the spray system with a liquid up to 75 l/min which was more than enough for this application.

Two different spray configurations were utilized. The simpler one with deluge system located outside the flame zone, align with the jet nozzle with one spray nozzle on each side of the jet, as shown earlier in Figure 4.17, at an axial distance varying between 4000–4500 mm. The system loop was composed of filter, shut-off valve, flow meter, pressure indicator, pressure regulator valve, pipes, water hoses, nozzles, and necessary fittings (couplers, tees, and elbows) to connect the components as shown by illustration in Figure 4.19. The pressure and flow rate were monitored and recorded manually.

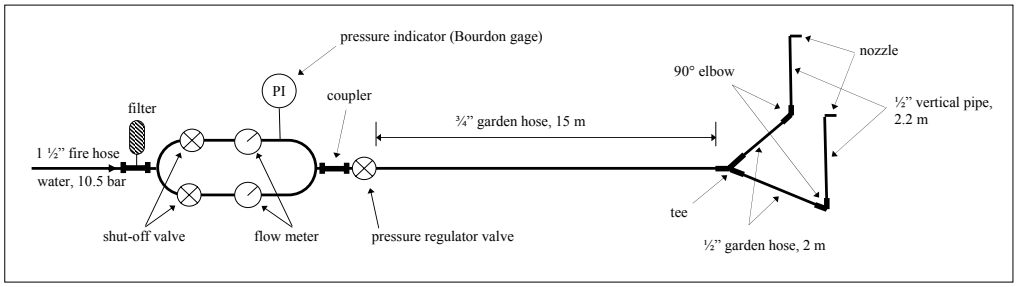

Figure 4.19: Layout for deluge outside flame

The mass flow rate was kept constant during the experiments at a maxi-

mum rate of 0.4 kg/s for each nozzle. The flow rate was measured manually, simply by taking samples during a 15-second time and weighted. This was repeated three times to ensure reproducibility of the sampling. Right before and after each sampling the gage pressure was read, and if any significant change in pressure was noticed, about 5 %, the sample was then retaken. The values agreed well with theoretical calculation. In addition they were controlled versus readings monitored by Bourdon gage pressure indicator located upstream. The latter showed values about 16 % higher, merely because it does not take into account the pressure lost along the pipelines and fittings downstream.

The nozzles employed were simply of garden-application type. Reasons for choosing this type of nozzle were its long spraying distance, flexibility to regulate spray angle during experiment, easy replacement, last and not least low cost investment, although it could not provide uniform droplet sizes. In addition the hole foundation could quickly be repositioned during the experiment, if necessary. Each spray nozzle and its corresponding pipe 2200 mm height were mounted on a supporting bar which could be adjusted in height. The nozzles were located about 700 mm higher than the center point of the surfaces pointing toward them, and slightly inclined, about 10°, downward. The purpose was to compensate as a counterbalance for gravity of the droplets, ensuring the droplets to reach the surfaces without significant loss of momentum.

The other spray configuration located directly inside the flame, had among others the advantage to reduce amount of water used, which indeed is of high concern for industry to avoid or minimize the damages caused by excess water. The system loop was basically build up as the previous one, but included new components such as pressure transducer connected to computer logging system to take record of pressure change and hence recording the flow rate. The layout is shown in Figure 4.20.

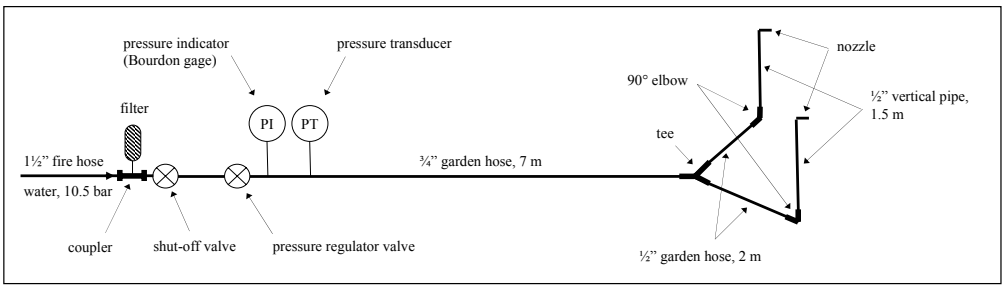

Figure 4.20: Layout for deluge inside flame

In this category two experiments utilizing different nozzles were conducted. Two types of conventional nozzles were employed, one with circular and the other one with square shaped spray pattern with 30° and 65° spray angle, respectively. Se images of both nozzles shown in Figure 4.21. While Figure 4.22 illustrates the nozzle with 65° spray angle in position.

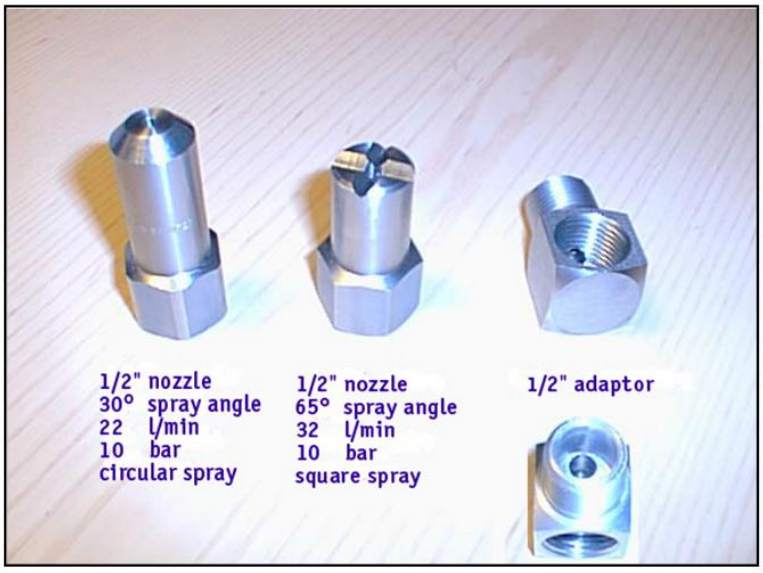

Figure 4.21: Spray nozzles and positioning adaptor

Figure 4.22: Nozzle with 65° spray angle in position, jet fire nozzle in background

Illustration in Figure 4.23 shows a typical spray pattern for a solid con with circular shape. A circular exit orifice preceded by a swirl chamber with a multi-slotted in-line distributor causes the spray to take solid circular shape. With the addition of two machined "V" grooves at the nozzle tip a square patterned spray can be formed.

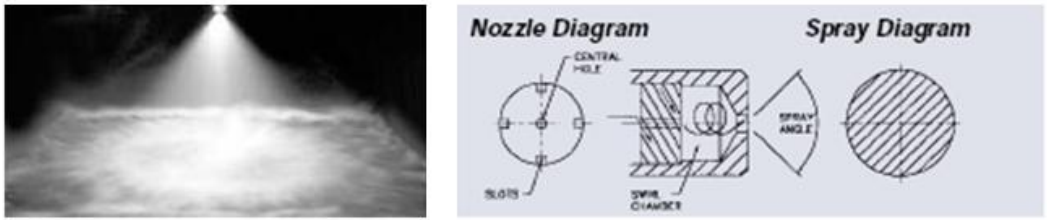

Figure 4.23: Typical spray pattern for a solid circular shape

Detail descriptions and characteristics of the nozzles are given in Table 4.1. The estimated droplet sizes of the liquid provided by manufacturer (Delavan Spray Technologies Ltd., 2003) are at a dynamic viscosity of 10^{-3} kg/ms and a surface tension of 0.073 N/m. The nozzles with 1/2" inside diameter, internally threaded, were screwed on adaptors and fitted to vertical pipes.

Table 4.1: Nozzle characteristics

Nozzle Type	Spray Pattern Shape	Spray Angle (degree)	Inside Diameter (inch)	Orifice Diameter (mm)	Maximum Pressure (barg)	Maximum Flow Rate (l/min)	Nozzle Pressure Drop (barg)	Flow Rate (l/min)	Droplet Size, SMD[1] (μm)
Solid Cone, Inernally Threaded	Circular	30	½	3	10	22	2	9.7	603
							5	15	454
							10	22	372
	Square	65	½	4.5	10	32	2	15.96	446
							6	24.95	336
							8	28.48	307

The Sauter mean diameter (SMD) which is used for processes involving evaporation, reaction or combustion is a hypothetical droplet whose ratio of volume to surface area is equal to that of the entire spray. The manufacturer's field experience (Delavan Spray Technologies Ltd., SDX Spray Drying, Product Guide) shows that the effect of liquid properties such as viscosity and surface tension on droplet diameter may be estimated from the following correction factors

$$\overline{d} \; \alpha \; \mu^{0.25}, \tag{4.1}$$

and

$$\overline{d}\ \alpha\ \sigma^{0.33}, \tag{4.2}$$

where $\overline{d}$ is mean droplet diameter, μ is dynamic viscosity, and σ is surface tension of the liquid.

Spray pressure influences the formation of the droplets, as can be seen from Table 4.1. The spray solution emerges from the nozzle in a thin sheet, and droplets form at the edge of the sheet. Higher pressures cause the sheet to be thinner, and the sheet breaks up into smaller droplets. Large orifice nozzles with higher volume flows produce larger drops. See diagrams shown in Figure 4.24 applicable for the spray nozzles used.

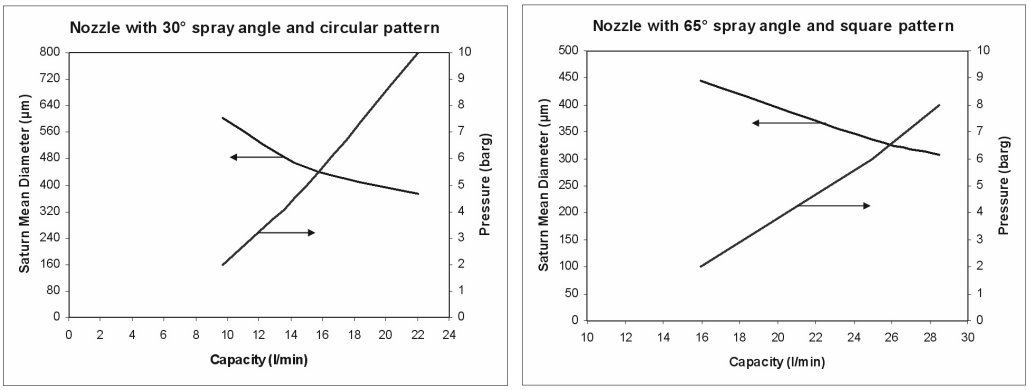

Figure 4.24: Variation of SMD as a function of nozzle pressure

Nozzles that have wider spray angles produce a thinner sheet of spray solution and smaller droplets at the same pressure. However, wide angle nozzles can be placed closer to the target, and the benefits of lower nozzle placement outweigh the disadvantage of slightly smaller droplets. Lower pressures can be used to reduce the amount of fine droplets [115].

The size or capacity of the nozzle also influences droplet size. The larger orifice increases the droplet size at a common pressure.

The manufacturer's given data on capacity of spray refers to nozzle pressure. Therefore to account for pressure drop between the supply pump and the release point of deluge at the nozzles, the actual flow rate was measured at issuing point of spray by taking samples at a 15-second duration for every 0.5 barg pump pressure increment between 1 and 10.5 barg, totally twenty measurements. Each sample was then weighted. The procedure was repeated three times for each sample at the given pressure to ensure reproducibility of the sampling. Right before and after each sampling the gage pressure was read, and if any significant change in pressure was noticed, about 3-5

%, the sample was then retaken. The results are plotted in Figure 4.25 and compared with manufacturer's characteristics curves. The deviation between measured values and manufacturer's data, as expected, is justified by the fact that the later does not involve pipe and fitting friction losses, since measurement is conducted directly at the nozzles. The gap between the two curves for 65° nozzle is significantly high at comparable pressures, where the capacity is dropped by about 55 % at 1 barg and 27 % at 10 barg due to friction losses along pipeline, valves, couplers, and fittings. Whilst similar values for 30° nozzle are 40 % and 11 % at 1 and 10 barg, respectively.

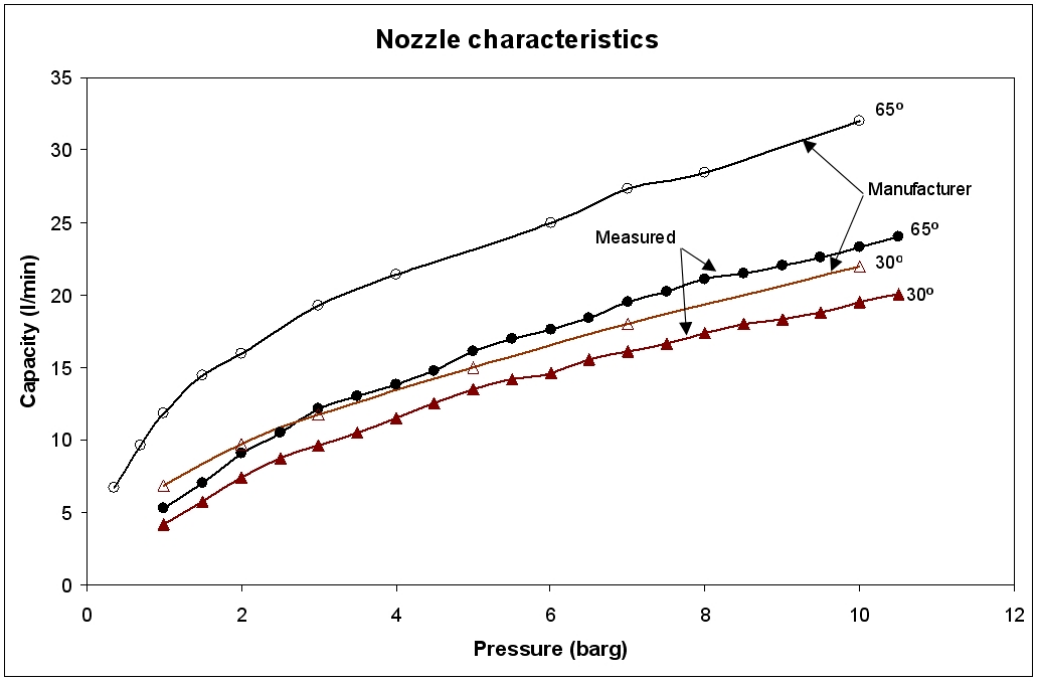

Figure 4.25: Characteristic of 30° and 65° spray nozzles

A conclusion may be drawn from the above results that the pressure drop is bigger for nozzles with larger orifice and higher flow rate.

In order to obtain some qualitative impression, the spray pattern and behavior was visually observed by conducting a deluge test prior to the experiments. The test involved the nozzle with 65° spray angle at different pressures between 1 to 10.5 barg with 0.5 bar pressure interval, as highlighted by Figure 4.26. It should be anyhow emphasized that, as earlier indicated, the pressures are not at nozzle but rather measured about ten meters upstream the nozzle.

The type of pressure transducer employed was Tecsis 3276.076.001 with

Figure 4.26: Deluge test with nozzle with 65° spray angle at various pressure

0–16 bar operating range, 0.5 % accuracy, 4–20 mA output signal, DC 10-30 V supply voltage, 1/2" externally threated, and material type SS 316. An image of the instrument together with pressure gage, pressure regulator valve, block valve, and filter is shown in Figure 4.27.

4.3 Instrumentation

The major instrumentation used in this work was composed of thermocouples and heat flux meters. They are briefly discussed in the following two sections.

4.3.1 Thermocouples

Two different types of thermocouple were used to determine the temperature, both of them of K-type. In the first type, the dissimilar thermocouple wires of 0.5 mm diameter are insulated with high temperature glass fiber. Then they are packed together and furthermore insulated by glass fiber. The

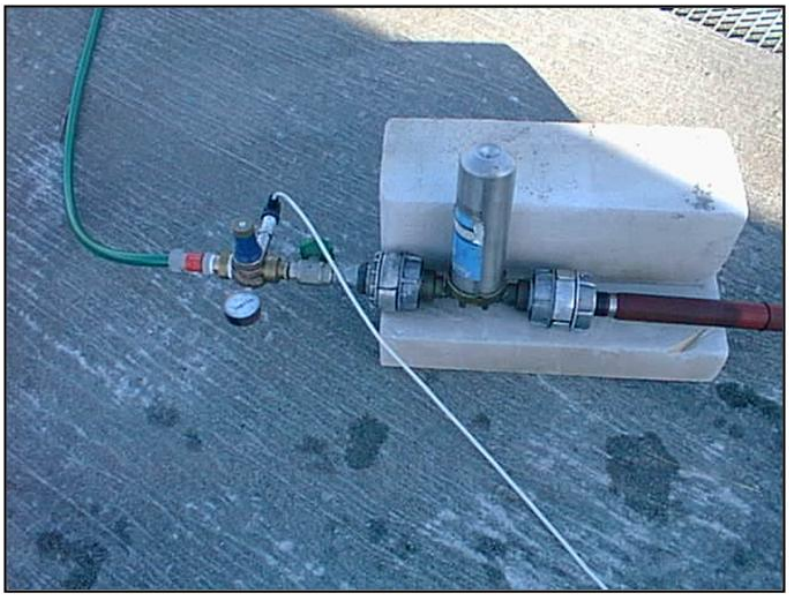

Figure 4.27: Flow measurement and regulating equipment

thermocouple is designed for an operating range up to 1000 °C. While in the other type the wires of NiCr-Ni material designed for an operating range up to 1200 °C are in similar manner individually insulated and wrapped in a sheath that served to hold the wires together and protect them from harsh mechanical and thermal environments. The end of the wires are stripped and brought together at a junction and welded. The junction and the corresponding wires are then insulated by a 5 meter metal shell of type SS 316, with ungrounded junction, to withstand a hot environment, before it is connected to a compensation cable of silicon material (-50/+180 °C).

4.3.2 Heat Flux Gages

Two types of instrument were used for direct measurement of heat transfer rates from fire, heat flux transducers and infrared radiometers manufactured by Medtherm.

Heat Flux Transducers: The transducers are of Schmidt-Boelter thermopile sensor type, called "total" heat flux transducers, which measure sum of the convective and radiative flux. They are not designed to touch the source or to measure conduction heat transfer. The linear thermopile sensor generates a millivolt output directly proportional to the net heat transfer rate absorbed

by the thermopile sensing element. The sensitive portion of the sensor is at the center of the 25 mm diameter front face of the transducer. Schmidt-Boelter thermopiles absorb heat at the front surface and transfer the heat into the body normal to the absorbing surface. The difference in temperature which generates the output EMF is developed between the surface and the body plane beneath the surface. The transducer is made with an optical black coated sensor with an absorptance of 0.96, and can be cleaned with a mild detergent solution. Since it operates as a differential thermopile, no reference junction is required.

The sensor will respond to the total net absorbed heat flux, i.e. the net sum of all convective and radiative heat flux components. For application in which the convective heat flux component is negligible the transducer may be used an an infrared radiometer. For applications in which the radiant heat flux component is negligible the absorptance of the optical black coating is not relevant and the transducer may be used without the coating. The absorptance of the uncoated sensing element is approximately 0.8. This configuration of the thermopile as stated is not suited for heat conduction measurement by contact of the sensing element with a solid object.

The unit is water cooled through two 3 mm diameter cooling water tubes, either of which may be used as the inlet. Tap water of 4 bar supply or higher provides sufficient water, about 0.05 l/min. The temperature of the cooling medium may be any steady value from 10 to 65 °C. Condensation on the outer surface of the transducer should be avoided, as it might reduce the absorptance ability of the sensor either due to a thin water film and/or to collect particle matters in a sooty environment. A water temperature of about 50–60 °C may prevent this condensation in humid surroundings. Without cooling water, the maximum operating transducer body temperature is about 200 °C. The allowable gas temperature is determined by the selected range for the heat transfer rate and the mentioned body temperature specification.

According to manufacturer the response time of the unit is less than 120 ms for incident heat flux in the range 500 to 1000 kW/m^2, less than 250 ms in the range 20 to 300 kW/m^2, and less than 350 ms at 2 to 10 kW/m^2.

Schematic view and a photo of a total heat flux gage is shown in Figure 4.28.

Radiation Heat Flux Meter: Also called ellipsoidal infrared radiometer, the sensing head is constructed with a reflective gold plated highly polished ellipsoidal cavity with the radiometer aperture at one focus of the ellipsoid and a heat flux sensor at the other focus coated with optical black. An inert gas purge, in this work nitrogen, is provided to keep the sensor cavity clean. In clean environment the unit may be operated without the gas purge. The cav-

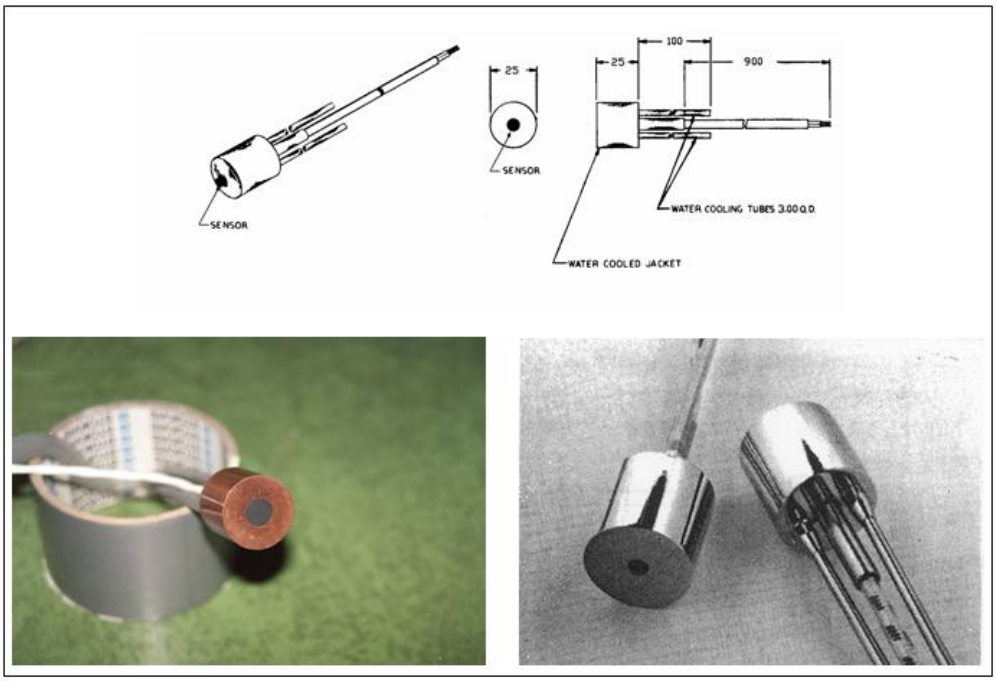

Figure 4.28: Physical specification and image of a heat flux transducer

ity or restrictor with a view angle more than 160° serves also as an eliminator for convective heat transfer. The sensor maintains a linear output directly proportional to the incident radiant flux entering the 3 mm aperture. This probe is also like transducers designed for water cooling when subject to high temperature environment.

If the convective heat flux is desired to be measured, a total heat flux transducer can be used to measure the total heat flux. The convective heat flux is then the difference between the total heat flux and the radiant heat flux measured by the radiometer.

The cylindrical body of both heat flux gages with an outside diameter of 25 mm and 25 mm long is copper. They are equipped with leadwire of standard nickel plated copper duplex wire with teflon over each conductor, nickel plated copper braid over both.

Physical dimension and sensor detail as well as an image of an ellipsoidal infrared radiometer is shown in Figure 4.29.

The heat flux ranges for both total and radiation used in this work were 10, 50, and 300 kW/m^2, with a linear output signal up to 20 millivolts at the design heat flux level full range. They had anyhow overrange capacity up to 150 % of full range.

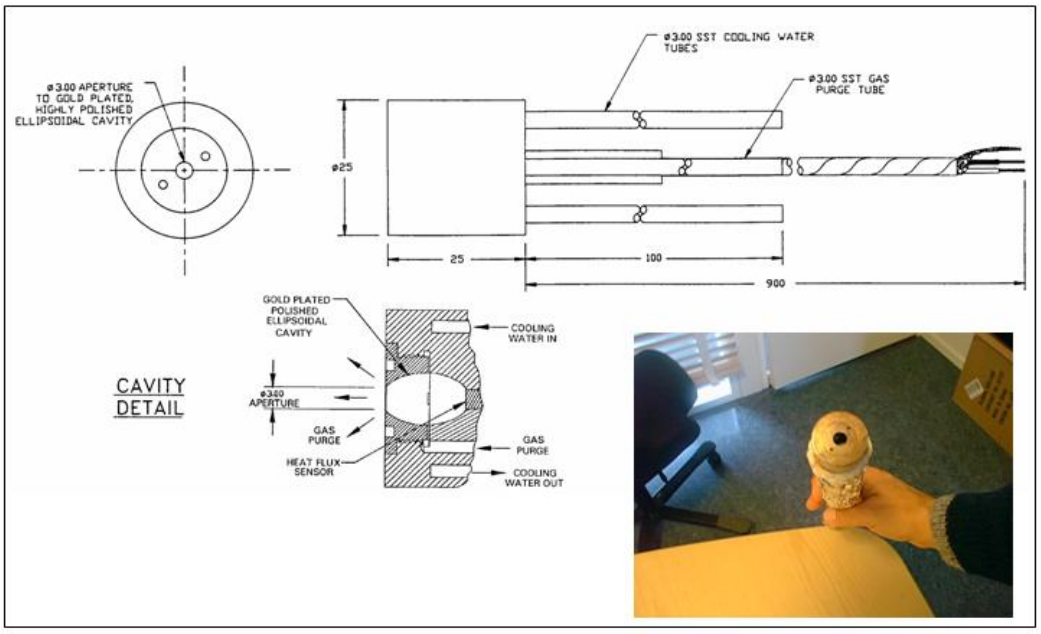

Figure 4.29: Physical specification and image of an ellipsoidal radiometer

Calibration of Heat Flux Gages

The shipped flux meters were originally calibrated on August 2001 at the production factory of Medtherm by direct comparison to a working standard heat flux meter using a wide source of uniform radiant heat flux. The calibration is traceable to the National Institute of Standards and Technology (NIST).

Medtherm suggests to establish a recalibration schedule of 6 months or 12 months. But the desired frequency of recalibration will depend on the frequency and severity of usage.

The experience of this work confirms the above statement, that for heavy duty the recalibration is necessary more often. One may indeed say it is wise to recalibrate the unit almost after each experiment, if it is located within the flame zone or subject to similar severe environment more than 30 seconds.

Calibration Setup: The calibration facility utilized was a spherical black body calibration source, of type Mikron M300, with furnace inner wall made of fire resistance clay. The furnace cavity with large internal area is fitted with 51 mm aperture attached to a cylindrical tube, with opening at other end for inserting the the sensor housing assembly. See illustration shown by Figure 4.30 [116]. The well insulated furnace chamber is electrically heated

with a temperature range 100–1200 °C and an accuracy of digital indication ±0.25 % of reading ±1 °C. The spherical chamber acts as a nearly blackbody emitter with an emissivity of 0.999±0.0005. The temperature level of the furnace is very uniform at high precision. The aperture is water cooled, while the exterior of the furnace is fan cooled.

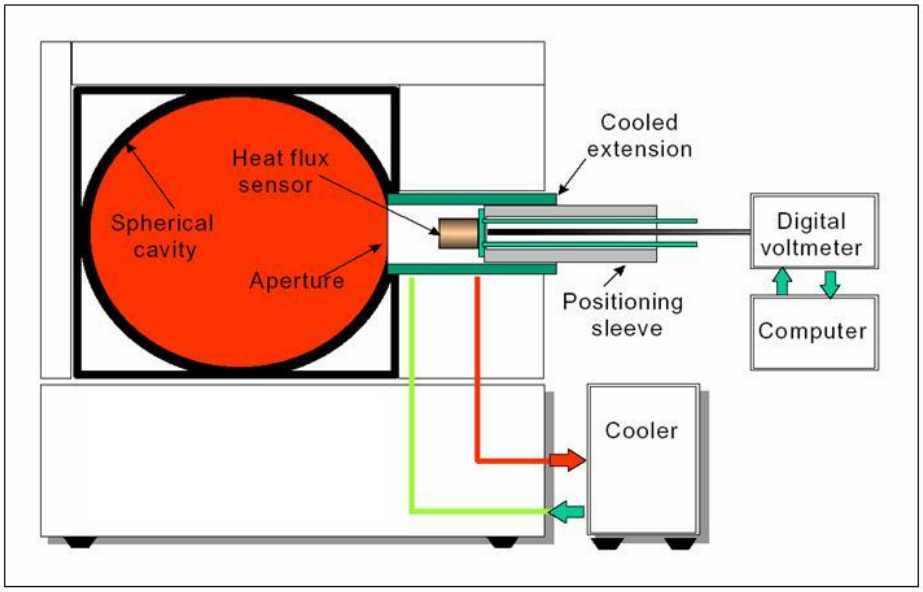

Figure 4.30: Schematic layout of spherical blackbody [116]

The outside diameter of the flux meters is 25 mm, which is half the furnace aperture. To minimize the influence of convection heat transfer onto surface of the sensing element, a ring with 50 mm outside diameter and 26 mm inside diameter was fitted on the gage housing. This also served as a heat loss minimizer from the furnace chamber through the aperture. The ring was welded to a 250 mm bar acting as a supporter as shown in Figure 4.31.

Calibration Procedure: Calibration took place in the laboratory in an environment with still air at room temperature.

Calibration procedure was in accordance with manufacturer's method, and in many ways, where applicable, it was followed the international practice, like those described in NIST 1999, Nordtest Method, and NIST 2000 [116, 117, 118].

Prior to each calibration the aperture of the furnace was connected to cooling water, and the temperature of the chamber was raised to the desired

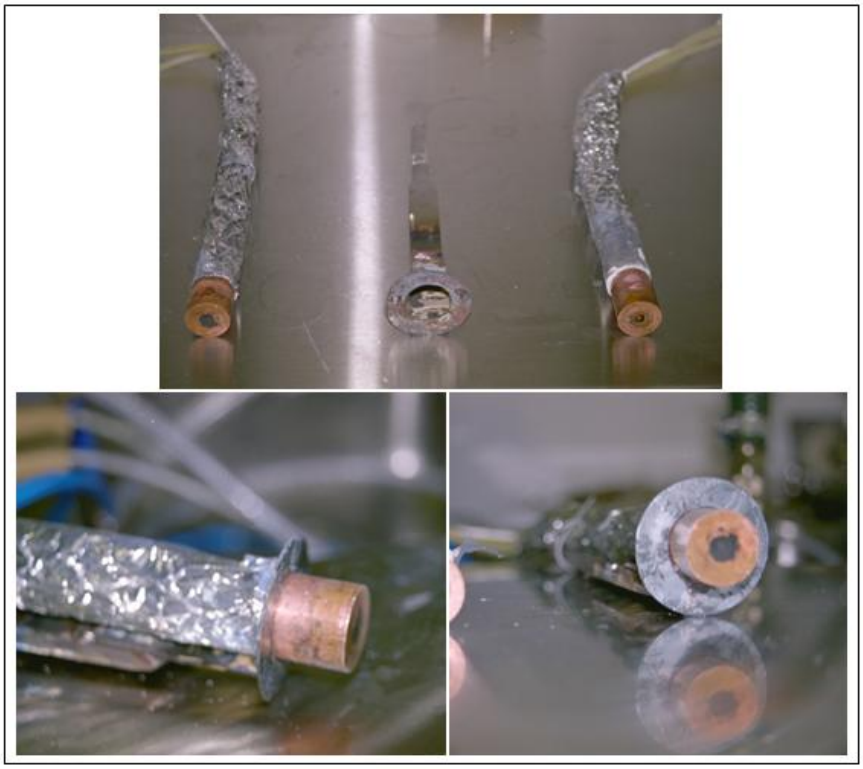

Figure 4.31: Fitting device for heat flux gage

level. Lifting up the temperature was a tardy process, while to bring it down it was far more time demanding. Whenever the cavity temperature reached the set point, the steady state was attained for several minutes before calibration started. Heat flux meter was first fitted into the supporting and fitting device, and then inserted through the aperture into the furnace in such manner that the sensor surface was immersed few millimeters inside the cavity to insure seeing only the black body emitter. The body of the gage (water hoses and leadwire) inside the aperture was protected by insulation material as it can be seen in Figure 4.31, while the exposed surface was water cooled. Figure 4.32 shows an image taken from one of the calibrations with a heat flux meter in position connected to cooling water, and the connection for cooling of the furnace aperture.

The temperature of the cooling water was about 27 °C. The outlet temperature of the cooling medium of the aperture and gage were continuous monitored under performance. At cavity temperature above 800 °C the water flow rate was slightly increased, particularly for heat flux meters. At

Figure 4.32: Heat flux gage in position during a calibration

the highest furnace temperature, i.e 1200 °C, the temperature of the later reached so high as 52 °C.

The logging time was about 140–170 seconds with 5 seconds interval for the first group of gages. But the experience showed that the sensors with reasonable fast response time (less than 350 msec) stabilized almost within 10 seconds, so that the future calibration or recalibration was based only on 60 seconds data logging with 2 seconds interval.

Each calibration was performed at minimum three individual points, e.g. 250, 750, and 1000 °C for a 50 kW/m^2 sensor.

The above procedure may be summarized in a chronological order as follows:

1. Switch on the furnace to start the cooling fan and connect the aperture to cooling water.

2. Insulate the heat flux gage and connect it to cooling water.

3. Adjust the temperature of the cooling water.

4. Connect the leadwire of the gage to data logger via signal converter Fluke.

5. Reset the data logger and prepare for start.

6. Raise the temperature of the spherical cavity to the set point.
7. When the desired temperature is reached, insure steady state for few minutes.
8. Insert the heat flux meter into furnace through the aperture.
9. Start immediately the data logger to reduce thermal stresses of the gage.
10. Let the gage remain in the same position for at least 60 seconds or until the output signal shows steady state value. At temperatures above 800 °C the gage should preferably not to be exposed more than two minutes due to thermal stresses.
11. Stop the data logger.
12. Remove the gage.
13. Repeat step 5 to 12 for the next higher temperature level until a broad spectrum of temperature is covered.
14. After end performance, let the furnace be cooled down by air fan to under 200 °C, before switching off the unit.

Calibration Results: As stated earlier the gages exposed to high temperature zones need to be calibrated frequently. In this work it is applicable to those with higher range, i.e. 300 and 50 kW/m^2.

The results of calibration are shown in Figures 4.33 to 4.36. The y-axis represents the output signal of the gage measured in millivolts (mV), whilst the values along x-axis, i.e. net radiation rate of heat transfer (kW/m^2), are calculated based on calibration temperatures by

$$\dot{q}'' = F\epsilon\sigma(T_F^4 - T_w^4), \tag{4.3}$$

where

ϵ = sensor absorptance=0.96
σ = Stefan-Boltzmann constant=5.67×10^{-11} kW/m^{2}K^4
T_F = furnace temperature (K)
T_w = cooling water temperature (K)

In each diagram also the manufacturer's calibration curve is included for comparison, marked as Medtherm. The curves are represented by their trend lines which are almost linear. Some of the gages were recalibrated, and these are included in the same diagram for easier comparison, such as in Figure 4.34 and 4.36. To distinguish these results, they are identified by date of calibration. In most cases the measured millivolt signals showed overranged values at higher temperatures, which indeed means a heat flux gage may measure outside its range as well. It should be emphasized that the two Figures 4.34 and 4.35 refer to different pairs of heat flux gages, although both are of the same range 50 kW/m^2.

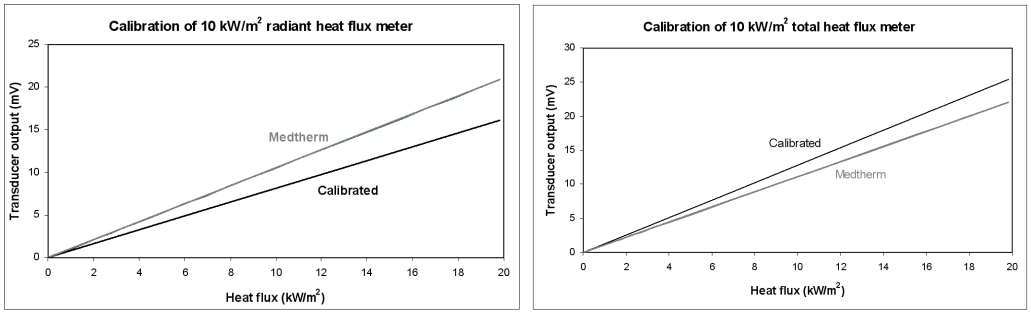

Figure 4.33: Calibrated radiant and total heat flux gage with range 10 kW/m^2

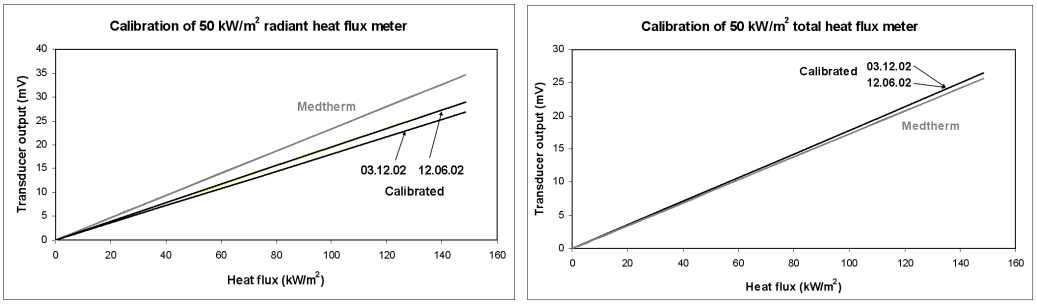

Figure 4.34: Calibrated radiant and total heat flux gage with range 50 kW/m^2

It is evident from the figures that the output signals of all the gages deviate from their original calibration curves. In some cases, like 50 kW/m^2 radiometer shown in Figure 4.35, the gap is so high as 75 % at highest temperature, and about 40 % for 300 kW/m^2 radiometer shown in Figure 4.36. While the deviation for two 50 kW/m^2 total heat flux meters shown in

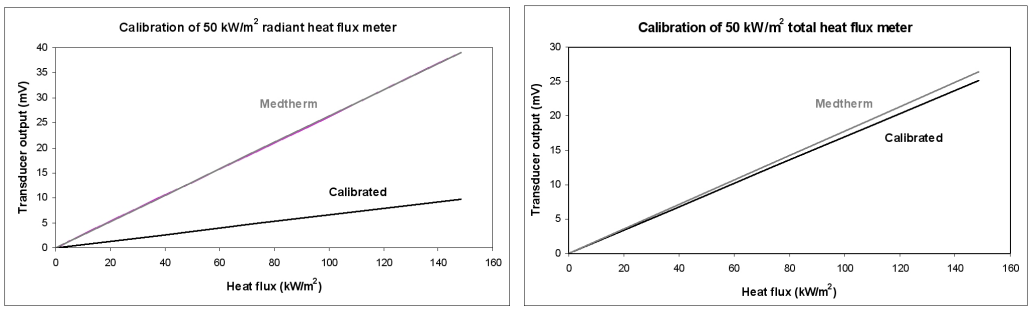

Figure 4.35: Calibrated radiant and total heat flux gage with range 50 kW/m^2

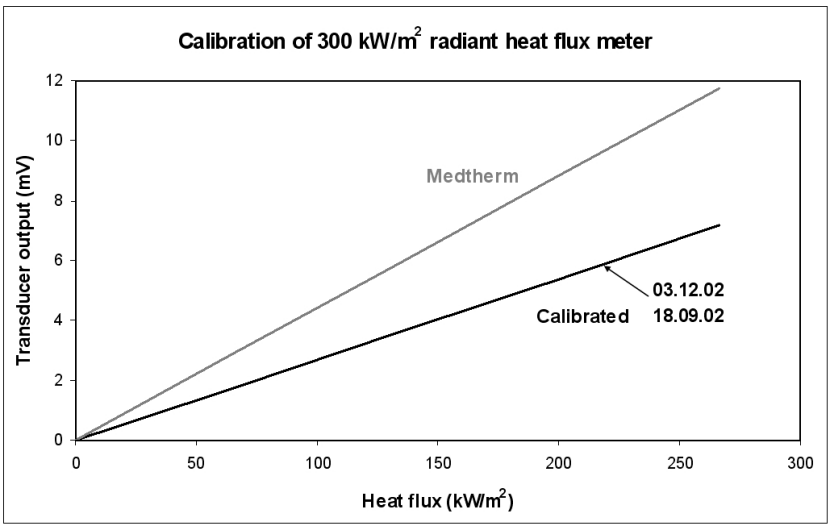

Figure 4.36: Calibrated radiant heat flux gage with range 300 kW/m^2

Figure 4.34 and 4.35 are quite low. Other interesting observations may be classified as follow:

- In most cases the calibration reveals that the maximum output signal reduces compared to factory calibration.
- In the event of recalibration the results are very close to the first calibration, sometimes the curves are coincided. Se the lines in black color in Figure 4.34 and 4.36.
- It is obvious that the gap between factory calibration and calibration at experimental site is larger for radiometers than for total heat flux gages. This may be an indication of that radiometers are more sensitive, and consequently exposed to earlier physical degradation.

Chapter 5

Analysis of Experimental Results

5.1 Introduction

In the following sections the results of the experimental work shall be presented and analyzed in the same sequence as described in the previous chapter.

5.2 Benchmark Steel Plate

As indicated earlier the surface concerned was heated by two methods before water droplets were applied. Heating by forced convection and radiation using a small scale propane flame, and by conduction using a 1500 W circular hot-plate.

The experiments were carried out indoors at room temperature. The reproducibility of the results was controlled by repeating each test minimum three times.

Flame-Heated Surface: After the maximum surface temperature was reached, i.e. 520 °C, the hand-pump based deluge water was activated and impinged upon the hot surface. By referring to Figure 4.3, either in upright or horizontal position, the ideal distance of release point of the deluge to surface showed to lie roughly between 400–500 mm. At release angles smaller than 90°, i.e. angle between the nozzle centerline and the surface, the cooling impact reduces. When the angle is reached to approximately 45° or lower, the water just wanders off the surface edge without making significant contact with the heated surface, particularly for the surface in upright position.

However at optimum orientation and distance of the deluge, the wetting of the hot surface starts at temperatures less then 165 °C. This is quite close

to the temperature where the liquid droplets start experiencing critical heat flux condition leading into transition boiling. The heat flux level at this point is somehow similar to the value obtained in next experiment, as discussed below.

Conductive-Heated Surface: Maximum attainable temperature was around 353 °C. After reaching the steady state temperature of the surface, the gravity-generated water droplet was gently impinged on the horizontally positioned hot surface area where the thermocouples were situated. The drop generator which generated about 1.5 droplets per second produced roughly droplets of 3–5 mm in diameter. In this case the ideal distance from the droplet release point to the surface showed to be around 200 mm. This gave an impact velocity of about 1 m/s with a water mass flux nearly 0.15 g/cm^{2}s. In contrast to the former case the release angle could not be varied, but kept at normal to the surface.

In the early phase the droplets did not maintain and rather jumped over the surface and floated over thin vapor layers. As the surface temperature was lowered further, wetting started at about 240–250 °C, although part of the droplet beaded off as tiny drops. The transition between these two states is the Leidenfrost transition, which describes the phenomenon of two-phase heat transfer, i.e. heat is transferred from the surface to the droplet through a vapor layer formed between them. This point approximately corresponds to point E on the boiling curve of the water as shown in Figure 2.7, i.e. 240-100=140 °C at minimum heat flux. When the surface temperature reached to about 180 °C, the entire droplet was in touch with the hot surface with almost no break-up, which believes that the droplet underwent the transition boiling where the vapor is formed very rapidly (point E–D). While at about 150 °C, the droplet began to rest with no stress. It spread out with a contact angle approaching zero and causing to cool down a larger area than its spherical projection area, which suppose to represent point D on the diagram, i.e. critical heat flux (CHF), before it reached the saturation point of water. Applying Equations (2.56) and (2.57), the corresponding maximum and minimum heat flux at above mentioned temperatures (150 and 240 °C) are about 1750 and 60 kW/m^2, respectively. The CHF calculated agreed with literature's almost 1680 kW/m^2, which has used droplet diameter ranged 2.3–3.8 mm [109].

At the point of CHF, the maximum droplet diameter right after spreading showed visually to be approximately 3 times larger than its initial spherical diameter, hence giving a spreading factor equivalent to 3 according to Equation (3.48). Solving Equation (3.47), one obtains cooling efficiency of the droplet to be about 8 %. The low effectiveness seems to be in agreement

with what literature reports about larger drops [106]. Namely large, slow droplets cool less effectively than small, fast droplets. The corresponding Weber number is 68, which indicates that the inertia forces dominating over the surface tension forces of the droplet.

5.2.1 Conclusion

The droplet release angles normal to hot surface gives the best cooling impact. Reducing the angle, reduces the cooling impact. As the angle reduces further and approaches 45°, the water just wanders off the surface edge with minimized effect.

It is obvious that lowering the impact velocity combined with larger droplet size are major contributors in higher wetting temperature, when the surface positioned in horizontal plane. It seems these two factors would be in favor of increasing the droplet contact area, i.e smaller contact angle, and hence reducing the surface tension, which in turn causes the droplet rests longer on the hot surface before it evaporates. This phenomenon is similar to that of the discussion covered previously by Section 2.3.2 Shape and Size of Water Droplets, that when a liquid drop gently wets a solid surface might have a contact angle as close as to zero, causing larger wetting surface area and resulting in more effective mechanism of heat transfer.

But the big challenge would remain how to overcome the effect of the gravity of large droplets when the spray direction is horizontal or eventually upward without increasing their velocity, particularly over longer distance.

5.3 Characterization of Jet Flame

Since the experiments were conducted outdoors the ambient condition was measured prior to each experiment, i.e. wind speed, direction, and air temperature, and any considerable change in direction and speed of the wind during the performance was noted down. The wind speed varied in the experiments between 0.2–2.0 m/s at angles ranged 45°–270° measured between jet centerline and wind direction clockwise from a direction pointing upstream of the jet. It was mostly in the range of 0.5–1.5 m/s at approximately 150°, but quite often changed in direction. This is illustrated schematically by arrow number 4 in Figure 5.1. As an example, wind with 0° angle corresponds to a wind direction co-current to the gas issuing from the nozzle or parallel to the nozzle centerline, arrow 1 on the figure. Whilst, wind with 180° angle is similar to 0° angle, except the direction is counter current to the gas flow, arrow 5 on the figure. Wind direction demonstrated by 3 having

normal angle to centerline, also known as cross wind, while 2 and 6 form 45° and 310° angle to jet centerline, respectively.

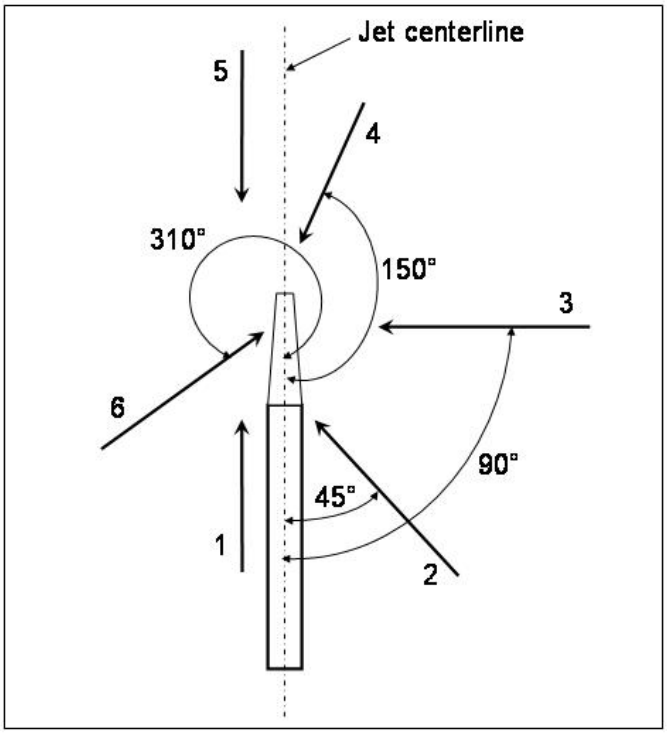

Figure 5.1: Illustration of wind direction

The flame of concern had an approximately length of 5.5 m plus a lift-off distance of about 0.6 m, with 1 m in diameter in the thickest region. In contrary to heavier hydrocarbon fuels, the propane flame was quite low-sooted, partly due to elevated temperature of the gas before release which is a favorable factor for combustion.

Temperature Measurement: Temperatures measured corresponds to layout shown in Figure 4.4. During data processing after accomplishing the temperature measurement, one could notice that one of the thermocouples may have malfunctioned in 5 of 21 experiments showing unreliable values. Since this should have occurred during the tests, it was not possible to be discovered. However in treating the results, the temperature corresponding to this thermocouple was interpolated between the values recorded by the two adjacent thermocouples.

The temperature plot is provided in Figure 5.2 with the center of temperature field located approximately at y = 0.0 m. y-axis represents the

radial direction or cross section of the flame, while x-axis refers to the axial direction.

Indeed the center point of the temperature field deviated to some extent from y = 0.0 m, due to constant fluctuating of wind direction. Since it could be crucial to model such scenario in CFD-code KFX, one assumed zero wind speed when simulated. Thus, in order to make the experimental and simulation results comparable, adjustments were made in MATLAB when plotting the temperature values from the experiment by displacing the center point so that its center point situated on y=0.0 m, without having any consequences for numerical values of the temperatures.

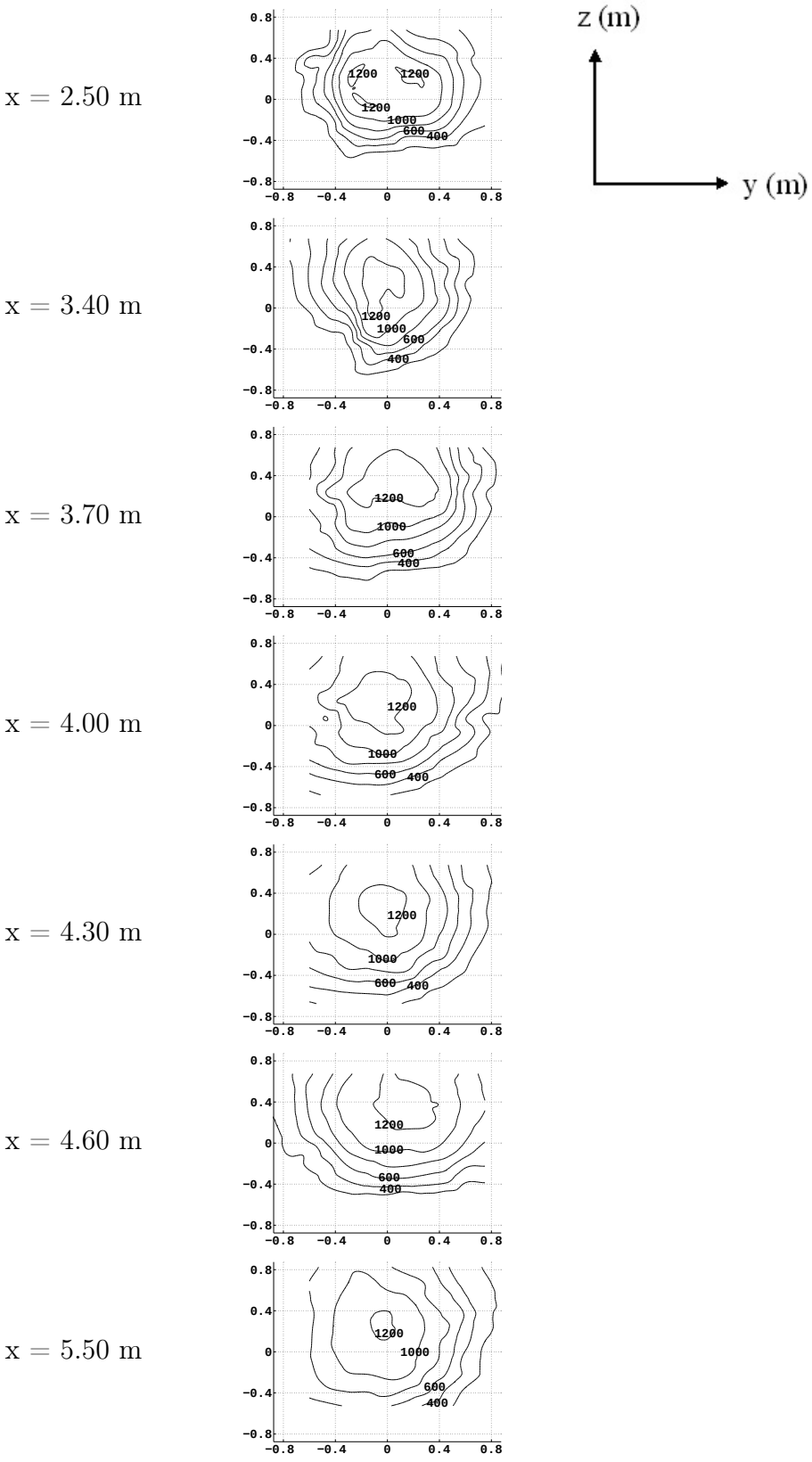

Figure 5.2: Temperature contour (°C) at various distances (x) from nozzle

The graphs shown in Figures 5.3 and 5.4 illustrate two major facts, fluctuation of flame movement due to swinging wind direction and premature combustion zone (upstream) contra fully developed combustion area (downstream). Each diagram refers to four measurement points, almost on periphery of the flame, located on four outer corners of the grid shown earlier by Figure 4.4. The value given by x identifies the distance of the cross section from the nozzle. The abbreviation on the diagrams stand for: UL=upper left, LL=lower left, UR=upper right, and LR=lower right.

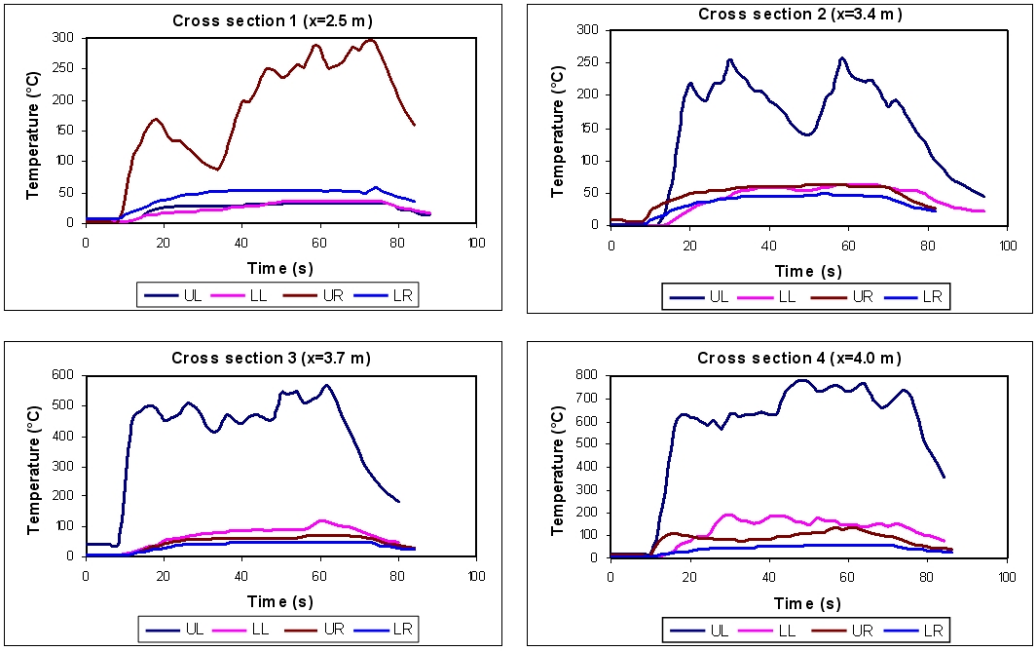

Figure 5.3: Flamelet temperature at cross sections 1-4

Movement of the flame as a function of fluctuating wind direction is evident by the fact that, for example upper left (UL) shows higher temperature in five of seven cases, while in cross sections 1 and 6 the upper right rules. With another word the earlier denotes that in most of the cases the wind direction dominated by pushing the flame toward left, if looking downstream.

The combustion quality is distinguished by higher temperatures as one moves downstream. The hottest zone across a flame is somewhere between the flame core and its outer edge or the periphery, as may be seen in Figure 5.2, irrespective whichever cross section is concerned.

The flame length was roughly measured by observation and analysis of photographs. It showed to be around 5.5 m, not including the lift-off distance. This agrees almost with the flame length predicted by Equation (3.13)

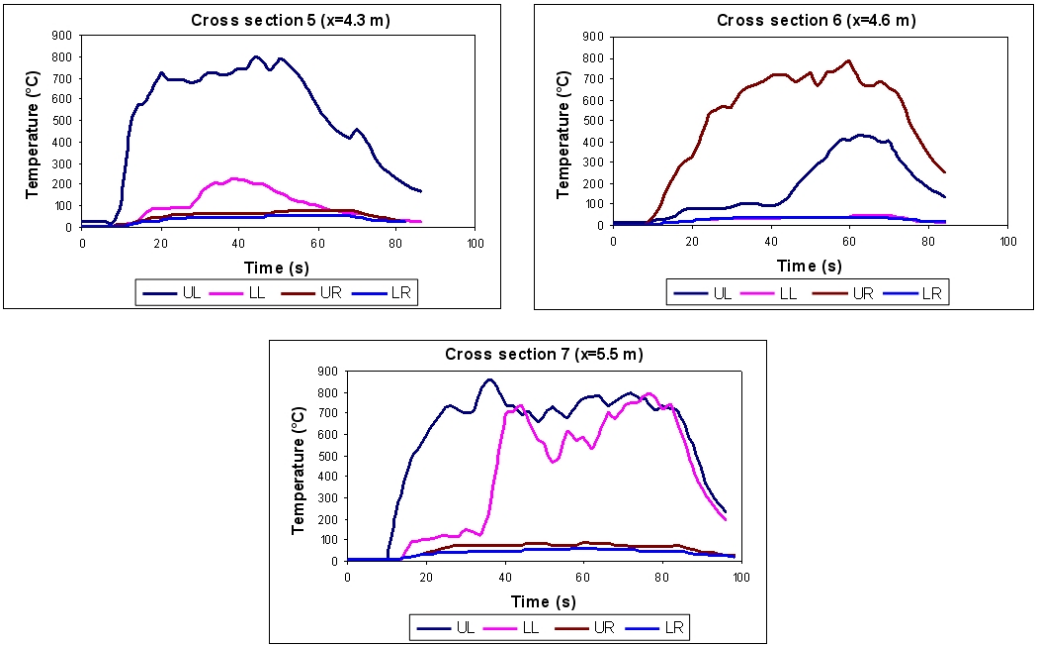

Figure 5.4: Flamelet temperature at cross sections 5-7

for non-vertical flame length, giving 5.3 m. The model is intended for natural gas at much higher flow rates. The prediction presumes lower heat value of propane 45.6 MJ/kg with a mass flow rate of 0.3 kg/s. In similar manner the lift-off distance found to be about 60 cm. The model which estimates the distance best, is described by Equation (3.12) for sonic gases at the lower range, i.e. $B/u_e = 2.5$ ms, which gives about 65 cm. This model is based on fire sizes above 20 MW. While flame of concern in this study is about 14 MW.

Heat Flux Measurement: Heat flux was measured according to arrangement shown in Figure 4.5, i.e at four positions directly located within the flame and two locations outside, all at jet axis level about 1.5 m above floor level. At each location nett radiation heat flux, total heat flux (sum of radiation and convection), and temperature were measured.

In spite of purging gas applied to keep the inner surface (polished area) of the radiometers' restricter clean, the high turbulent gas flow had inevitably entered the window causing the inner surface to be coated by soot. Hence reducing the emissivity and causing unreliable and low radiation values, except the one located in low radiation field farthest away from the flame at a radial distance of 3.0 m. Indeed the unit at y=1.5 m is also located outside the flame zone, but apparently an oscillating turbulent flame has often touched

the probe. Images in Figure 5.5 show condition of the heat flux gages before (5.5a) and after experiment (5.5b). The photos are taken from different experiments. The probes were located inside the flame region.

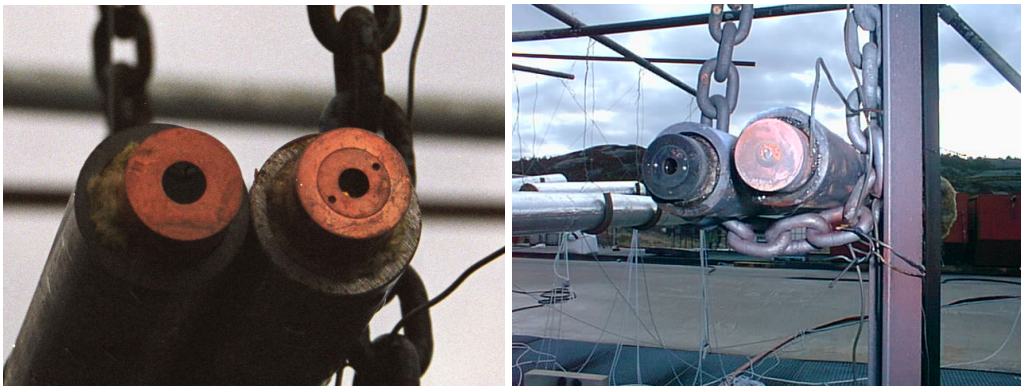

(a) **(b)**

Figure 5.5: Physical condition of heat flux sensors before (a) and after experiment (b)

This implied to treat the radiation results analytically based on the temperature measured in experiment and simulated gas velocity in KFX. This was done first by calculating the convective heat transfer coefficient for turbulent flow over a flat surface [119] using Equation (5.1)

$$h = 0.033 \frac{\rho C_p \nu^{0.2} u^{0.8}}{d_g^{0.2}}, \tag{5.1}$$

where

$$\begin{aligned} \rho &= \text{gas density (kg/m}^3\text{)} \\ C_p &= \text{specific heat capacity of gas (kJ/kgK)} \\ \nu &= \text{kinematic viscosity of gas (m}^2\text{/s)} \\ u &= \text{gas velocity (m/s)} \\ d_g &= \text{outside diameter of heat flux gage (m)} \end{aligned}$$

Then using the simple relation $Q_c = h(T_2 - T_1)$, the convection heat transferred to the heat flux meter was calculated. T_1 and T_2 are the temperatures of the heat flux body (≈ambient temperature) and the flue gas,

respectively. By subtracting this value from the total heat flux measured in the experiment, a theoretical radiation corresponding to the experimental value was then found, and the results are plotted as shown in Figure 5.3. Values of heat flux measured at low radiation field, i.e. outside the flame area, are provided in Figure 5.6b.

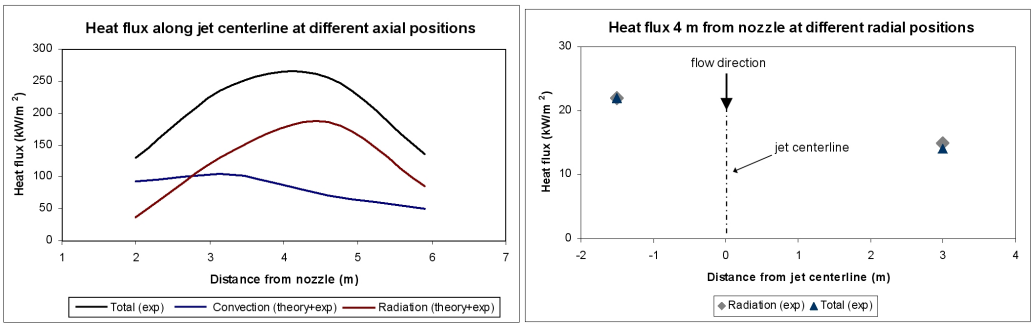

(a) Inside flame **(b)** Outside flame

Figure 5.6: Heat flux measured within and off jet flame

To give a visual sense, the numerical values of the heat flux are summarized and written on an image of the flame of concern, and related to their locations in an xy-plane as illustrated in Figure 5.7. For example the identifier T14 is read 14 kW/m^2 total heat flux. The photo is indeed taken in an xz-plane.

5.3.1 Conclusion

As may be seen from the Figures 5.2–5.4 the hottest zone of the flame is slightly over halfway downstream the flame, where combustion is completely developed. The highest temperature at any cross section of the flame is somewhat between center point and outer edge of the cross section concerned. At center region and outer edge the temperature is lower, because the fuel-air ratio at these zones is rich and lean, respectively. The earlier is under-oxidized, hence not all energy is liberated. While, in the later the system is reversed, i.e. over-oxidized, then causing to cool down the flame, known as heat lost to surrounding.

As expected and can be observed from Figure 5.6–5.7 the radiation fraction near the jet release is lowest, about 28 %, merely due to bluish part of the flame. While this value increases as one moves away along the jet center line to order of magnitude 57 %, and reaches to its maximum 73 % at 4.6 m from the nozzle before it drops to 63 % further downstream. While values of

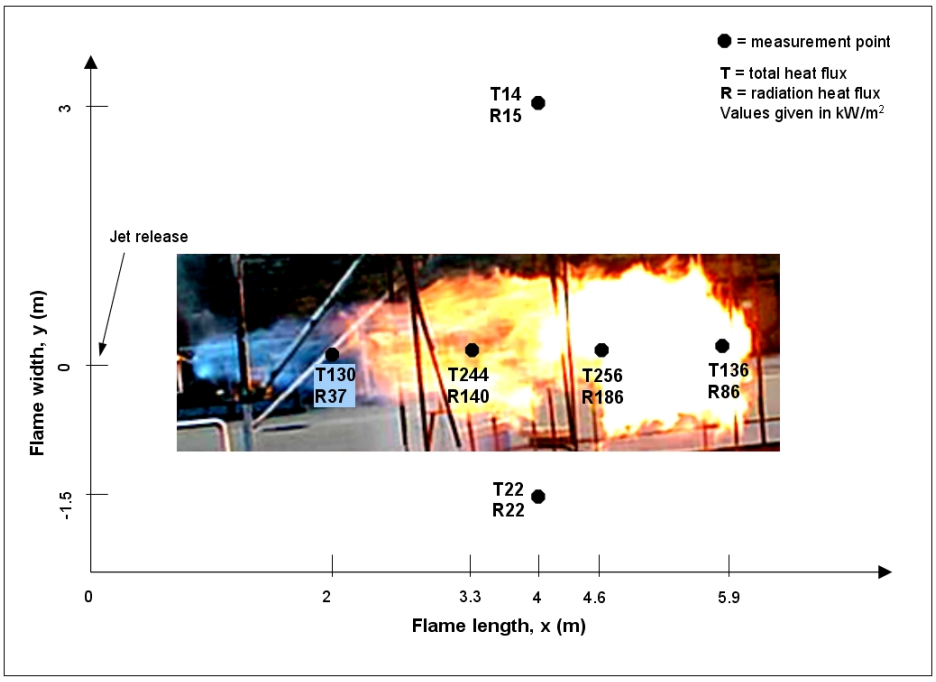

Figure 5.7: Value of heat flux at different locations within and off jet flame

radiation and total heat flux outside the flame are almost the same, which evidently indicates no effect of heat convection is present. Indeed in the case farthest away from the flame, the total heat flux is slightly lower than the radiation heat flux. An obvious impact of cold ambient air as entrainment caused by the high gas velocity.

To measure the radiation part of the flame seems to be a challenging task. As mentioned earlier, to prevent the turbulent gas not to enter the restrictor of the radiator device is almost impossible. Hence, difficult to keep the polished area clean. A possible concept to overcome this problem might be to position the probe with its window opening looking downstream. This might in turn result in lower convection effect, if the total heat flux meters are oriented in similar manner.

5.4 Large Scale Jet Fire Test with Steel Channel

As stated in the previous chapter, no water spray was applied in carrying out experiments with the quadratic steel channel. A number of outdoor tests were conducted[1] where the object was exposed to jet fire, and distance between nozzle and object was varied. Temperature was measured at various locations in accordance with the illustration provided in Figure 4.11. A thermocouple was mounted closed to exposed surface to take record of the flame temperature, henceforth denoted by T_{flame}. The pressure and mass flow rate of the gas was 10.5 barg and 0.3 kg/s, respectively, at an ambient temperature between 12–16 °C. The results are shown in Figure 5.8–5.10.

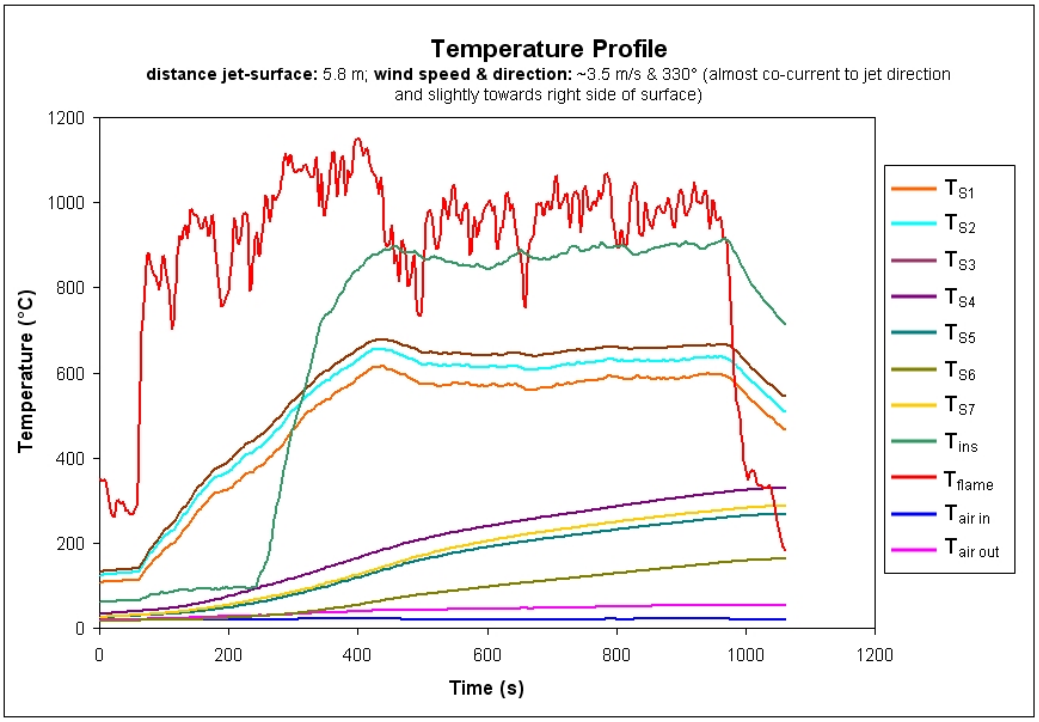

Figure 5.8: Temperature profile at a wind speed and direction 3.5 m/s & 330°

The basic parameter to consider before terminating an experiment was when the temperatures of the exposed surface (T_{S1}, T_{S2}, T_{S3}) have reached

[1] As a pre-study the object went through a couple of pool fire tests, prior to jet fire experiments. The results are not discussed here, but full temperature recording data is available.

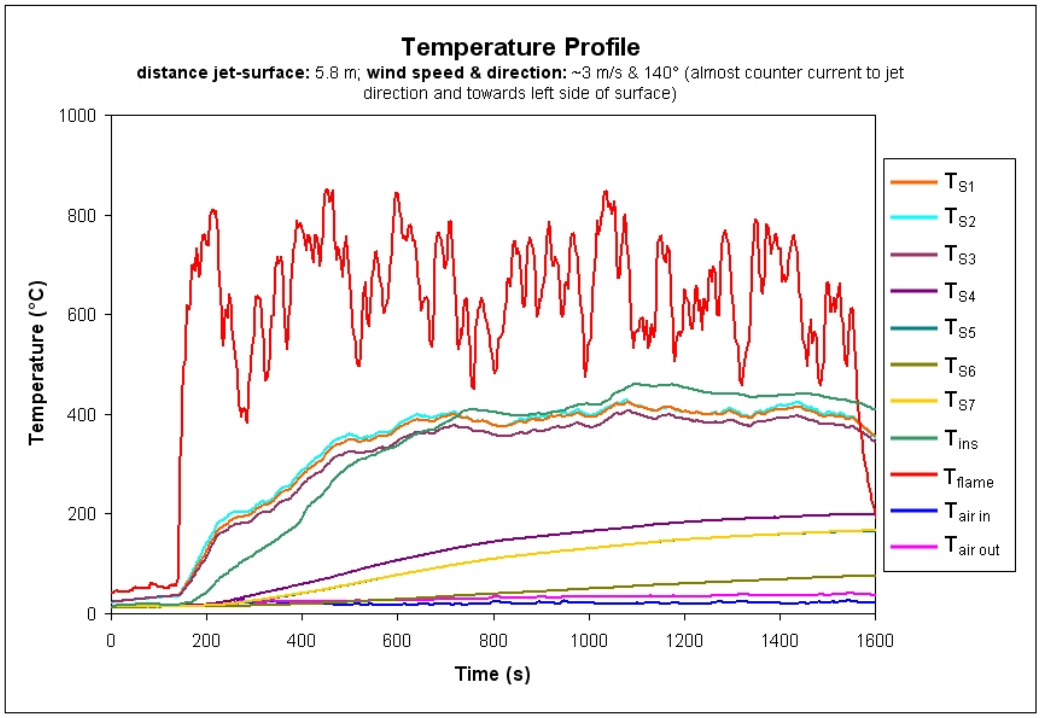

Figure 5.9: Temperature profile at a wind speed and direction 3 m/s & 140°

and kept steady state over long time. The steady state temperature level varies, anyhow, for all the cases due to different conditions as directly specified on each diagram.

The first two cases illustrated by Figure 5.8 and 5.9 are pretty much similar, except the wind direction. The impact of the wind is visible, where the temperature at each location shown by Figure 5.9 drops considerably by about 200 °C, except for the air which is not directly influenced. Neither the insulation temperature, T_{ins}, follows this rule. Apparently the flame is pushed away backward by counter current wind and to the left side of where the thermocouple is situated, so that the temperature fall at this location is almost 400 °C.

Furthermore, the temperature of insulated portion of the exposed surface, T_{S4}, seems to remain about 200 °C under those of the exposed area, and temperature increase occurs mainly by heat conduction from the exposed side and partly through insulation section. The temperatures of protected surfaces (T_{S5}, T_{S6}, T_{S7}) seem to behave identical for aforementioned three cases. In Figure 5.10 this applies up to about 450 seconds. The temperature of topside, T_{S5}, and rear side, T_{S7}, show always higher values than the bottom

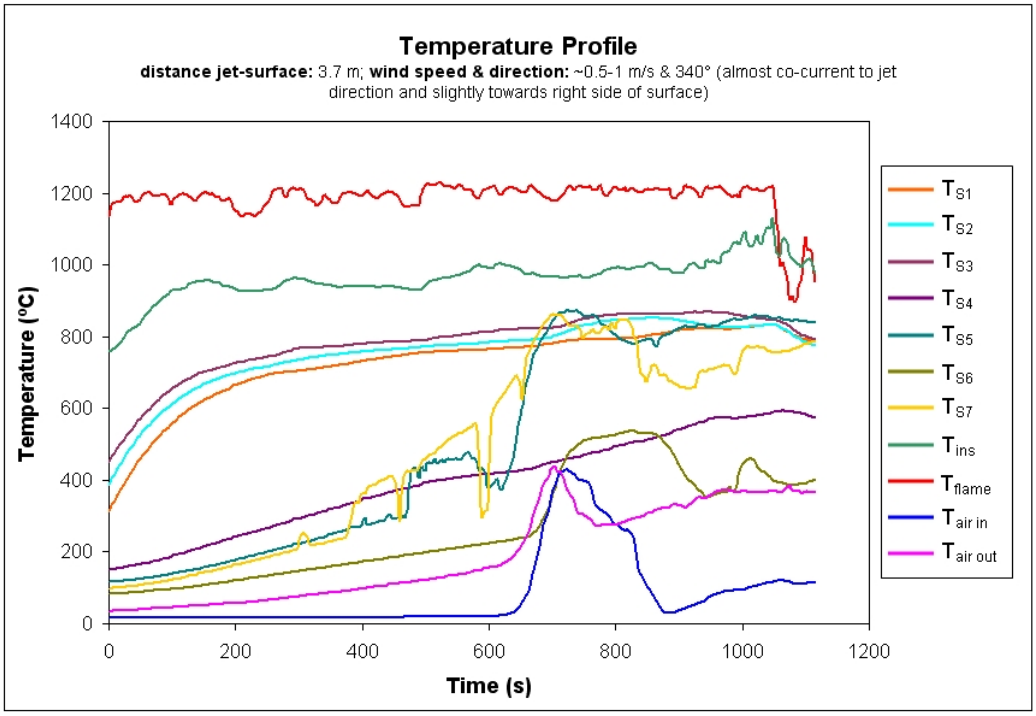

Figure 5.10: Temperature profile at a wind speed and direction 1 m/s & 340°

side, T_{S6}. Although the nature of temperature development is the same as for T_{S4}, but nevertheless the conduction heat is transferred possibly easier upward than downward.

The oscillating flame temperature in Figure 5.8 and 5.9 is a conspicuous sign of fluctuating wind direction. The higher wind speed causes the wind to fluctuate more. On the other hand the same temperature in Figure 5.10 shows more harmony, partly due to milder wind speed (0.5–1 m/s) and partly because the object is moved upstream nearer nozzle (3.7 m) where the flame does less radial movement.

The temperatures shown in Figure 5.10 are generally higher than the other two cases, due to lower wind speed and closer object location. It is further obvious that after about 450 seconds an unexpected and massive change in temperature takes place. This concerns the temperature of three protected surfaces (T_{S5}, T_{S6}, T_{S7}), inlet, and outlet air. Closer inspection after experiment revealed that the insulation material inside the metal encasing had crumbled and partially burned due to intensive heat as shown in Figure 5.11, in addition a large external part of insulation was burned down as it can be seen in Figure 5.12.

(a) **(b)**

Figure 5.11: Physical condition of extension pipe and insulation material inside encasing on right side of channel (a) and on left side of channel (b)

Figure 5.12: Physical condition of external insulation material on right side of channel

These signs may indicate that the flame may have penetrated through the side opening into the metal encasing on the right side of the exposed surface, and/or simply due to intense heat transport through the encasing wall the insulation material is gradually incinerated or crumbled, hence transferring the heat further to insulated areas.

The whole incident is attributed to an unusual long exposure time. The experiment is indeed an immediate repetition of another experiment which was interrupted after about 800 second due to power failure. In addition as it can be seen from the diagram, the experiment itself had started earlier and data in earlier stage has not been logged. So that the object altogether was exposed about 40 minutes to continuous heat. In spite of this, it seems the exposed surface itself has well withstood the thermal stresses, except a

portion of the surface layer was peeled off .

5.4.1 Conclusion

Since this part of the work is not completely accomplished, i.e. no water droplets were applied due to the complications discussed earlier, it would be too crucial to draw any specific conclusion.

Anyhow a careful conclusion based on the results achieved so far, although conservative, may be that passive fire protection does not necessary guaranty to protect the equipment against any type of fire scenario, particularly in fires with long exposure time. Besides, equipments subject to jet fires are extra exposed due to impact of erosion.

Further, one would believe if in case liquid droplets were employed, the reaction of the hot surface to cooling effect of impinging droplets would most likely be similar to that of the steel plates as shall be discussed in the next section, i.e. Large Scale Jet Fire Test with Steel Plates.

5.5 Large Scale Jet Fire Test with Steel Plates

The main task in this part of the work was to map the nature and behavior of hot spot, i.e. how it is formed, how it can be eliminated and what can be done to prevent it.

As reported earlier two types of experiment were conducted with two different nozzle configurations, i.e. water spray nozzles located inside and outside the flame region. The measurement of temperature and heat flux follows as explained previously, and it is also summarized in sketches shown in Figure 5.13. For category nozzles within the flame, the measurement program follows only the pattern shown by Figure 5.13a, i.e. without heat flux measurement. All the notations and symbols used in discussions in this section refer to Figure 5.13.

Spray Nozzles Located Outside Flame

The spray nozzles mounted on their own foundations, and were located outside the flame almost at the same axial distance from the plates as the jet nozzle. Two types of experiments were conducted in this category with varying gas pressure, 5 barg and 10 barg. Water mass flux was kept constant throughout both experiments at a flow rate equivalent to 4.4 kg/m^{2}s per nozzle corresponding to an impaction area of 0.09 m^2, which is the surface area of a plate.

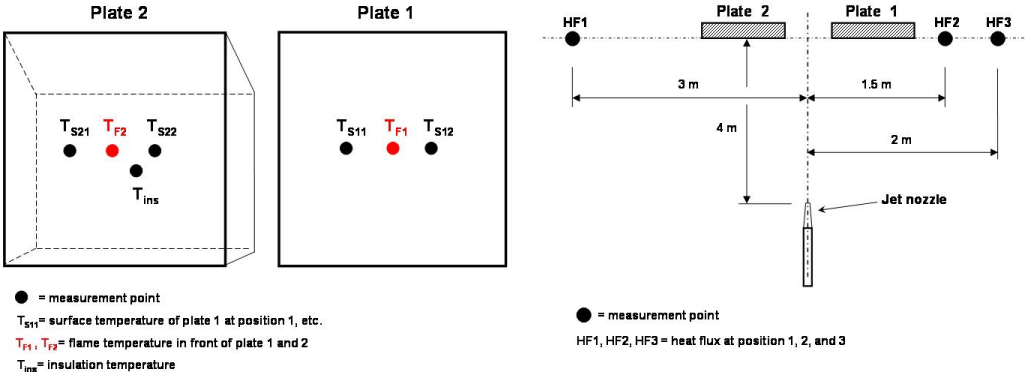

(a) Temperature **(b)** Heat flux

Figure 5.13: Location of measuring points with steel plates

In case of test at low gas pressure (5 barg), the ambient air was at 18 °C and the wind speed was measured to be at an average of 2 m/s forming an angle of about 330° to jet centerline. The results are plotted in Figure 5.14 and 5.15.

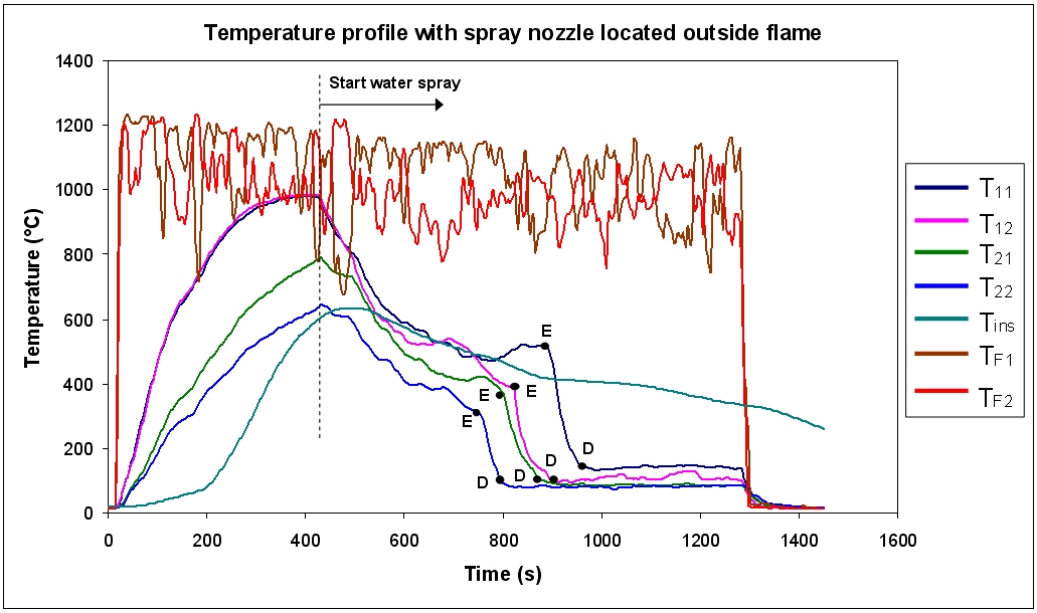

Figure 5.14: Temperature profile of water sprayed hot steel surface at low gas pressure

As it can be seen from temperature diagram in Figure 5.14 the insulation

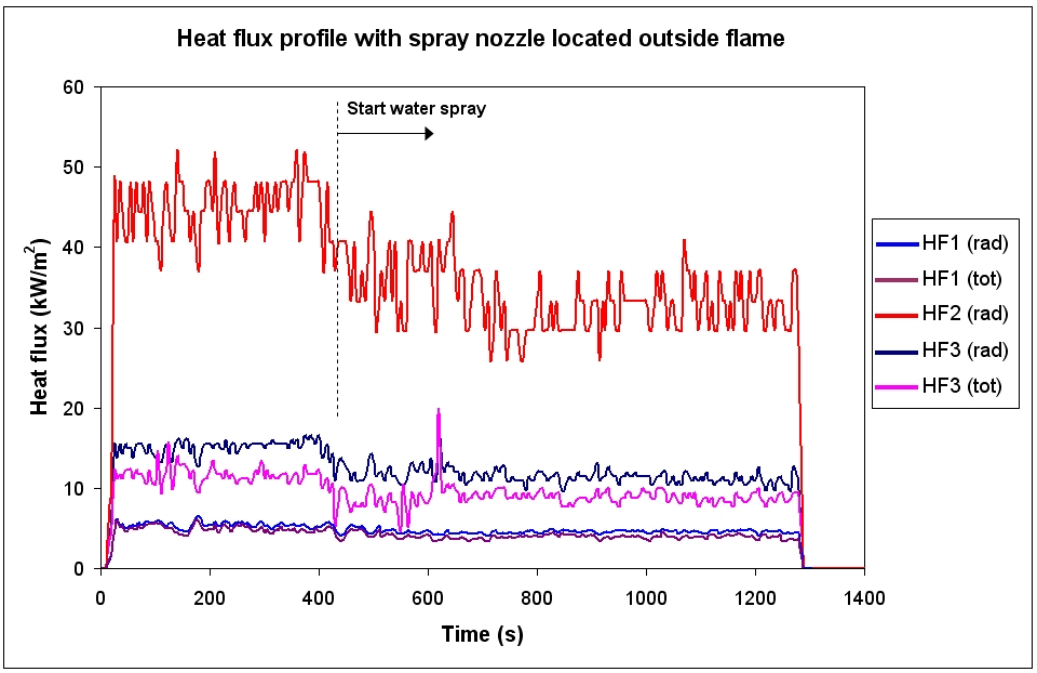

Figure 5.15: Heat flux profile of surrounding region at low gas pressure

material on the rear side of the plate 2 keeps the maximum surface temperature (T_{22}) about 200 °C under that of uninsulated plate 1 (T_{11} and T_{12}). The later indicates that the surface would be heated from the rear side as well. Since the wind direction pushes the flame tip slightly away from the center point and toward plate 1, it results the left side of the plate 2 to be less exposed and having the lowest temperature, i.e. T_{21} ≈650 °C. The temperature of the insulation box (T_{ins}) is kept fairly low until 200 seconds, before it escalates and rapidly jumps to about 650 °C, due to conduction heat transfer from all directions. Indeed its insulation effect gradually disappears as the exposure time is extended.

From the time the deluge is activated, it takes about 400 seconds to depress the surfaces temperature to about 400 °C, before all the temperatures quickly drop to evaporating temperature of water. During this period of cooling the liquid droplets undergo the film boiling regime moving toward the Leidenfrost point marked with E on the curves approximately at the break points in Figure 5.14, before entering the transition boiling regime and toward critical heat flux point D, and furthermore moving in direction of the saturation temperature through nucleate boiling. The two points E and D correspond to boiling curve of the water in Figure 2.7.

The effect of wind direction is also visible in the cooling period. It is evi-

dent that the flame impingement area is more concentrated on the right side of the plate 1 resulting in the highest temperature, represented by T_{12}. On the other hand the left side of the plate 2 stands for the lowest temperature, T_{21}.

The flame temperatures which are merely measured to keep record of heat intensity of the flame at impaction area, are not necessarily affected by deluge, most likely due to thermocouple's very small contact area at the tip.

The deluge also cools down the flame, specially its impact on combustion quality resulting in lighter flame color (less soot) causes the radiation part to decrease. The heat flux measured outside the flame plotted in Figure 5.15 gives a clear indication of heat flux level before and during the deluge activation. The radiation level at 1.5 m from the jet centerline, HF2 (rad)[2], drops by 22 % from about 45 to 35 kW/m^2, while similar values for the locations 2 m and 3 m away from the centerline are about 20 % (down from 15 to 12 kW/m^2) and 17 % (down from 6 to 5 kW/m^2), respectively. Values for total heat flux at location 2 m and 3 m dropped by about 25 % (down from 12 to 9 kW/m^2) and 20 % (down from 5 to 4 kW/m^2), respectively. Total heat flux at position 1.5 m, nearest the flame, was not measured due to lack of appropriate device. Two factors are noticeable. As one moves away from the flame in radial direction, the drop in heat flux level is lower (both radiation and total). Logical explanation would be that the heat flux level is lower longer away, likewise does its change. Another matter is that the total heat flux is indeed lower than the radiation part. This is justified by effect of entrainment ambient air at lower temperature than flue gases, which strikes over the sensor surface and cools it down. The effect is greater as one moves nearer the flame, because a higher gas velocity escalates the entrainment effect. Consequently the convection fraction would further decrease. This is only valid up to a certain distance, further approach toward the flame would indeed reverse the process due to either preheated surrounding air or direct involvement of the flue gases or both.

The next experiment in this category was conducted with a gas pressure at 10 barg. The ambient air was at 8 °C and the wind with an average speed of 1 m/s blew in a direction forming about 160° angle to the jet centerline. The wind condition may be characterized as counter current to gas flow pushing the flame slightly toward left side where plate 2 is located. The results are provided in Figure 5.16 and 5.17.

Some unexpected incidents occurred during this test as follow:

1. The plate 1 was rotated halfway under the experiment from its original position by about 20° in clockwise direction.

[2]Abbreviation in parenthesis stands for: rad=radiation; tot=total

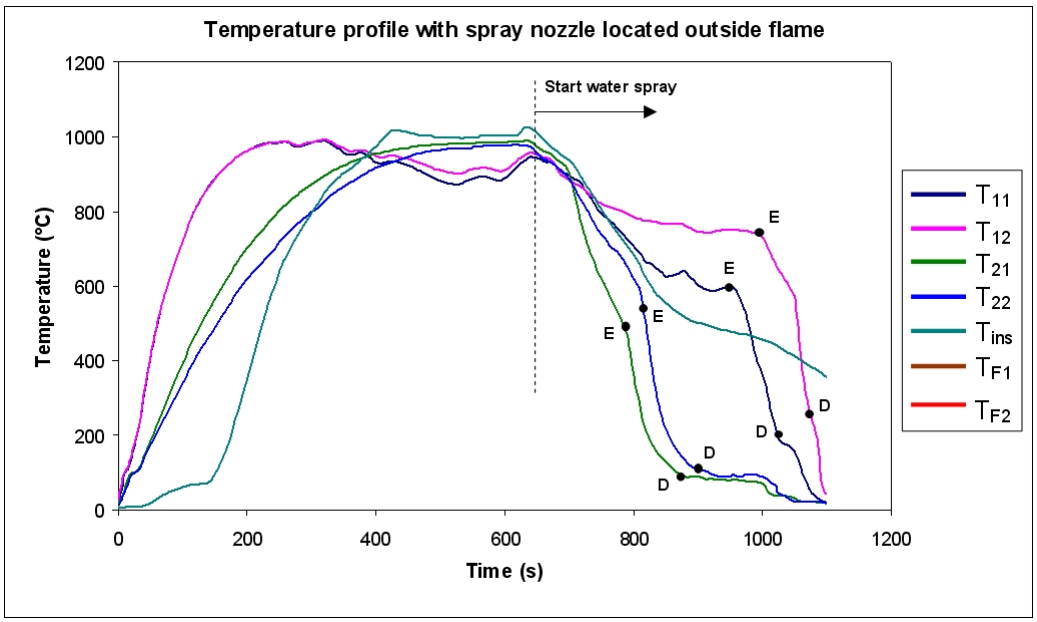

Figure 5.16: Temperature profile of water sprayed hot steel surface at high gas pressure

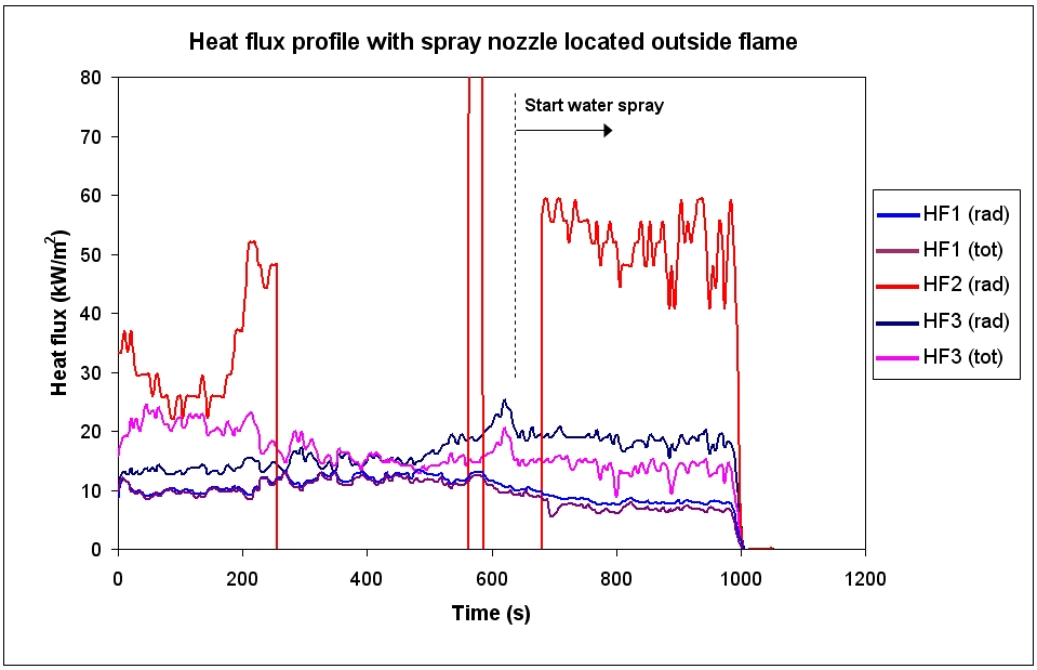

Figure 5.17: Heat flux profile of surrounding region at high gas pressure

2. The nozzles[3], in particular nozzle 1, were slightly deformed by heat during standby, and gave uneven and poor spray spreading. The reason was that both nozzles in this experiment were slightly moved forward in axial direction, hence nearer the flame.

3. The two thermocouples intended for measuring the flame temperature fall off their supporting points due to thermal stresses while performance was in progress, thus showing untrustworthy values. Therefore, the flame temperatures are not included in Figure 5.16.

4. Heat flux values nearest the flame identified by HF2 (rad), seems to have fallen outside range of the gage prior to deluge activation, possibly exposed directly to the flame.

As it can be seen from Figure 5.16, the surface temperature of the plate 1 drops after about 300 seconds. This is believed to be due to the deviation caused by rotation of the plate. See Figure 5.18 taken after experiment. In one way the flame slides over the plate 1 rather than impinging directly upon it, causing temperatures T_{11} and T_{12} to fall some. On the other hand it seems the slanted plate 1 guides the flame to reach easier on the rear side of the plate 2, and transferring extra heat to insulation material through the insulation box with thinner wall than the plate, hence raising the insulation temperature T_{ins}.

Otherwise the maximum surface temperature, i.e. ca. 1000 °C, before activation of the deluge is well comparable to the previous case with gas at low pressure. But the fundamental difference is the preheating time to reach this level. In the later it takes about less than half of the time for surface to attain the maximum temperature. A clear indication that objects, when exposed to high pressure gas fires, are severely subject to thermal stresses.

After deluge activation it seems that the surface 2 gets cooled faster, although the surface temperature is higher than that of the plate 1. A possible explanation is that part of the deluge water issuing from the nozzle 1 at the start was oriented toward plate 2 due to aforementioned deformation, before the nozzle was readjusted back toward the plate 1. Due to an uneven situation of nozzle 1, anyhow, it took longer time to cool down the surface 1. Figure 5.19 shows unevenly deluge spreading.

A similar phenomenon as in the previous case with test at low gas pressure is also experienced here after the deluge is applied. Namely the curves break at a point, i.e. the liquid droplets pass through a completely film boiling region to a minimum heat flux. The break point in this case is raised since the fire intensity has increased.

[3]As stated earlier, these nozzles were of garden-application type, i.e. of PVC material.

Figure 5.18: Plate 1 rotated in clockwise direction

Figure 5.19: Uneven deluge due to nozzle deformation, nozzle 1 on right side

It should be emphasized that, just as in the previous case or similar cases which shall be discussed in next category of the experiments, the deluge not only cools down the surfaces, but contributes in suppressing the flame

temperature as well.

When the heat flux measurement is concerned (Figure 5.17), the values at position 2, HF2 (rad), seem to fall outside the flux meter's range before the deluge is activated. Because most likely the device has been engulfed by a fluctuating turbulent flame, since the gage is located very closed to the periphery of the flame. Images in Figure 5.20 may be illustrate the addressed problem. A situation when it arises may knock out the gage if the values fall far outside its range, as experienced during the flame characterization. But as soon as the flame is cooled down after application of water spray it functions normal again. However, the radiation heat flux level at this stage, about 50 kW/m^2, is 40 % higher than the corresponding value in test with low gas pressure.

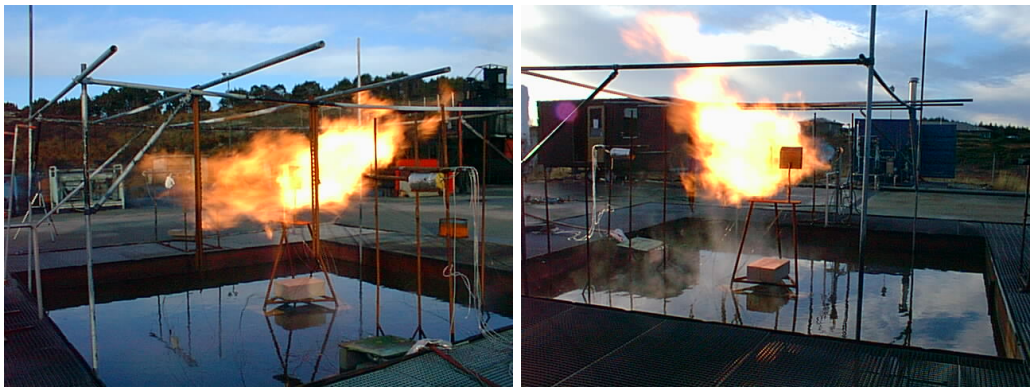

(a) **(b)**

Figure 5.20: Flame movement toward right side before deluge activation with tip of HF2 almost inside flame (a), while plate 2 is nearly situated outside flame (b)

At position 3, the total heat flux, HF3 (tot), is higher than its radiation part, HF3 (rad), up to about 300 seconds. As explained earlier, the total heat flux outside the flame used to be equal to the radiation. With other word it is purely radiation, since the convection effect is nearly zero. While in this case, it indicates that the flame should have moved to right side due to wind, and approached where the gage is located and causing HF3 (tot) to rise. However, it drops by about 20 % after deluge activation.

On the other hand the radiation fraction at position 3, HF3 (rad), is kept relatively low, about 18 kW/m^2 in average, and increases gradually before deluge is activated. Irregularity is owed by the same explanation, i.e. due to wind. One would expect indeed its value could be higher, may be around 25

kW/m^2 as it shows right before the water spray is switched on. No reduction is recorded after the deluge, since the preheating period showed uncertain and unusual low value.

The gage HF1 behaves fairly as it does in case 1 with gas at low pressure. After about 300 seconds when the flame moves back to its original position, i.e. from right to centerline, the values of total heat flux and radiation are slightly increased from about 10 to 13 kW/m^2 for both, since the flame comes nearer the gage. They drop by about 40 % and 30 %, respectively, after activation of the water spray. Compared to test with gas at low pressure, the level of total heat flux and radiation are higher by almost 130 % and 90 %, respectively, before activation of deluge, and 75 % and 60 % after activation.

Radiation heat flux measured at a position 1.5 m from the centerline, both at high and at low gas pressure, indicates that this value before deluge activation should approximately lie about 50 kW/m^2. This may be a more realistic value than the figure calculated by Equation (5.1), i.e. 22 kW/m^2, as discussed under Section 5.3 Characterization of Jet Flame. This assumption seems to be supported well by the simulation results predicted by CFD-code KFX, discussed later under Section 6.3 Modeling of Jet Flame, and as shown in Figure 6.5.

However, lower calculated value based on temperature measured may be argued by the fact that the thermocouple's mantel with shining surface with low emissivity combined with small sensor surface area at the mantel tip reduces its ability for radiation absorption.

Pool Boiling: The two temperature-time history diagrams shown in Figure 5.14 and 5.16 have been analyzed closer, and an effort was made to identify and locate different boiling regimes. The analysis is based on boiling curve of the water provided in Figure 2.7, and its corresponding theory discussed in Section 2.3.2 under Drop Interaction with Solid.

The focus was made on minimum and peak pool boiling, marked on the curves with E and D, respectively. In mapping the locations concentration was aimed at sharp slopes or high gradients which normally indicate transition to a new phase. It was a laborious and tricky job to spot some of the points, particularly those in Figure 5.16. The later pertains, among others, point E on temperature curve T_{12}. The temperature reading at this position and its resulting vapor film or droplet interface temperature (about 415 °) falls indeed in superheated region, which then does not give adequate data entry for saturated steam. One then moved slightly lower and selected the next possible break point. Therefore, one should count on some errors in accuracy of the locations and their subsequent data readings. Based on the temperature readings from the diagrams, the vapor film temperature at dif-

ferent locations was calculated using the expression $T_f = (T_w + T_{sat})/2$. This was used to read the thermodynamic properties of water vapor. T_w is the surface temperature, read from the diagrams. Then the critical heat flux (CHF) at point D and minimum heat flux (MHF) at point E are determined by applying Equations (2.56) and (2.57), and the results are tabulated in Table 5.1.

Table 5.1: Maximum and minimum heat flux (kW/m^2) of boiling regime at low (LP) and high gas pressure (HP)

Temperature Curve	$\dot{q}''_{max\ (LP)}$	$\dot{q}''_{max\ (HP)}$	$\dot{q}''_{min\ (LP)}$	$\dot{q}''_{min\ (HP)}$
T_{11}	1665	2030	400	400
T_{12}	1280	2160	210	430
T_{21}	1155	2690	185	330
T_{22}	1085	1245	115	425

Looking closer to the figures, it shows that the average CHF at high gas pressure for plate 1 and 2 has increased by 40 % and 75 %, respectively, compared to the test at low gas pressure. Whilst, average MHF has increased by 35 % and 150 %, respectively.

The interesting factor is that the increase for CHF and MHF on plate 2 is substantially higher than that of the plate 1. This is indeed due to higher increase of temperature of surface 2 as described earlier.

Heat Transfer to Steel Plates: Based on the temperature gradient of the surfaces throughout the fire test, the rate of heat transfer to the plates may be calculated using the following expression given by

$$\dot{q}'' = (\rho C_p L)\,\frac{dT}{dt} \tag{5.2}$$

where ρ, C_p, and L are the density, specific heat capacity, and thickness of the plate, respectively, while $\frac{dT}{dt}$ is the change in temperature of the plate as a function of time [77].

Applying the above equation, the average rate of heat transfer to the plates at low and high gas pressure is provided in Figure 5.21 and 5.22, respectively.

As one may easier observe during early phase of the fire, the amount of heat transfered to the plate 1 (either at low or high gas pressure) is significantly higher than that of the plate 2, almost with a factor of 2.5. It is quite

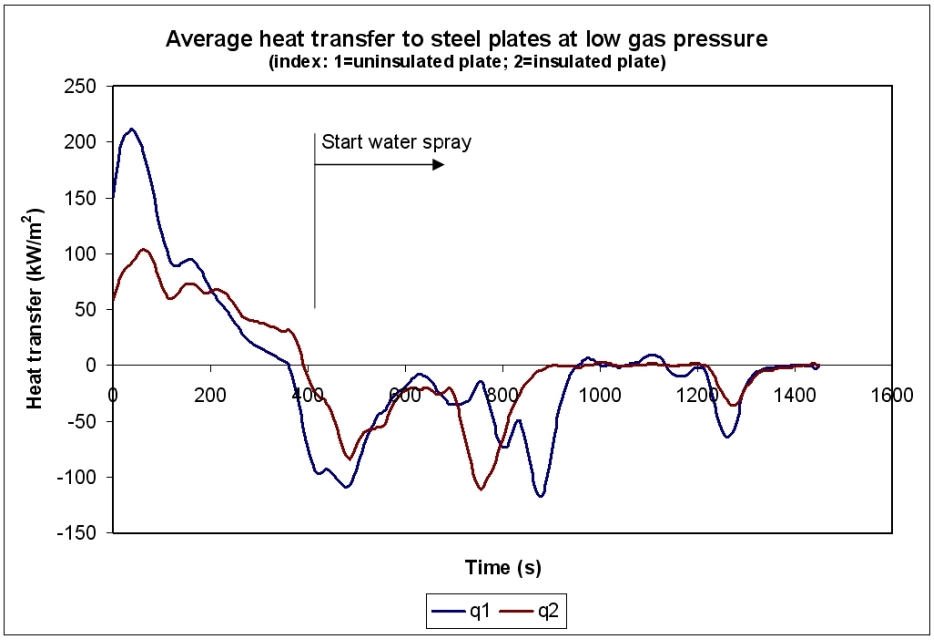

Figure 5.21: Rate of heat transfer to steel plates at low gas pressure

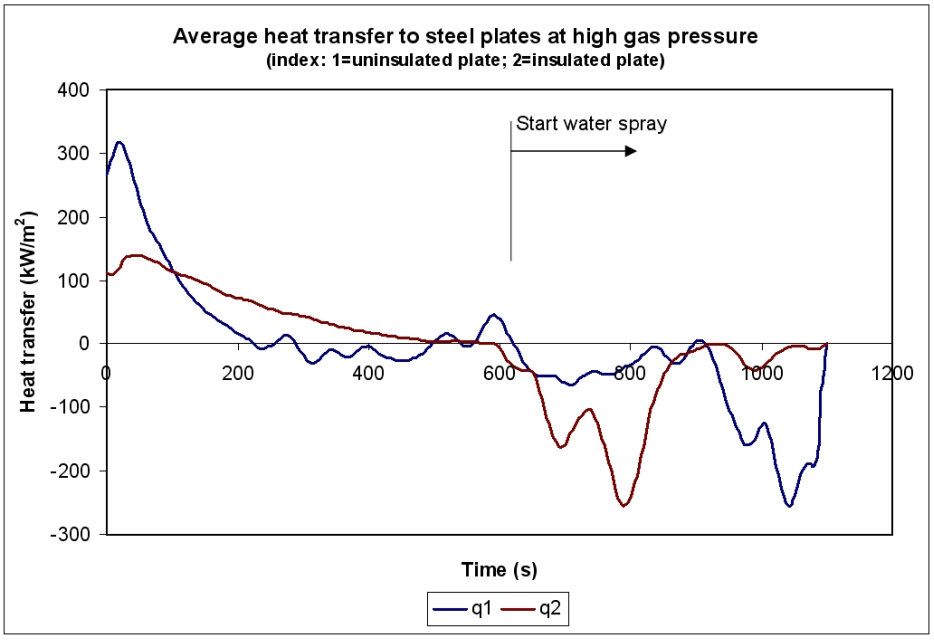

Figure 5.22: Rate of heat transfer to steel plates at high gas pressure

obvious that this is merely due to the fact that the uninsulated plate 1 is

subject to thermal stresses on both sides, i.e. the front and the rear side. Another fact is that when the gas pressure is raised from 5 to 10 barg, the rate of heat transfer has increased too, approximately by a factor of 2 as it can be seen from Figure 5.21 and 5.22.

As one moves toward right side of the diagrams the rate of heat transfer is reduced. This is indeed due to reduction in temperature difference (ΔT), since the difference from one time step to the next becomes smaller, although the heat load and consequently the temperature level is still high. Later on, the curves move into negative region, which indicate that heat is being removed due to water cooling.

Spray Nozzles Located Inside Flame

Also two types of experiment were performed in this category using two different types of nozzle, i.e. conventional nozzles with 30° and 65° spray angle. The gas pressure was kept constant at 10.5 barg throughout both experiments. Contrary to previous tests, the water mass flux varied and the values are given per nozzle corresponding to an impaction area of 0.09 m^2. All data were recorded with 2 seconds interval.

The distance between the nozzles and the plates were 40 cm and 80 cm for nozzle with 65° and 30° spray angle, respectively. These figures were chosen based om theoretical calculation and experimental test to ensure that the spray pattern could fully cover the plates with deluge water, even at the lower flow rates.

The first experiment carried out employed 65° spray angle nozzle in an environment with air temperature 8 °C and an average wind speed of 2.5 m/s at a direction about 330°. The water mass flux during the experiment varied between 1–4.4 kg/m^2s per nozzle. The results are shown in Figure 5.23.

The second experiment using nozzle with 30° spray angle was conducted with an ambient air temperature of 7 °C and an average wind speed equal to 2.5 m/s at a direction about 330°. The water mass flux in this case varied between 0.8–3.7 kg/m^2s per nozzle. The results are plotted as shown in Figure 5.24.

The experiments in this category were conducted as described earlier, i.e. as soon as the jet flame was established the water deluge was also activated with its maximum flow rate at 10 barg. Then the flow was gradually decreased by 1 barg at each step to the lowest flow at 0.5 barg. In case of 30° spray angle nozzle the lowest flow was set to 1 barg, because at lower rate the droplets did not reach the surface. The pressure increment was set to 0.5 barg for the three and the two lowest flow rates for 65° and 30° nozzle, respectively. The basis before proceeding to the next flow rate was attainment

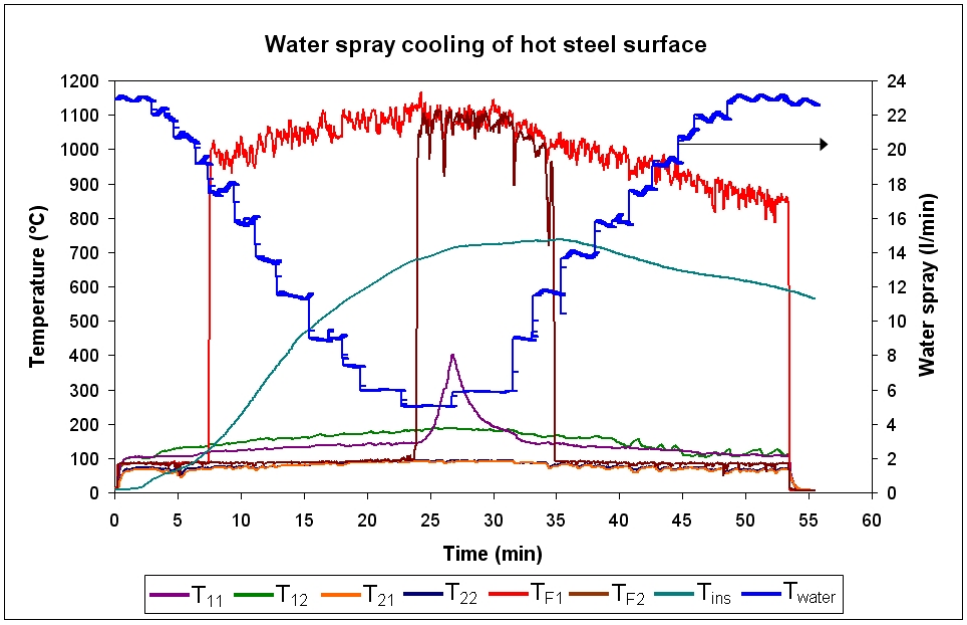

Figure 5.23: Cooling of hot steel surface with deluge using nozzle with 65° spray angle

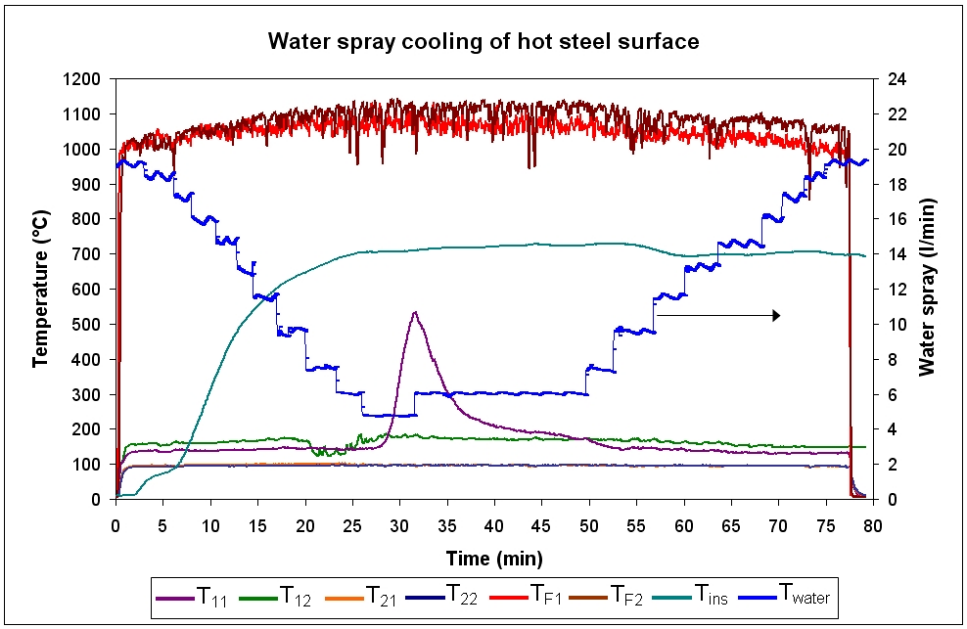

Figure 5.24: Cooling of hot steel surface with deluge using nozzle with 30° spray angle

of steady state temperature of the surface for several minutes, except at the lowest flow rate. The lowest flow rates are about 5.4 l/min and 4.3 l/min according to Figure 5.23 and 5.24, respectively. These values are simply read from the corresponding curve for water and using the axis on the right side of the diagram as the arrow shows.

At the lowest flow rate hot spots, indeed dry patches, were provoked by waiting long enough to let the surface temperature to increase exponentially before increasing the flow rate back to the next lowest value. The later turned out to be at a flow rate of about 6 l/min for both nozzle types, which is the minimum flow required to keep the surface temperature within nucleate boiling regime. The generated droplet size (SMD=Sauter Mean Diameter) at this flow is about 600 μm and 700 μm for 65° and 30° spray angle nozzle, respectively. Although it seems the surface temperature comes under control at the flow rate mentioned, the situation could be more challenging if the number of thermocouples were increased to take record of temperature development at every corner. A closer visual inspection during the tests revealed that in order to avoid the dry patches completely, the flow rate indeed had to be increased approximately to 13.9 l/min equivalent to 2.6 kg/m^{2}s in case of 65° nozzle, and 14.6 l/min equivalent to 2.7 kg/m^{2}s in case of 30° nozzle. These correspond to a droplet size (SMD) of around 450 μm for both cases. Alternative to overcome the problem of surface coverage is to increase the number of nozzles per surface and reducing instead the flow rate per nozzle. Photo taken after the experiment with 65° nozzle provided in Figure 5.25 illustrates the areas impressed by dry patches on the left side of the surface 1 (the plate on the right side) and the right side of the surface 2 at lower flow rates, visualized as a "half-moon". An indication that not the entire surface is impinged upon by droplets, when the flow rate is too low.

Otherwise both types of experiment have some common features which shall be reviewed below:

- The surface temperatures of the plate 2, T_{21} and T_{22}, were approximately kept at evaporation temperature of water or in natural convection region throughout the experiment, most likely due to insulation on rear side. While those of the surface 1, T_{11} and T_{12}, were nearly at 150–190 °C and remained almost at nucleate boiling regime in the experiment, except T_{11} as described below. This might be partially also a coincidence effect of wind direction pushing the flame tip slightly toward surface 1. This is also evident where T_{12} is almost higher than T_{11} during the experiment (T_{12} is situated on the right side of T_{11}). Additional evidence might be the nozzle 1 deposited with soot as shown in Figure 5.25, indicating that the nozzle 1 has spent most of the time in

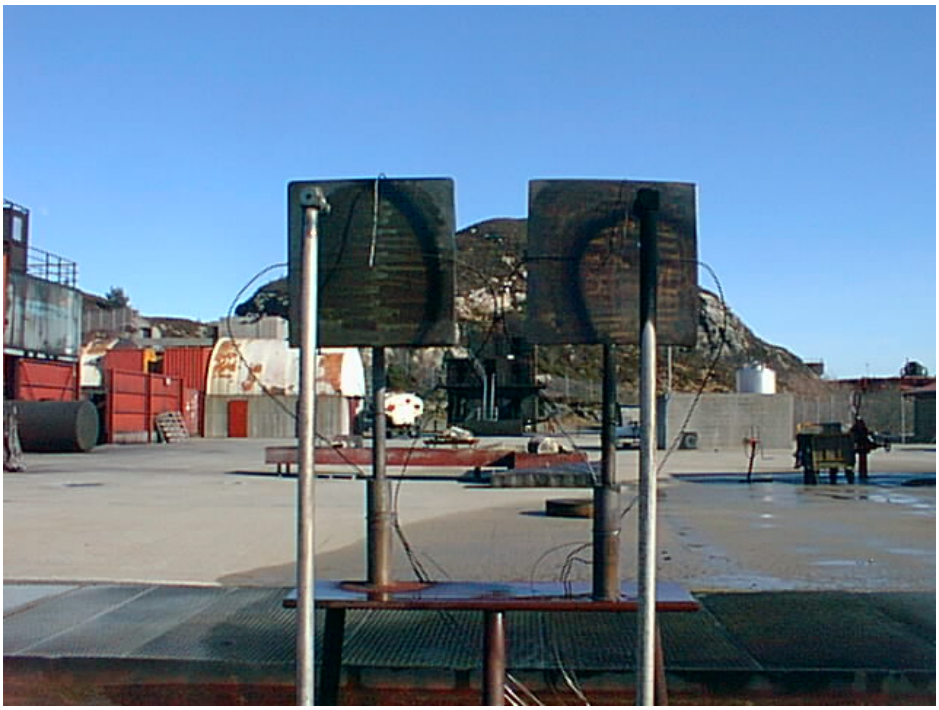

Figure 5.25: Areas showing sign of dry patches on both surfaces, photo taken after experiment

the flame than nozzle 2 does.

- When the dry patch arises, only T_{11} elevates. The only period the droplets undergo film boiling if they have impacted the area. As earlier illustrated by images in Figure 4.26, deluge at the lowest pressure could hardly cover the entire surface with sufficient liquid. As discussed above, the increase in T_{11} rather than T_{12} might be justified by wind effect which disturbs the droplets to reach that area.

- As Figure 5.23 and 5.24 indicate, a minimum flow rate of 6 l/min equivalent to a mass flux of 1.1 kg/m^{2}s is required to keep the surface temperatures under 200 °C. But as mentioned, the reality could be quite different if the entire surface would have been free for dry patches. In that event, the water mass flux should be raised to 2.6 kg/m^{2}s and 2.7 kg/m^{2}s for 65° and 30° spray angle nozzle, respectively.

- The longer duration of dry patch is, the longer it would take to depress the temperature, a phenomenon also experienced in connection with nozzles outside the flame.

- The insulation material and its supporting box seem to keep the temperatures of the surface 2 well around evaporating temperature. While non-insulated surface 1 does not appear to benefit having the rear side exposed to eventually dripping water droplets contra heat transfer from rear side.

- The insulation temperature seems to hold constant throughout the experiment at about 700 °C.

- The flame temperatures seem to reach their maximum level, slightly above 1100 °C at the lowest flow rate of water deluge. A difficult issue is associated with T_{F2} belonging to surface 2. It behaves as if the corresponding thermocouple is in good touch with water droplets almost throughout the experiment, except during the period at lower flow rates.

It should be emphasized that as long as the jet flame was on, the deluge system had to be on too, in order to protect itself, i.e. nozzle and accompanying components. For instance, when the mass flow rates was at its lowest level, the deluge system was almost at a critical point. Consequently in such particular event the longer duration had to be avoided. On the other hand the long duration at this stage was not any further necessary, if the purpose would have been to let the surface temperature rises to its maximum. Because this type of the test has already been examined with previous setup, i.e. deluge outside the flame, and it was proved that the surface temperature could be depressed.

Heat Transfer to Steel Plates: Average rate of heat transfer to the plates when spray is located within the flame region may be calculated in the same manner as described in the previous case, i.e. using Equation (5.2). The results with 65° and 30° spray angle nozzles are given in Figure 5.26 and 5.27, respectively. Both figures are based on the temperature history shown in Figure 5.23 and 5.24.

The figures illustrate large deflections at the start and at the end due to start and stop of the fire while the deluge was on, resulting in extremely high rate of heat transfer for a very short period due to very large gradient or steep slope. Additional event to notice is the sharp slope of the curve 1 ($\dot{q}''_1$) at the middle part of the diagram. This period refers to when the mass flow rate of the spray water is minimized and provoking dry patches, causing the heat transfer rate to raise exponentially (upper portion of the curve above x-axis). Then the mass flow rate of the liquid is increased again, resulting in heat removal represented by a sharp drop on the curve (lower portion of

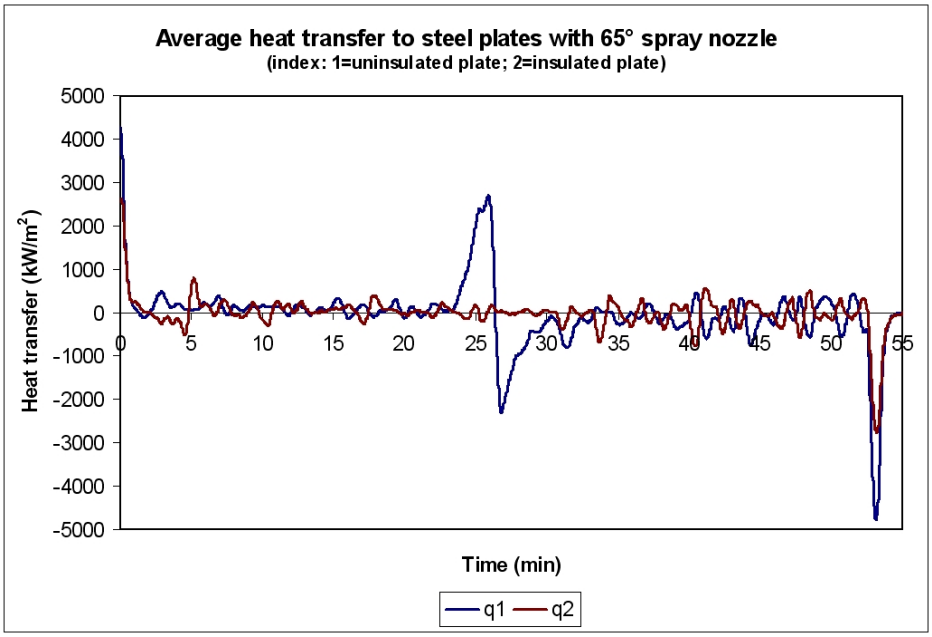

Figure 5.26: Rate of heat transfer to steel plates with 65° spray angle nozzle

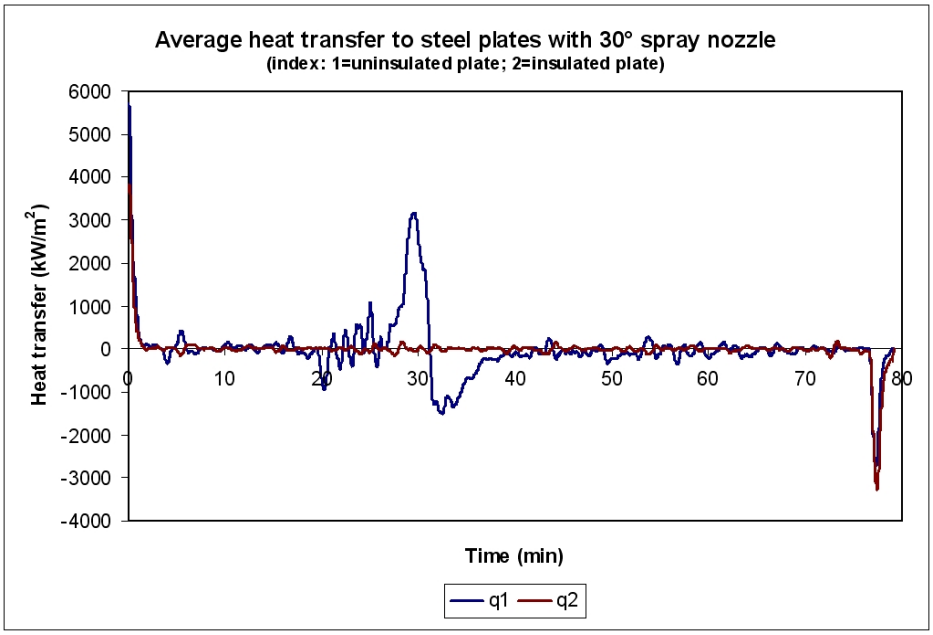

Figure 5.27: Rate of heat transfer to steel plates with 30° spray angle nozzle

the diagram below x-axis). Otherwise, the rate of heat transfer is quite low and almost constant, as long as the surface temperature is suppressed by impaction of droplets.

It should be noted that the diagrams shown in Figure 5.26 and 5.27 as well as those in the previous case shown by Figure 5.21 and 5.22 are based on a slope composed of several time steps rather than one, in order to make the curves more smooth for better interpretation. That is the reason the curves do not intersect the x-axis at zero.

5.5.1 Conclusion

Nozzles Located Outside Jet Flame

By doubling the gas pressure from 5 to 10 barg the effect escalates rapidly. It takes only half the time the surface temperature to reach the highest level. A situation may be considered as critical when objects exposed to high pressure gas fires, and demands quick handling. Although the temperature profile in deluge period for these two cases may be not directly comparable due to uneven deluge spreading in case 2, nevertheless it is not unreasonable to assume that the profile could undergo similar course just as well in case 1, if the nozzles were in good condition.

It takes almost as long time as in the preheating period to suppress the surface temperature by liquid droplets to reach the break point at minimum heat flux (Leidenfrost point E on boiling curve of water), before approaching the evaporation temperature level. The higher surface temperature does, however, takes longer time to cool down the surface and reach the break point. Even with deluge delayed, the very highly elevated temperature of the surface could be pressed down.

When the deluge is activated, the peak temperature as well as the radiation level of the flame is reduced. The later would have a reduction effect on surrounding, so that the nearby objects which are not directly exposed would have benefit of that. The radiation level on surrounding increases by a factor from 1.5 to 2, when the gas pressure is doubled.

By locating the deluge nozzle outside the flame at a higher elevation than the surface's center point, seems to have the advantage of letting the droplets also to reach on rear side of the surface. It has also advantage of flexibility to regulate the nozzle position in axial and radial direction as well as regulating the elevation, while experiment is in progress. The disadvantage is the high momentum required to transport the droplets over longer distance to reach the surface. This makes the system less flexible to reduce the mass flow rate, hence leading to high water consumption. A factor which probably has to

be considered in industrial scale regarding damages the excess water might cause.

The rate of heat transfer to uninsulated plate is almost 2.5 times higher than that of the insulated plate, since the plates are subject to fire both on the front and the rear side. By raising the pressure of emerging gas by a factor of 2 (from 5 to 10 barg), the rate of heat transfer is almost doubled.

Nozzles Located Inside Jet Flame

When nozzles are situated within flame zone, it is necessary to activate the deluge as soon as the jet flame is established. The aim is to protect the deluge system. In return, as the diagrams in the Figures 5.23 and 5.24 showed, with having sufficient mass flux, the surface temperature is under control throughout the experiment. The spray system is also flexible to regulate.

The surface temperature could be kept under 200 °C applying a water mass flux of 1.1 kg/m^{2}s for the given case, without experiencing critical situation. However, if the intention is to eliminate dry patches anywhere on the hot surface, and avoid break-even point in an eventually larger scale, e.g. a vessel with fluid content, the flow rate must be increased to 2.6 kg/m^{2}s and 2.7 kg/m^{2}s for 65° and 30° spray angle nozzle, respectively. In an actual event of fire, it means this would give sufficient time to take other measures such as to shut-off the supply, etc. to avoid accident.

The insulation material seemingly helps the exposed surface to keep its temperature under that of uninsulated surface by about 100 °C.

Active fire protection (deluge) would have bigger chance than passive fire protection (insulation) to avoid an accident, hence rescue life and material. Combining these two, magnifies the possibilities to hinder serious accidents.

The main conclusion for both categories, i.e. nozzle located outside and inside flame, would be that even long after the highest surface temperature is attained, yet the temperature could be brought down by adequate deluge, and hot spot can be eliminated if the entire exposed area is covered with water droplets. This pertains only if the object, let say a vessel, is empty. However, should the vessel contain, e.g. hydrocarbon, the situation would be different. In such circumstances not only the external surface is of concern, likewise the content of the vessel is an impending danger, due to pressure build-up when the fluid is heated through the vessel's wall. The pressure build-up from inside and material weakening from outside (yield point) escalates exponentially the danger of material rapture.

Although the rate of heat transfer at the start and the end seems to be quite high due to high temperature gradient, nevertheless it is reduced considerably and kept at low and almost constant level throughout the test

as long as the cooling process continued.

Chapter 6

Analysis of CFD Modeling Results

6.1 Introduction

The CFD software KFX was employed for modeling of experimental work on characterization of jet flame, quadratic steel channel, and steel plates. No CFD calculation is carried out on benchmark steel plate. In the succeeding sections an overview of the program would be given and the results of CFD simulation shall be presented. The achieved CFD results shall be compared and analyzed to those obtained in experimental work in the next chapter.

Some of the most essential mathematical structure of KFX is based on the theories covered by Section 2.2 Turbulent Combustion.

6.2 Brief Description of CFD-Code KFX

KFX is a three-dimensional gas dispersion and field model fire simulator developed at Norwegian University of Science and Technology (NTNU) and SINTEF Energy, Department of Applied Thermodynamics and Fluid Dynamics in Trondheim, Norway.

KFX is capable of calculating heavy and light gas dispersion and hydrocarbon fires in connection with practical fire safety studies. It can handle liquid pool fires as well as gas jet and fires, in enclosures and in open air. It has been tested against experimental data ranging from small-scale laboratory flames to large-scale jet and pool fires. It also includes a water spray model that can be used for analysis of fire mitigation and extinction, and is suitable for simulation of various kind of water sprinkler and deluge systems.

The code can in general be used for almost any safety related analysis

related to gas dispersion and fire. It has in recent years been widely used nationally as well as internationally, among others in offshore industry.

The software has recently been among seven other fire models in an international joint industry project on Blast and Fire Engineering for Topside Structure to provide information on the characterization and mitigation of hydrocarbon fires and explosions.

The purpose was to provide data for the development and validation of models for predicting loads generated by fires and explosions on offshore platforms. The predictions from each model were compared with the experimental results for radiation and flame geometry for unconfined jet fires tests; gas velocities, gas temperature, steel temperature, radiative, and total heat fluxes for confined jet and pool fire tests. The predictions of most parameters were in the range of $0.5 \leq$(Predicted over Observed)≤ 2.0 [120].

The Pre-Processor: The software is equipped with a front-end with graphical user interface (GUI). The pre-processor is called Lizard. By using Lizard, user can define geometry and inspect it both in two and three-dimensional pictures, put up boundary conditions as well as running parameters like time step control and equation solvers. The post-processor provides color graphics of any cross section and any variable in the calculation domain.

The recent version released in 2004 includes two major features. CAD import of complex geometries which eases the work with respect to do the geometry modeling faster and more precise. The other feature is a new model for calculating jet characteristics, e.g. release diameter, gas velocity, temperature, etc., which gives more realistic image of the jet fires concerning the flame geometry.

KFX includes a number of sub-models as shortly described below [121].

The Numerical Models: KFX uses a Cartesian finite volume technique to solve the averaged basic transport equations from fluid dynamics. It uses a seven-node formulation for the discretized equations for three-dimensional cases. The transient behavior is modeled with the backward Euler scheme. Equations for the following Favre averaged physical quantities are solved:

- The three Cartesian velocity components
- Enthalpy
- Species mass fractions
- Soot mass fraction.

The $k-\epsilon$ Turbulence Model: The model predicts the turbulent dispersion of momentum and scalars through predicting the length and time scales, where k is the averaged kinetic energy of the turbulent fluctuations and ϵ is the dissipation rate of k. A turbulence fluctuation is the instantaneous velocity component minus an averaged value of the velocity component.

The Energy and Species Model: The model controls the mass and energy conservation during the computation by solving simultaneously the enthalpy and species mass fraction. By this approach it controls the source terms of the equations to fulfill elemental conservation even if the source terms are not fully explicit formulated.

The Eddy Dissipation Concept of Turbulent Combustion: It hand-les premixed as well as diffusion flames, and reflects the physical nature of turbulent combustion.

The EDC divides the lump of mass into two zones, the burning fine structure reactors and their surroundings. The mass fraction of the fine structures are formulated as a function of k and ϵ, based on analysis of the cascade process of the energy transfer from the large scaled turbulent structures to the fine structures. The fraction of fine structures burning is modeled as a function of fuel and oxidizer already burned. Given the mass fraction of burning fine structures, the density weighted average of an arbitrary specific variable may be formulated from its specific value in the burning fine structures and their surroundings weighted by the mass fraction of the two zones correspondingly. When the reactor conditions are determined the averaged reaction rates are easily deduced for use in the averaged transport equation of each species.

The Eddy Dissipation Soot Model: This is divided into a soot formation model and the soot combustion model. The soot and nucleus combustion is modeled according to the EDC assuming infinite fast combustion with the reaction rates of soot and nucleus proportional to the reaction rate of fuel.

The Discrete Transfer Model for Radiation: The model solves the radiation by an enhanced version of the Discrete Transfer Model. It is based on rays sent from an internal box just enclosing the flame, instead of sending them from the boundaries of the calculation domain. All the rays are still traced to the boundaries of the calculation domain to calculate the heat flux from the flame also in the regions outside this box. This causes a much bigger portion of the rays to be traced through the flame. Consequently, a smaller portion of the rays is traced through cold air only and the calculation effort is reduced.

Lagrangian Two-Phase Spray Model: A model for handling of water systems for fire suppression. The release of water sprays may be positioned freely in the computational domain and trigged by simulated temperature sensors.

6.3 Modeling of Jet Flame

Prior to the experimental work, a number of CFD-simulations were carried out using KFX in order to point out the proper positions of instrumentation, i.e thermocouples and heat flux meters. After the experimental part of the work was completed, similar scenarios were modeled in KFX and simulated. The gas velocity profile along the flame path was simulated but not measured experimentally.

The calculation domain size was 13 $m \times 7\ m \times 9\ m$ (L × W × H) with a grid resolution $63 \times 55 \times 60$ equivalent to 207 900 grid nodes. The volume consisted of a floor boundary with isothermal solid cells mostly covered with solid isothermal core as domain cells. These cells formed a pool which was located below the jet flame area. The walls and roof were defined as wind boundary cells. The nozzle was placed 2.0 m above the floor at the point (x, y, z) = (0, 0, 0) with jet release in positive x-direction. The mesh resolution was distributed fairly fine around the nozzle, with the smallest cell at release point and gradually increasing in axial and radial direction. The view is provided in Figure 6.1. Figure 6.1b reflects the concept used for measuring the heat flux in the experiments.

Although the ambient condition in the experiments was almost still with a wind speed in the rang 0.5–1.5 m/s, but its direction varied quite often. This made it too complicated to implement in KFX. It was then decided to model with neutral ambient condition, i.e. to let the wind speed to be zero. The transient time step was set to 10 μs which gave best numerical stability and prediction. The criterion for convergence was based on carbon and hydrogen balance in calculation domain. To verify this, the difference between the carbon and/or hydrogen entering and leaving the calculation domain should not exceed approximately 3 % according to ComputIT [122]. For this study the values were under 0.3 %.

The calculated parameters were temperature, radiative heat flux, and gas velocity. The location of temperature and heat flux measurement followed exactly that of the experiment. While the velocity of the gas was calculated at 65 different positions along the flame path according to the illustration shown in Figure 6.2. To locate the positions where the gas velocity had to be calculated, a simulation contour image as shown in Figure 6.2a was

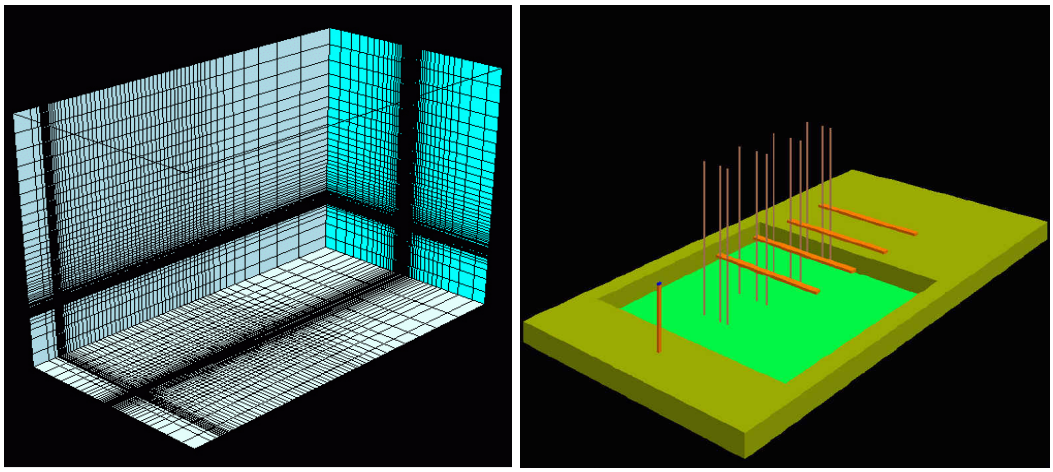

(a) **(b)**

Figure 6.1: Grid nodes (a) and setup for heat flux (b)

employed where the coordinates of a number of points along the flame axis (trajectory) were read using the grid system and support lines in PowerPoint and GhostView, and the results are reflected on the diagram in Figure 6.2b. Additional points were also selected near outer layer of the flame at different cross sections as can be seen marked by rectangles. Based on these locations a coordinate file was then build up, and fed into KFX as input file for simulation.

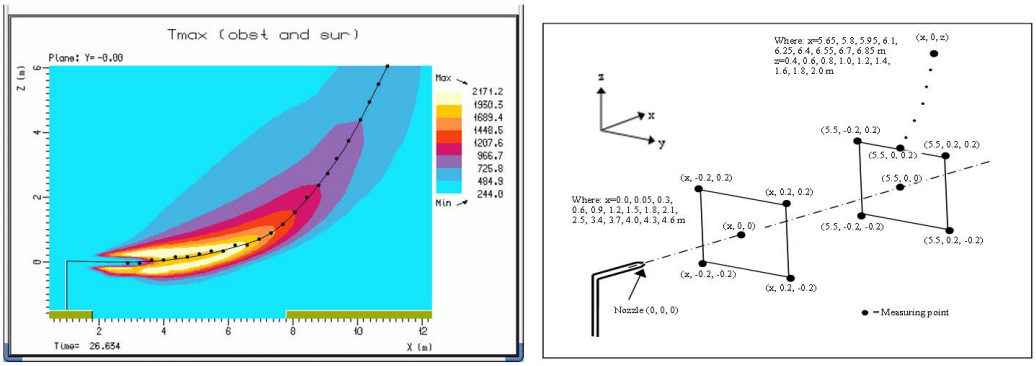

(a) **(b)**

Figure 6.2: Flame pattern (a) used to locate positions (b) for calculating gas velocities

As stated above the KFX's transport equations are based on mean values,

one would consequently experience that the flame shapes, plots of result, etc. are quite smooth compared to those of the experiments which are spotty. Images in Figure 6.3 compared to any experimental flame shown earlier may reflect this.

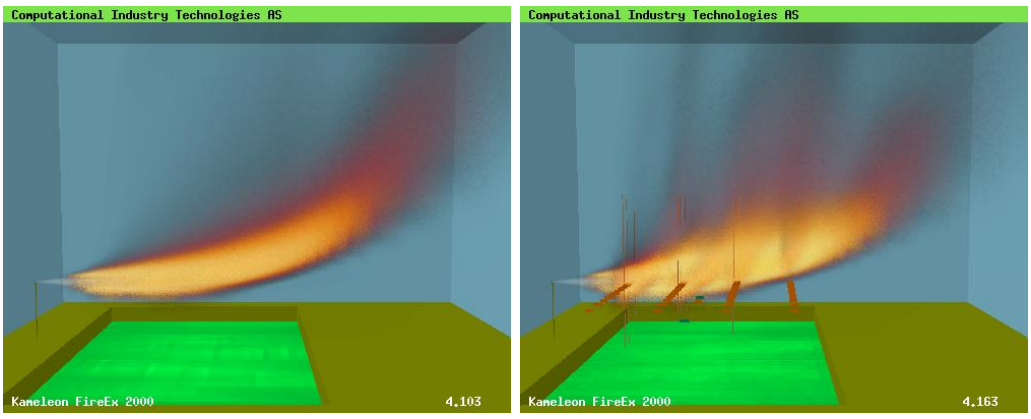

(a) **(b)**

Figure 6.3: Flame geometry from calculation of temperature (a) and heat flux (b)

The flame geometries shown in Figure 6.3 are indeed the ultimate result of numerous simulations conducted. Earlier geometries shown to be dominated by slightly more buoyancy forces on the end part of the flame, causing the flame to bend off and rise up earlier compared to the experimental flame. After a number of discussions with ComputIT [122], it was concluded that the second constant in $k-\epsilon$ equation of turbulence model, i.e. $C_{\epsilon 2}$ in Equation (2.9) covered by Section 2.2.2, has to be set to 1.81 rather than the default value 1.92. The argumentation was based on the fact that if the jet fires are not subject to crosswind and/or do not run across hindrances (obstacles, etc.), the suitable value for the constant $C_{\epsilon 2}$ is 1.81. This leads to increased momentum of the flame, hence reducing the impact of buoyancy forces and giving more realistic picture of the flame. With other word this assumption fits the flames which are axis symmetrical. This concerns in particular the flame geometry from temperature calculation.

The other constants in Equation (2.9) are taken as discussed in Section 2.2.2, i.e. $\sigma_\epsilon = 1.3$ and $C_{\epsilon 1} = 1.44$.

The result of calculation of temperature is provided in Figure 6.4.

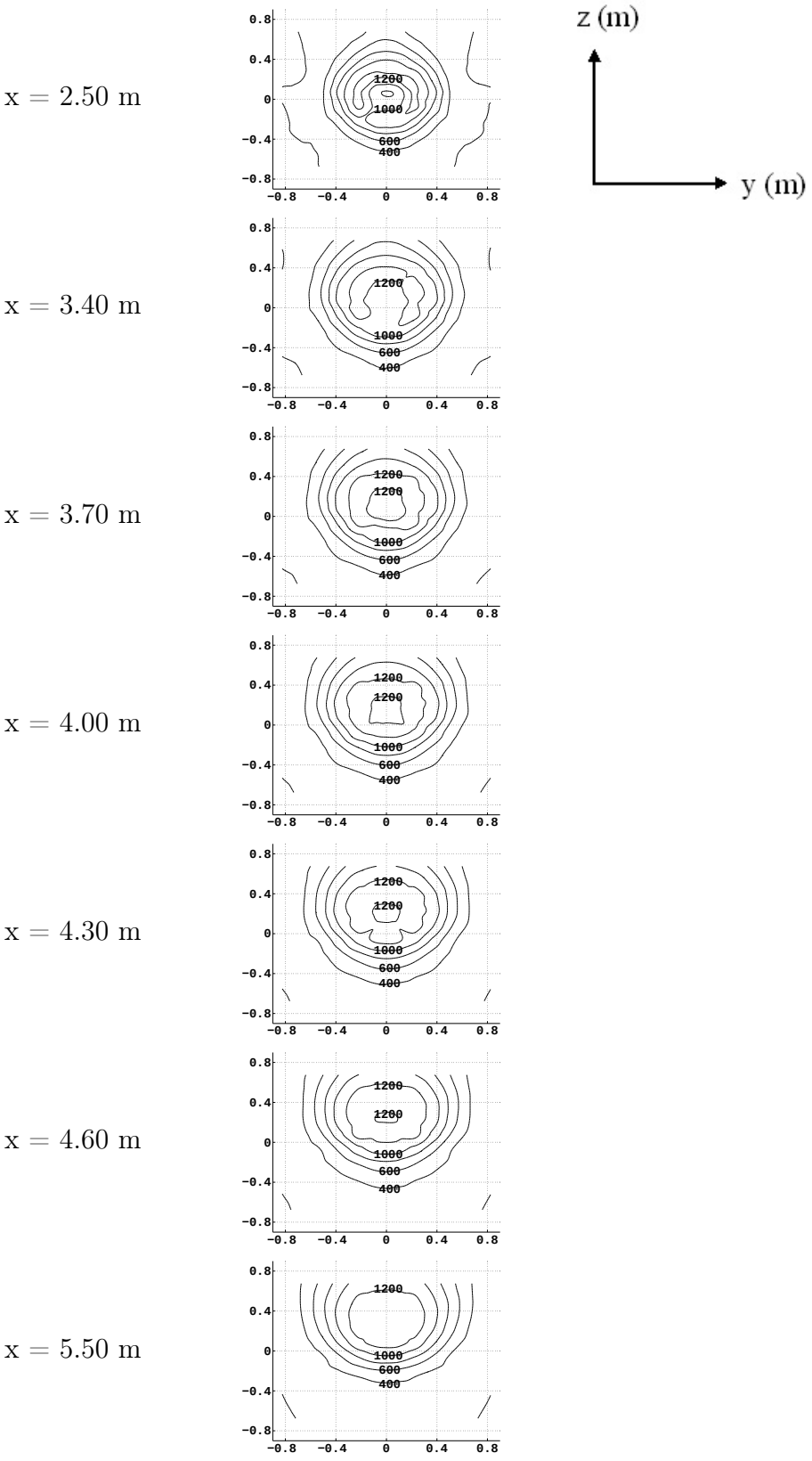

Figure 6.4: Temperature contour (°C) at various distances (x) from nozzle

The simulation results on radiation, both inside and outside the flame region, are shown in Figure 6.5.

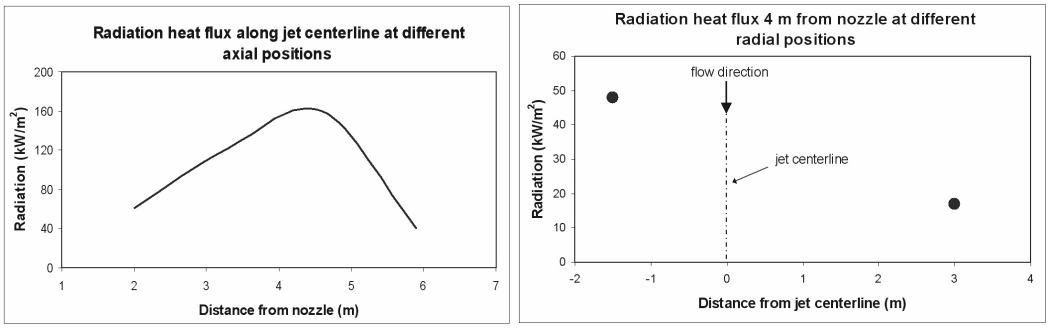

(a) Inside flame **(b)** Outside flame

Figure 6.5: Heat flux calculated within and off jet flame

While calculated gas velocity as a function of distance from the release point is highlighted in Figure 6.6.

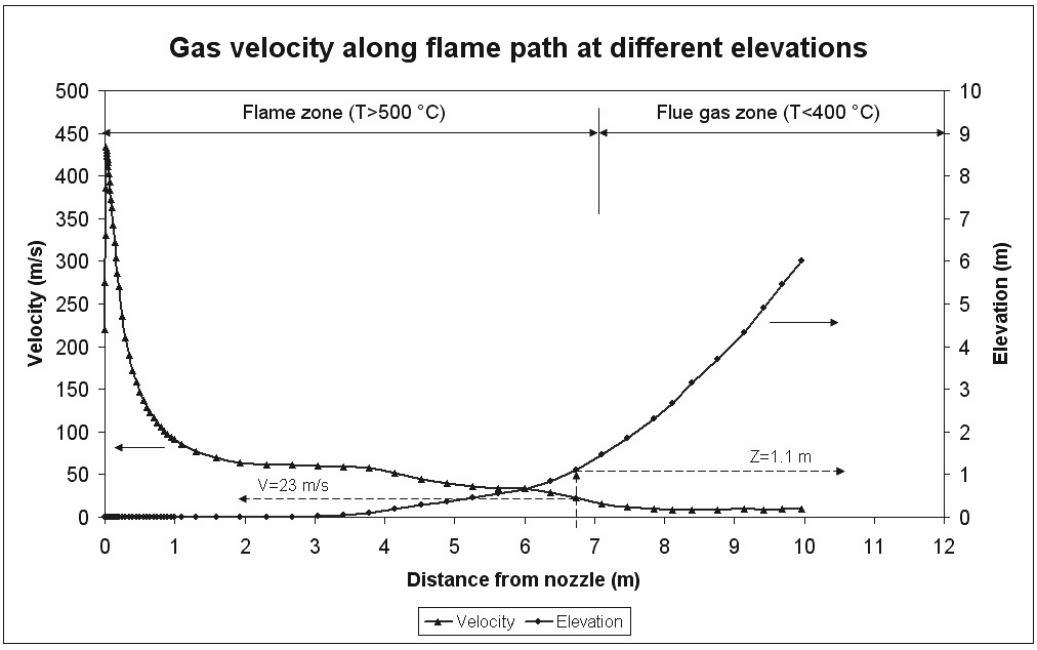

Figure 6.6: Calculated gas velocity along jet flame path

The reference for elevation is the jet centerline. To locate the velocity of the gas at a certain position, simply draw a vertical line from that point

to intersect both curves and read their values from the corresponding curve. For example, at 6.7 m from the nozzle the gas velocity is 23 m/s at 1.1 m above the jet centerline.

6.3.1 Conclusion

KFX solves the transport equations based on the mean values. This leads to flames, plots, etc. with smooth surface giving an impression that the combustion is quite calm rather than turbulent. One should bear in the mind that the wind impact was totally ignored in this study due to its uneven direction, hence it contributes to extra smoothness.

When the jet flames are symmetrical around their axes, i.e. do not come across obstacles, the proper value of the second constant ($C_{\epsilon 2}$) in the $k - \epsilon$ equation is 1.81.

For the given domain size, 207900 grid nodes showed to be a reasonably sufficient resolution. This choice combined with a transient time step of 10 μs gave good numerical stability, and one fulfilled the convergence criteria with extremely good margin, i.e. less than 0.3 %. An increase in resolution, which also has been tried, did not necessarily lead to improvement of results, but rather increases the CPU calculation costs.

Altogether, the CFD tool used showed to predict reasonably well the temperature and radiation values measured in the experiments, as well as the flame shape. Such verification might open up the marked for utilizing the CFD-codes instead of costly experimental investigation, and saving the oil industries with huge amount of expenses. Despite this fact, application of experimental work once in a while, even in smaller scale, should not be overlooked.

6.4 Modeling of Jet Fire Test with Steel Channel

After the experimental work was accomplished, the scenario was modeled in KFX and simulated. The geometry was simplified and only the exposed portion of the channel was modeled as shown in Figure 6.7. Also shown in figure is in-zoomed channel, meshing, and the exploded model of the geometry which demonstrates the position of different surfaces with their corresponding insulation as well as locations where temperature was calculated. These points are identified by figures 1-9.

The size of calculation domain was 8 $m \times 6$ $m \times 6$ m (L $\times$ W $\times$ H) with a total number of 22134 grid nodes. The ambient wind speed was modeled at

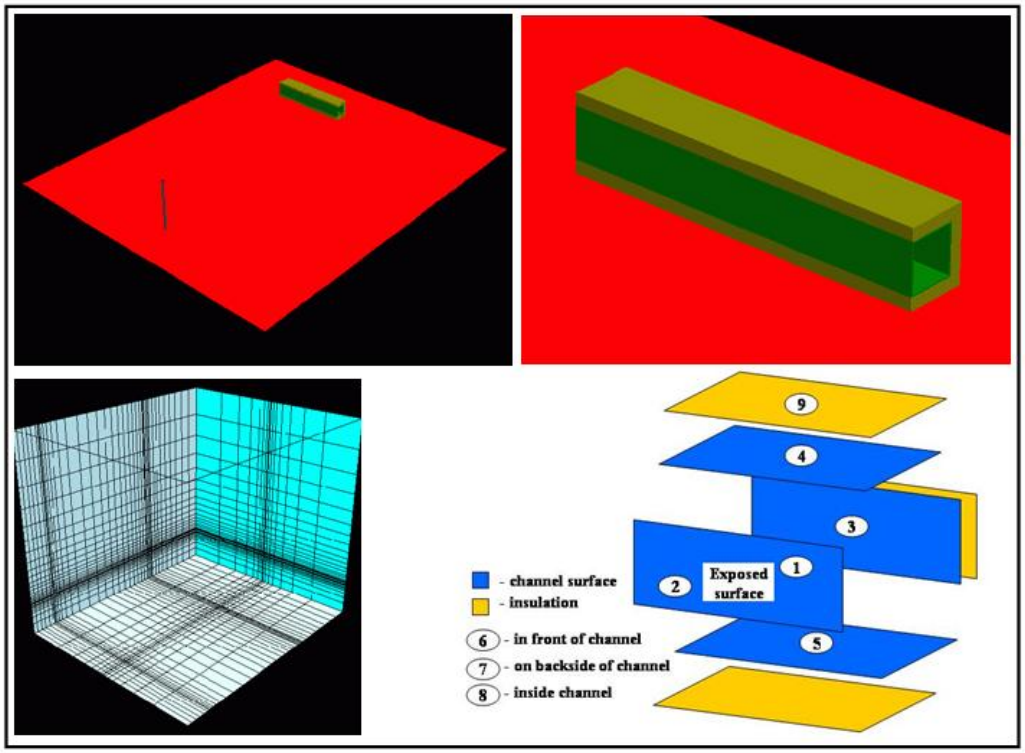

Figure 6.7: Modeling setup for channel

0.5 m/s in x-direction and -0.5 m/s in y-direction. The transient time step was set to 5 ms while solid time step order of 5 s was chosen for solving solid heat transfer equations. The results of predicted temperatures are provided in Figure 6.8.

The notations T_{flame}, $T_{flame\ (rear\ side)}$, T_{air}, and T_{ins} in Figure 6.8 refer to the locations 6, 7, 8, and 9 in Figure 6.7, respectively.

T_{air} refers to inside the channel, behind the exposed surface which corresponds somehow to the outlet air in the experiments. The air flow through the channel is guided by ambient condition. While, T_{ins} located on top of the channel is comparable in a manner to that of the experiments located in front side. $T_{flame\ (rear\ side)}$ which is used only in calculation was meant to investigate the situation on rear side of the channel. It was suspected that the flame would gradually establish itself in this region, causing warmer area due to less turbulence which the results confirm this. The corresponding surface temperature in this area, i.e. T_{S3}, shows also tendency to rise at the end as a function of increase in $T_{flame\ (rear\ side)}$.

The temperature of the exposed surface, denoted by T_{S1} and T_{S2}, shows

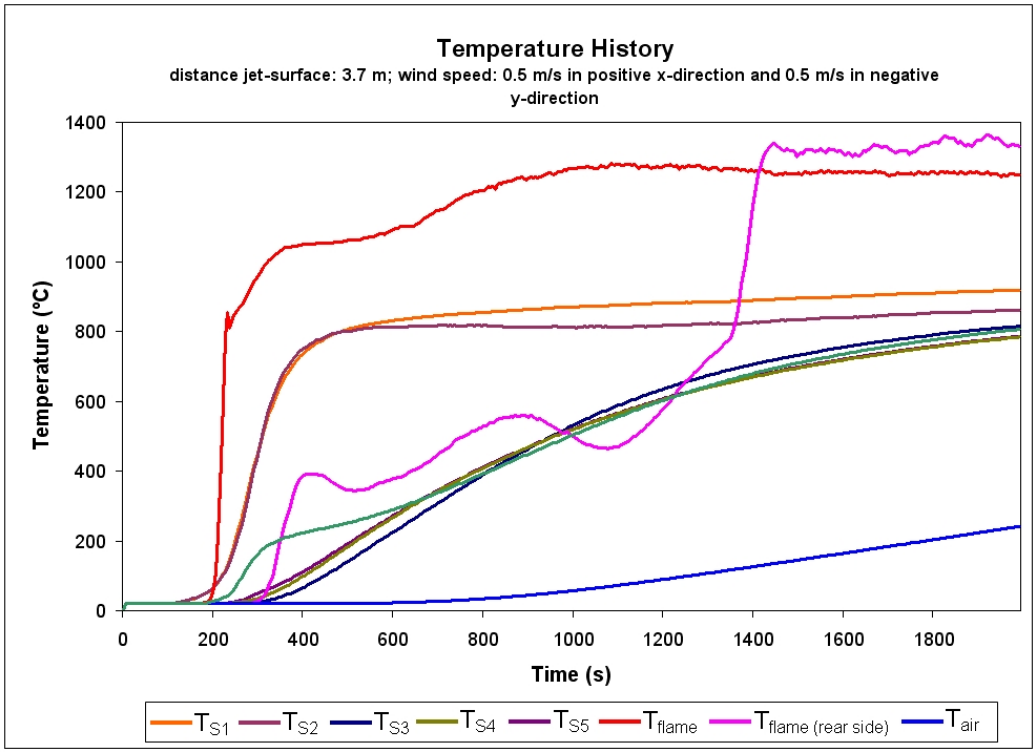

Figure 6.8: Calculated temperature history of channel surface, insulation, flame, and air

slightly lower value at location 2, about 70 °C. This is possibly due to buoyancy effects causing the flame to bend up. Location 2 which is located lower might therefore be most in touch with outer layer of the flame which normally has lower temperature.

A number of attempts were made and new simulations were conducted in order to model a case more similar to the geometry and conditions as in the experiments, as well as improving the resolution by increasing the number of grid nodes. The modification implied prolonging the length to include the whole channel and the air fan pushing the air through the channel. Three dimensional views of two of the cases with their corresponding flame images are shown in Figure 6.9. The upper and lower views refer to case number 4 and 7 in Table 6.1, respectively.

None of those cases gave satisfactory results as summarized in Table 6.1. KFX 2000 was employed to perform the calculations. Ambient temperature was set to 20 °C. Insulation temperature is calculated in middle of the material, while that of the steel is calculated on the surface. Figures in parenthesis refer to cell type used in KFX where 17=channel cell; -1=isothermal cell;

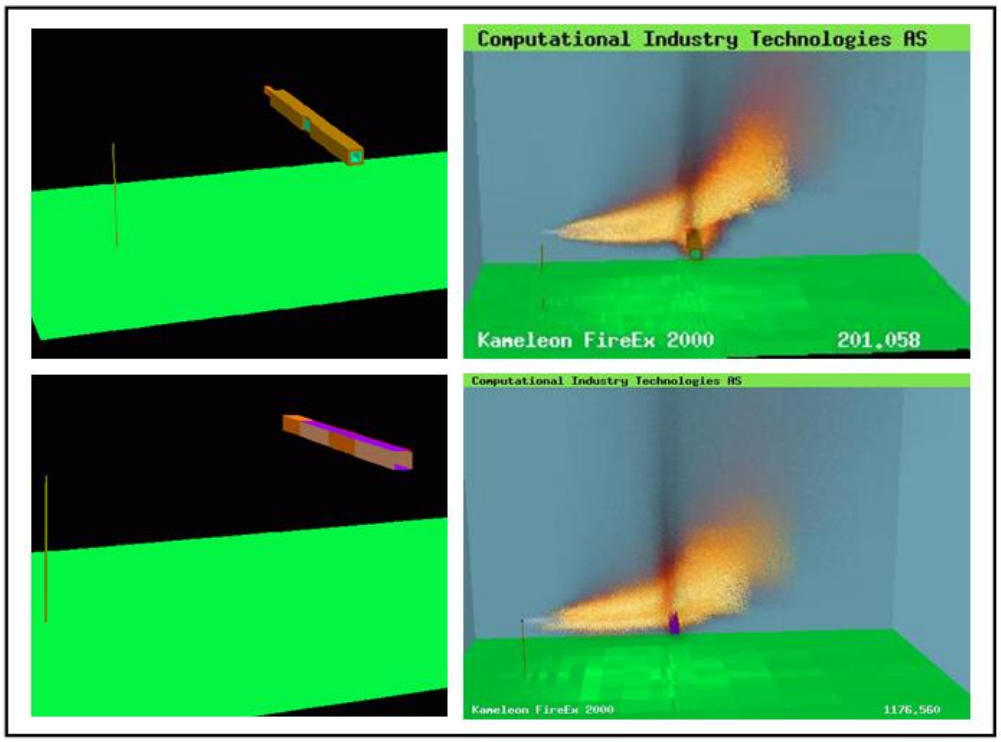

Figure 6.9: Alternative modeling of channel

1=solid solved temperature cell; 0=thin wall with free flow cell with porosity. The average temperatures are taken when calculation reached steady state and are slightly rounded off. The sign " ÷ " indicates the value is under-predicted, otherwise it is over-predicted. Despite the differences the flame temperature compared well, about 1300 °C.

Table 6.1: Summary of results of alternative modeling of channel compared to experiment

Case No.	Simulation Time (s)	No. of Grid Nodes	Property of Channel Surface		Applied Insulation	Average Temperature (°C)						Deviation Compared to Experiment (%)					
			Exposed Surface	Insulated Surface		Exposed Surface	Insulated Surface				Insulation	Exposed Surface	Insulated Surface				Insulation
							Front	Rear	Top	Bottom			Front	Rear	Top	Bottom	
1	530	43065	steel (17)	steel (17)	yes (-1)	850	0	0	0	0	-	~0	÷100	÷100	÷100	÷100	-
2	660	66000	steel (17)	steel (17)	yes (1)	900	0	0	0	0	570	8	÷100	÷100	÷100	÷100	÷43
3[1)]	260	66000	steel (17)	steel (17)	yes (1)	730	0	0	0	0	130	÷12	÷100	÷100	÷100	÷100	÷87
4	220	66000	steel (1)	steel (1)	yes (1)	220	20	20	20	20	700	÷73	÷96	÷96	÷97	÷95	÷30
5	8[2)]	72600	steel (17)	steel (17)	yes (1)	910	0	0	0	0	680	10	÷100	÷100	÷100	÷100	÷32
6	60	72600	steel (0)	steel (0)[3)]	no	130	850	730	1130	1030	NA	÷84	42	46	126	170	-
7	25[4)]	66000	steel (17)	steel (17)[5)]	no	20	-	830	980	830	NA	÷97	-	66	96	118	-
8	1170	15288	steel (0)	steel (0)[6)]	no	160	450	1130	1030	960	NA	÷80	÷25	126	106	150	-
9	90	8721	steel (0)	steel (0)[7)]	no	780	1030	780	780	1030	NA	÷6	72	56	56	170	-
Experiment	-	-	steel	steel	yes	830	600	500	500	380	1000	-	-	-	-	-	-

[1)] Difference between case 2 & 3 is wall thickness of insulation material in Domain Records, which is set to 0 and 0.025 m, respectively.
[2)] Case 5 is similar to case 2, but in addition a value was given to solid time step. The calculation terminated after about 8 s, since the early indication showed that the surface temperature at insulated areas showing the same tendency as for case 2 & 3, i.e. zero.
[3)] Surface with conductivity equal to that of insulation material, while density and specific heat capacity followed that of steel.
[4)] Simulation terminated after 25 s, since early indication showed no temperature progress on the exposed surface.
[5)] Surface with thermal properties equal to that of insulation material (conductivity, specific heat capacity, and density).
[6)] Surface with thermal properties equal to that of average of steel and insulation material.
[7)] Surface with thermal properties equal to that of insulation material.

After aforesaid trial and errors a last attempt was made to reproduce the case described above which was originally simulated using the previous version of KFX. The simulation crashed after about 100 iterations. It should be emphasized that the simulation described in previous section concerning characterization of the jet flame employed both versions of KFX too. Anyhow, no differences were experienced during that part of the work.

6.4.1 Conclusion

The simplified model, which also was the only case that went through, gave fairly good results. However, the influence of buoyancy effects were more visible in this part of the study, as one could observe the phenomenon better at impaction point. However, as a compensation to engulf the object, the channel in later cases was slightly lifted up to a higher elevation compared to release point of the jet .

Despite modeling the channel in a number of ways, due to an unknown reason or reasons none of them predicted the temperatures correctly. In some cases no value was recorded and showing zero. Due to limited time, it was not possible to investigate further to find out the answer.

6.5 Modeling of Jet Fire Test with Steel Plates

After completion of the experiments the spray system and the test geometry consisting of both plates were modeled, where one of the them was insulated on the rear side with 5 mm thick insulation material as in the experiments. The simulation was carried out only with the spray system located outside the flame. Because this alternative was considered as the most severe case where the objects are primarily exposed to jet fire, reaching steady state surface temperature before the spray is activated. The deluge concept followed the experimental setup, i.e. one spray nozzle for each plate and aligned with the jet nozzle, one on each side of the jet and 1 m above the surface level.

The calculation domain with a size of 12 $m \times 4\ m \times 12\ m$ (L $\times$ W $\times$ H) had a resolution equivalent to 44485 grid nodes. The ambient condition was modeled as neutral. The transient time step was set to 5 ms with a solid time step of 5 s to solve the solid heat transfer equations. The droplet diameter was set to 1 mm with an initial release velocity equal to 4.5 m/s and a mass flow rate of 0.4 kg/s for each spray nozzle.

The result of calculations for high gas pressure is given in Figure 6.10. Temperatures T_{11} & T_{12} refer to plate 1, while T_{21} & T_{22} refer to plate 2. T_{ins} represents the temperature of the insulation material.

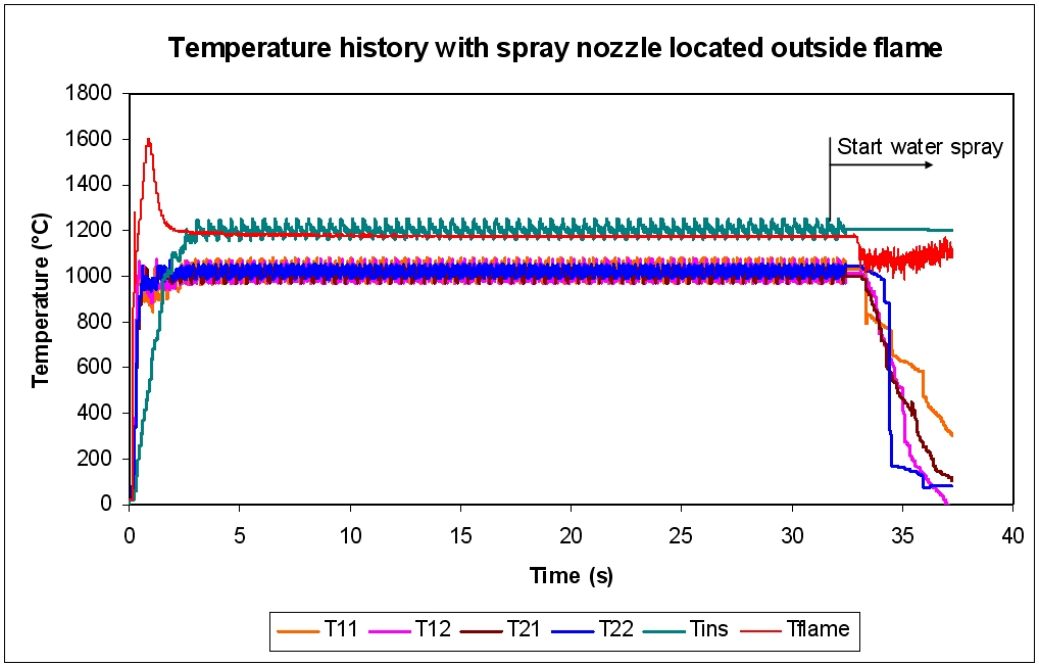

Figure 6.10: Calculated temperature history of steel plates at high gas pressure

As it can be seen from the figure the surfaces are first exposed to fire, reaching the highest possible temperature before activation of the deluge. As soon the cooling stage begins, the temperatures fall rapidly. Roughly said, the the film boiling regime ends at about 400 °C before entering the transition region. It seems the insulation on rear side of the plate did not respond as expected an insulation material suppose to do. No effect on the surface temperature of the plate 2 (T_{21} & T_{22}) has been recorded compared to uninsulated surface, neither before nor after the cooling. This is also evident of the insulation temperature, which indicates it is as hot as the flame.

The two views in Figure 6.11 show the surface temperature of the exposed solids before deluge is activated (left) and during the cooling period (right). The lower images are the two exposed surfaces of the plates, with insulated plate on the right side. The upper images refer to rear side of the insulation material. The temperatures are given in Kelvin.

The result of predicted temperatures show even value for the steel surfaces, either on the exposed or unexposed side of the surface or at the center point. Although it was expected that in case of the plate 2, the temperature of the unexposed side covered by the insulation should have been lower. Temperature of the insulation shown in Figure 6.10 refers to the center point,

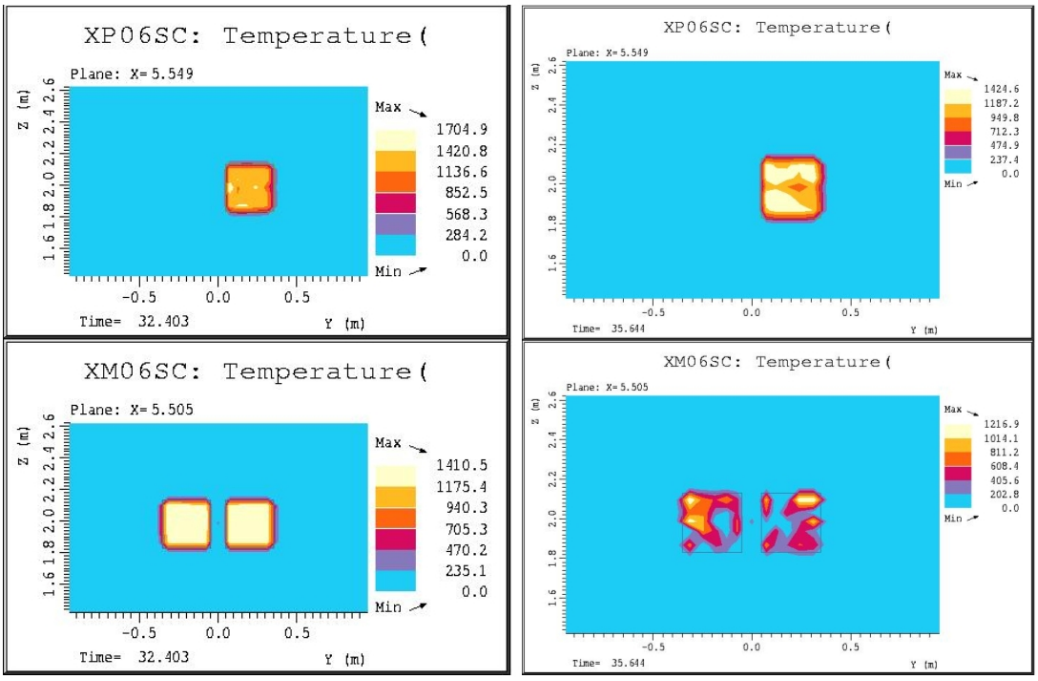

Figure 6.11: Surface temperature of solids before (left) and during activation of deluge (right)

reflecting the experimental setup. The temperature of the insulation on the side adjacent to the surface was about 20 °C prior to spray activation. After the deluge was activated it rose surprisingly to about 900 °C in average with strong oscillation as the diagram in Figure 6.12 shows.

The calculation stopped at the end of the cooling process and did not allow further mitigation of the surface temperatures toward the saturation point of the liquid. This irregularity is visible in Figure 6.10 as one of the temperatures (T_{12}) drops indeed to zero, even below. It was strived to investigate the cause, a number of attempts were made by modeling the scenario in different ways with no result. Limitation of time did not allow further research to refine the modeling in order to judge or make a final statement for the cause. Anyhow, KFX seems to predict fairly. Because the results indicate that the surfaces are getting cooled and temperatures are moving in right direction and approaching the saturation point of the water.

6.5.1 Conclusion

The scenario modeled gave fairly good prediction of temperatures for the surface of the plate 1. But the values for the plate 2 are reasonably higher

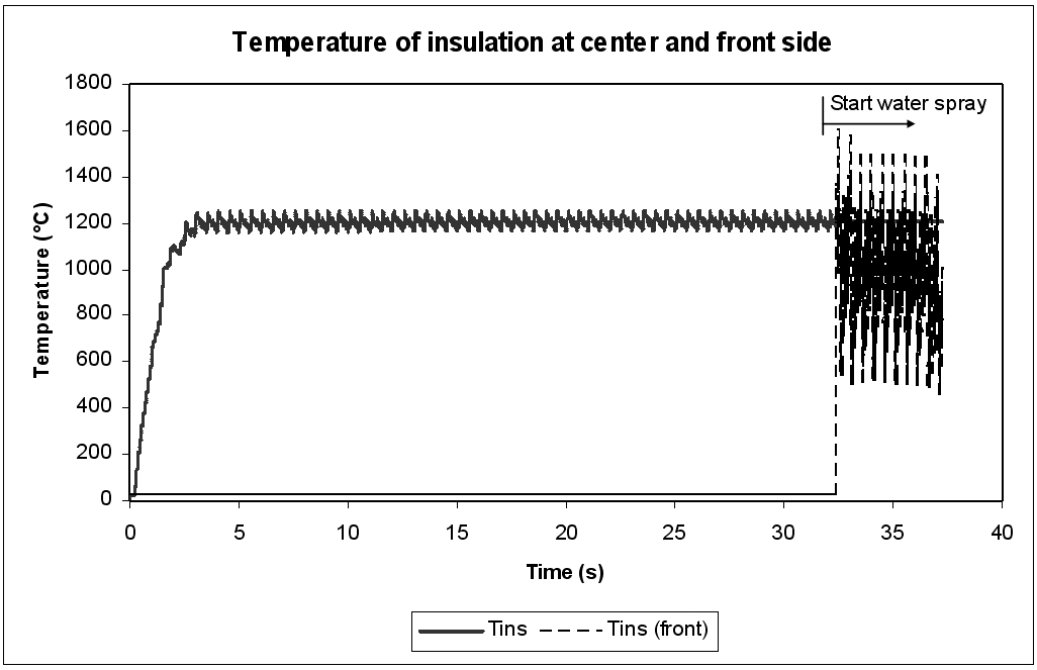

Figure 6.12: Calculated temperature history of insulation material

than expected, since the rear side of the solid was insulated with 5 mm thick insulation material. Likewise the temperature of the insulation was quite high. With another word, the insulation material behaved in some degrees differently and did not act in every aspect as one would expect an insulation material should do.

Upon activation of the deluge, the surface temperatures were quickly suppressed to approximately under 300 °C. Although the calculation terminated due to an unanswered reason before the temperatures reached the saturation area, nevertheless they moved in a right direction.

Chapter 7

Discussions and Comparison of Experimental Data with Theoretical CFD Calculations

7.1 Jet Flame

The temperatures predicted by calculation agree well with that of the measurement as shown in Figure 7.1. Due to slightly higher influence of buoyancy, one would experience that the CFD flame is accordingly lifted up at the end-part of the flame as visible in the figure.

Another matter which distinguished these two flames was the lift-off distance. The CFD flame gave slightly shorter lift-off than the experimental flame does. A closer investigation showed that the CFD model is based on the chemical property of the methane, which is then likely the reason it leads to a shorter length.

Although the CFD flame diameter might look thinner, nevertheless it could be justified by the fact that the transport equations are solved based on the mean values and the ambient condition is chosen as neutral. Otherwise the flame length in both cases agreed pretty well.

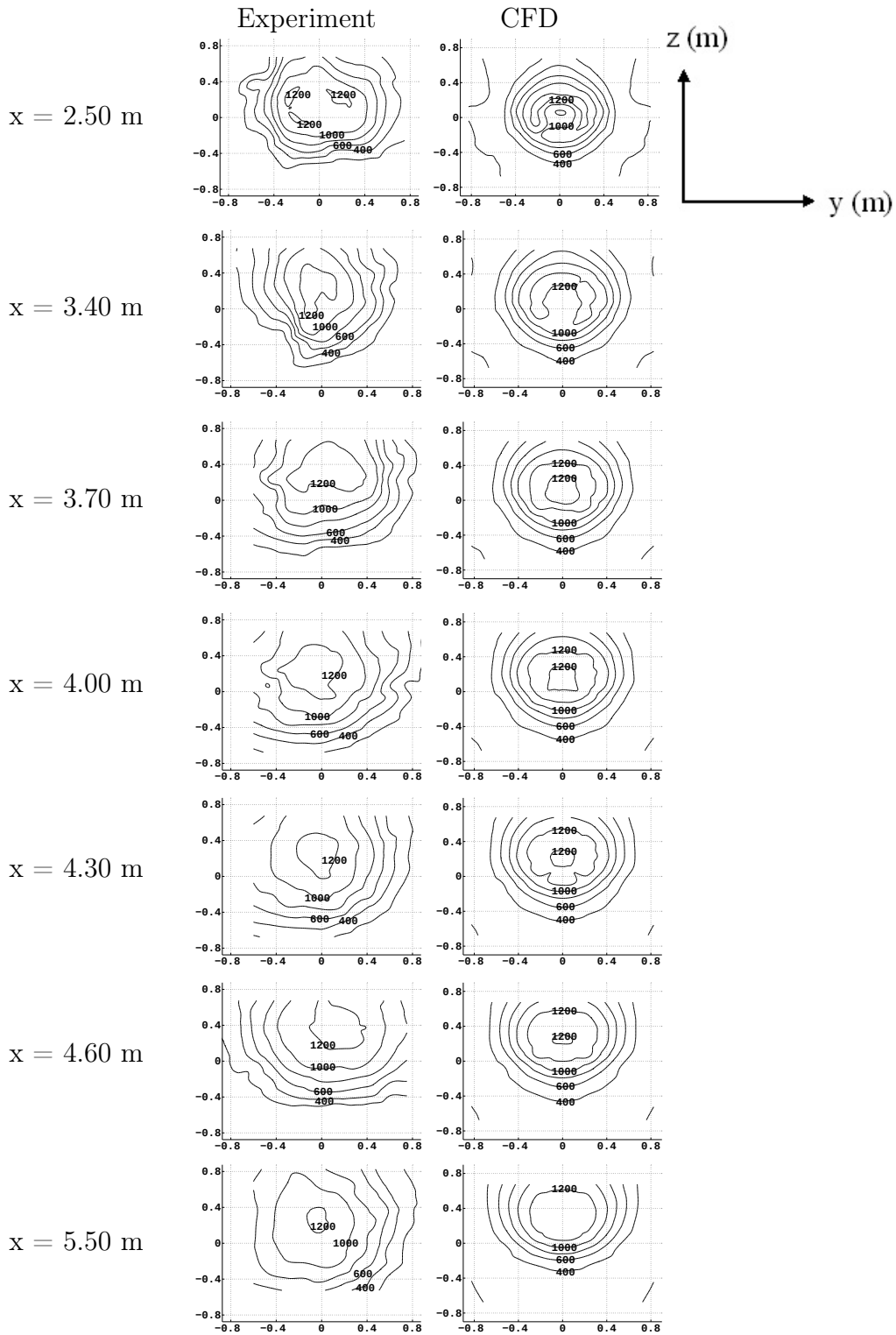

Figure 7.1: Calculated temperatures vs. measured (°C) at various distances (x) from nozzle

Similar diagram for measured and simulated radiation heat flux at various positions related to the flame are provided in Figure 7.2.

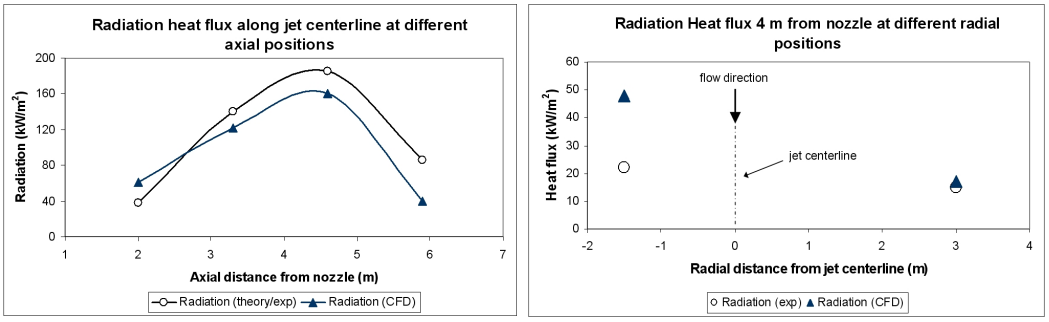

(a) Inside flame **(b)** Outside flame

Figure 7.2: Heat flux calculated and measured within and off jet flame

Radiation measurement within the flame (Figure 7.2a) is partly based on calculation done using analytical model due to the complication described in Chapter 5, i.e. penetration of soot into sensor window, hence disturbing the measurement. With other word, the accuracy of the experimental results obtained here are in some degree uncertain since they are not purely measured values. Anyhow, the two profiles almost follow each other, and the experimental values show in average about 30 % lower.

Measured radiation heat flux outside the flame (Figure 7.2b) at radial distance of 3 m compares quite well with the predicted value, while at 1.5 m the difference is over 100 %. The later suffers indeed of the same problem as mentioned above, although the value was recorded by probe. However, during an independent measurement carried out later in connection with the spray tests, discussed earlier in Chapter 5, it showed that its value is about 50 kW/m^2. See Figure 5.15 and Figure 5.17. This seems to be more reliable value, since the sensor is located so closed to the flame. It also agrees well with the simulation result.

7.2 Steel Channel

In this part of the work only temperature of the channel (surface, insulation, and air) was studied. The corresponding result of measurement and calculation at high gas pressure is given in Figure 7.3.

The temperatures of the exposed surface in the experiment (T_{S1}, T_{S2}, and T_{S3}, Figure 7.3a) are in well agreement with those of the calculation

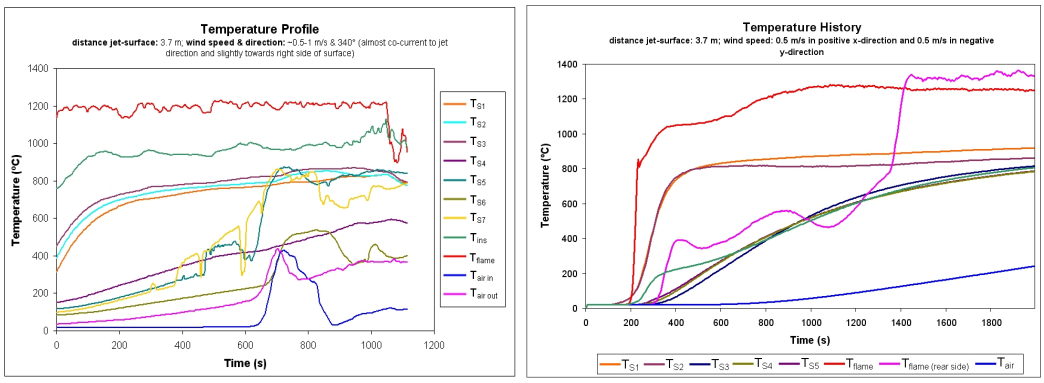

(a) Measurement **(b)** CFD

Figure 7.3: Calculated and measured temperature of channel

(T_{S1}, T_{S2}, Figure 7.3b). The same does the flame temperature. When the surface temperature of insulated areas is concerned, KFX seems to predict considerably higher surface temperature (T_{S3}, T_{S4}, and T_{S5}) compared to the experiment (T_{S4}, T_{S5}, T_{S6}, and T_{S7}), if the simulation was continued. It could even reach as high as the temperature of exposed surface. Presupposed that one presumes the profile in the experiment follows T_{S4}, and ignores T_{S5}, T_{S6}, and T_{S7} which show uneven values after about 600 seconds due to the interruptions described earlier.

The air temperature is in some degree comparable, T_{air} in calculation vs. the experiment's $T_{air\ out}$.

Otherwise for comparison of more result of these two models, experiment and CFD, one is referred to Table 6.1 where several CFD-cases are summarized and compared to that of the experiment.

7.3 Steel Plates

The experiments were performed in two categories, i.e. deluge nozzles located outside and within the flame. The category 1 was composed of two types of test, with emerging gas at low and high pressure. Also two types of test were conducted in the category 2 with two different nozzle configurations. Calculation was done just based on the concept of category 1 at high gas pressure. Because one believes that this is the most serious case, where the plates are subject to considerably higher thermal stresses. The results of prediction and the experiment are shown in Figure 7.4.

In case of the experiment, if one ignores the slight drop of the surface

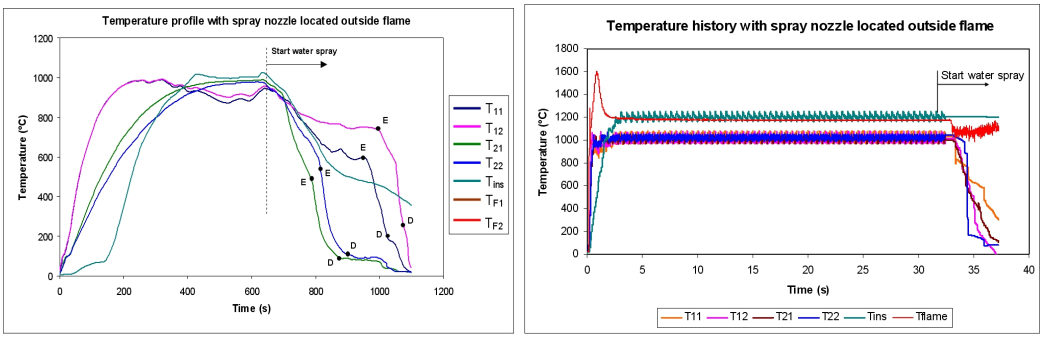

(a) Measurement **(b)** CFD

Figure 7.4: Calculated and measured temperature of plates

temperature of the plate 1 (T_{11} and T_{12}) after about 300 seconds, which is possibly due to rotation of the plate as described earlier, the two models agree in some degree until activation of the spray. But the rotation of the plate 1 is still subject to question. Would, for example, the surface temperature of the plate 2 increase at the same time as the temperature of the plate 1 decreases? Unlikely. Due to this uncertainty, a conservative conclusion would be that the CFD-model possibly predicts higher temperature on surface 2, which is insulated on the rear side.

However, after activation of the deluge the cooling process of the simulation takes place faster, just as in the preheating period.

Additionally, the CFD-code predicts the temperature of the insulation higher by about 200 °C, as high as the flame temperature, and is not affected by the deluge. The reaction of the insulation is very similar to that of the calculation conducted with steel channel, as explained in Section 6.4.

Chapter 8

Conclusion

8.1 Introduction

The main purpose of the research was to investigate the phenomenon of *hot spot* in solids when exposed to jet fire, by exploring its mechanism of occurrence and finding a method to prevent or mitigate it. This work was mainly experimental, and it was composed of four major parts. Experiments on benchmark steel plate, large outdoor fire test with full scale steel channel and steel plates, and characterization of jet flame. Besides, the last three parts were examined theoretically as a comparative study by conducting simulations utilizing the CFD-code KFX. Conclusion from each part is summarized, and the most essential parts are highlighted below.

8.2 Benchmark Steel Plate

- The droplet release angles normal to hot surface gives the best cooling effect, when the plate is i upright position. Otherwise the water just wanders off the surface edge with minimized effect. Partial wetting starts at about 165 °C.

- Lowering the impact velocity combined with larger droplet size contributes to higher wetting temperature, when the surface positioned in horizontal plane. These lead to smaller contact angle of the droplet, causing increased wetting area with higher rate of heat transfer from the plate to the droplet.

- When droplet of around 5 mm in diameter impinges gently on a hot surface, partial wetting starts at about 240–250 °C (Leidenfrost point).

- The droplet wets completely at around 150 °C (peak pool boiling), and spreads out to a maximum diameter three times larger than the initial droplet diameter, leading to higher cooling impact.

- The minimum and maximum heat flux corresponding to above temperatures are 60 and 1750 kW/m^2, respectively.

- The cooling effectiveness at CHF is about 8 % with a Weber number equivalent to 68.

8.3 Characterization of Jet Flame

- The physical dimension of the visible flame was about 5.5 m long with a lift-off distance of 60 cm.

- The warmest region of the jet flame is about 70 % downstream the visible flame length (i.e. not including lift-off). The average of the concerning cross section is around 1100 °C.

- The highest temperature of the flame along any cross section is somewhere between the flame core and outer edge of the flame.

- The radiation fraction along nozzle centerline at positions 25 %, 50 %, 70 %, and 95 % downstream the visible flame length is 28 %, 57 %, 73 %, and 63 %, respectively.

- As one moves outside the flame in radial direction, the radiation fraction increases. At 3 m distance from the jet centerline, it is equal to the total heat flux. This indicates that the convection fraction is almost zero.

- Radiation heat flux sensors are extremely sensitive to unclean environment. Even utilizing purging gas, it does not necessary keep the soot and other particles away from inner surface of the gage's restrictor.

- The CFD-code KFX predicts correct flame length, but estimates slightly shorter lift-off distance.

- The end part of the KFX-flame is more influenced by buoyancy and deviates some from that of the experiment.

8.4 Full scale Steel Channel

- Insulation keeps the surface temperature about 200 °C below that of the exposed area, if it remains intact. This corresponds to 25–50 % lower than the exposed surface temperature, depending on the ambient condition.
- The channel itself had no difficulties to withstand the jet fire, even in case of long durations.
- However, due to high degree of thermal stresses and erosion impact, the insulation material could not resist the fire. Even in well insulated areas, i.e. within encasing, it was affected, either burned or crumbled.
- KFX predicts pretty well the temperature of the exposed surface and the flame. But it seems to predict too high surface temperature at the insulated areas.

8.5 Full scale Steel Plates

Spray Nozzles Located Outside Flame

- Cross wind had significant effect on temperature progress of the surface, just as experienced in the previous section.
- The water mass flux impacting on each plate was kept constant at 4.4 kg/m^{2}s throughout the experiments.
- Three boiling regimes (film boiling, transition boiling, and nucleate boiling) are identified along each temperature profile. The critical (CHF) and minimum heat flux (MHF) for each temperature curve is calculated. Average CHF at high gas pressure for plate 1 and 2 has increased by 40 % and 75 %, respectively, compared to the test at low gas pressure. While, average MHF has increased by 35 % and 150 %, respectively.
- The surface temperature in preheating zone at high gas pressure reaches double so fast to its maximum level (∼1000 °C) compared to situation at low gas pressure.
- Despite very hot surfaces, one managed to depress the temperature by deluge from film boiling to nucleate boiling regime within reasonable time.

- The deluge has considerable effect on the flame, causing the total and radiation heat flux to drop by about 25 % in average within a 3 m radial distance.
- The radiation level on the surrounding area increases by a factor ranging 1.5 to 2, when the gas pressure is doubled.
- The amount of heat transfer to plate 1 is higher than plate 2 by a factor of 2.5.
- The rate of heat transfer to plates was increased by a factor of 2, when the gas pressure was raised from 5 to 10 barg.
- KFX predicts the temperature of surface 1 correctly, while that of surface 2 and insulation is predicted too high. The spray model estimates the cooling process fairly well.

Spray Nozzles Located Inside Flame

- The minimum mass flux of water required to keep the surface temperature within nucleate boiling is 1,1 kg/m^{2}s for both types of spray nozzle. Lowering the rate, the temperature would rise rapidly causing dry patches, and film boiling takes place. The droplet size (SMD) is around 650 μm.
- Closer inspection after experiments indicates that, anyhow, the mass flux probably should be increased to 2.6 and 2.7 kg/m^{2}s for 65° and 30° spray angle nozzle, respectively, to ensure that the entire surface is covered by spray water. The average droplet size for both nozzles is 450 μm.
- The deluge system should always be remained active, as long as the jet flame is on, in order to protect the nozzle and accompanying components.

Chapter 9

Recommendation for Further Work

Flame characterization: As discussed previously the heat flux gages are quite exposed when located within the flame region, and hence their sensor surfaces are sensitive to contamination when deposited by soot. To avoid or minimize such problem, one possible alternative might be to locate the heat flux meters, in particular the radiometers, with their tips (sensor field) oriented in axial direction rather than radial, and co-current to gas flow. This assumes that the whole device including its connection (water hoses, transmission cable) are well insulated, preferably by metal encasing. Medtherm has probably solution for such concept designed for use in combustion chamber, or in case to be designed upon order. The side effect of this concept may be reduction of the convection fraction of the heat.

The simulation carried out employed the KFX version 2000. While typesetting this report, version 2005 has been released which among others includes a new jet calculator called *super jet*. One is then encouraged to test the new calculator to check out whether the influence of buoyancy forces on the end part of the flame would disappear or be diminish, and if the lift-off length could be corrected.

Steel channel: In order to simulate pipework installation, etc. by investigating the temperature progress of the metal, it would be interesting to conduct tests applying water droplets. The challenging question would be weather the channel would behave in similar manner as the steel plates did, i.e. to bring the hot spots under control. Determining how fast the surface temperature could be depressed, and the minimum required mass flux of the liquid.

Further KFX-investigation is recommended in order to find out why calcu-

lation with combination of steel and insulation material did not give reliable results.

Steel plates: As a feature issue it would be interesting to conduct tests with salt water to find out the cooling impact by this substance. One believes that the salt water has better cooling characteristic due to its physical and thermodynamical properties. If it is the case, this would in turn reduce consuming amount of liquid. Different studies done with salt water on micro analysis level (laboratory scale) draw a such conclusion. So it would be interesting to check out when salt water is applied in larger scale.

In employing the spray model of KFX, the water cooling process of the solids did not terminate properly as it did in the experiments. More examination is suggested to bring down the surface temperature within the nucleate boiling regime.

Appendix A

Published Article

The article attached is presented as poster paper in the 10^{th} International Fire Science & Engineering Conference Interflam 2004, Edinburgh, Scotland, July 2004; and is published in Volume 1 of the Conference Proceedings (pp. 683-689).

CHARACTERIZATION OF A HIGH MOMENTUM TURBULENT JET FLAME, A COMPARATIVE STUDY

Leiv Anfin Drange[*], **Zia Kazemi**, **Torgrim Log**
Stord/Haugesund University College, Norway

Bjørn F. Magnussen
Computational Industry Technologies AS, Norway

ABSTRACT

An experimental full scale characterization of a turbulent propane jet flame has been made in terms of temperatures and radiation. Sonic propane gas releases were achieved at steady pressure and near steady flow. The size of the fire was 13-14 MW. The pressure drop across the horizontally mounted nozzle was 10.3 barg. The experimental setup was simulated using the CFD-code Kameleon FireEx, and characterizations were made for temperature, radiation and gas velocity. The results from experiments and simulations were visualized and compared using interpolation techniques. Time-averaged values were plotted. The simulation results showed good correlations with the experiments. Some deviation was found in terms of radiation. The turbulence equations in the $k-\epsilon$-model compute the average values which then results in a more smooth flame, while the physical setup produced more jagged fields. The simulation predicted slightly higher influence of buoyancy in the back 10 % of the flame, and a shorter lift-off at nozzle. The later causes consequently the flame to move somewhat near the release point. There was a small gap between the measured and the simulated values for radiation within the flames. The deviation at comparable positions is of magnitude 14 %.

INTRODUCTION

The aim of this work has been to validate information achieved by simulation on temperature and radiation fields within and near a high momentum turbulent jet flame. Also, information of the velocities involved at different points in the flow field was needed for further studies. However, there was no available equipment or method to measure this. Therefore, the fluid dynamic effects were studied only by simulation. The characterization was done for a 13-14 MW propane gas jet flame (average burning rate 0.3 kg/s). The purpose of characterizing the flame was to understand the flame properties better, which indeed is a part of a bigger project. Radiative and convective heat transfer inside and around the flame was studied.

The pressure drop for propane in gas phase across the nozzle was increased compared to the vapor pressure at ambient temperature. It was done by increasing the pressure by preheating prior to release of propane in liquid phase, before evaporating it into gas phase. This increased the turbulent energy of the jet compared to a release at ambient temperature. The effects of these mechanisms were measured by placing a number of thermocouples, radiometers and total heat flux gages, the latter two commonly called heat flux gages, into and around the region of combustion.

EXPERIMENTS

A rig consisting of a 14 m^3 liquid propane tank, a pump and an evaporator to convert the propane from liquid to gas phase was used as a fire source. The liquid propane was led through an outlet nozzle and expanded to ambient pressure through a series of shock waves. The physical dimensions of the nozzle are shown in Fig. 1. To ensure that the propane was in gas phase at release, a liquid switch was installed between the evaporator and the nozzle, shutting down the supply of propane in case of liquid

[*]Drange and Kazemi have made equal contributions in the process of producing this article.

passing through the evaporator. Three pilot flames at low pressure were applied to the main jet stream approximately 400 mm downstream of the outlet. This was necessary in order to avoid blowout of the flame, due to the high velocity gradients in the gas jet.

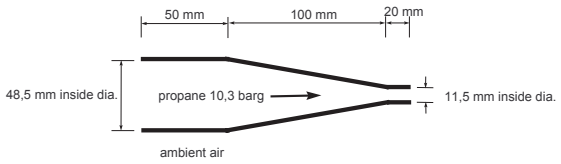

Figure 1: *Outlet nozzle*

Temperatures were recorded at 840 points distributed over seven different cross sections in the flame. The cross sections normal to jet axis were located at distances 2.5, 3.4, 3.7, 4.0, 4.3, 4.6 and 5.5 m from the outlet of the gas. Each cross section formed a grid of 120 measurement points. The sections had their center points on the jet axis and were positioned in y-z-directions as shown in Fig. 2. The available 40 thermocouples were arranged in a grid of 10 rows (150 mm apart) and 4 columns (150 mm apart), and the arrangement could easily be moved across and along the jet axis. This demanded three sets of experiments to be performed at each section, which consisted of 120 single temperature measurements. Thus, a total number of 21 experiments were performed, in order to cover a total of 840 measurement points.

The thermocouples used were of K-type, single-shield of 1.6 mm outside diameter with 0.23 mm conductors isolated by magnesium oxide. The thermocouples in each column were supported on an angle iron 20×20 mm. The four iron angles in each arrangement were located with their angle-sides facing the jet nozzle in order to minimize disturbances of the gas flow. In order to eliminate or minimize the effect of radiation on thermocouple readings originated from glowing metal, their tips were placed approximately 100 mm upstream from the angle irons and parallel to the jet axis. A photograph from one of the experiments is shown in Fig. 2.

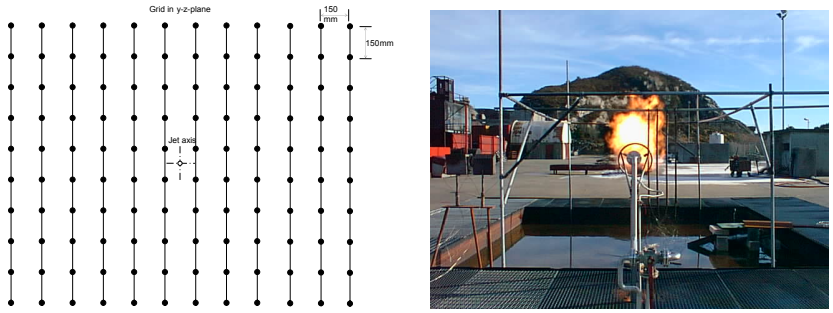

Figure 2: *Setup for temperature measurements*

The experiments were conducted outdoors under calm wind conditions. The wind speed varied from $0.0 - 2.0$ m/s at angles from $45° - 270°$ measured anticlockwise from a direction pointing upstream of the jet. It was mostly in the range of $0.5 - 1.5$ m/s at approximately 150°.

Heat flux measurements were carried out using Medtherm heat flux meters (Schmidt-Boelter sensor type). Six pairs of total heat and radiation flux meters were mounted within and around the flame region. A total flux meter measures sum of the radiation and convection heat. All flux meters were placed at the jet axis level, i.e. at $z = 0.0$ m. Four pairs were directly located in the flame zone, along the jet axis, at $x = 2.0, 3.3, 4.6$ and 5.9 m, while the other two pairs were placed outside the flame at the locations $x = 4.0$ m, $y = -1.5$ m, and $x = 4.0$ m, $y = 3.0$ m. All flux meters were pointing horizontally, with their centerlines normal to the nozzle centerline so that the surfaces of the flux meters were parallel to the jet axis or gas flow. They were supported in the same manner as the thermocouples. In order to minimize, or avoid, the effect of adjacent glowing angle iron, acting as a support for the gages, the support was located

100 mm behind the gage surface. Each pair of the flux meters were water cooled, except for those placed in the low radiation field outside the jet flame. In addition, the open casing (the view restrictor) around the black body of the radiation flux meters located inside the combustion zone were nitrogen purged in order to keep the sensor surfaces clean from soot and other particles.

CFD MODELLING

The CFD program Kameleon FireEx 2000 (denoted KFX) was used for the modelling. The simulator uses a Cartesian finite volume technique to solve the averaged basic transport equations from fluid dynamics. Sub-models include among others the $k - \epsilon$ turbulence model [1, 2]. Prior to the experimental work, number of CFD-simulations was carried out using KFX in order to point out the proper positions for instrumentation (thermocouples and heat flux meters). After the experimental part of the work was completed, similar scenarios were modeled in KFX and simulated. The gas velocity profile along the flame path was simulated, but not measured experimentally.

The geometry used had dimensions $13 \times 7 \times 9$ m ($LxWxH$) with a grid resolution $63 \times 55 \times 60$ equivalent to 207 900 grid nodes. The volume consisted of a floor boundary with isothermal solid cells mostly covered with solid isothermal core as domain cells. These cells formed a pool which was located under the jet flame area. This water pool protected the concrete floor from the radiative heat in the experiments. The walls and roof were defined as wind boundary cells. The nozzle was placed 2.0 m above the floor at the point $(x, y, z) = (0, 0, 0)$ with jet release in the positive x-direction. The mesh resolution was distributed fairly fine around the nozzle, gradually increasing with decreasing flow speed. The view is provided in Fig. 3. The figure on the left side reflects the concept used for measuring the heat flux in the experiments.

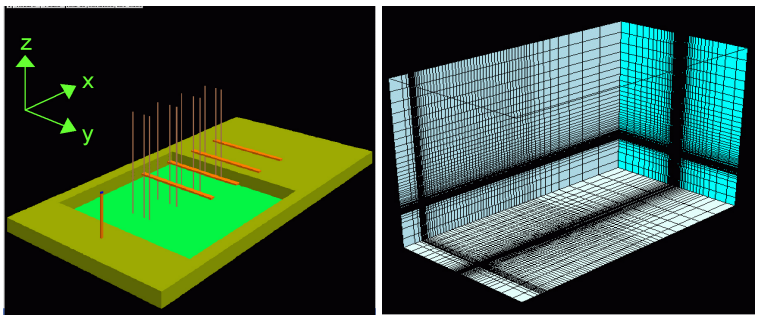

Figure 3: *Setup of simulation model*

The specification of scenarios simulated was similar to the experimental work, i.e. mass flow rate of propane, system pressure, temperature, nozzle geometry, type of thermocouple, etc. as described earlier. As previously mentioned the wind velocity in the experiments was very low (i.e. $0.5 - 1.5$ m/s), but quite varying in direction. Due to this matter its value in simulation was assumed to be zero. As discussed later in RESULTS AND DISCUSSION, similar adjustments were made in plotting the temperature values from the experiment so that the center of temperature field lied on $y = 0.0$ m. The transient time step was set to 1.0e-05 s and a Courant number to 100. Criterion for convergence was based on carbon and hydrogen balance in calculation domain. To verify this, the difference between the carbon and/or hydrogen entering and leaving the calculation domain should not exceed approximately 3 % according to ComputIT [3]. For this study the values lied under 0.3 %.

The calculated parameters were temperature, radiative heat flux, and gas velocity. The location of computed points for temperature and heat flux is as described under EXPERIMENTS. While the velocity of the gas was calculated at 65 different positions along the flame path.

The temperature difference between the metal junction inside the thermocouple and the actual gas temperature was calculated by KFX. The model works in the opposite direction of what an experiment would do, by first calculating a gas temperature. Based on heat balances, a theoretical thermocouple reading was calculated.

RESULTS AND DISCUSSION

As stated in the previous section the wind velocity was set to zero. In order to match this in treating the results, similar adjustments were made in plotting the temperature values from the experiment so that the center of temperature field lied on $y = 0.0\ m$ without having any consequences for their numerical values.

The results of field measurements and CFD simulations compared quite well for the temperatures, see Fig. 4. Only a minor difference was observed concerning buoyancy forces on the end part of the flame (approximately 10 %) in simulations compared with the experiments which indeed is insignificant as it can be seen in Fig. 4 & 5.

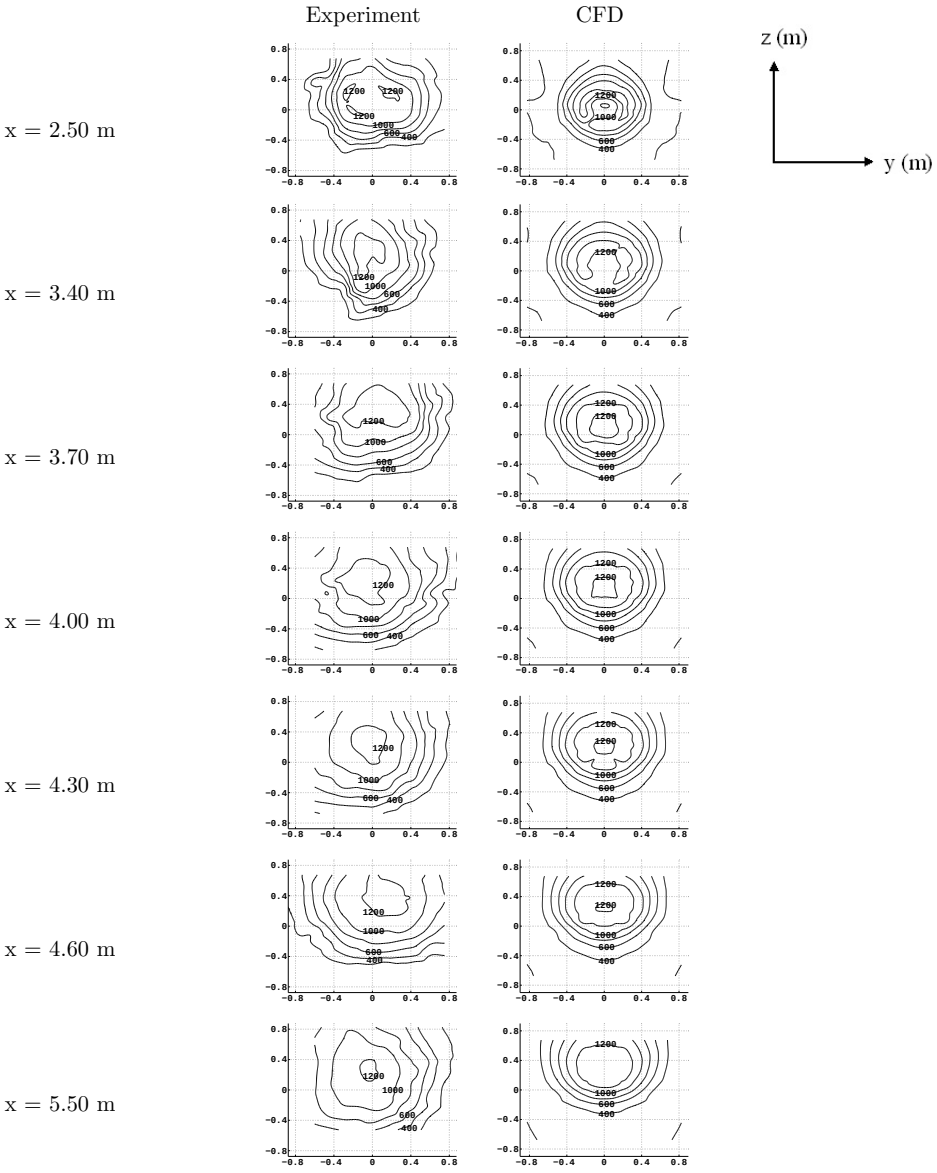

Figure 4: *Temperatures (°C) at various distances, x (m), from nozzle*

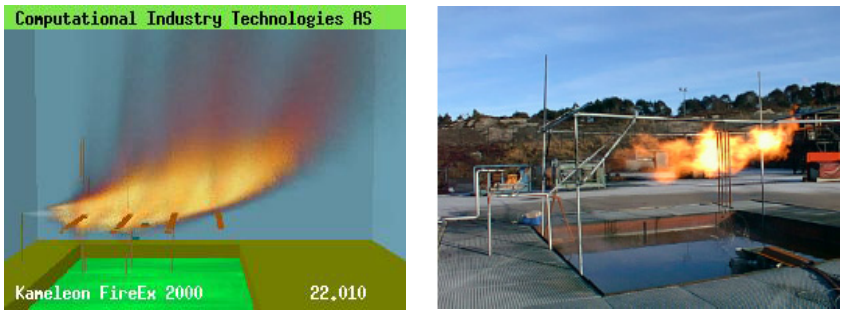

Figure 5: *Visual comparison of simulation and experiment*

Another matter which visually distinguished these two flames was the smooth temperature fields in the simulations contra the unsteady temperature fields from the experiments. Because the turbulence equations in the $k-\epsilon$-model calculate the average values which then result in a more smooth flame, while the experimental setup produced more turbulent and jagged fields. This might be overcome by increasing the number of grid nodes considerably. But this in turn demands powerful computer capacity which indeed is limited. Even though having access to such computers, it would never give a 100 % realistic picture of a turbulent flame [3]. The other possible reasons might be that in case of the simulation the wind effects were ignored (set to zero) and the effects of angle irons in the flame (used to support the thermocouples and flux meters in experiments) and the surrounding objects (buildings, equipment etc.) were neglected.

Due to closure of the liquid switch several times during the heat flux experiments, the data recorded during closure had to be ignored. Ignoring the data was decided in accordance with manual time registration for closure. These data compared well with the changes in heat flux recorded by computer.

In order to eliminate the convective heat transfer when measuring radiation, the heat flux sensor surface is covered with a window attachment. Internal surface of the window which is formed as an ellipsoidal cavity is gold plated and is highly polished.

Although nitrogen purging was applied to keep the sensor surface clean during the experiments, the gas flow inevitably entered the window and covered the polished area by soot. This resulted in emissivity reduction of the reflecting plate, causing unreliable and very low radiation values except the one located farthest outside the flame at $y = 3.0\ m$

The plotted radiation results from experiment are then calculated values based on the measured temperatures and simulated gas velocities. Equation (1) was used to calculate the convective heat transfer coefficient of the gas [4].

$$h = 0.033 \frac{\rho c_p \nu^{0.2} V^{0.8}}{d^{0.2}} \quad (kW/m^2\ K) \tag{1}$$

where:

$$\begin{aligned} \rho &= density\ (kg/m^3) \\ C_p &= specific\ heat\ capacity\ (kJ/kg\ K) \\ \nu &= kinematic\ viscosity\ (m^2/s) \\ V &= velocity\ (m/s) \\ d &= flux\ outside\ diameter\ (m) \end{aligned}$$

By using the equation $Q_{convection} = h(T_2 - T_1)$ the amount of heat convection transferred to the heat flux transducers was calculated. T_1 and T_2 are the heat flux body and the flue gas temperature, respectively. By subtracting this value from the total heat flux measured, a theoretical radiation corresponding to the experimental value was then found and the results are plotted in the diagrams shown in Fig. 6. Heat flux

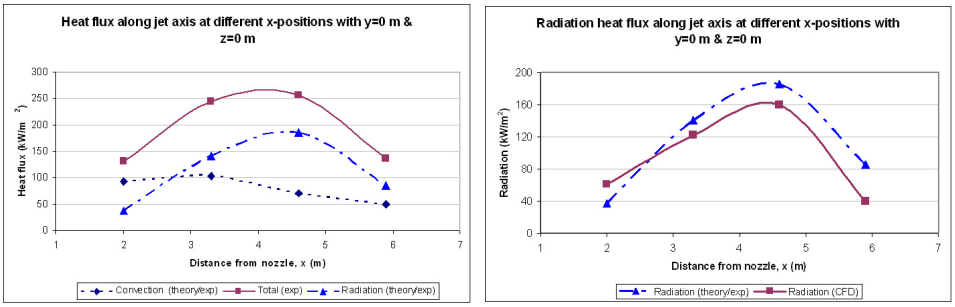

Figure 6: *Measured and calculated heat flux along jet centerline*

measured and simulated outside the flame, and gas velocity calculated along the flame path are shown in Fig. 7. The flame had approximately a diameter of 1.0 m and a length equivalent to 7.0 m.

The results of radiation show also fairly correlation for two methods at comparable positions. But some deviation was anyhow found. The simulation predicted slightly a shorter lift-off at the outlet. The later is due to the fact that the CFD-code uses the default value for methane [3]. This causes consequently the flame to move somewhat near the release point. As a result the first position of the measurement, i.e. 2.0 m from the nozzle will lie in a more active combustion zone in case of simulation. This will be reflected in terms of higher radiation value as it can be seen in Fig. 6. For the same reason the situation is reverse on the other end of the flame, i.e. combustion accomplishes earlier and in addition due to higher buoyancy effects the flame bends off earlier and resulting the last position (5.9 m from the outlet) to lie almost outside the flame region. This will cause lower value for radiation in simulation. While the position 2 (3.3 m) and 3 (4.6 m) in both cases are well situated in flame zone. The deviation for these comparable positions is at most of magnitude 14 %

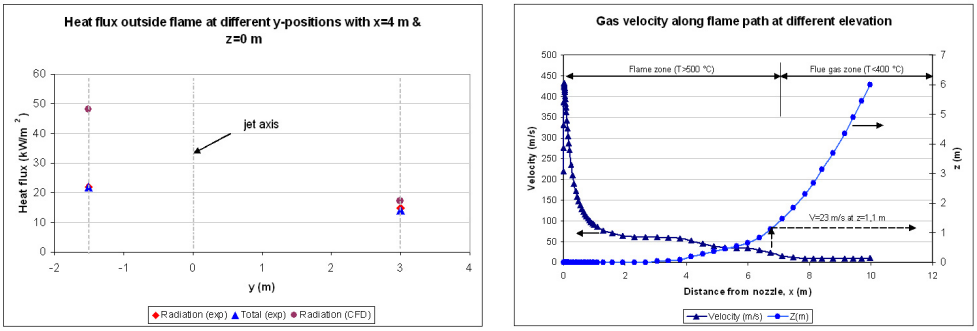

(a) Measured and calculated heat flux outside flame

(b) Calculated gas velocity along flame path

Figure 7: *Heat flux and gas velocity*

CONCLUSION

The simulated results for the temperatures compared well with the measured values. The two methods show anyhow some minor deviation on the heat flux radiation. Using the transport equations in a $k-\epsilon$-model tends to return smooth temperature fields, while a physical setup produces more jagged fields.

The simulation predicted slightly higher influence of buoyancy on the back 10 % of the flame. This effect combined with a shorter lift-off stand for the major part of the radiation deviation. Indeed a physical correction for later will further bring these two flames closer to each other.

However in order to draw a trustworthy conclusion concerning radiation differences and rely on the radiation results from the field tests, we believe a more experimental investigation is necessary. Because the

radiation heat flux meters are pretty sensitive and a far better measurement method is required in order to keep their surfaces clean despite an unclean environment.

Altogether the CFD-code KFX seems to estimate fairly the measured parameters and could well be used to minimize the costly experimental works.

ACKNOWLEDGEMENT

The authors would like to thank the employees at ComputIT AS for their valuable support in the process of simulation in this work, in particular Mr. Nils Lilleheie and Mr. Bjørn Erling Vembe.

REFERENCES

[1] Vembe, B.E.; Rian, K.E.; Holen, J.K.; Lilleheie, N.I.; Grimsmo, B.; Magnussen, B.F. *Kameleon FireEx 2000 User Manual*, ComputIT report no. R0122.

[2] Vembe, B.E.; Rian, K.E.; Holen, J.K.; Lilleheie, N.I.; Grimsmo, B.; Myhrvold, T. *Kameleon FireEx 2000 Theory Manual*, ComputIT report no. R0123.

[3] ComputIT (Computational Industry Technologies AS) *Kameleon FireEx 2000*, Bassengbakken 1, N-7042 Trondheim, Norway.

[4] Kreith, F; Black, W.Z. *Basic Heat Transfer*, Harper & Row, ISBN 0-711-22518-8.

Bibliography

[1] Daniel Holtom and Elizabeth Fisher. *Enjoy Writing your Science Thesis or Dissertation—A step by step guide to planning and writing dissertations and theses for undergraduate and graduate science students.* Imperial College Press, London, 2003.

[2] Joan Bolker. *Writing your dissertation in fifteen minutes a day: a guide to starting, revising, and fifishing your doctoral thesis.* An owl book. H.Holt, New York, 1998.

[3] James E. Mauch and Jack W. Birch. *Guide to the successful thesis and dissertation: a handbook for students and faculty.* Books in library and information science. Marcel Dekker, New York, 4th edition, c1998.

[4] Brian R. Holloway. *Technical writing basics: a guide to style and form.* Prentice Hall, NJ, 2nd edition, c2002.

[5] Staale Sinding-Larsen. *Teori og praksis for avhandlinger.* Tapir, 2001. (In Norwegian).

[6] H. Olsson and S. Sörensen. *Forskningsprosessen—kvalitative og kvantitative perspektiver.* Tapir, 2003. (In Norwegian).

[7] Olav Bø. *FoU metodikk.* Tapir, 1995. (In Norwegian).

[8] Judith Bell. *Introduktion til forskningsmetodik.* Tapir, 1993. (In Swedish).

[9] Leslie Lamport. *LaTeX—A Document Preparartion System, User's Guide and Reference Manual.* Addison-Wesley, 2nd edition, 1994.

[10] Michel Goossens, Frank Mittelbach, and Alexander Samarin. *The LaTeX Companion.* Addison-Wesley, USA, 2000.

[11] Antoni Diller. *LaTeX Line by Line—Tips and Techniques for Document Processing.* John Wiley & Sons, England, 2nd edition, 1999.

[12] Bernice Sacks Lipkin. *LaTeX for Linux—A Vade Mecum.* Springer, New York, 1999.

[13] Tobias Oetiker, Hubert Partl, Irene Hyna, and Elisabeth Schlegl. *The Not So Short Introduction to LaTeX 2ε.* Swiss Federal Institute of Technology, Swiss, September 2003. Version 4.13.

[14] Piet van Oostrum. *Page layout in LaTeX.* Department of Computer Science, Utrecht University, The Netherland, 1996.

[15] Piet van Oostrum. *Headers and footers in LaTeX.* Department of Computer Science, Utrecht University, The Netherlanfd, September 1994.

[16] Dag Langmyhr. LaTeX en kort innføring, September 2003. (In Norwegian).

[17] Dag Langmhyr. LaTeX for viderekomme, October 2003. (In Norwegian).

[18] Dag Langmyhr. *LaTeX for nybegynnere.* Det matmatisk-naturvitenskapelige fakultet, Universitetet i Oslo, Oslo, August 2003. (In Norwegian).

[19] Dag Langmyhr. *Lokal guide til BibTeX.* Institutt for informatikk, Universitetet i Oslo, Oslo, November 1998. (In Norwegian).

[20] Dag Langmyhr. *Lokal guide til farger i LaTeX.* Institutt for informatikk, Universitetet i Oslo, Oslo, July 2001. (In Norwegian).

[21] Norwegian Government. Lillestrøm-ulykken 5. april 2000. Norges offentlige utredninger NOU 2001: 9, Statens forvaltningstjeneste—Informasjonsforvaltning, Oslo, Norway, 2000. (In Norwegian).

[22] Ivar S. Ertesvåg. *Turbulent strøyming og forbrenning - frå turbulensteori til ingeniørverktøy.* Tapir akademisk forlag, Trondheim, Norway, 2000. ISBN 82-519-1568-6 (In Norwegian).

[23] C. Truesdell. The mechanical foundations of elasticity and fluid dynamics. *J. Rat. Mech. Anal.*, (1):125–300, 1952.

[24] Suhas V. Patankar. *Numerical Heat Transfer and Fluid Flow.* Hemisphere, Washington, 1980.

[25] Kenneth Kuan-yun Kuo. *Principles of Combustion.* John Wiley & Sons, New York, 1986. ISBN 0-471-62605-8.

[26] Paul A. Libby and Forman A. Williams (eds.). *Turbulent reacting flows.* Springer, Berlin, 1980.

[27] B.E. Laundar and D.B. Spalding. The numerical computation of turbulent flows. *Computer Methods in Appl. Mech. and Eng.*, (3):269–289, 1974.

[28] W.P. Jones and B.E. Launder. The prediction of laminarization with a two-equation model of turbulence. *Int. J. Heat Mass Transfer*, (15):301–314, 1972.

[29] Irvin Glassman. *Combustion.* Academic Press Inc, UK, 2^{nd} edition, 1986. ISBN 0-12-285851-4.

[30] R. Goulard, A.M. Mellor, and R.W. Bilger. Combustion measurements in air breathing propulsion engine. Survey and research needs. *Comb. Sci. Technol.*, (14):195–219, 1976.

[31] D. Brian Spalding. Development of the eddy-break-up model of turbulent combustion. *Sixteenth Symp. (Int.) Comb.*, pages 1657–1663, 1976. Comb.Inst., Pittsburgh, Pennsylvania.

[32] K.N.C. Bray. Turbulent flows with premixed reactants. *Turbulent reacting flows*, pages 115–183, 1980. Springer, Berlin.

[33] Bjørn F. Magnussen and Bjørn H. Hjertager. On mathematical modeling of turbulent combustion with special emphasis on soot formation and combustion. *Sixteenth Symp. (Int.) Comb.*, pages 719–729, 1976. Comb. Inst., Pittsburgh, Pennyslvania.

[34] Ivar S. Ertesvåg and Bjørn F. Magnussen. The eddy dissipation turbulence energy cascade model. *Combustion Science and Technology*, 159:213–236, 2000.

[35] Bjørn F. Magnussen. On the structure of turbulence and a generalized eddy dissipation concept for chemical reaction in turbulent flow. Presentated at 19th American Institute of Aerodynamics and Astronautics Aerospace Science Meeting, January 1981. St. Louis, Missouri, USA.

[36] Bjørn F. Magnussen. Modeling of NO_x and soot formation by the eddy dissipation concept. Presentaed at International Flame Research Foundation. First Topic Oriented Technical Meeting, October 1989. Amsterdam, The Netherlands.

[37] Bjørn F. Magnussen. Some features on the structures of mathematical model of turbulence. Report, Norwegian Institute of Technology, Trondheim, Norway, 1975.

[38] Lene K. Hjertager, Jørgen Osenbroch, Bjørn H. Hjertager, and Tron Solberg. Validation of the eddy dissipation concept for fast chemical reactions in turbulent flows. *Chemical Reaction Engineering VII: CFD*, August 2000. Quebec City, Canada.

[39] Bjørn F. Magnussen. Modeling of reaction processes in turbulent flames with special emphasis on soot formation and combustion. Partculate carbon formation during combustion, 1981. Plenum Publishing Corporation.

[40] Bjørn F. Magnussen. Heat transfer in gas turbine combustors - a discussion of combustion, heat and mass transfer in gas turbine combustors. In *Conference proceeding no. 390*. Advisory group for aerospace research and development, 1985.

[41] S.S. Sadhal, P.S. Ayyaswamy, and J.N. Chung. *Transport Phenomena with Drops and Bubbles*. Mechanical engineering series. Springer, New York, N.Y., 1996. ISBN 0-387-94678-0.

[42] Personal conversation with Professor Torgrim Log at Stord Haugesund University College, Norway, 2003.

[43] C.E. Lapple. Particle technology. *Satndards Res. Inst. J.*, (5):95–102, 1961.

[44] L.C.E. Blackman, M.J.S. Dewar, and H. Hampson. An investigation of compounds promoting the dropwise condensation of steam. *J. Appl. Chem.*, (7):160–171, 1957.

[45] T. Furman and H. Hampson. Experimental investigation into the effects of cross flow with condensation of steam and steam-gas mixtures in a vertical tube. *Proc. Instn. Mech. Engrs.*, (173):147–169, 1959.

[46] H. Hampson. Dropwise condensation on a metal surface. *Engineering*, (179):464–469, 1955.

[47] H. Hampson. Condensation of steam on a tube with filmwise or dropwise condensation in the presence of non-condensable gas. In *Int. Dev. in Heat Transfer, Proc. 1961-62 Int. Heat Transfer Conference*, pages 310–318. ASME, 1963.

[48] H. Hampson and N. Ozisik. An investigatin into the condensation of steam. *Proc. Instn. Mech. Engrs.*, (1B):282–293, 1952.

[49] A. Eucken. Energie- und stoffaustausch an grenzflächen. *Naturwissenschaften*, (25):209–218, 1937.

[50] A. Umur and P. Griffith. Mechanism of dropwise condensation. *ASME J. Heat Transfer*, (87):275–282, 1965.

[51] M. Jakob. Heat transfer in evaporation and condensation - II. *Mech. Engrg.*, (58):729–739, 1936.

[52] C. Graham and P. Griffith. Drop size distribution and heat transfer in dropwise condensation. *Int. J. Heat Mass Transfer*, (16):337–345, 1973.

[53] Kirk D. Hagen. *Heat Transfer with Applications*. Prentice Hall, USA, 2000. ISBN 0-13-520941-2.

[54] A.F. Mills. *Basic Heat and Mass Transfer*. Prentice Hall, USA, 2nd edition, 1999. ISBN 0-13-096247-3.

[55] L.T. Cowley and A.D. Johnsen. Oil and gas fires: characteristics and impact. HSE Offshore Technology Information OTI 92 596, UK, 1992.

[56] L.T. Cowley and V.H.Y. Tam. Pressurised LPG releases - The isle of grain full scale experiments. The 13th International LNG/LPG Conference and Exhibition, Gastech 88, Kuala Lumpur. Gastech Ltd., Herts., UK, October 1988.

[57] R.H. Sabersky, A.J. Acosta, and E.G. Hauptmann. *Fluid Flow - A First Course in Fluid Mechanics*. Macmillan Publishing Co., Inc., New York, second edition, 1971. ISBN 0-02-979770-5.

[58] *API recomended practice 521*, second edition, September 1982.

[59] H.G. Wertenbach. Spread of flames on cylindrical tanks for hydrocarbon fluids. *Gas and Erdgas*, 112(8), 1971.

[60] R. McMurray. Flare radiation estimated. *Hydrocarbon processing*, pages 175–181, 1981.

[61] A.L. Suris, E.V. Franklin, and S.N. Shorin. Length of free diffusion flames. *Combustion Explosion and Shock Waves*, (13):459–462, 1977.

[62] B.J. McCaffery and D.D. Evans. Very large methane jet diffusion flames. pages 25–31. 1986.

[63] W.R. Hawthorne, D.S. Weddell, and H.C. Hottel. Mixing and combustion in turbulent gas jets. *3rd Int. Comb. Symp.*, pages 266–288, 1949.

[64] G.T. Kalghatgi. The visible flame shape and size of a turbulent hydrocarbon jet diffusion flame in a crosswind. *Combustion and Flame*, (52):91–106, 1983.

[65] G.T. Kalghatgi. Lift-off heights and visible lengths of vertical turbulent jet diffusion flames in still air. *Combustion Science and Technology*, (41):17–29, 1984.

[66] G.A. Chamberlain. Developments in design methods for predicting thermal radiation from flares. *Chem. Eng. Res. Des.*, (65):299–309, 1987.

[67] O.K. Sønju and J. Hustad. An experimental study of turbulent jet diffusion flames. Norwegian Maritime Research, pages 2-11, 1984.

[68] B.J. McCaffrey. Momentum diffusion flame characteristics and the effect of water spray. National Bureau of Standards, Center for Fire Research, Gaithersburg, NBSIR 86-3442, 1986.

[69] N. Peters and F.A. Williams. Lift-off characteristics of turbulent diffusion flames. *AIAA-Journal*, 21(3), 1983.

[70] R.B. Schuller, J. Nylund, O.K. Sønju, and J. Hustad. Effect of nozzle geometry on burning subsonic hydrocarbon jets. In *Fire Dynamics and Heat Transfer*, page 33. The 21st National Heat Transfer Conference, Seattle, July 1983.

[71] A.D. Johnson, L.C. Shirvill, and A. Ungut. CFD calculation of impinging gas jet flames. Offshore Technology Report OTO 1999 011, Health and Safety Executive, UK, April 1999.

[72] D.K. Cook, M. Fairweather, G. Hankinson, and K. O'Brien. Flaring of natural gas from inclined vent stacks. *I. Chem. E. Symp.*, (102):289–300, 1987.

[73] National Fire Protection Association. *The SFPE Handbook of Fire Protection Engineering*. NFPA, Quincy, Massachusetts, 3rd edition, 2002.

[74] D.K. Cook, M. Rairweather, J. Hammonds, and D.J. Hughes. Size and radiative chracteristics of natuarl gas flares. *Chem. Eng. Res.*, (65):310–325, 1987.

[75] J. Cook, Z. Bahrami, and R.J. Whitehouse. A comprehensive program for calculation of flame radiation levels. 1st Int. Conf. on Loss of Containment. *J. Loss Prev.*, 3(1):150–155, 1990.

[76] D.S. Burgess and M. Hertzberg. *Advances in Thermal Engineering* , chapter 27, page 413. John Wiley & Sons, Chichester, UK, 1974.

[77] D. Drysdale. *An Introduction to Fire Dynamics*. John Wiley & Sons, UK, 2nd edition, 1998. ISBN 0-471-97291-6.

[78] P.H. Thomas. The size of flames from natural fires. *9th Int. Combustion Symp.*, page 844, 1963. Combustion Institute, Pittsburgh, PA, USA.

[79] G. Hekestad. Luminous heights of turbulent diffusion flames. *Fire Saftey Journal*, (5):103–108, 1983.

[80] G. Hekestad. Peak gas velocities and flame heights of buoyancy-controlled turbulent diffusion flames. *18th Symposium (International) on Combustion*, pages 951–960, 1981. The Combustion Institute, Pittsburgh.

[81] K.S. Mudan. Thermal radiation hazards from hydrocarbon pool fires. Progr. Energy. *Comb. Sci.*, (10):59–80, 1984.

[82] M. Shokri and C.L. Beyler. Radiation from large pool fires. *J. Fire Protection Engineering*, (1):141–150, 1989.

[83] J.A. Eyre and W.J.S. Hirst. Maplin Sands experiments 1980: Combustion of large LNG and refrigerated liquid propane spills on the sea. Proc. 2nd Symp. on Heavy Gas and Risk Assesment II, West Germany, 25-26th May, 1983. D. Reidal Publishing Co. Netherlands, 1983.

[84] D.R. Blackmore, J.A. Eyre, and G.G. Summers. Dispersion and combustion behaviour of gas clouds resulting from large spillages of LNG and LPG on the sea. Tran I Mar E (TM), 94, Paper 29, 1982.

[85] G.A. Mizner and J.A. Eyre. Radiation from liquefied gas fires on water. *Combustion Science and Technology*, (35):33–57, 1983.

[86] J. Moorhouse and M.J. Pritchard. Thermal radiation hazards from large pool fires and fireballs - A literature review. I. Chem. E. Symposium Series, No. 71, The Assesment of Major Hazard, Manchester, 14-16th April 1982.

[87] J.B. Gayle and J.W. Bransford. Size and duration of fireballs from propellant explosions. NASA Tech Mem No. x-53314, 1965.

[88] A.F. Roberts. The effect of conditions prior to loss of containment on fireball behaviour. I. Chem. E. Symposium Series, No. 71, The Assesment of Major Hazard, pages 397–429, Manchester, 14-16th April 1982.

[89] D.M. Johnson, M.J. Pritchard, and M.J. Wickens. Large scale catastrophic releases of flammable liquids. British Gas draft report for the Commission of the European Communities, Contract No. EV4T.0014.UK, June 1990.

[90] A.F. Roberts. Thermal radiation hazard from release of LPG from pressurised storage. *Fire Safety Journal*, (4):197–212, 1982.

[91] J.F. Bennett, L.C. Shirvill, and M.J. Pritchard. Efficacy of water spray protection against jet fires impinging on LPG storage tanks. HSE Contract Research Report 137/1997, UK, 1997.

[92] L.C. Shirvill and J.F. Bennett. Efficacy of water spray protection against butane jet fires impinging on Liquefied Petroleum Gas (LPG) storage tanks. HSE Contract Research Report 298/2000, UK, 2000.

[93] Y. Lev and D.C. Strachan. A study of cooling water requirements for protection of metal surfaces against thermal radiation. *Fire Technology*, August 1989.

[94] K.J. Choi and S.C. Yao. Mechanism of film boiling heat transfer of normal impacting spray. *Int. J. Heat Mass Transfer*, (13):311–318, 1987.

[95] M. di Marzo. Dropwise evaporative cooling. In *Sparse water sprays in fire protection*, NIST-GCR-96-687, pages 1–23, USA, June 1996. National Institute of Standards and Technology.

[96] M. di Marzo and D.D. Evans. Evaporation of a water droplet deposited on a hot high thermal conductivity surface. *J. Heat Transfer*, 111:210–213, 1989.

[97] C. Bonacina, S. Del Giudice, and G. Comini. Dropwise evaporation. *J. Heat Transfer*, 101:441–446, 1979.

[98] J.J. Rizza. A numerical solution to dropwise evaporation. *J. Heat Transfer*, 103:501–507, 1981.

[99] M. Klassen, M. di Marzo, and J. Sirkis. Infrared thermography of dropwise evaporative cooling. *Experimental Thermal and Fluid Science*, 5:136–141, 1992.

[100] M. di Marzo, C.H. Kidder, and P. Tartarini. Infrared thermography of dropwise evaporative cooling of a semifinite solid subjected to radiant heat transfer. *Experimental Heat Transfer*, 5:102–114, 1992.

[101] S.C. Tinker and M. di Marzo. Effect of dissolved gases on spray evaporation cooling with water. In *Sparse water sprays in fire protection*, NIST-GCR-96-687, pages 196–220, USA, June 1995. National Institute of Standards and Technology.

[102] S.C. Tinker, M. di Marzo, P. Tartarini, S. Chandra, and Y.M. Quiao. Dropwise evaporative cooling: effect of dissolved gases and effect of surfactants. International Conferance on Fire Research and Engineering, pages 90–96, Orlando, September 1995.

[103] S.G. Kandlikar and M.E. Steinke. Contact angles of droplets during spread and recoil after impinging on a heated surface. *IChemE Journal of Chemical Engineering Research and Design*, 79(A3):491–498, April 2001.

[104] S.G. Kandlikar and M.E. Steinke. Contact angles and interface behavior during rapid evaporation of liquid on a heated surface. *International Journal of Heat and Mass Transfer*, 45:3771–3780, 2002.

[105] S. Chandra, M. di Marzo, Y.M. Qiao, and P. Tartarini. Effect of solid-liquid contact angle on droplet evaporation. In *Sparse water sprays in fire protection*, NIST-GCR-96-687, pages 168–194, USA, June 1995. National Institute of Standards and Technology.

[106] M. Pasandideh-Fard, S.D. Aziz, S. Chandra, and J. Mostaghimi. Cooling effectiveness of a water drop impinging on a hot surface. *International Journal of Heat and Fluid Flow*, 22:201–210, 2001.

[107] S.C. Yao and K.J. Choi. Heat transfer experiments of monodispersed vertically impacting sprays. *International Journal of Multiphase Fow*, 13:639–648, 1987.

[108] J. Schmidt and H. Boye. Influence of velocity and size of the droplets on the heat transfer in spray cooling. *Chemical Eng. Technol.*, 24(3):255–260, 2001.

[109] P.J. Halvorson, R.J. Carson, S.M. Jeter, and S.I. Abdel-Khalik. Critical heat flux limits for a heated surface impacted by a stream of liquid droplets. *ASME Journal of Heat Transfer*, 116:679–685, August 1994.

[110] S.W. Akhtar. Droplet impaction on a hot surface. *http : //www.me.umist.ac.uk/asrgpage/Wip/drop_imp.html*, May 2003.

[111] M. Seki, H. Kawamura, and K. Sanokawa. Transient temperature profile of a hot wall due to an impinging liquid droplet. *J. Heat Transfer*, 100:167–169, 1978.

[112] M. di Marzo and D.D. Evan. Dropwise evaporative cooling of high thermal conductivity materials. *Heat and Technology*, 5(1-2):126–136, 1987.

[113] M. di Marzo, P. Tartarini, Y. Liao, D. Evans, and H. Baum. Evaporative coolind due to a gently deposited droplet. *Int. J. Heat Mass Transfer*, 36(17):4133–4139, 1993.

[114] H.F. Dawson and M. di Marzo. Multi-droplet evaporation cooling: experimental results. *AIChE Symposium Series*, 89(295):26–35, 1993.

[115] L. Schulze, R. Grisso, and R. Stougaard. Spray drift of pesticides. Cooperative Extension, Institute of Agriculture and Natural Resources, University of Nebraska-Lincoln.

[116] W.L. Grosshandler. Heat flux transducer calibration: summary of the 2nd workshop. Technical Report NISTIR 6424, National Institute of Standards and Technology (NIST), USA, November 1999.

[117] Nordtest method. Heat flux meters: calibration. Technical Report NT FIRE 050, NORDTEST, Finland, May 1995. ISSN 0283-7188.

[118] A.V. Murthy, B.K. Tsai, and R.D. Saunders. Radiative calibration of heat-flux sensors at NIST: facilities and techniques. *J. Res. Natl. Inst. Stand. Technol.*, 105(2):293–305, March-April 2000.

[119] F. Kreith and W.Z. Black. *Basic Heat Transfer*. Harper & Row, New York, 1980. ISBN 0-700-22518-8.

[120] C.A. Selby and B.A. Burgan. Joint industry project on: Blast and Fire Engineering for Topside Structures - Phase 2. Technical Report SCI-P-253, The Steel Construction Institute, Berkshire, UK, 1998.

[121] B.E. Vembe, K.E. Rian, J.K. Holen, N.I. Lilleheie, B. Grimsmo, and T. Myhrvold. *Kameleon FireEx 2000 Theory Manual*. ComputIT AS, Trondheim, Norway, June 2001. Report no. R0123.

[122] ComputIT. Computational Industry Technologies AS. Trondheim, Norway, 2003. (Personal Conversation).